

# **Nano-design of metal oxide electrodes for Li- and Na-ion hybrid energy storage**

Dissertation  
zur Erlangung des Grades  
der Doktorin der Naturwissenschaften  
der Naturwissenschaftlich-Technischen Fakultät  
der Universität des Saarlandes

von

**Hwirim Shim**

Saarbrücken  
2020

**Tag des Kolloquiums:** 30. November 2020

**Dekan:** Prof. Dr. Jörn Eric Walter

**Berichterstatter:** Prof. Dr. Volker Presser  
Prof. Dr. Tobias Kraus

**Akad. Mitglied:** Dr.-Ing. Frank Aubertin

**Vorsitz:** Prof. Dr. Guido Kickelbick

## Table of Content

Tag des Kolloquiums:.....	i
Table of Content.....	ii
Acknowledgements.....	iii
Zusammenfassung.....	iv
Abstract.....	v
1. Introduction to Electrochemical Energy Storage.....	1
1.1. Supercapacitors.....	3
1.1.1. Electrical double-layer capacitors.....	3
1.1.2. Pseudocapacitors.....	6
1.2. Batteries.....	7
1.2.1. Concept & mechanism.....	7
1.2.2. Li-ion batteries (LIB).....	8
1.2.3. Na-ion batteries (NIB).....	14
1.3. Hybrid EES.....	15
2. Electrochemical Measurement Techniques.....	19
2.1. Cyclic voltammetry / Galvanostatic cycling with the potential limitation.....	20
2.2. Galvanostatic intermittent titration technique (GITT).....	21
2.3. Electrochemical stability testing.....	22
3. Overview.....	27
4. Results and Discussion.....	30
4.1. Nanosized titanium niobium oxide/carbon electrodes for lithium-ion energy storage applications.....	31
4.2. Fast and stable lithium-ion storage kinetics of anatase titanium dioxide/carbon onion hybrid electrodes.....	52
4.3. Hybrid anodes of lithium titanium oxide and carbon onions for lithium-ion and sodium-ion energy storage.....	68
4.4. Comparison of organic electrolytes at various temperatures for 2.8 V–Li-ion hybrid supercapacitors.....	87
4.5. High voltage asymmetric hybrid supercapacitors using lithium-and sodium-containing ionic liquids.....	109
4.6. Understanding interlayer deprotonation of hydrogen titanium oxide for high-power electrochemical energy storage.....	124
5. Conclusions and Outlook.....	139
6. References.....	142

## ACKNOWLEDGEMENTS

I would like to thank my supervisor, Prof. Volker Presser, for giving me the opportunity to do my Ph.D. research in the Energy Materials group at INM - Leibniz Institute for New Materials. With his patient and careful guidance, I enjoyed the journey of 3.5 years as a Ph.D. student. This thesis was funded by the German Federal Ministry for Economic Affairs and Energy (BMWi) in support of the HyBaCap project (award number 03ET6113C) as a joint project between INM, Bosch, and IOLITEC.

I want to thank Prof. Tobias Kraus from INM and Saarland University for fruitful discussions and the effort to be the reviewer of my thesis. I am very grateful for Prof. Eduard Arzt, CEO of the INM, for his continuing support.

During my time working at INM, I received tremendous supports from colleagues all over the departments. Without the help and support I received, it would have been impossible to finish my thesis. I express my special thanks to current and former members of Energy Materials Group, whom I spend the most time with inside and outside INM. It was indeed an honor to work with wonderful colleagues. I thank Dr. Mesut Aslan, Dr. Choonsoo Kim, Dr. Eunho Lim, Anna Schreiber, Dr. Marco Zeiger, Dr. Nicolas Jäckel, Dr. Juhan Lee, Dr. Mathias Widmaier, Dr. Benjamin Krüner, Dr. Aura Tolosa, Dr. Simon Fleischmann, Dr. Pattarachai Srimuk, Öznil Budak, Yuan Zhang, Maike Ulbricht, Dr. Samantha Husmann, Mohammad Torkamanzadeh, Stefanie Arnold, and Lei Wang for the scientific help and all the great time we spent together.

I want to express gratitude to Dr. Robert Drumm, Dr. Marcus Koch, Dr. Ingrid Grobelsek, members of the workshop, and the analytical department for the kind support on technical aspects and measurements. I also want to thank Dr. Mario Marinaro and Dagmar Weirather-Köstner at ZSW for allowing me to visit ZSW and conduct measurements.

Finally, with my love, I thank mom, dad, Simsoo, and AB&B for pouring me unconditional love and support during my time as a Ph.D. student even from far away. Without your support, this would have been not possible.

## ZUSAMMENFASSUNG

Der wachsende Einsatz mobiler elektronischer Geräte und der weltweite Übergang hin zur Elektromobilität hat die Nachfrage nach Energiespeichern wie Lithium-Ionen-Batterien und Superkondensatoren stark erhöht. In diesem Zusammenhang besteht ein besonders großer Bedarf an Technologien, welche die Leistungsmerkmale heutiger Speichermodule in Bezug auf Energie und Leistung deutlich übertreffen können. Ein vielversprechendes Beispiel sind Hybrid-Superkondensatoren (HSC), welche Eigenschaften von Lithium-Ionen-Batterien und Superkondensatoren synergetisch kombinieren.

Der Fokus dieser Promotionsarbeit liegt auf dem Nano-Design von Hybridmaterialien aus Metalloxiden und Kohlenstoff für eine verbesserte elektrochemische Leistung in hybriden Lithium- oder Natriumionen-Energiespeichern. Die Hybridisierung von Metalloxid- und Kohlenstoffsubstrat kann durch eine angepasste Sol-Gel-Synthese erreicht werden, was zu einer homogenen und nanoskaligen Verteilung des Metalloxids im resultierenden Hybridmaterial führt. Elektroden, welche solche Hybridmaterialien einsetzen, können besser Leistungsmerkmale erreichen, als vergleichbare Komposit-Materialien, welche durch rein physikalisches Mischen zweier Phasen erreicht werden. Dieser Umstand lässt sich allerdings nicht pauschal für alle Arten von (Nano)kompositen anwenden. Neben dem Elektrodenmaterial beeinflusst auch die Wahl des Elektrolyten die Leistungsmerkmale von elektrochemischen Energiespeichern. Der Einsatz alternativer organischer Lösungsmittel oder Li- bzw. Na-haltiger ionischer Flüssigkeiten ermöglicht die betriebssichere Verwendung von Li- und Na-HSC Systemen selbst bei erhöhten Temperaturen bzw. erhöhter Zellspannung.

## **ABSTRACT**

The growing use of portable devices and a global transition to electric vehicles has tremendously increased the demand for energy storage devices such as lithium-ion batteries and supercapacitors. Especially the interest is established for better devices exceeding the energy and power performance of current technology. The hybrid supercapacitor (HSC) concept addresses the limits of each device and utilizes the distinct electrochemical features of lithium-ion batteries and supercapacitors. The focus of this Ph.D. thesis is the nano-design of hybrid materials of metal oxides and carbon for better electrochemical performance in lithium- and sodium-ion hybrid energy storage devices. The hybridization of metal oxide and carbon substrate can be achieved by tailored sol-gel synthesis, yielding a homogeneous distribution of nanosized metal oxide domain in the hybrid material. The performance of the hybrids was superior to the composite concept electrodes, but this is not a statement that can be generalized for all sorts of (nano)composites. In addition to the electrode material, also the electrolyte choice has a strong impact on the device operation and safety. The use of alternative solvents and Li- or Na-containing ionic liquids allows to increase the upper temperature and cell voltage at which Li- and Na-based systems can be safely operated at.

## 1. Introduction to Electrochemical Energy Storage

The world has stepped into the 4<sup>th</sup> industrial revolution era, and the growing demand of electricity seems critical and indispensable. The global action to substitute the high greenhouse gas emission towards the renewable energies such as wind power, solar energy, or geothermal energy has been growing, that the net renewable energy production increased doubled from 2010 to 2018, and reached 26% of the world electricity production in 2018.[1] In the first three months of 2020, 52% of the produced electricity in Germany was generated by the use of renewable sources.[2]. Moreover, Germany had recorded 77% of the entire electricity from renewable energy in 6 hours a day in 2019, which was enough to cover the demand of the entire country.[3] However, the source of renewable energies is not constantly available; for example, solar and wind power generation fluctuates as a function of weather patterns and geographic constrains. These issues are contrary to the requirement of plannable power generation to match energy demand and to ensure grid stability. Therefore, for a steady and continuous distribution of renewable energy production, the energy storage system is invincible for the grid.[4, 5]

Concerning reducing the emission, the expansion of vehicles is accelerating every year in the automotive industry, which also increases the demand for stable energy supply. The types and the possible application site of energy storage vary depending on the technique or mechanism of storing electrical energy. The energy can be stored directly as an electrical charge or can be converted to potential, kinetic, or chemical energy. For example, the pumped hydro storage or compressed air energy storage (CAES) store energy by converting electrical energy via potential energy. The flywheel is one example of the conversion of electrical energy to kinetic energy.[6] Electrochemical energy storage (EES) stores energy by converting electricity to chemical energy, for example, by cycling batteries through different states-of-charge (SOC).[6]

Among alternative storage technologies, EES may be the most promising candidate for fulfilling the demand for portable devices, e-mobility, and stationary applications for the green grid. Typical EES comprises two electrodes separated by a separator (microporous membrane) to avoid mechanical contact and connected by an ion-conducting electrolyte phase and current collectors. The difference in the electrochemical mechanism and the charge storage mechanism determines the type of the EES devices and its application range. The performance of the EES is determined by the rate or amount of energy stored.[4] For comparison among different systems, the values are normalized to their volume or mass. The amount of stored energy in a system is specific energy with a unit of Wh/kg, and the rate or speed of energy stored or released is specific power with a unit of W/kg. In **Figure 1**, the specific energy and specific power of different EES devices are shown, so-called a Ragone plot. The high specific power application, such as capacitors, establishes short charge and discharge time, which is suitable for applications with high input fluctuations.

The energy storage mechanism of capacitors or EDLC (electrical double-layer capacitor) is utilizing the reversible electrosorption of ions at the electrode/electrolyte interface. However, the stored energy is relatively low compared to the batteries. Contrarily the high energy applications are responsible for a larger amount of energy storage over a longer period, such as lithium-ion batteries (LIBs) or pseudocapacitors that possibly promote the Faradaic reactions but have low power than supercapacitors.

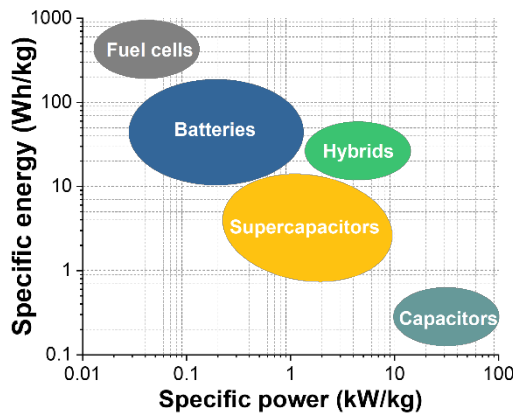


**Figure 1.** Ragone plot of energy storage devices and fuel cells representing specific power against specific energy based on the total cell mass.

For the practical application, the increased daily use of portable applications that require energy storage ranging from smartphones to passenger cars has drawn attention for better and smaller EES world-wide. Especially the electric vehicles require high power performance of EES due to peak power at a short range of time. The users of those devices with EES applications expect a better performance, which is longer using time, shorter charging time, and a longer lifetime with low-performance decay of the EES. This requires both high specific energy and high specific power, which is still not yet achieved from the individual devices due to its drawbacks; that batteries achieve less power density, and supercapacitors exhibit lower energy density. An alternative was presented by Ragone, namely a combination of two different EES, such as batteries and supercapacitors, to form a hybrid device that achieves better performance than individual devices utilizes the high energy or high power of each system.[7] To understand the feasibility of hybridization, the distinctive features and mechanisms of supercapacitors and batteries will be presented in the next chapters.

## 1.1. Supercapacitors

### 1.1.1. Electrical double-layer capacitors

Electrical double-layer capacitors (EDLC) store energy via electrosorption of the charged species at the interface of the electrolyte and polarized electrodes. Conventional EDLC devices consist of two symmetric porous carbon electrodes, which has a high surface area, separated by insulating separators soaked with charge containing electrolytes. When a potential difference is applied to the EDLC, the system is being charged (**Figure 2**). Ideally, the negatively polarized electrode has three possibilities to achieve charge neutrality, meaning the equal number of species at each interface, by (1) ejecting the negatively charged species (co-ion expulsion), (2) electro-adsorption of the positively charged species (counter-ion adsorption), and (3) exchanging the oppositely charged species (ion exchange).[8] There are several models to describe the electrical double layer formation and their dependency on ion species concentration such as Helmholtz, Gouy-Chapman, or Stern model. [8] During the discharge process, the electrons migrate opposite to **Figure 2**, from the negative to the positive electrode, which leads to the release and diffusion of charged species back into the electrolyte.

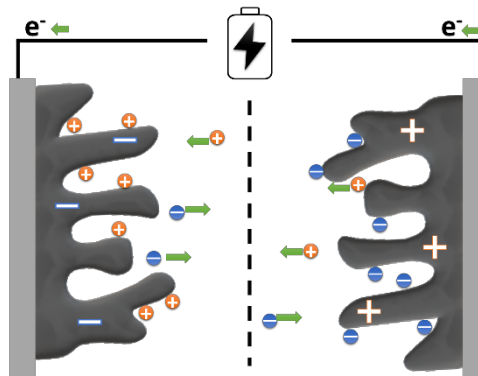


**Figure 2.** A schematic representation of EDLC during the charging process

The EDLC stores charge in analogy to a series of two parallel plate capacitors. Therefore, for each electrode, an electrical double-layer is formed. The capacitance of the EDL can be obtained from the following equation (Helmholtz equation; [Equation 1](#)):

$$C = \frac{Q}{U} = \frac{\epsilon_0 \epsilon_r}{d} A \quad \text{(Equation 1)}$$

where  $Q$  is the charge,  $U$  is the applied potential,  $\epsilon_0$  is the permittivity of vacuum,  $\epsilon_r$  is the dielectric constant of the electrolyte,  $d$  is the distance of the charge separation, and  $A$  is the interface area of the electrode surface with the electrolyte. The capacitance increases as the area of the increases and the distance between the charge separation decreases. From the calculated capacitance of a single EDL, the capacitance of the EDLC device level can be obtained via [Equation 2](#) since two parallel EDLs connected in series build asymmetric EDLC devices.

$$\frac{1}{C_{cell}} = \frac{1}{C_{pos}} + \frac{1}{C_{neg}} \quad \text{(Equation 2)}$$

where  $C_{pos}$  and  $C_{neg}$  are the capacitance of the positive and negative electrode, respectively. For better comparison of the capacitance in various devices, the capacitance can be normalized to the active mass of an electrode, in the case of symmetric EDLC, where the specific capacitance of both electrodes is the same.

The energy of the EDLC device follows Equation 3:

$$E = \frac{1}{2} CV_{max}^2 \quad \text{(Equation 3)}$$

where  $V$  is the applied voltage to the cell. The energy can be normalized by either mass (specific energy) or the volume (energy density) of the cell.

The power of an EDLC is respected to the energy and time of the EDLC device. The maximum power of the EDLC device can be extracted

$$P_{max} = \frac{V_{max}^2}{4R} \quad \text{(Equation 4)}$$

where the  $R$  is the equivalent resistance (ESR) of the EDLC. Like the energy metrics, the power is often normalized by mass or volume.

During continued operation, the initial capacitance cannot be maintained indefinitely. The loss of energy and capacitance is unavoidable due to factors such as the resistance of the components or self-discharging.[9, 10] Especially the resistance of interfaces at each terminal, electrode, separators, and electrolytes in the EDLC contribute to the ESR. The charging or discharging process could be the point of energy loss. Compared with the batteries, the rate of self-discharge in supercapacitors is higher, which leads to the loss of energy and charge.[11] Self-discharge of EDLC occurs independently of the charging or discharging process, but depending on the external factors, such as operating temperature, cell voltage, or the previous charging aspect, which cannot be easily monitored.[10] Cell voltage decay may be related to short-circuiting or due to irregular charge distribution.[12] The first type, self-discharge from short-circuiting of electrodes, which is referred to as an ohmic leakage, can be addressed by careful assembly of cells.[11] The inhomogeneous charge distribution, which frequently occurs with the double-layer formed in porous carbon, induces the charge redistribution that causes the potential drop in the cell. For materials such as porous carbon, charging speed is different at the outer electrode and the bulk, therefore, has different potential throughout the electrode. When the charging stops, the charges migrate through the materials to balance the inequality in the potential.[10] The charge redistribution is dependent, among other factors, on the state-of-charge, amount of electrolytes, voltage holding time, temperature, and the electrode material; therefore, it is difficult to distinguish the accurate contribution to the voltage decay.[12]

The most commonly used electrode material for EDLC is porous carbon because of the high natural abundance and suitable electronic conductivity. For the enhancement of the contact area of electrolyte and the electrode, highly porous activated carbon is employed as electrode material in the conventional EDLC. Activated carbons provide a highly porous structure with a high specific surface

area (SSA, typically 1500-3000 m<sup>2</sup>/g) and promising capacitance to the EDLC device.[8] To enhance the performance of the EDLC, advanced carbons can be used with a higher surface area (increased charge storage) or optimized porosity (to speed up ion transport).[13, 14] Typically, modification of the carbon pore structure involves activation, either involving physical activation in a gas (like CO<sub>2</sub>) or wet chemical activation (e.g., etching with KOH).[15]

Commonly, pores are differentiated by size, resulting in micropores (pore size <2 nm), mesopores (2-5 nm), and macropores (pore size > 50 nm), as defined by the International Union of Pure and Applied Chemistry (IUPAC).[16] Macropores, including the ones formed by space in-between the particles, mainly contribute towards ion exchange, while the charge storage capacity of micropores is the largest.[17]

Larger pores facilitate fast ion transport and cation/anion exchange processes. However, large pores fail to provide a large surface area and, therefore, limit the achievable charge storage capacity. Vice versa, small pores may kinetically limit ion transport but will contribute the most to the charge storage capacity.[18] It has been reported both theoretically and experimentally that the pore size of carbon influences the capacitance.[19-21] The ion species are transported in the electrolyte and within meso- and macropores with a solvation shell and have a larger size compared to bare ions. Several studies showed that higher capacities are achieved when the pore size larger than the bare ion but smaller than the solvated ion.[20, 21] Partial loss of the solvation shell and preferred positioning of the ions in places of high confinement within carbon nanopores benefit the capacity enhancement.[22] This motivates the need for optimized pore size for carbon used and the appropriate selection of salt and solvents for EDLCs. EDLCs can use a variety of electrolytes, including electrolytes based on aqueous and organic solvents or ionic liquids. The selection of appropriate electrolytes for EDLC has influenced the electrochemical performance. The electrolyte has the electrochemical stability limits, which determine the safe operation potential range of EDLC and the specific energy/power of the device.[8] Also, the ionic conductivity of electrolyte influences power performance (Equation 4) since the ionic conductivity is inversely proportional to the resistance.[8]

An aqueous electrolyte has been reported advantageous due to its low cost, and high conductivity (~1 S/cm), for instance, using acid and alkali-based chemistry.[23] The power performance is high, but there is a limited electrochemical stability window of 1.2 V; therefore, restricted energy performance is resulted in using the voltage range of 1 V.[8, 24] The possibility of enlarging the operation voltage range is dependent on a combination of electrode material and the electrolyte.[24, 25] Bu et al. has reported the 'water-in-salt' concept as an electrolyte for better rate performing EDLC cell at a wide operating voltage.[26] Also, Demarconnay et al. [27] and Gao et al. [28] investigated EDLC cells employing an aqueous electrolyte with neutral pH value, which resulted in enhanced cycling performance.

The most commonly used organic electrolyte used in EDLC comprises salt and organic solvents, such as propylene carbonate (PC) and acetonitrile (ACN).[8] PC is selected as a solvent for electrolyte due to its wide electrochemical stability window and lower vapor pressure.[29] However, the conductivity of PC-based electrolyte ( $\sim 15$  mS/cm at 25 °C) is rather low ascribed to the high viscosity of PC. ACN has low viscosity, consequently has higher ionic conductivity when utilized as a solvent for electrolyte ( $\sim 35$  mS/cm at 25 °C) therefore, allowing the power of the EDLC device to be higher, but the volatility is a problem to operation at elevated temperature, with a safety risk.[8, 30] The selection of the salt requires careful attention considering the possibility of hindrance/enhancement to the ionic conductivity of the electrolyte.[31] Quaternary ammonium salts are commonly utilized in combination with organic electrolytes, such as tetraethylammonium tetrafluoroborate (TEA-BF<sub>4</sub>).[31, 32] The electrolyte concentration of 1-2 M is used to maximize the conductivity and, thereby, to enable high power applications.[33]

McEwen et al. [34] have addressed the possibility of employing ionic liquids (ILs), especially imidazolium-based cations, 1-ethyl-3-methylimidazolium (EMIM), and various anions (BF<sub>4</sub><sup>-</sup>), as an electrolyte for the EDLCs, since the ionic liquid has a greater operational temperature and high electrochemical stability window.[35] Some ILs can be used directly as electrolytes, such as *N*-butyl-*N*-methylpyrrolidinium bis(trifluoromethanesulfonyl)imide (PYR<sub>N</sub>-TFSI) and still can achieve a promising result without compromising the benefits of ILs.[36, 37] The volatility of ionic liquids is negligible, mitigating the safety risk, and the nature of IL that is highly ionized and higher electrochemical stability window compared to the aqueous and organic electrolytes. The ionic conductivity of the IL is rather low compared to the organic electrolyte ( $\sim 5$  mS/cm at 25 °C). The appropriate combination of electrode material and the electrolyte is critical since the size of the ionic species in ILs is much larger than in the organic electrolyte. Jäckel et al. [38] have the enhanced electrode expansion of ionic liquid supercapacitors (up to 2%), which possibly compromise the stability of EDLC. Yet, the reversible volume change can also be used for actuation, as demonstrated by the group of Alvo Aabloo.[39]

### **1.1.2. Pseudocapacitors**

Among the energy storage process at the electrodes in EES other than EDLC, most of the processes follow Faraday's law. A surface redox reaction, intercalation of ions into interstitial sites, alloying, or conversion reaction may follow Faraday's law, which involves charge transfer across the fluid/solid interface. The energy storage mechanism of pseudocapacitive materials follows surface redox reaction or intercalation; however, the kinetic response of the electrochemistry shows capacitor-like electrosorption.[40] Since the behavior of the material show characteristics of both capacitor-like or battery-like, it is expected to achieve higher energy density than EDLC and enhanced kinetic than LIBs. Augustyn et al. [41] distinguished three major types of pseudocapacitance, which are underpotential

deposition (adsorption pseudocapacitance), redox pseudocapacitance, and intercalation pseudocapacitance. The underpotential deposition typically happens with a difference in redox potential that the one metal ion forms a layer at another metal's surface. Lead deposition on the gold surface is an example of pseudocapacitive behavior of underpotential deposition.[40] The electrochemical response of such materials sometimes does not show a pronounced surface Faradaic reaction.[40] The redox pseudocapacitance develops as the charge migrates and adsorbs on the material surface, followed by subsequent Faradaic reaction at the material surface.[40, 41]. A typical example of the redox pseudocapacitance is shown from the electrochemistry of the RuO<sub>2</sub> thin film electrode in acidic electrolyte.[42]. Lastly, the intercalation pseudocapacitance results from the insertion of lithium or sodium ions in a redox-active insertion host material, using a Faradaic reaction. The change in crystallographic phase from the ion-insertion is not observed, for example, the insertion of lithium-ion in Nb<sub>2</sub>O<sub>5</sub>. [43, 44]

## **1.2. Batteries**

### **1.2.1. Concept & mechanism**

A battery stores electrical energy by converting it to chemical energy using the electrochemical redox process.[45] An electrochemical cell, a basic concept of battery, consisting of negative and positive electrodes connected to an electric circuit, separated by a charge containing electrolyte, mostly consisting of an organic solvent with a dissolved inorganic salt. The electrodes are separated by a microporous membrane to avoid mechanical contact and, therefore, a short circuit between the electrodes. The separator often consists of cellulose fibers, glass fibers, or polymers and is permeable for electrolyte and ions. Since the electrodes are employed based on the difference of chemical potential, the active material at the anode and the cathode are different.

The negative electrode is often called the anode, and it releases electrons, and the electrode is simultaneously oxidized to the electrical circuit; the released electron is transferred to a positive electrode. The positive electrode is called the cathode, and it receives the electron released by the anode, and reduction takes place at the cathode during the reaction.[45] Conventionally the name anode is the electrode where discharge occurs, and the cathode is where charge occurs; the anode and cathode terms are swapped from the direction of an electron moving during a charge or discharge of a cell. Therefore, to avoid confusion, anode refers to the negative electrode, which stores lithium when the battery is charged. Since the electrodes are employed based on the difference of chemical potential, the active material at the anode and the cathode are different.

Batteries are distinguished mainly in two types (primary and secondary battery) based on the possibility of recharging. A primary battery is designed for a single-use, and the system is not designed to allow (safe) recharging of the device once it has been discharged. Such devices can be optimized for high energy storage applications or more compact form factors (e.g., for hearing aids). Contrarily a

secondary battery, the so-called rechargeable battery, is capable of multiple-use, by a reverse of the electrochemical reaction occurred during discharge with external electricity. Therefore, with applied electricity, the oxidation of a positive electrode, and the reduction of negative electrode takes place. The Gibb's free energy of the cell is determined from the theoretical voltage of a battery,  $E^0$ , the number of electrons participating in the electrode redox reaction,  $n$ , and the Faraday constant,  $F = e N_A = 96\,485,309\text{ C/mol}$  (Equation 5). The theoretical voltage of a battery (cell) can be calculated from Equation 6, the sum of the standard reduction potential of a cathode, and the standard oxidation potential (the inverse of reduction potential) of the anode.

$$\Delta G^0 = -nFE^0 \quad \text{(Equation 5)}$$

$$E_{cell} = E_{Cathode} - E_{anode} \quad \text{(Equation 6)}$$

From the electrode materials in the battery, the theoretical capacity of a cell can be calculated. The theoretical capacity articulates the charge, which is the maximum quantity of electricity that the cell can provide from the electrochemical reactions, with the unit of Ah, as presented in Equation 7.

$$Q = nF \quad \text{(Equation 7)}$$

From the obtained cell voltage and the capacity of the cell, the theoretical energy of the cell can be determined, and the unit is Wh, as expressed in Equation 8.

$$\text{Energy} = E_{cell}Q \quad \text{(Equation 8)}$$

For better comparison, the term specific energy is used, that the calculated energy normalized to the volume or mass of the prepared battery cell, Wh/L, or Wh/kg, respectively.

### 1.2.2. Li-ion batteries (LIB)

Chilton Jr. and Cook first reported the concept of the lithium battery in 1962 for satellite applications.[46] In the early 1970s, the introduction of lithium metal-based battery employing nonaqueous electrolytes from Matsushita Battery (lithium/carbon monofluoride) and Sanyo (lithium / Manganese dioxide).[47] Since these were primary batteries, many research activities were conducted to evolve to lithium secondary batteries. In 1974, Whittingham et al. [48, 49] introduced  $\text{Li}_x\text{TiS}_2$  as a lithium intercalation material. The initial rechargeable batteries with lithium metal were found to have issues with lithium dendrite formation during the recharge process. Due to the remaining safety concerns, lithium intercalation materials have drawn attention to be the replacement of lithium metal anode. Goodenough [50], Armand[51], Yoshino [52], and many others have continued the research on improving the concept and performance, and finally, Sony presented the first commercially available lithium-ion battery (LIB) in 1991. In 2019, Goodenough, Whittingham, and Yoshino were awarded the Nobel Prize for the development of LIB.

A conventional LIB cell consists of two electrodes, a separator, and a lithium-containing electrolyte, as shown in **Figure 3**.

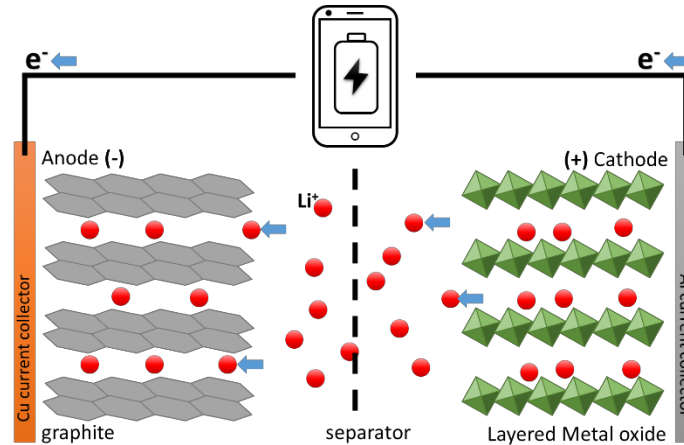
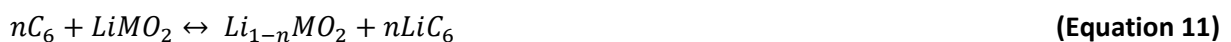


**Figure 3.** Schematic representation of a typical Li-ion battery during the charging process.

State-of-the-art LIBs use graphite as anode and transition metal oxide that contains lithium as a cathode, such as  $\text{LiMn}_2\text{O}_4$  (LMO) or  $\text{LiFePO}_4$  (LFP).[47] During charging and discharging, the amount of lithium in the anode and cathode varies. The anode coated on copper foil and cathode coated on aluminum foil are separated in an organic electrolyte, which has about 1 M lithium-containing inorganic salt dissolved in a mixture of carbonate-based solvent.[53] The reason for the selection of the current collector is that copper starts to dissolve from 3.2 V vs.  $\text{Li}/\text{Li}^+$ , which would not be suitable for coating cathode material. Also, the aluminum reacts with lithium-ion at a potential lower than 0.6 V vs.  $\text{Li}/\text{Li}^+$ , which is not suitable as a current collector for anode material.[54] Commercially available cylindrical 18650 LIB cell can exhibit specific energy of 250 Wh/kg at a cell nominal voltage of around 3.7 V, employing graphite as anode, and  $\text{LiNi}_{1-x-y}\text{Mn}_x\text{Co}_y\text{O}_2$  (NMC) or  $\text{LiNi}_{0.8}\text{Co}_{0.15}\text{Al}_{0.05}\text{O}_2$  (NCA) as the cathode.[55]

The equations below demonstrate the principle electrode materials and reactions of a typical LIB where  $\text{MO}_2$  is a transition metal oxide (e.g., Co, Ni, Mn, and Al) cathode, and  $\text{C}_6$  is a graphite anode.



During the charging process of a LIB, external energy is applied to the cell leading to current flow between two electrodes. The current flows as long as the cathode material is being oxidized, resulting in the extraction of lithium ions from the cathode into the electrolyte. The electrons are transferred via the external circuit from the cathode to anode, proceeding the anode to be reduced and the intercalation of  $\text{Li}^+$  ion from the electrolyte into the graphite interlayers, theoretically yielding up to 375 mAh/g with fully charged  $\text{Li}_6\text{C}$ . [56] During the discharge process of a LIB, the cell undergoes the reverse of the charging process.

Graphite is an appealing candidate for anode material for LIB due to its low cost, high availability, high reversibility, and good electrochemical performance.[57] The intercalation of lithium-ion into graphite occurs at the very low potential between 50 mV and 300 mV vs. Li/Li<sup>+</sup>, which is below the lower stability limit of the carbonate-based organic electrolytes. Also, the mechanical volume change of about 10% during the intercalation enlarge the safety concern of the LIB.[58, 59]

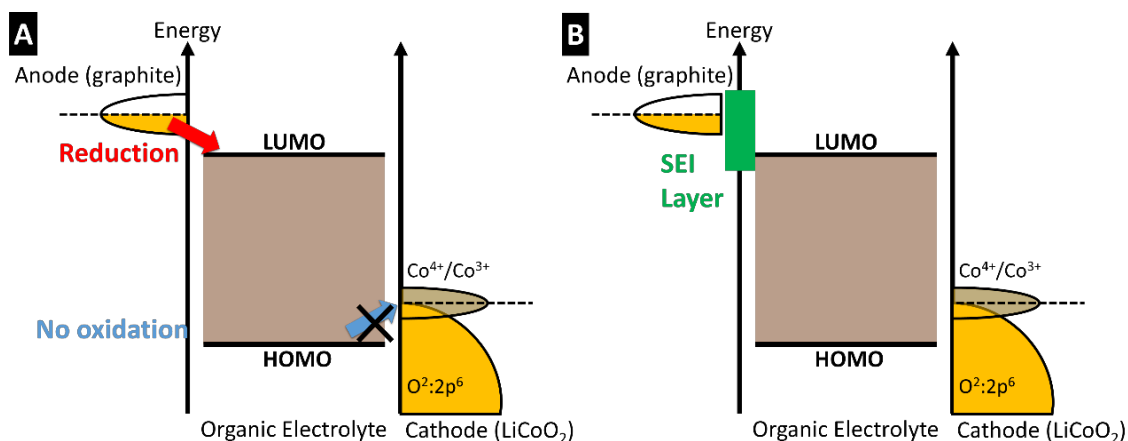


**Figure 4.** Schematic representation of electrochemical energy of anode, carbonate-based electrolyte and cathode, and their relative energy positions. Modified from Ref. [60].

According to the energy state, the higher electrochemical potential of graphite than the lowest unoccupied molecular orbital (LUMO) of electrolyte would result in a reduction of electrolyte (**Figure 4A**). However, the reduction of electrolyte at the initial stage allows the formation of solid electrolyte interphase (SEI) at the anode-electrolyte interface (**Figure 4B**).[60] The as-formed SEI layer serves as a passivation layer, which allows the lithium diffusion but prevents the further reduction of the electrolyte triggered by the energy gap, enhancing the longevity of the cell.[60] The formation of the SEI layer occurs depending on the selection of electrode, solvent, and lithium salt. For example, when 1 M LiClO<sub>4</sub> in PC is employed as the electrolyte with a graphite anode, the continuous decomposition of the electrolyte is observed.[61] It has been reported that some electrolyte additives enable better cycling stability of the graphite-based LIBs.[62] An ideal SEI layer behaves electronically insulating but lithium conductive and is evenly coated thoroughly in between the interface. The SEI formation is an irreversible process that partially depletes the material composition of the cell, consumes the lithium from the electrolyte, and it also increases the possibility of lithium deposition on the surface are the reported drawbacks.[60, 63]

Beyond graphite, intercalation materials that do neither exhibit SEI formation nor a significant volume expansion have drawn significant attention. A very attractive candidate is lithium titanite ( $\text{Li}_4\text{Ti}_5\text{O}_{12}$ , LTO) because of its high lithium intercalation/de-intercalation potential at around 1.55 V vs. Li/Li<sup>+</sup>. [64] This operational voltage for an anode lays within the stability limit of the conventionally used LIB electrolytes (around 0.8 V vs. Li/Li<sup>+</sup>), which eliminates the SEI formation and electrolyte decomposition. [65] Owing to the negligible volume change during the intercalation, LTO is reported to achieve high cycling stability and high Coulombic efficiency. [56, 66]

The intercalation of three lithium-ions utilizes the theoretical capacity of 175 mAh/g, according to Equation 12. LTO has been reported to have a low electrical conductivity of  $10^{-13}$  S/cm, and a low lithium-ion diffusion, which has a significant impact on the rate capability. [64, 67-69] Various approaches to enhance the intrinsic conductivity of LTO were investigated to strengthen the electrochemical performance, such as generating deficiency or vacant state of oxygen in the LTO structure. [70, 71] The process is mainly conducted by adjusting the condition of thermal treatment using different gas atmosphere or vacuum [70] leading to higher preference in the implementation of conductive source by the mechanical or chemical approach. [72]



Implementing conductive additives may be accomplished with composites or hybridization of the electrochemically active phase with carbon. Initially, the physical admixing of the conductive carbon dominated the research activities (i.e., composites). [47] Researchers investigated numerous routes of preparing nanocomposite LTO electrodes, using, for example, carbon black, [73, 74] carbon nanotubes, [75], or graphene [76, 77]. Hybridization of LTO, for example, can be accomplished by surface coating with a carbon source during the synthesis. Since the synthesis of LTO is performed at the range of 700-1000 °C, the carbonization of sucrose, [78] glucose, [79] organic solvents, [80, 81] acids, [82] or the deposition of gaseous species [83] on the surface of LTO can be used. Either via composite design or hybridization: the goal of both approaches is to have an intimate interface between the electrically conductive and the Faradaic phase within the electrodes.

The importance of the sub-micrometer length scale homogeneity of carbon / LTO distribution was investigated, for example, by Widmaier et al. [84]. Widmaier et al. reported that the stability of the electrode, which has enough conductive phase content, degrade redundantly, mainly ascribed to the hindered charge percolation and local degradation from the non-homogeneous distribution of the conductive phase. [84] The relative narrow operational voltage of LTO, and its low specific capacity and specific energy compared to graphite remain challenges when combined with a cathode to a LIB cell.

Similar to the characteristics of LTO, titanium- and niobium-based oxides have drawn attention due to their relatively high operation potential above 1.0 V vs. Li/Li<sup>+</sup> and a reported capacity of around 170-250 mAh/g.[85-87]. Colin et al. (Ti<sub>2</sub>Nb<sub>2</sub>O<sub>9</sub>) and Goodenough et al. (TiNb<sub>2</sub>O<sub>7</sub>) reported for the first time in 2011 that the titanium niobium oxide is electrochemically active and feasible for lithium intercalation (**Figure 5**).[88, 89]

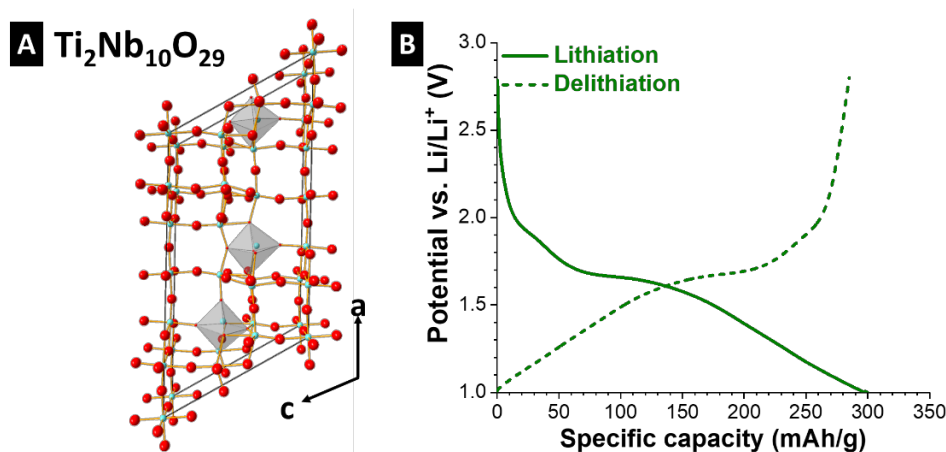


**Figure 5.** (A) A crystal structure of Monoclinic TNO (Ti<sub>2</sub>Nb<sub>10</sub>O<sub>29</sub>), and (B) the electrochemical lithium storage profile from the galvanostatic charge-discharge cycle of TNO, adapted from Ref. [90].

TiO<sub>2</sub> and Nb<sub>2</sub>O<sub>5</sub> have been separately explored. The mixed metal oxide phase TiNb<sub>2</sub>O<sub>7</sub> has a theoretical capacity of 388 mAh/g utilizing the redox couple of Ti<sup>4+</sup>/Ti<sup>3+</sup>, Nb<sup>5+</sup>/Nb<sup>4+</sup>, and Nb<sup>4+</sup>/Nb<sup>3+</sup> and up to 5 lithium-ion intercalations into its monoclinic structure.[88] Ti<sub>2</sub>Nb<sub>10</sub>O<sub>29</sub> has a similar theoretical capacity of 396 mAh/g.[91] The overlap of Ti and Nb redox couples occurs at the potential between 1.3-1.6 V vs. Li/Li<sup>+</sup>, which is outside of the SEI formation potential of electrolyte, resulting in a stable rate capability performance.[43, 91-95] Recently, the Toshiba Corporation utilized the TNO as a new anode and achieved LIB (SCiB), yielding high volumetric capacity and a long lifetime[96].

Currently, alternative anode materials for LIB are under investigation extensively. The, but such as Si anode,[97] Li metal,[98] alloying,[99] or conversion materials,[100] which promise higher capacities than graphite anode.[101] Si anode has a high theoretical capacity over 4000 mAh/g; however, the high volume expansion (~400%) during lithiation leads to cracks, which hinders the practical use of it as an anode for LIBs.[97] Lithium metal is still under investigation to avoid dendrite formation. Alloying and conversion materials also have been reported with similar issues of irreversible capacities which leads to low cycling performance.[99, 100]

Typical cathode materials employed for LIBs are layered transition metal oxides such as  $\text{LiCoO}_2$  (LCO, theoretical capacity: 274 mAh/g), NCA (279 mAh/g), NMC (280 mAh/g), olivine-type materials such as LFP (170 mAh/g), and spinel-type materials such as LMO (285 mAh/g).[102] There remains a strong demand for new cathode active materials, which give a significantly higher specific energy and energy density as this may reduce the number of batteries needed for a battery pack and thus weight/volume and the total cost.[103] The higher specific energy/energy density can be achieved by either increasing the capacity of the cathode material or by increasing its working potential. The main challenge for high voltage cathode materials, such as the spinel  $\text{LiNi}_{0.5}\text{Mn}_{0.5}\text{O}_4$ , is to find a suitable electrolyte which is stable at these high potentials.

The conventionally used electrolyte of LIBs is around 1 M lithium salt, mainly  $\text{LiPF}_6$ , dissolved in a mixture of linear or cyclic carbonate solvents, such as dimethyl carbonate (DMC) or ethylene carbonate (EC). Most frequently, carbonates, such as open-chain carbonates as ethyl-methyl carbonate  $\text{C}_4\text{H}_8\text{O}_3$  (EMC), diethyl carbonate  $\text{C}_5\text{H}_{10}\text{O}_3$  (DEC), and dimethyl carbonate  $\text{C}_3\text{H}_6\text{O}_3$  (DMC), or cyclic carbonates like ethylene carbonate  $\text{C}_3\text{H}_4\text{O}_3$  (EC) and propylene carbonate  $\text{C}_4\text{H}_6\text{O}_3$  (PC), are used.[53] Commercially available electrolytes have short names based on the types of salt and solvents. For instance, LP stands for  $\text{LiPF}_6$  salt, and LC stands for  $\text{LiClO}_4$  salt, and the following numbers indicate the type of solvent or solvent mixtures. LP30 is an electrolyte of 1 M  $\text{LiPF}_6$  in EC:DMC (1:1 by mass), LC30 is an electrolyte of 1 M  $\text{LiClO}_4$  in the same solvent mixture, and LP57 is an electrolyte of 1 M  $\text{LiPF}_6$  in EC:PC:DMC (1:1:3 by mass).

Requisites for an electrolyte include a high level of electrochemical and chemical stability, chemical inertness, low flammability, high operating temperature range, as well as cost efficiency and environmentally friendly properties. The reason for employing a mixture of solvents is to combine beneficial properties, such as ion mobility and electrochemical stability.[53] It is known that the open-chain carbonates have low viscosity and moderate dipole moments. In contrast, cyclic carbonates have higher viscosity and high dipole moments. In order to achieve the best properties, cyclic carbonates are often combined with open-chain carbonates in electrolytes.[45, 65] Therefore, EC is employed for its high permittivity and high melting point, and open-chain carbonates (DMC, DEC) or carboxyl esters are employed for the low viscosity, consequently providing high conductivity. The ionic conductivity of commercially available electrolytes achieves 10 mS/cm.[65] The lithium-containing salts traditionally used in LIB are lithium hexafluorophosphate ( $\text{LiPF}_6$ ), lithium perchlorate ( $\text{LiClO}_4$ ), lithium tetrafluoroborate ( $\text{LiBF}_4$ ), or lithium hexafluoroarsenate ( $\text{LiAsF}_6$ ).[104]

The electrolyte combinations above-mentioned are all liquid electrolytes that are flammable and prone to lithium dendrite formation. As a promising alternative, solid electrolytes have emerged, such as Li-ion conductor (LiSICON), lithium argyrodites, perovskites, and glass materials.[105] However, there remain some challenges needed to overcome, including low ionic conductivity, poor electrode/electrolytes.[106]

### 1.2.3. Na-ion batteries (NIB)

LIB is delivering promising energy and power in commercial EVs. However, lithium is not the most abundant material on Earth. An especially large portion (~30%) of the cost of the LIB is the cathode material cost.[107, 108] As a result of the increasing demand for batteries, scarcity of fossil resources of lithium, and the resulting rise in price, further alternatives are sought. The alternative to LiB, NIB has drawn attention since sodium is very abundant in the Earth and promises a more environmentally friendly and simple production of electrode materials. Excluding lithium, sodium is the lightest and smallest (1.02 Å) alkali metal.[109-111] In the 1970s and 1980s, when LIB was extensively studied, NIBs were also investigated alongside; however, the LIB research was developing more rapidly than NIB.[112] One of the commercially available sodium-based batteries is a sodium-sulfur battery that utilizes molten sodium metal, which has an operating temperature of about 300 °C. [113] The charge storage mechanism of rechargeable NIB is very similar to LIB as in **Figure 3**, that all the lithium-ion are replaced by the sodium ions, consists of hard carbon anode and layered oxide cathode.[114] Since the standard reduction potential of Na/Na<sup>+</sup> (-2.71 V) is close to Li/Li<sup>+</sup> (-3.04 V), various lithium storage systems were explored as sodium ion hosting material, and the results were promising.[115-118]

The electrolytes from LIBs were also explored by replacing the lithium-ion to sodium-ion in the lithium-containing salts, for example, NaPF<sub>6</sub>, NaClO<sub>4</sub>, or NaTFSI, in combination with the linear and cyclic carbonate solvent mixtures.[110, 119] It has been expected that the SEI layer formation is more challenging since the solubility of the decomposed species in Na-based electrolytes are higher, so careful approach on the selection of electrolyte is invincible.[118] Also, the role of additives in the electrolyte and the binders are extensively studied that the selection of polyvinylidene fluoride (PVdF) binder in the electrode material does not deliver stable electrochemical performance. However, the addition of fluoroethylene carbonate (FEC) enhances cyclic stability effectively[120, 121]. Replacing the PVdF binder with an environmentally friendly water-based carboxymethyl cellulose (CMC) binder enhanced the reversibility of the NIB cell even without the addition of FEC additive.[122]

It has been demonstrated that the FEC additive could increase the SEI stability on the sodium metal electrode.[119] Also, it prevents the decomposition from EC and DMC to the well-known by-product ethylene glycol bis-(methyl carbonate) because FEC has higher oxidation potential than those of EC and DMC.[119] This leads to the result that FEC will be reduced primarily at a potential of about 0.7 V and forms a beneficial SEI on the electrode.[121] These can finally enhance stability. By reduction of FEC, a polymer is formed, but the nature of the precise compound is still under debate.[119, 121, 123] Graphite has been used widely for commercial LIBs; however, the insertion of the Na-ion into graphite interlayers requires a combination of physical and electrochemical approaches yielding very low inserted Na-ion with  $\text{NaC}_{64}$ . [118] Hard- or soft-carbons with a lower degree of crystallinity have been explored, resulting in better Na-ion hosting environments.[124] Benefiting the relatively lower carbonization temperature of the soft carbon around 700 °C, the reversibility of the Na-ion intercalation is enhanced than using graphite, yielding higher capacity than graphite-based LIB.[118] Contributing the structural advantage of hard carbon, consist of both graphene-like layer structure and micropores, the study by Stevens and Dann reported the reversible Na-insertion/extraction into hard carbon at room temperature with a reversible capacity of around 300 mAh/g.[118, 125] Not only carbon materials, but also the titanium-based metal oxides, such as  $\text{TiO}_2$  [126] or LTO [127], or Na alloying material, such as SnSb,[128] red phosphorus/carbon composites,[129] Sb/C composites,[130] or layered  $\text{SnS}_2$ -reduced graphene oxide composites,[131] and conversion type materials, like Molybdenum Phosphide and  $\text{Sb}_2\text{O}_3$ , [132] are explored for possible anode for NIBs. Since most of the studies for the NIB focus only on the anode material, there is a great challenge to investigate the performance of NIB at a full-cell level. The cathode materials investigated for NIB used in 1988 was P2 type  $\text{Na}_x\text{CoO}_2$ . [133] Widely investigated cathode materials for NIBs are two- or three-dimensional layered oxides such as  $\text{Na}_{1-x}\text{MO}_2$ , where M is transition metals (e.g., Mn, Ni, Ti, V, Cr, and Co) and metal fluorides. Also, NASICON type materials or polyanion materials such as phosphate-based or pyrophosphate-based materials, for example,  $\text{NaVPO}_4\text{F}$ ,  $\text{Na}_3\text{V}_2(\text{PO}_4)_2\text{F}_3$ , and  $\text{Na}_4\text{Co}_3(\text{PO}_4)_2\text{P}_2\text{O}_7$ , have been intensively studied for NIBs in the specific capacity range of 120-200 mAh/g.[134]

### 1.3. Hybrid EES

As seen from **Figure 6** below, the electrochemical profiles of EDLC and a LIB demonstrates a big difference. The specific power and energy performance of each device has distinctive features, as the Ragone plot in **Figure 1** displays. The hybridization of the devices or materials possesses the capability of introducing enhanced specific power, specific energy, or cycling stability on a device level (**Figure 6C**), or on a material level (electrodes), as seen from **Figure 6D**.

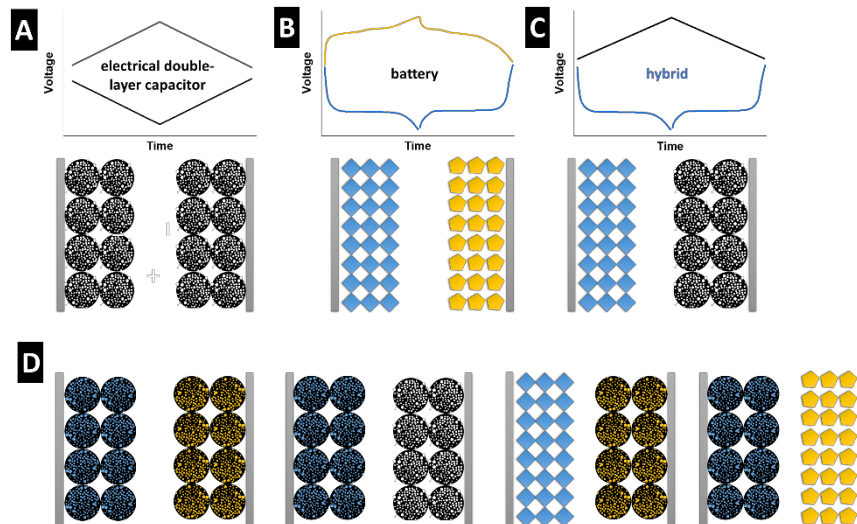


**Figure 6.** Schematic concept of electrode components of (A) an EDLC, (B) a lithium-ion battery, and (C) a hybrid supercapacitor device that utilizes LiB anode and EDLC cathode. Concept of the material level design of (D) composite material, and (E) hybrid material. Adapted from Ref. [30].

A few of the following aspects require consideration for a beneficial architecture of hybrid electrodes. First, the conductivity of the hybrid electrode is required to be high for better electrochemical performance.[130] Moreover, an adequate method needs to be selected for a nanoscopic scale of hybridization, which positively influences the process parameters of the hybrids, for example, for the homogeneous distribution of carbon substrates and Faradaic materials, or the good adjustment in the ratio of carbon to Faradaic material.[67] A large interface to electrolyte or large reactive sites is favored for high power performance, which possibly achievable via adjustment of the thickness of deposition or coating.[130] The adequate adjustment of ratio between the Faradaic material and carbon substrate is crucial to meet the agreement in the power and energy performance.[130]

### 1.3.1. Device-level hybridization

A hybrid supercapacitor (HSC) concept was introduced to improve the limiting aspects of each device and to benefit and to enhance the distinct advantageous electrochemical features. Amatucci et al.[7] introduced the concept of a device, which is composed of Faradaic materials as the negative electrode (anode), such as LTO, and highly porous carbon as the positive electrode (cathode), and a Li-containing electrolyte. During the charging process, the Li-ion is inserted into the interstitial sites of LTO, which is the charge storage mechanism of LIB. At the same time, the EDL is formed at the positively polarized AC-electrolyte interface, and electrosorption of anions occurs.[72, 135-137] The concept is often called asymmetric hybrid supercapacitors (AHSC) or just HSC, where one electrode employs electrosorption as an energy storage mechanism, and the other electrode employs lithium-ion intercalation.

One of the commercially available AHSC is the so-called lithium-ion capacitors (LIC), which consists of a graphite anode, activated carbon cathode, and organic electrolyte like LIB.[138, 139] Since both

anode and cathode cannot serve as the lithium source in this LIC, the lithium in the electrolyte will be consumed, which induces the decrease in lithium concentration, consequently a decrease in conductivity. To avoid this issue, the graphite anode needs to undergo a pre-lithiation step.[8, 138] The anions from the lithium-containing salt ( $\text{PF}_6^-$ ,  $\text{ClO}_4^-$  or  $\text{TFSI}^-$ ) in the electrolyte serves as a charge carrier in the electrosorption process at the EDL.[138] The possible combinations of the asymmetric HSCs are broad in the selection of electrolyte, lithium-ion intercalation material, and porous EDL material, such as  $\text{MnO}_2$ /activated carbon employing aqueous electrolyte device has been explored.[25] To achieve the optimized performance of a hybrid cell, the properties of each anode and cathode need to be considered to hybridize into one device synergistically. When building a hybrid device using LTO anode and LMO-AC electrode, the capacity at 100% SOC LTO anode should be equal to the 100% SOC at LMO-AC cathode at the maximum cell voltage, since the same amount of charge is applied to each electrode. Since the theoretical capacity of LTO anode (Faradaic material) is higher than the LMO-AC cathode (a mixture of Faradaic and capacitive), an adequate mass balancing between the two electrodes is necessary.[8, 140] The inequality in the capacities of two electrodes in a cell can procure lower cell voltage and possible degradation of an electrode due to exceeding the stability limit.[140] Possible outcomes of the combination of hybrid devices are as following: LIB anode//capacitive cathode, LIB anode //hybrid cathode, hybrid anode//capacitive cathode, hybrid anode//hybrid cathode, or hybrid anode//LIB cathode.

### **1.3.2. Electrode material level hybridization**

The concept of hybrids includes the combination of a Faradaic charge storage material and a conductive carbon substrate to fabricate an active material for electrochemistry. There are two main concepts: composite materials and hybrid materials. Often the Faradaic charge storage materials are intrinsic insulators. Therefore, introducing a conductive additive during the electrode preparation process is a common approach from both research and industry; this approach is mainly used for the preparation of battery electrodes by physical admixing of a lithium-ion intercalating Faradaic material and carbon black. The prepared electrode is identified as composite electrodes, and so far, many researchers have reported such material combinations.[72, 137]

The other variations investigate a combination of a Faradaic charge storage material and nanoporous carbon on a nanoscopic level during the synthesis procedure, which produces hybrid materials.[72, 137] The nanoscopic implementation of a Faradaic material into carbon nanotubes,[141, 142] carbon nanofibers,[43, 143] carbon onions,[87, 90, 144] graphene,[145-147] or activated carbon [148] are possible examples of hybridization.

The carbon substrates which are used are classified as exohedral or endohedral carbons.[149] Endohedral carbons exhibit high specific surface area gained from the excessive pores located predominantly inside the carbon particles, such as activated carbon or templated carbon. Contrarily, exohedral carbons have limited or no pores, which results in a low specific surface area, which is mainly derived from the outer surface of the carbon. Carbon nanotubes, carbon onions, or graphene.[149] For the preparation of such hybrid materials, various synthesis methods were explored like atomic layer deposition (ALD) of carbon surfaces with metal oxides,[150, 151] hierarchically ordered metal oxide and carbon structure,[44, 152, 153] nanoscale deposition via a sol-gel method,[87, 90] or metal oxide/carbon core/shell architectures.[79, 154-157] Fleischmann et al. have reported that the hybrid material concept enables the modification in the charge storage mechanism, which leads to the change in electrochemical performance.[72] A cautious approach is required for the selection of carbon substrates to avoid pore blocking (i.e., creation of dead mass) but to capitalize on a large surface area (to enable a high mass loading with the Faradaic species).[72, 158]

An in-situ synthesis approach is widely used for the synthesis of hybrid materials.[159] During the in-situ synthesis, each structural component is either deposited or composed from precursor and transformed into the final hybrid material. For a deposition method, a precursor of the desired Faradaic material is directly deposited on various carbon substrate in the form of crystalline or amorphous, which can lead to advantageous thin layer formation at the surface of the carbon.[72, 159] One of the main advantages of the deposition method allows a short diffusion distance within the synthesized hybrid material.[72, 158] Via wet-chemical methods and vapor deposition, Faradic materials, for example, transition metal oxides, can be incorporated onto the accessible surface of carbon substrates.[151, 160] A downside of this methodology is the high prospect of blocked pores due to the coated metal oxides, which induces limited access to ions and charges, as Zeiger et al. [158] have reported. ALD has drawn attention because it can precisely control the thickness of the deposition layer on an atomic scale compared to the other methods, which has a direct influence on the electrochemical performances.[72]

Another common approach is via the sol-gel method, which has the advantage of controlling the size of the desired products.[87, 90] The parameter variables during the sol-gel method, such as temperature, pressure, pH condition, or solvent, dramatically influence the structure of the product, especially acid or base.[86] Also, the precursors, usually metal alkoxides, provides different reaction rates to a sol-gel reaction based on the different size of alkyl groups.[159, 161] The as-prepared materials after the gelation usually require further thermal treatment to achieve the appreciated crystalline metal oxide. Annealing at adequate temperature can yield a simple core-shell material, generating carbon coating on the outer surface of metal oxide particles, which is originated from the remaining metal alkoxide precursors.[86, 155] Lim et al. [86, 157] introduced a reversed micelle concept to the sol-gel process, and with a subsequent annealing step, also achieve a nanoscale core-shell/carbon-coated material. In my thesis, *Chapters 4.1, 4.2, and 4.3* present the synthesis process of a hybrid material utilizing the sol-gel chemistry that the introduction of carbon substrates to impregnate with the metal oxide sols before the gelation occurs yields a homogeneous mixture of nanosized metal oxide and carbon substrates.[87, 90]

## **2. Electrochemical measurement techniques**

The main target application of EES materials is the reversible storage of energy with an appropriate cell voltage. Beyond simple simulation of duty cycles for a specific application, it is important to rigorously benchmark and test EES materials for their electrochemical behavior using established electrochemical methods.[162] The challenges related to this task begin with the appropriate preparation of an electrode and testing thereof the electrochemical performance in an electrochemical cell. Our group has designed a cell made out of a polyether ether ketone (PEEK) body with four side holes, titanium pistons for the contact to electrodes, and a brass screw lid (**Figure 7**).[163] A titanium screw is used for the reference electrode (RE) mount, allowing the RE material can be located near the other electrodes. The spring between the piston and the brass ensures the contact between all the components with 10 N. One of the main advantages of this cell configuration is that the modification of component material is possible; for example, the titanium piston can be replaced with copper or graphite piston. The modifiable cell material and cell design allowed to employ various electrode materials such as alkali metals and electrolytes, ranging from aqueous, organic electrolytes, and ionic liquid. Another advantage is facile electrolyte filling. The firm contact between the electrodes and separator materials approve minimal space for the liquid electrolytes to be filled. Also, the tight sealings among the cell body to pistons and screws allow us to fill electrolytes via the vacuum-back filling method, which ensures the cell contains only the appropriate amount of electrolyte filled. This can save the expensive electrolyte, compared to the coin cells, where the excessive electrolyte is required to fill the dead volume of the cell.

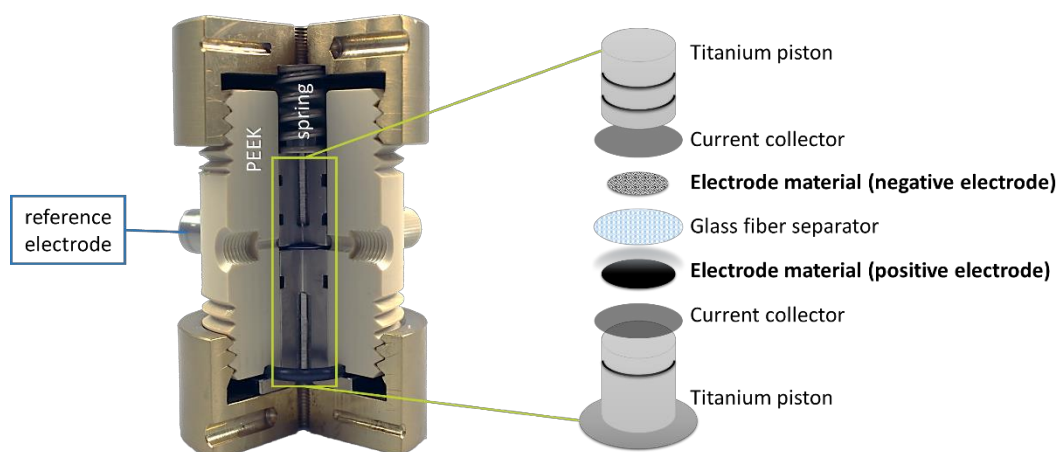


**Figure 7.** Design of custom-built cell and its possible components.

## 2.1. Cyclic voltammetry / Galvanostatic cycling with the potential limitation

The commonly used procedure of the first experiment for an EES involves checking is the electrochemical charging and discharging behavior of the electrodes. During loading and unloading of charges, the distinctive characteristic of the material is revealed. Cyclic voltammetry (CV) cycles between the potentials  $U_i$  and  $U_f$  linearly with a fixed scan rate. During the forward scan from the initial potential  $U_i$  to  $U_f$ , the electrode is reduced, and simultaneously a cathodic peak is observed. In the backward scan from vertex potential  $U_f$  to  $U_i$ , the oxidation of reduced material back occurs. The scan rate of the CV acquires attention depending on the material on the investigation.[164] Depending on the scan rate, the reduction or oxidation response of a material may not be completed. For example, the scan rate of 100 mV/s may be too high to complete the lithiation/delithiation process in an LTO electrode, while it may be adequate for an EDLC system. Furthermore, the field of supercapacitors utilizes CV as a determining technique for the stability of a cell.[36]

From the cathodic and anodic peak measured during CV scan at different scan rates, the contribution of kinetics on a charge storage process can be characterized.

$$I = av^b \quad \text{(Equation 13)}$$

where  $a$  and  $b$  are variables,  $I$  is the specific current at the cathodic peak, and  $v$  is the scan rate of the CV scan. According to the obtained  $b$  value from fitting, the contribution of diffusion-controlled ( $b=0.5$ ) and surface-controlled ( $b=1$ ) processes can be estimated.[165, 166] For quantifying the contribution between the diffusion-controlled and surface-controlled process, Equation 13 can be modified to Equation 14.

$$I = k_1v + k_2v^{0.5} \quad \text{(Equation 14)}$$

$k_1$  and  $k_2$  are the parameters obtained from fitting, which allows the calculation of diffusion-controlled and surface-controlled charges from the stored charge. [166]

As pointed out by Opitz et al. [166], it is important to select an appropriate range of scan rates of CV scans. The CV of higher scan rates, such as 100 mV/s, deliver distorted results due to the strong influence of Ohmic polarization than at the lower scan rates (e.g., 0.1 mV/s).[166] Another dynamic method is galvanostatic charge-discharge cycling with potential limitation (GCPL). From the open circuit potential of an EES cell, a constant current is applied until the potential of the cell is reached the desired set potential  $U_f$ . After the potential has reached the  $U_f$ , the inverse of the applied current during the first cycle is applied, and the potential of  $U_i$  is reached. A set of different currents is used to demonstrates the operation charge and discharge of the EES device/cell at rates.

$$C_{capacity} = \int_{t_0}^t I dt \quad \text{(Equation 15)}$$

$I$  is the applied current, and  $t$  denotes the duration of the applied current. Lastly, the capacity is calculated from the stored charge and the time consumed to reach the termination potential. For effective comparison between the material or the cell, gravimetric or volumetric normalization of obtained values is necessary. The capacity results obtained from GCPL can be plotted against cycles to determine the rate capability of the tested electrode material. It is essential to examine the power performance of the material, especially when a high charge/discharge current is applied. Furthermore, the longevity performance of a cell or a material can be also be established via GCPL at a fixed applied current for numerous repetitions, for example, 1000 cycles. When utilizing the reference electrode possibility of the cell configuration presented in Section 2, the potential development and decay during the GCPL can be observed.

## 2.2. Galvanostatic intermittent titration technique (GITT)

For intercalation electrodes, the chemical diffusion coefficient,  $D$ , of the intercalating ion ( $\text{Li}^+$  or  $\text{Na}^+$ ) traveling through the host material lattice is a very useful characteristic to measure.[162, 167] One technique to identify  $D$  is the galvanostatic intermittent titration technique (GITT).[168-170] GITT allows evaluating the equilibrium potential curve and partial conductivity, which can be extracted from one experiment.[162, 168]

In a GITT experiment, a constant current is applied to the working electrode for a set period, followed by a given resting period without any applied current. These apply-rest cycles are repeated until the working electrode is fully discharged, or certain equilibrium is reached. The term of each resting pulse can be varied upon the desire of pulse.

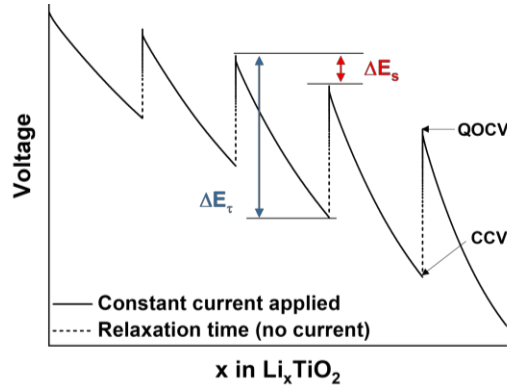


**Figure 8.** Experimental illustration of GITT (current applied on the solid line and current off/on the dotted line) to determine  $\Delta E_s$ ,  $\Delta E_\tau$ , QOCV, and OCV (adapted from Ref. [87]).

**Figure 8** shows an example of voltage profiles of GITT is tested on a cell, where the voltage of the cell changes as the current is applied for the same period. The voltage at the end of the constant current application is called closed-circuit voltage (CCV). As soon as the applied current is stopped, the increase in voltage is observed during the relaxation period, and this increase is continued to reach quasi-open-circuit voltage (QOCV).

The combination of Fick's law and the Nernst equation can be used to analyze GITT data (**Equation 16**) since the current pulse and relaxation create a concentration change of species. The difference in the QOCV between each current pulse and relaxation term is observed and stated as  $\Delta E_s$ , and the difference between QOCV and CCV in the same relaxation term is stated as  $\Delta E_\tau$ . Using the Ohmic law, the internal resistance of the cell at each QOCV-CCV voltage transit can be obtained, and the resistance difference between the insertion of ion and extraction of the ion is quantified.

$$D = \frac{4}{\tau\pi} \left( \frac{m_B V_m}{M_B A} \right)^2 \left( \frac{\Delta E_s}{\Delta E_\tau} \right)^2 \quad \text{(Equation 16)}$$

where  $M_B$  and  $m_B$  are the molar mass and the active mass of the electrode material, respectively,  $V_m$  is the molar volume of the electrode, and  $A$  is the geometric electrode area. From the derived  $D$ , at each CCV-QOCV transition, the visualization of change in the diffusion coefficient is possible. The  $\Delta E$  is dependent on the imposed relaxation time, which requires careful attention when comparing the  $D$  value obtained from different experiment conditions.

### 2.3. Electrochemical stability testing

No electrochemical energy storage devices enable fully reversible charge/discharge cycling. Instead, every cell will undergo, sooner/later and faster/slower, degradation. The degradation strongly depends on the way the cell is operated. Critical parameters include charge/discharge rate, initial/final state-of-charge, and operational temperature. For any given application, ultimately, the operational conditions unique to the application must be considered when evaluating the performance stability of electrode material, which eventually affects device longevity.

This applies in particular to intermittent operation. However, in the field of developing new electrode materials, it is not practical to test a myriad of application-specific profiles; instead, two types of performance stability testing are applied: either an extensive number of cycling (where a constant rate (either galvanostatic or voltammetry) is applied between a set range of potential)[171, 172] or voltage holding[173, 174]. Both approaches will yield different insights and differently address electrochemical stability. Continued charge and discharge cycling stress the electrode material, for example, to probe the structural electrode material stability during reversible lithiation/delithiation. Voltage holding accelerates any possible electrochemical instability near the edge of the stable electrochemical potential window. The latter most often relates to the stability of the electrolyte, but also, the electrode material(s) may degrade at certain potentials. Thereby, a voltage floating is of specific relevance for electrical double-layer capacitors where the stability window is mostly defined by the stability of the electrolyte (and this also includes side-reactions at the interface between nanoporous carbon and the electrolyte). In the following sections, the operation techniques will be discussed.

### **2.3.1. Voltage floating**

To illustrate the aging of the electrolyte-containing electrochemical system, Ruch et al. and Cericola et al. presented the method by holding the electrochemical device at the nominal cell voltage for a given amount of time and discover the performance of the device.[173, 174] Especially for the EDLCs, which does not have the issue of the charge transfer reaction below the nominal cell voltage, the voltage holding method allows us to determine a more profitable stability limit.[172] By applying a constant load on the cell at the stability, limit allows the cell to perform a more representative aging process compared to charge/discharge cycling. During the charge/discharge cycling, the applied current is fixed and usually corresponds to the timescale of seconds, which makes the exposure to the voltage range at the stability limit rather short. Therefore, the contribution of reaching stability limits and phenomena of aging is difficult to infer just from the capacity change from charge/discharge cycling. In contrast, during the voltage floating, the current decreases as the voltage being fixed at a charged state, which represents the leakage current of the device.

**Figure 9A** demonstrates the concept of voltage floating with the voltage profiles of a cell. The cell is charged and discharged several times, then the cell is charged to the nominal voltage, then the chronoamperometry is started for a given amount of time. After the holding period is finished, the cell is discharged to the lower cut-off voltage, and then the entire process is repeated for the designated number of loops. The discharge capacities of the tested cell after each voltage floating loop are collected and presented against the time (**Figure 9B**). The severe changes of the capacity can be observed as the voltage floating loops continue over time depending on test conditions (e.g., temperature, held voltage, or holding time) or different cell designs. The work of Weingarth et al. compared the capacity performance via voltage floating using two different cell voltages and showed the possibility to determine the stable cell voltage based on the voltage holding results.[172]

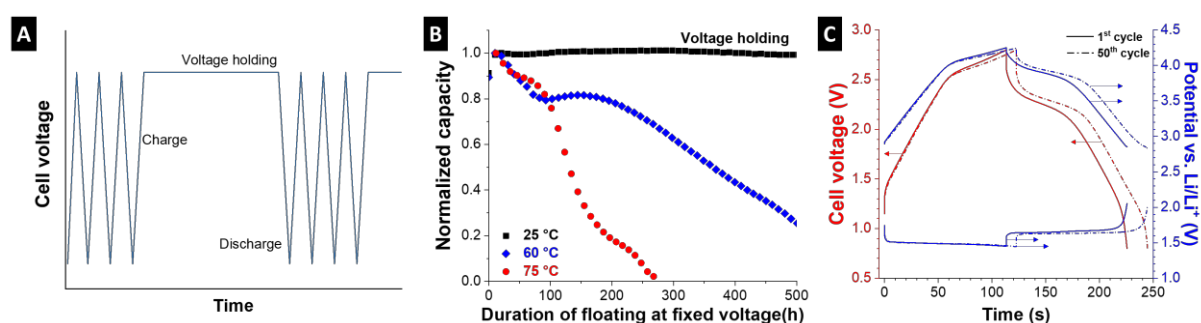


**Figure 9.** (A) Illustration of the voltage profile of a cell during the voltage holding test (B) An example of the stability testing by using 10 h voltage holding at charged state. The normalized capacity values are calculated from the third charge/discharge cycle after each 10 h voltage holding at three different temperatures (C) Voltage profiles of a full-cell tested after the 1<sup>st</sup> and the 50<sup>th</sup> voltage holding cycle. The potential at anode and cathode was monitored with carbon as a quasi-reference electrode (adapted from Ref. [30]).

An example of voltage profile changes after the voltage holding test is plotted in **Figure 9C**. The comparison of the change in voltage profiles over the voltage floating tests allocates the determination of the fading electrode during the voltage floating test. The voltage profiles at each electrode throughout the voltage floating possibly present, for example, different  $iR$  drop, overpotential of insertion/extraction of ions, or complete distorted profile compared to the initial profile. The possible degradation factors comprise electrode active material (temperature combination, current collector), lithium salt combination, or electrode active material/electrolyte combination and more. Fic et al.[175] recently reported the gas evolution during the 2 h-voltage floating test at different voltages in an aqueous electrolyte. This voltage floating method has the potential to help determine the aging mechanism of the device and is further discussed in *Chapter 4.4* [172-174].

### 2.3.2. S-value testing

The stability windows define the maximum electrode potential in which the cell can safely operate without degradation. This is of particular importance for EDLC systems, which are limited by electrolyte degradation. The latter can be identified via the onset of a Faradaic current. Degradation, in general, may relate to the degradation of the electrolyte, the electrode material, or the fluid/solid interface (e.g., redox reactions of surface groups). The electrochemical stability is very important for EES devices because the operation potential range influences the performance, including cycle life, specific energy, and specific power.[176]

Xu et al. have introduced a reliable test method to identify the electrochemical potential window for carbon electrode using cycling voltammetry. [177] It was originally suggested as *R*-value (“*R*” standing for reversibility) by Xu et al., but Weingarth et al. proposed to designate it as “*S*” value, since it quantifies the “stability” of the system.[178]

$$S = \frac{Q_{charge}}{Q_{discharge}} - 1 \quad \text{(Equation 17)}$$

The cyclic voltammetry is continued using the same scan rate throughout the investigation by widening the vertex potential of the cell. From the cyclic voltammetry cycles, the charge *Q* of charge and discharge are calculated, respectively, for both anodic and cathodic scans. After obtaining the *S*-values for each window opening cycle at different vertex potentials, the vertex potential where the *S*-value is higher than a certain value can be defined as the end of the electrochemical stability window. Typically, a value of 0.1 portrays the potential range exceeding the degradation limit. [176] The value 0.1 represents an irreversible contribution of 10%.[178]

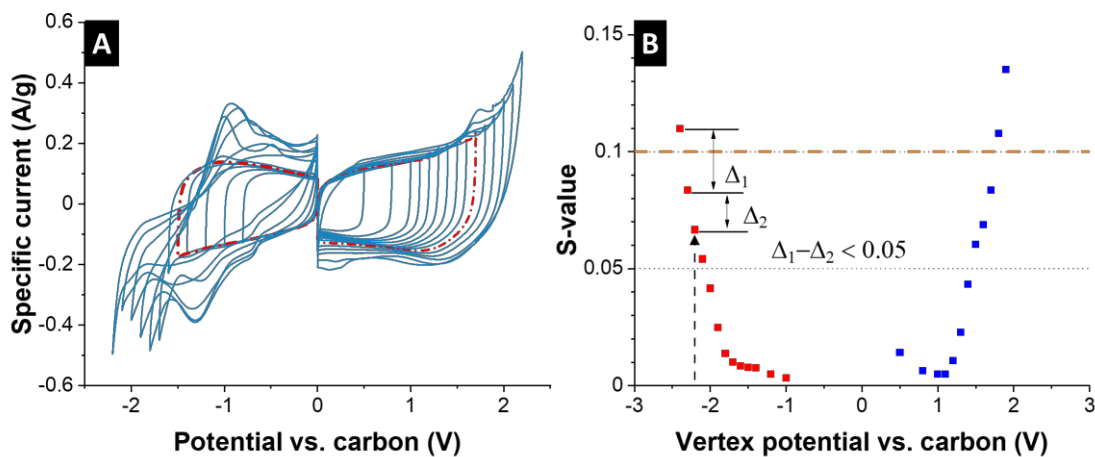


**Figure 10.** (A) Cyclic voltammetric window opening experiment (red dash-dot line: possible maximum stable potential). (B) Presentation of two different criteria to determine the stable potential limit using calculated *S*-value obtained from a window opening experiment (adapted from Ref. [178]).

**Figure 10A** displays an example of a window opening experiment performed using CV. Using individual cells, anodic and cathodic potentials were increased to 0.5 V, 0.8 V, and 1.0 V and steps of 0.1 V until the vertex potential of 2.5 V was reached. The red dotted-dash line in **Figure 10A** demonstrates the possible maximum potential limit. When the voltammogram was demonstrating a very irregular shape, the cell was stopped in a safety concern. **Figure 10B** depicts examples of calculated S-values from a window opening CV experiment. The dotted line at  $S = 0.1$  is the stability criterion suggested by Xu et al. [176]. According to Xu's criterion, the stable anodic and cathodic limit of the electrolyte in **Figure 10B** is -2.3 V and +1.9 V, respectively.

Weingarth et al. and Moosbauer et al. proposed that the  $S=0.1$  criterion introduced by Xu et al. is not sufficiently sensitive to identify the actual stability range of electrolytes.[178, 179] Especially the window opening results from the test conducted at different temperatures by Weingarth et al. indicates the need for flexible criterion instead of a constant value criterion.[178] Therefore Weingarth et al. proposed to compare the changes of S-values obtained at two adjacent vertex potentials, that the second derivative of the S-value should be smaller than 0.05 (**Figure 10B**).[178]

$$\frac{dS^2}{d^2V} < 0.05 \quad \text{(Equation 18)}$$

This criterion explains that when the Faradaic contribution via  $dS^2/d^2V$  exceeds 5%, the region is indicated unstable. Also, the advantage of using this criterion is that the unwanted current contribution is possibly eliminated.[178]

Another important aspect is the cause of electrochemical irreversibility. When using an electrochemically inert electrolyte in an electrical double-layer capacitor, it is trivial to assume degradation of either the electrolyte itself or poisoning of the electrolyte by parasitic side-reactions occurring at the fluid/solid interface between electrolyte and electrode. Therefore, it is sometimes appropriate to translate any irreversibility to the emergence of charge-transfer processes. However, it is an often-made mistake to automatically assign any irreversibility to the distinction between Faradaic and non-Faradaic without further investigation of the degradation mechanism(s). Also, in the context of pseudocapacitors or batteries, where non-Faradaic processes are not important, we will have to discern between reversible and irreversible charge transfer processes.

### 3. Overview

My thesis explores hybridization and composite technology for electrode materials by using metal oxides and carbon nanoparticles. The combination of these two types of materials is highly promising to exceed the performance metrics of state-of-the-art electrochemical energy storage devices, such as supercapacitors and lithium-ion batteries.

The first part of my research is focused on the material level hybridization, utilizing the highly conductive carbon, such as carbon onions, with a nanoscale combination of a Faradaic material for electrochemical storage such as lithium-ion batteries, lithium-ion hybrid supercapacitors, or sodium-ion batteries. The nano-scale synthesis of the metal oxide complements the better distribution of metal oxide and carbon substrate; however, not always is hybridization superior to the composite strategy, and the resulting performance metrics (including stability and rate handling) strongly depend on the architecture of the obtained electrodes.

- The first study (**Chapter 4.1**) provides a comparison between hybridized nanoscale carbon and metal oxide electrodes and the physically admixed composite electrode. The data show the electrochemical difference of the hybrid materials with different types of metal oxides and two types of carbon with different pore sizes and surface area via thorough material and electrochemical characterization. The impact of an appropriate selection of carbon substrate and the crystal structure/lattice parameters are evaluated.
- The second study (**Chapter 4.2**) demonstrates the importance of the nano-sizing of the intercalation material. With a thorough investigation of the lithium storage mechanism of the hybrid material, the quantitative comparison between hybrid and non-hybrid material is possible. As shown by the electrochemical performance data, a homogeneous distribution of the carbon substrate network enhances the rate handling ability of the cell.
- The third study (**Chapter 4.3**) explores the hybridization of nanosized LTO with carbon onions produced at different conditions. This hybrid approach yielded enhanced rate performance and cycling performance at lithium-ion storage. The importance of the homogenous distribution of carbon within the hybrid material is addressed. The LTO-OLC hybrid further was investigated on sodium-ion energy storage performance.

The next part of my research is focused on the device level hybridization and the influence of electrolytes of hybrid supercapacitors.

- **Chapter 4.4** assesses the stability of six different combinations of lithium-containing salt and organic solvents plus ionic liquid for the hybrid supercapacitor consist of LTO anode and LMO-activated carbon cathode. One of the solvents, tri-methoxypropionitrile, is explored for the first time in the context of a hybrid supercapacitor. The stability of the electrolyte and the lithium-containing electrolyte is confirmed by the electrochemical benchmarking of voltage floating test at room temperature, above and below ambient temperature.
- **Chapter 4.5** explores the electrochemical stability window of ionic liquid to promote a large operation voltage of LTO/activated carbon hybrid supercapacitors. The enhanced energy performance of the cell visualizes the importance of continuous investigation of lithium-containing ionic liquids.
- **Chapter 4.6** explores the concept of hybridization on the device level with the new synthesis approach of proton exchange, and doping is investigated. After a comprehensive material characterization and electrochemical testing, the LMO/activated carbon cathode in combination with protonated titanium oxide (HTO) anodes were prepared, achieving high power performance. The promising power and energy performance can propose the potential for further investigation of protonated titanium-based materials.

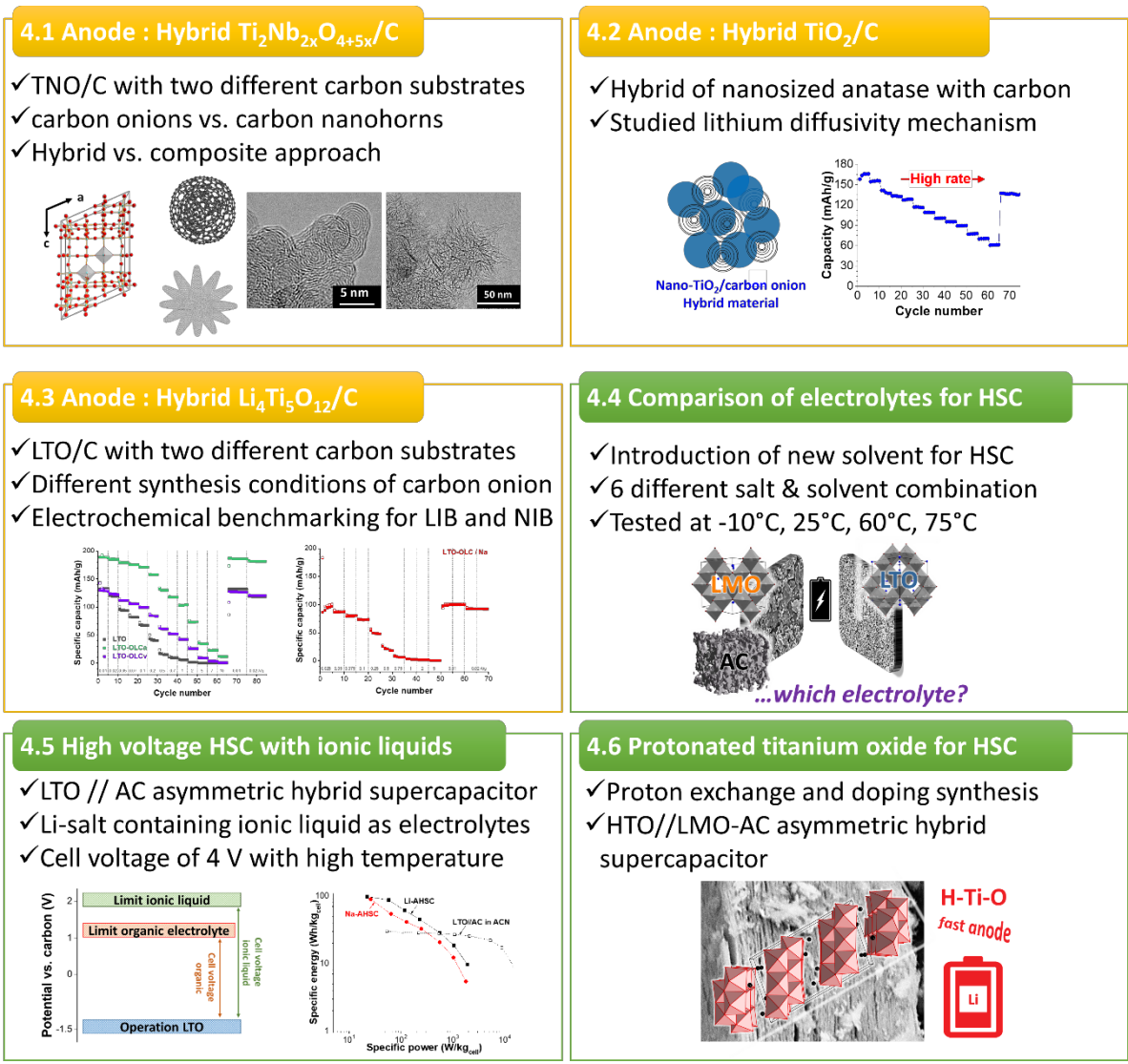


**Figure 11.** Overview of the different chapters of this thesis. All segments refer to peer-reviewed publications.

## **4. Results and discussion**

- 4.1. Nanosized titanium niobium oxide/carbon electrodes for lithium-ion energy storage applications**
- 4.2. Fast and stable lithium-ion storage kinetics of anatase titanium dioxide/carbon onion hybrid electrodes**
- 4.3. Hybrid anodes of lithium titanium oxide and carbon onions for lithium-ion and sodium-ion energy storage**
- 4.4. Comparison of organic electrolytes at various temperatures for 2.8 V–Li-ion hybrid supercapacitors**
- 4.5. High voltage asymmetric hybrid supercapacitors using lithium-and sodium-containing ionic liquids**
- 4.6. Understanding interlayer deprotonation of hydrogen titanium oxide for high-power electrochemical energy storage**

# Nanosized titanium niobium oxide/carbon electrodes for lithium-ion energy storage applications

**Hwirim Shim<sup>1,2</sup>, Eunho Lim<sup>1</sup>, Simon Fleischmann<sup>1</sup>,  
Antje Quade<sup>3</sup>, Aura Tolosa<sup>1</sup>, Volker Presser<sup>1,2</sup>**

<sup>1</sup> INM - Leibniz Institute for New Materials, 66123 Saarbrücken, Germany

<sup>2</sup> Department of Materials Science and Engineering, Saarland University, 66123 Saarbrücken, Germany

<sup>3</sup> Leibniz Institute for Plasma Science and Technology, 17489 Greifswald, Germany

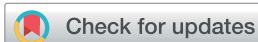
## Citation:

H. Shim, E. Lim, S. Fleischmann, A. Quade, A. Tolosa, & V. Presser (2019). Nanosized titanium niobium oxide/carbon electrodes for lithium-ion energy storage applications. *Sustainable Energy & Fuels*, 3(7), 1776-1789.

## Own contributions:

Planning, synthesis, X-ray diffraction measurements, Raman measurements, thermogravimetric analysis, scanning electron microscopy, transmission electron microscopy, electrochemical measurements, writing.

## PAPER



Cite this: DOI: 10.1039/c9se00166b

## Nanosized titanium niobium oxide/carbon electrodes for lithium-ion energy storage applications†

Hwirim Shim,<sup>ab</sup> Eunho Lim,<sup>a</sup> Simon Fleischmann,<sup>a</sup> Antje Quade,<sup>c</sup> Aura Tolosa<sup>a</sup> and Volker Presser<sup>\*ab</sup>

High demand for safer and more stable lithium-ion batteries brings up the challenge for finding better electrode materials. In this work, we study the functionalities of titanium niobium oxide (TNO)/carbon hybrid materials using carbon onions (OLC) and carbon nanohorns (NS), which are synthesized by well-controlled sol-gel chemistry, for anodes in lithium-ion batteries. We used two different molar ratios of titanium to niobium (1 : 2 and 1 : 5), and we compared the TNO-OLC and TNO-NS hybrid materials to conventional composite electrodes using physically admixed carbon. TNO-OLC-1:2 and TNO-OLC-1:5 nanohybrid materials displayed good electrochemical performance, with initial capacity values of 284 mA h g<sup>-1</sup> and 290 mA h g<sup>-1</sup>, respectively, normalized to the metal oxide mass. Moreover, they maintained 68% (TNO-OLC-1:2) and 69% (TNO-OLC-1:5) of the initial capacity at 1 A g<sup>-1</sup>, outperforming the carbon nanohorn hybridized and composited electrode which maintained less than 50%. The long-term cycling stability of 800 cycles presents good capacity retention of 73% (TNO-OLC-1:2) and 76% (TNO-OLC-1:5), while the TNO-NS-1:2 hybrid material yields better capacity retention of 90% despite its low capacity. Our study demonstrates that the combination of TNO with appropriate carbon substrates enables good electrochemical performance but requires careful evaluation of the interplay of crystal structure, phase content, and particle morphology.

Received 15th March 2019  
Accepted 18th May 2019

DOI: 10.1039/c9se00166b

rsc.li/sustainable-energy

## 1. Introduction

The development of lithium-ion battery (LIB) electrode materials with high charge storage capacity, high cycling stability, and high rate capability remains an ongoing challenge.<sup>1-5</sup> Commonly, LIB anodes employ abundantly available graphite because the reversible lithium intercalation/de-intercalation into graphite provides high theoretical capacity.<sup>6</sup> However, graphite-based LIB cells have safety issues, for example, in regards to lithium dendrite formation because of its working potential at lower than 0.2 V vs. Li/Li<sup>+</sup>.<sup>7</sup> In addition, the rate capability of the graphite is not remarkable. To replace graphite, alternative materials have been explored, such as TiO<sub>2</sub>, Nb<sub>2</sub>O<sub>5</sub>, or Li<sub>4</sub>Ti<sub>5</sub>O<sub>12</sub> that show intercalation at a safe working potential above 1.0 V vs. Li/Li<sup>+</sup>.<sup>8-11</sup> In particular, anatase TiO<sub>2</sub> or Li<sub>4</sub>Ti<sub>5</sub>O<sub>12</sub> have drawn attention due to their high

reversible redox potential at about 1.6 V vs. Li/Li<sup>+</sup>. However, the practical capacity achieved by TiO<sub>2</sub> or Li<sub>4</sub>Ti<sub>5</sub>O<sub>12</sub> (170–200 mA h g<sup>-1</sup>) is small compared to graphite (372 mA h g<sup>-1</sup>).<sup>12,13</sup> Among transition metal oxides, titanium niobium oxides have attracted attention as promising anodes because of their safe operation potential at 1.0–2.0 V vs. Li/Li<sup>+</sup>. Both TiNb<sub>2</sub>O<sub>7</sub> and Ti<sub>2</sub>Nb<sub>10</sub>O<sub>29</sub> (TNO) phases are favorable for lithium-ion insertion since they offer high theoretical capacities of 388 mA h g<sup>-1</sup> and 396 mA h g<sup>-1</sup>, respectively, due to electron charge transfer from the Ti<sup>4+/3+</sup>, Nb<sup>5+/4+</sup>, and Nb<sup>4+/3+</sup> redox couples with excellent rate capability behavior.<sup>14-21</sup>

A practical approach for achieving fast charge storage and recovery rates is the implementation of nanoscale electrode materials.<sup>22-24</sup> For example, Fei *et al.*<sup>25</sup> and Lou *et al.*<sup>26</sup> have used a solvothermal method and a template to synthesize TNO nanoparticles. Further, Aravindan *et al.*,<sup>27</sup> Pham-Cong *et al.*,<sup>28</sup> and Fu *et al.*<sup>29</sup> employed electrospun TNO nanofibers to enhance the electrochemical performance. Yet, nanoscale metal oxide particles still require an optimized (nanoscale) implementation of an electrically conductive phase, such as carbon.<sup>30,31</sup> For example, Li *et al.*,<sup>32</sup> Wang *et al.*,<sup>33</sup> and Deng *et al.*<sup>34</sup> have applied this concept to fabricate nanocomposite TNO/C material using graphene and improved the electrochemical performance of TNO nanoparticles compared to the performance of TNO without carbon with rate capability of

<sup>a</sup>INM – Leibniz Institute for New Materials, 66123 Saarbrücken, Germany. E-mail: volker.presser@leibniz-inm.de

<sup>b</sup>Department of Materials Science and Engineering, Saarland University, 66123 Saarbrücken, Germany

<sup>c</sup>Leibniz Institute for Plasma Science and Technology, 17489 Greifswald, Germany

† Electronic supplementary information (ESI) available: Thermograms, ideal crystal structures, scanning electron microscopy, X-ray photoelectron spectroscopy, and Raman data for carbon onions and carbon nanohorns, electrochemical kinetic analysis. See DOI: 10.1039/c9se00166b

180 mA h g<sup>-1</sup> at 100 °C, 165 mA h g<sup>-1</sup> at 0.5 A g<sup>-1</sup>, and 163 mA h g<sup>-1</sup> at 60 °C. Furthermore, core-shell type carbon implementation (ref. 35 and 36) and creating oxygen vacancy during TNO synthesis (ref. 35 and 37) are explored to increase the electrical conductivity of TNO.

Going beyond nanocomposites, achieving the hybridization of metal oxides with nanoscale carbon particles with high electrical conductivity is of great interest. For example, carbon onions (onion-like carbon: OLC) have been explored as a conductive carbon to hybridize with birnessite MnO<sub>2</sub> or Mn<sub>3</sub>O<sub>4</sub> (ref. 38 and 39), NiO or Ni(OH)<sub>2</sub> (ref. 40), TiO<sub>2</sub> (ref. 41), or VO<sub>2</sub> (ref. 42). Carbon onions are conveniently derived by thermal annealing of nanodiamonds and consist of several layers of spherical graphitic carbon shells.<sup>43,44</sup> Capitalizing on their small size of 5–10 nm and abundant mesopore volume between the individual carbon onion particles, a homogeneous distribution of nanosized metal oxides during hybridization is expected. Carbon nanohorns are nanoscale-textured materials, which consist of conical single-walled sp<sup>2</sup>-hybridized graphitic carbon sheets with a size of about 50 nm.<sup>45,46</sup> There exist a number of different synthesis methods for carbon nanohorns, including thermal modification of fullerene or heating and modification of graphite.<sup>47,48</sup> Their high electrical conductivity (~5 S cm<sup>-1</sup>) and high surface area (~300–1250 m<sup>2</sup> g<sup>-1</sup>) make carbon nanohorns attractive for the hybridization with metal oxide nanoparticles.<sup>45,49</sup>

In this study, we use an optimized sol-gel reaction to prepare nano-TNO-carbon hybrid materials using either carbon onions or carbon nanohorns for hybridization and evaluate their electrochemical performances. Nanoscale TNO domains alongside nanocarbon substrates will be beneficial for enhancing the rate capability of the material, as diffusion pathlengths are limited and adequate electron transport is ensured. TNO-OLC hybrids display higher discharge capacity and rate capability than TNO-NS hybrid materials. Our work also compares TNO-C hybrids (*i.e.*, a nanoscale intergrowth of the metal oxide and nanocarbon) with TNO+C composites (*i.e.*, the physical mixture of metal oxide particles and nanocarbons) to demonstrate the advantages of nanoscale chemical interaction between the TNO and the conductive carbon phase.

## 2. Experimental description

### 2.1. Material preparation

Carbon onions (OLC) were synthesized by thermal annealing of nanodiamond powder purchased from NaBond Technologies (China) at 1700 °C for 1 h under Ar atmosphere.<sup>44</sup> Graphitic carbon nanohorns (Graphene NanoStars, NS) were purchased from Graphene Laboratories and used without further modification. More data on the structure and properties of carbon nanohorns can be found in ref. 50.

We used a tailored sol-gel reaction to synthesize nanometer-sized TiNb<sub>2</sub>O<sub>x</sub> and TiNb<sub>5</sub>O<sub>x</sub> sols. Titanium(IV) isopropoxide (TTIP, Sigma Aldrich) and niobium ethoxide (NbOEt, Sigma Aldrich) were used as Ti and Nb sources, respectively. Using tetrahydrofuran (THF, Sigma Aldrich) as the solvent, 1 : 2 or 1 : 5 molar ratio of TTIP (1 mmol) and NbOEt (2 mmol or 5

mmol) were added dropwise to the solvent and stirred vigorously. 445 μL or 907 μL of concentrated HCl (37 mass% in water) were added dropwise to the stirred solution of 1 : 2 or 1 : 5 molar ratio, respectively. These precursor solutions were stirred for 1 h and then added to different carbon substrates by wet impregnation. The total content of the carbon substrate was calculated to be 20 mass% of the hybrid material after the synthesis procedure. The mixture was dried at 40 °C under 20 mbar for 12 h, then dried at 80 °C for another 12 h. The as-prepared TNO-C mixture was heat-treated at 900 °C for 2 h (heating rate 1 °C min<sup>-1</sup>) under an Ar atmosphere. TiNb<sub>2</sub>O<sub>7</sub> and Ti<sub>2</sub>Nb<sub>10</sub>O<sub>29</sub> without carbon addition were prepared identically up to 1 h stirring, then the solution was transferred to a Petri dish on a hotplate and dried for 12 h at 40 °C. The resulting material was further dried at 80 °C for another 12 h. The as-prepared TNO sols were calcinated at 900 °C for 2 h (heating rate 1 °C min<sup>-1</sup>) under a synthetic air atmosphere (80 vol% N<sub>2</sub> and 20 vol% O<sub>2</sub>).

Our work has adopted a uniform nomenclature to reflect both the synthesis conditions and composition. The resulting materials were named after the molar ratio of Ti : Nb (*e.g.*, TNO-1:2 or TNO-1:5). TNO hybridized on carbon nanohorns are called TNO-NS-1:2 or TNO-NS-1:5, while TNO hybridized on carbon onions are called TNO-OLC-1:2 or TNO-OLC-1:5. TNO physically mixed with carbon onions are labeled TNO-1:2+OLC or TNO-1:5+OLC and composites electrodes with carbon nanohorns are called TNO-1:2+NS or TNO-1:5+NS. An overview of sample names and synthesis conditions is also provided in the ESI, Table S1.†

### 2.2. Material characterization

**2.2.1. Porosity characterization.** Gas sorption analysis (GSA) was conducted to obtain specific surface area (SSA), and pore volume of the samples. We carried out the measurements with a Quantachrome Quadrasorb system using nitrogen gas at -196 °C in a relative pressure range from 0.001 to 1.0 in 50 steps. Prior to the measurements, the powder samples were degassed at 250 °C and 10<sup>2</sup> Pa for 12 h. The values for the total pore volume were obtained at a relative pressure of  $P/P_0 = 0.95$ . We used the quenched solid density functional theory (QSDFT) and assumed slit-shaped pores for the calculation of the pore size distribution.<sup>51</sup>

**2.2.2. Structural and chemical characterization.** X-ray diffraction (XRD) was conducted in a D8 Discover diffractometer (Bruker AXS) with a copper X-ray source (Cu K<sub>α</sub>, 40 kV, 40 mA). We used a Göbel mirror in 0.5 mm point focus, and a two-dimensional X-ray detector (Vantec-500). The samples were placed on a sapphire single crystal for measurement and four steps with a measuring time of 1000 s were used to measure from 20° to 80° 2θ. We used Rietveld-refinement using TOPAS (Bruker AXS) to quantify the average coherence length (domain size) of the crystalline compounds.

We used a JEOL JSM-7500F for scanning electron microscopy (SEM) at an acceleration voltage of 3 kV and an emission current of 10 μA. Samples were dispersed in 5 mL of ethanol and sonicated for 5 min. The dispersion was then drop casted

multiple times on a carbon film tape on a steel sample holder and dried under vacuum for 30 min. Energy dispersive X-ray spectroscopy (EDX) was performed with X-Max-150 (Oxford Instruments) attached to the SEM system. The spectra were obtained at an acceleration voltage of 10 kV and an emission current of 10  $\mu$ A. Before the spectral acquisition of each sample, calibration was conducted with a silicon wafer. Transmission electron microscopy (TEM) was conducted using a JEOL JEM-2100F system at an operating voltage of 200 kV. The samples were dispersed in 5 mL ethanol and tip-sonicated for 30 s. The dispersion was then drop casted on a TEM copper grid with a lacy carbon film.

Thermogravimetric analysis (TGA) was performed with a Netzsch TG-209-1 Libra system to determine the carbon content in our hybrid materials. For each TGA measurement, the samples were heated to 800  $^{\circ}$ C under synthetic air condition with a flow rate of 20 sccm at a rate of 5  $^{\circ}$ C  $\text{min}^{-1}$ .

Raman spectra were obtained by using a Renishaw inVia system. An Nd-YAG laser with an excitation wavelength of 532 nm was used with a power of 0.5 mW at the focal point. The acquisition time was 30 s, and 10 accumulations were used to enhance the signal-to-noise ratio. Peak fitting of the measured spectra was accomplished assuming two Voigt peaks for the D- and G-mode individually.

Elemental analysis (CHNS/O) was performed with a Vario Micro Cube system from Elementar Analysensysteme. The reduction temperature was 850  $^{\circ}$ C, and the device was calibrated with sulfanilamide. Quantitative analysis of elemental oxygen was performed by using a rapid OXY cube oxygen analyzer at 1450  $^{\circ}$ C (Elementar Analysensysteme).

X-ray photoelectron spectroscopy (XPS) was conducted with an Axis Ultra DLD spectrometer (Kratos Analytical) using monochromatic Al  $K_{\alpha}$  as the photoelectron excitation source. At an X-ray radiation power of 150 W (15 kV, 10 mA) with a spot size of  $\sim$ 250  $\mu$ m, pass energy of 160 eV, 80 eV, and 10 eV were used for the wide-scan, elemental scan, and high-resolution scan of the samples.

**2.2.3. Electrochemical characterization.** For the preparation of the negative electrode, the active material was mixed with *N*-methyl-2-pyrrolidone (NMP, Sigma Aldrich) solvent and polyvinylidene fluoride (PVDF, Alfa Aesar) binder and casted on a copper foil using a 200  $\mu$ m doctor blade. 9 : 1 mass ratio between the active material (TNO and carbon substrate) and PVDF binder was chosen for hybrid materials. For the composites, 18 mass% conductive additives (*i.e.*, either carbon onions or carbon nanohorns) were used, which corresponds to the carbon mass from TGA results for the hybrid mixtures of TNO and carbon. The coated material was dried overnight in

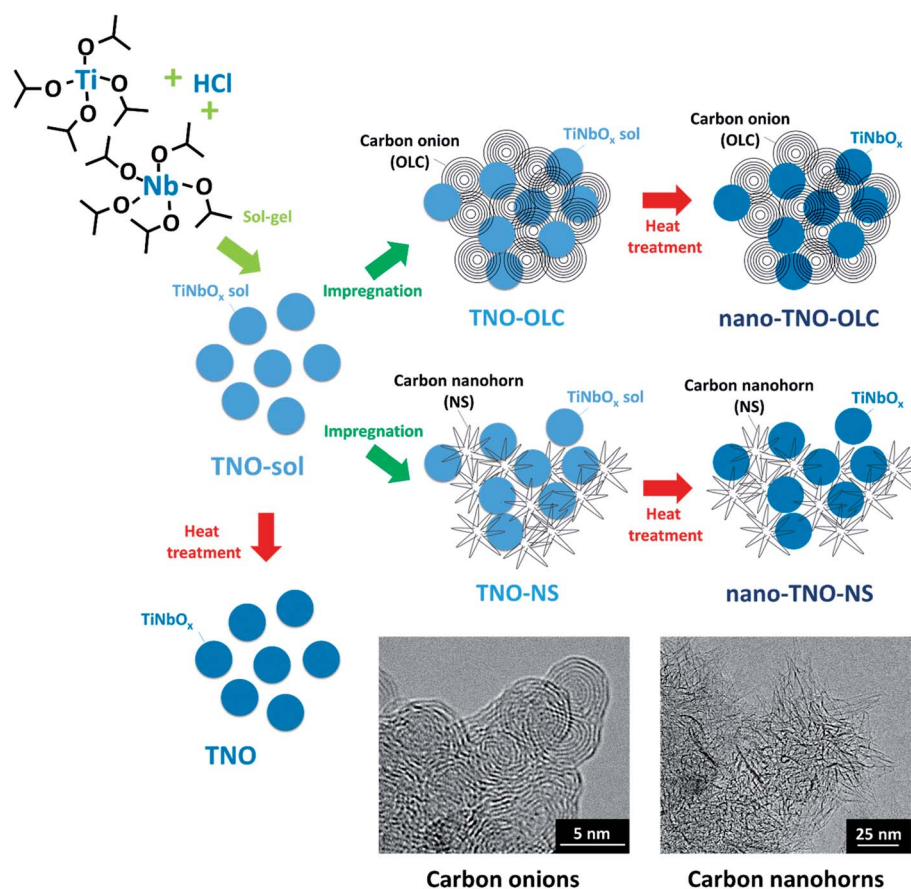


Fig. 1 Schematic representation of TNO and TNO-C preparation. The insets show transmission electron micrographs of carbon onions (OLC) and carbon nanohorns (NS) prior to their hybridization with the metal oxide.

a fume hood, then carried to a vacuum oven and dried overnight at 110 °C. The dried sheet was pressed in a hot-roll press machine, and we finally punched discs in 14 mm diameter for electrochemical characterization.

For the positive and quasi-reference electrode (QRE) preparation, coconut shell-derived activated carbon YP-80F, and YP-50F (Kuraray Chemicals) was used, respectively. To obtain defunctionalized activated carbon, YP-50F power was treated in nitric acid for 5 h at 95 °C, and more details about the preparation process are found elsewhere.<sup>52</sup> By admixing 10 mass% of polytetrafluoroethylene (PTFE, 60 mass% solution in water, Sigma Aldrich) to the each activated carbon powders dispersed in ethanol, electrodes were prepared with  $525 \pm 12 \mu\text{m}$  thickness by following the procedure from our previous work.<sup>53</sup>

For half-cell measurements, CR2032 coin cells paired the TNO working electrodes with a lithium disc as both counter and reference electrodes. We used a Whatman GF/F glass fiber separator and 1 M  $\text{LiPF}_6$  salt in a mixture of ethylene carbonate and dimethyl carbonate (EC : DMC, 1 : 1 by volume, BASF SelectiLyte) as the electrolyte.

Cyclic voltammetry (CV) carried out with a Biologic VMP300 potentiostat/galvanostat and performed in a potential window from 1.0 V to 2.8 V vs.  $\text{Li/Li}^+$  at scan rates of 0.1–10  $\text{mV s}^{-1}$ . Galvanostatic charge/discharge with potential limitation (GCPL) measurement was carried out with an Arbin Battery Cycler in a potential range 1.0 V to 2.8 V vs.  $\text{Li/Li}^+$  using specific currents of 0.01–10  $\text{A g}^{-1}$  to observe the rate capability and specific currents of 1  $\text{A g}^{-1}$  to quantify the cycling stability.

The specific capacity of the hybrid material is calculated by integrating the applied delithiation current over the delithiation time as in eqn (1):

$$C_{\text{sp}} = \frac{\int_{t_0}^t I dt}{m} \quad (1)$$

where  $I$  is the applied current,  $t$  is the time, and  $m$  is the mass of the metal oxide. The specific capacity was normalized to the total mass of the metal oxide in the electrode without the polymer binder and carbon used for electrode preparation, either as a hybrid or composite.

For the full-cell measurement, we used custom-built poly-ether ether ketone cells described in elsewhere.<sup>54</sup> TNO-OLC-1:5 electrode was employed as a negative electrode, a YP-80F electrode as a positive electrode and a YP-50F electrode as QRE. We used a Whatman GF/F glass fiber separator and 1 M  $\text{LiClO}_4$  in acetonitrile (ACN, BASF SelectiLyte) as the electrolyte. The prepared full-cell was pre-cycled at 1  $\text{A g}^{-1}$  for 10 cycles followed by GCPL measurement using specific currents of 0.025–25  $\text{A g}^{-1}$  to obtain Ragone plots. The stability measurement was continued after GCPL measurements at 1  $\text{A g}^{-1}$ . The specific energy of the full-cell is calculated by integrating the voltage profile over discharge time as in eqn (2):

$$E_{\text{sp}} = \frac{I \int_{t_0}^t U(t) dt}{m} \quad (2)$$

where  $I$  is the applied current,  $U$  is the time-dependent cell voltage,  $t$  is the time, and  $m$  is the mass of both electrodes. The

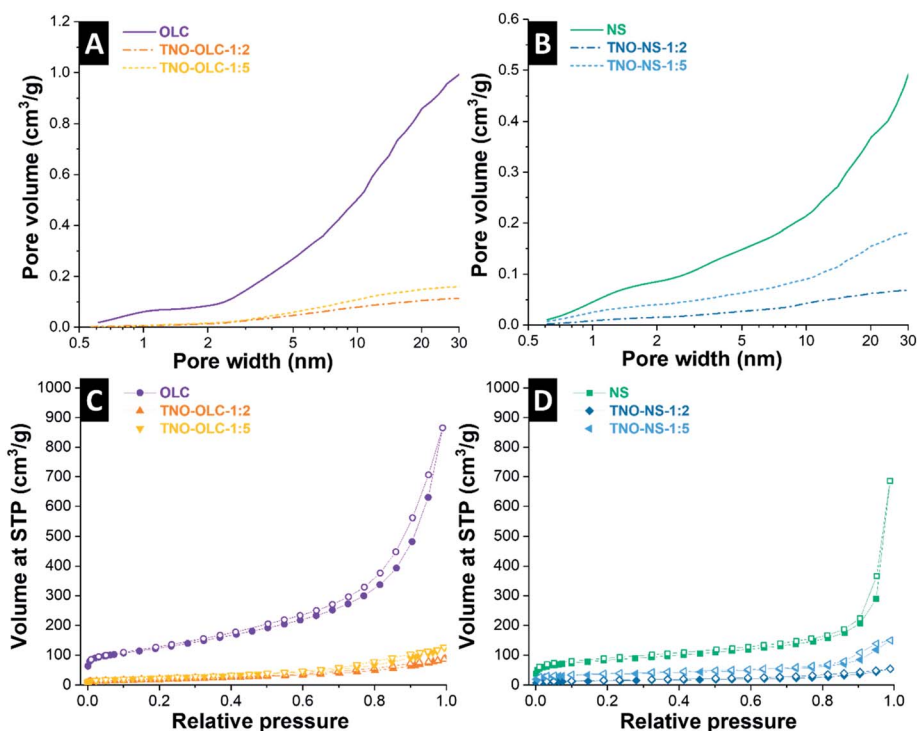


Fig. 2 Nitrogen gas sorption analysis at  $-196 \text{ }^\circ\text{C}$ . (A, B) Calculated pore size distribution pattern using quenched solid density functional theory and assuming slit-shaped pores. (C, D) Nitrogen gas sorption isotherms.

**Table 1** Porosity data derived from nitrogen gas sorption experiments at  $-196\text{ }^{\circ}\text{C}$ . The data was obtained by using the quenched solid density functional theory (QSDFT) and assuming slit-shaped pores

	BET surface area ( $\text{m}^2\text{ g}^{-1}$ )	QSDFT surface area ( $\text{m}^2\text{ g}^{-1}$ )	Pore volume at $p/p_0 = 0.95$ ( $\text{cm}^3\text{ g}^{-1}$ )
TNO-1:2	6	5	0.01
TNO-1:5	5	4	0.01
OLC	442	439	0.97
TNO-OLC-1:2	69	62	0.12
TNO-OLC-1:5	89	73	0.16
NS	296	271	0.45
TNO-NS-1:2	51	47	0.07
TNO-NS-1:5	113	98	0.20

specific power of the full-cell is calculated by dividing the specific energy by discharging time. The specific capacity, specific energy, and specific power values are presented with respect to the entire mass of both electrodes.

### 3. Results and discussion

#### 3.1. Synthesis, porosity, and chemical composition

Fig. 1 shows the synthesis procedure of the TNO-C nanoparticles. We prepared the nanoparticles using a controlled sol-

**Table 2** Chemical composition of the samples as determined by chemical analysis and energy dispersive X-ray spectroscopy (EDX)

	CHNS/O elemental analysis		Energy dispersive X-ray spectroscopy
	Carbon (mass%)	Oxygen (mass%)	Ti : Nb mass ratio
OLC	$98.8 \pm 0.2$	$1.9 \pm 0.5$	—
TNO-OLC-1:2	$14.7 \pm 0.2$	$17.3 \pm 0.4$	0.5
TNO-OLC-1:5	$17.5 \pm 0.3$	$22.1 \pm 0.6$	0.2
NS	$95.0 \pm 2.3$	$4.0 \pm 1.7$	—
TNO-NS-1:2	$18.8 \pm 0.1$	$19.9 \pm 0.4$	0.5
TNO-NS-1:5	$20.4 \pm 0.1$	$22.6 \pm 0.2$	0.2

gel reaction using titanium isopropoxide (TTIP) and niobium ethoxide (NbOEt) as Ti and Nb sources and highly concentrated hydrochloric acid (HCl) as an acid catalyst to promote the hydrolysis of metal alkoxides with inhibited inorganic condensation.<sup>55,56</sup> First, an appropriate amount of TTIP and NbOEt corresponding to a 1 : 2 and a 1 : 5 stoichiometric ratio of Ti : Nb was added to the THF, then HCl was added dropwise to the solution mixture. The mixture was vigorously stirred for 1 h to induce the formation of nanometer-sized TNO sols; then the sols were wet impregnated to carbon onions (OLC) and carbon nanohorns (NS). The mixture was dried at  $40\text{ }^{\circ}\text{C}$  under vacuum followed by  $80\text{ }^{\circ}\text{C}$  in an oven. For comparison, we also prepared TNO sol without adding any carbon. Well-dried sols were heat-treated 2 h at  $900\text{ }^{\circ}\text{C}$  under Ar for samples containing carbon and calcined in synthetic air for the carbon-free samples. A table with synthesis details used materials and sample labels are provided in Table S1 in ESI.†

The large outer surface areas of carbon onions and carbon nanohorns make these two materials of high interest for hybridization studies. The broad pore size distribution patterns of carbon onions and carbon nanohorns do not yield a meaningful average pore size; instead, as shown in Fig. 2 the pore size pattern and the measured nitrogen gas sorption isotherms.<sup>57</sup> As can be seen from Table 1, carbon onions have a specific surface area of  $442\text{ m}^2\text{ g}^{-1}$  and provide a pore volume of  $0.97\text{ cm}^3\text{ g}^{-1}$ ; for carbon nanohorns, we find a specific surface area of  $296\text{ m}^2\text{ g}^{-1}$  and a total pore volume of  $0.45\text{ cm}^3\text{ g}^{-1}$ . Both materials are predominately mesoporous with 6% (carbon onions) and 15% (carbon nanohorns) of the total pore volume being associated with micropores. The measured specific surface area of TNO-1:2 and TNO-1:5 with values of  $5\text{--}6\text{ m}^2\text{ g}^{-1}$  are consistent with nano-scaled metal oxide particles; assuming a crystal density of  $4.4\text{ g cm}^{-3}$  (derived from PDF 72-0159: two formula units per  $1117.02\text{ \AA}^3$ ) and spherical crystals, we would expect sub-micrometer-sized metal oxide agglomerates. Hybrid materials based on carbon onions or carbon nanohorns yielded specific surface areas of about  $50\text{--}110\text{ m}^2\text{ g}^{-1}$  per the porosity contribution of carbon nanomaterials.

The content of carbon and chemical composition of the hybrid materials TNO-OLC and TNO-NS were analyzed by

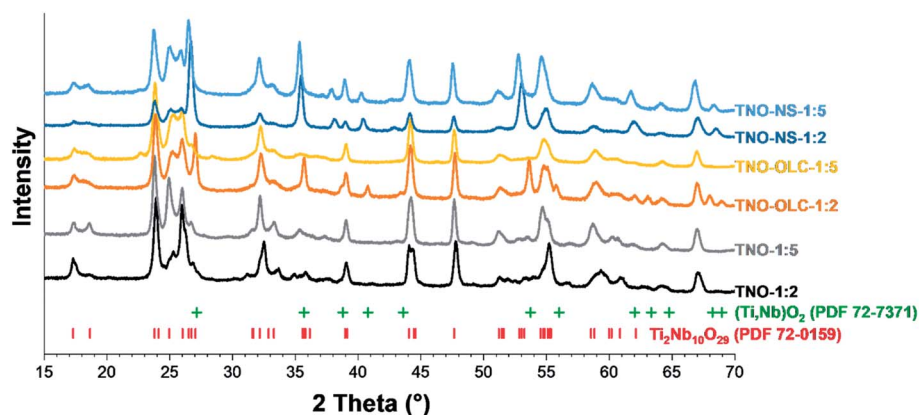


**Fig. 3** X-ray diffraction patterns of TNO-1:2, TNO-1:5, TNO-OLC-1:2, TNO-OLC-1:5, TNO-NS-1:2, and TNO-NS-1:5.

Table 3 Crystal phases, lattice constants, and domain sizes obtained from Rietveld-fitting based on the X-ray diffractograms seen in Fig. 3

	Crystal phase, space group, and PDF number	Fitted lattice parameters	Domain size (nm)	Amount (mass%)
TNO-1:2	$\text{Ti}_2\text{Nb}_{10}\text{O}_{29}$ monoclinic $A2/m$ (PDF 72-0159)	$a = 1.559 \text{ nm}$ , $b = 0.381 \text{ nm}$ , $c = 2.055 \text{ nm}$ , $\beta = 113.26^\circ$	38	90
	$(\text{Ti,Nb})\text{O}_2$ tetragonal $P4_2/mnm$ (structure based on PDF 72-7371)	$a = 0.461 \text{ nm}$ , $c = 0.300 \text{ nm}$	>100	10
TNO-1:5	$\text{Ti}_2\text{Nb}_{10}\text{O}_{29}$ monoclinic $A2/m$ (PDF 72-0159)	$a = 1.556 \text{ nm}$ , $b = 0.382 \text{ nm}$ , $c = 2.055 \text{ nm}$ , $\beta = 113.16^\circ$	36	94
	$(\text{Ti,Nb})\text{O}_2$ tetragonal $P4_2/mnm$ (structure based on PDF 72-7371)	$a = 0.461 \text{ nm}$ , $c = 0.300 \text{ nm}$	>100	6
TNO-OLC-1:2	$\text{Ti}_2\text{Nb}_{10}\text{O}_{29}$ monoclinic $A2/m$ (PDF 72-0159)	$a = 1.560 \text{ nm}$ , $b = 0.381 \text{ nm}$ , $c = 2.058 \text{ nm}$ , $\beta = 113.40^\circ$	27	87
	$(\text{Ti,Nb})\text{O}_2$ tetragonal $P4_2/mnm$ (structure based on PDF 72-7371)	$a = 0.479 \text{ nm}$ , $c = 0.296 \text{ nm}$	>100	13
TNO-OLC-1:5	$\text{Ti}_2\text{Nb}_{10}\text{O}_{29}$ monoclinic $A2/m$ (PDF 72-0159)	$a = 1.578 \text{ nm}$ , $b = 0.382 \text{ nm}$ , $c = 2.076 \text{ nm}$ , $\beta = 114.18^\circ$	26	95
	$(\text{Ti,Nb})\text{O}_2$ tetragonal $P4_2/mnm$ (structure based on PDF 72-7371)	$a = 0.474 \text{ nm}$ , $c = 0.300 \text{ nm}$	>100	5
TNO-NS-1:2	$\text{Ti}_2\text{Nb}_{10}\text{O}_{29}$ monoclinic $A2/m$ (PDF 72-0159)	$a = 1.568 \text{ nm}$ , $b = 0.381 \text{ nm}$ , $c = 2.070 \text{ nm}$ , $\beta = 113.43^\circ$	26	30
	$(\text{Ti,Nb})\text{O}_2$ tetragonal $P4_2/mnm$ (structure based on PDF 72-7371)	$a = 0.472 \text{ nm}$ , $c = 0.300 \text{ nm}$	>100	70
TNO-NS-1:5	$\text{Ti}_2\text{Nb}_{10}\text{O}_{29}$ monoclinic $A2/m$ (PDF 72-0159)	$a = 1.563 \text{ nm}$ , $b = 0.382 \text{ nm}$ , $c = 2.062 \text{ nm}$ , $\beta = 113.33^\circ$	25	60
	$(\text{Ti,Nb})\text{O}_2$ tetragonal $P4_2/mnm$ (structure based on PDF 72-7371)	$a = 0.475 \text{ nm}$ , $c = 0.301 \text{ nm}$	>100	40

means of thermogravimetric analysis (TGA) and CHNS/O elemental analysis. The quantitative results are presented in Table 2, and the corresponding thermograms are found in the ESI, Fig. S1.† All TNO-OLC and TNO-NS hybrid materials showed a metal oxide content of 80–83 mass%. These values are consistent with 14.5–20.4 mass% of carbon measured by CHNS/O analysis. Energy-dispersive X-ray spectroscopy (EDX) further confirmed that the molar Ti : Nb ratio was 1 : 2 and 1 : 5 for the two different stoichiometric ratios intended during synthesis (Table 2).

### 3.2. Phase and structure analysis

X-ray diffraction was used to study the crystal structure of prepared samples TNO, TNO-OLC, and TNO-NS (Fig. 3) and the corresponding crystal structures are shown in the ESI, Fig. S2.† Since TNO-1:2 and TNO-1:5 were only physically mixed with carbon onions or carbon nanohorns to obtain composite electrodes, our analysis only provided data for the initial metal oxide phases. All diffractograms show with a varying amount the presence of monoclinic dititanium decaniobium oxide ( $\text{Ti}_2\text{Nb}_{10}\text{O}_{29}$ , PDF 72-0159) and tetragonal niobian rutile  $(\text{Ti,Nb})\text{O}_2$  (PDF 72-

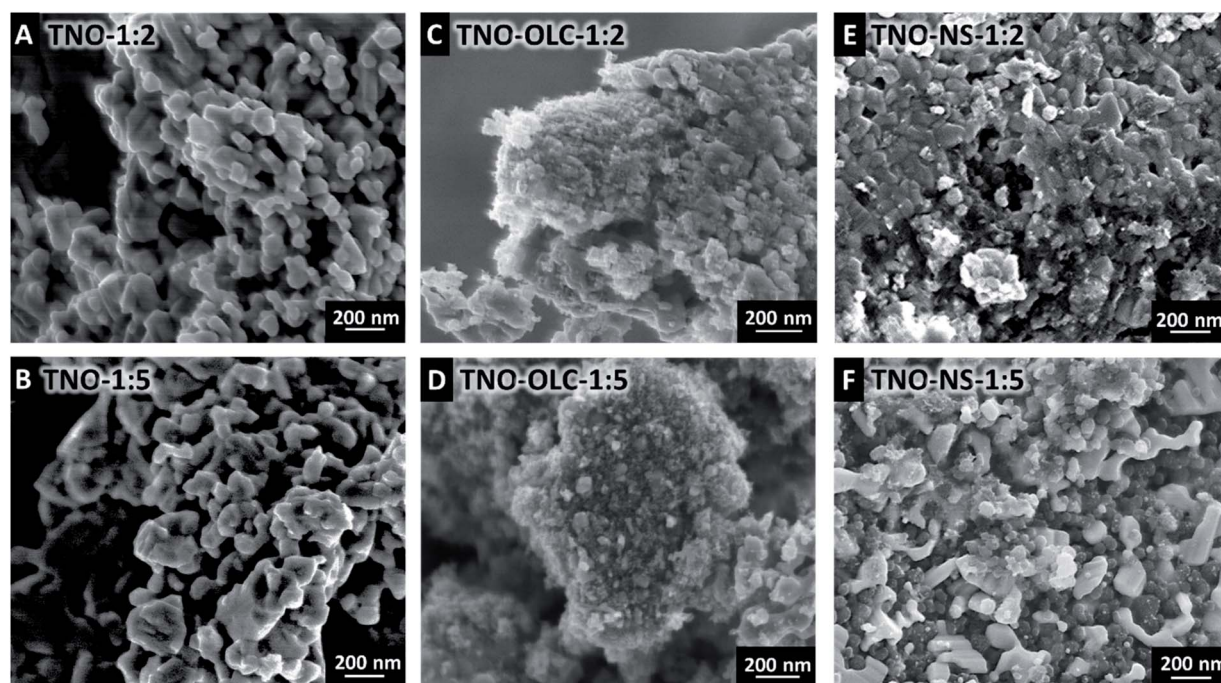


Fig. 4 Scanning electron micrographs (A) TNO-1:2, (B) TNO-1:5, (C) TNO-OLC-1:2, (D) TNO-OLC-1:5, (E) TNO-NS-1:2, and (F) TNO-NS-1:5.

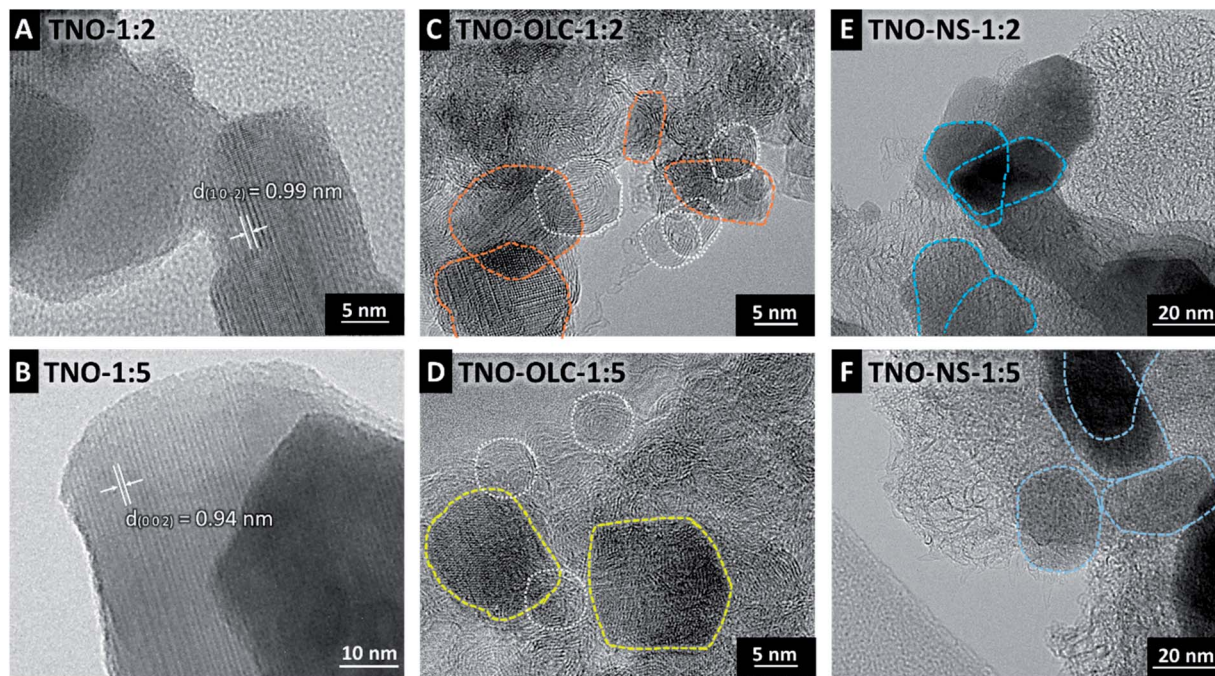


Fig. 5 Transmission electron micrographs of (A) TNO-1:2, (B) TNO-1:5, (C) TNO-OLC-1:2, (D) TNO-OLC-1:5, (E) TNO-NS-1:2, and (F) TNO-NS-1:5. White contours are outlining selected carbon onions while colored contours outline individual metal oxide domains (matching the color code used in other graphs).

7371). The signal intensity of either carbon onions or carbon nanohorns is small compared to the metal oxide phase, and we will later discuss the carbon structure based on Raman data.

Using Rietveld-fitting, we quantified the phase amount and lattice constants of  $\text{Ti}_2\text{Nb}_{10}\text{O}_{29}$ ,  $(\text{Ti,Nb})\text{O}_2$ . As seen from the data provided in Table 3, all samples showed nanoscale  $\text{Ti}_2\text{Nb}_{10}\text{O}_{29}$  with domain sizes of about 25–40 nm. Slightly larger domain sizes (36–38 nm) are found for TNO synthesized in the absence of carbon, compared to TNO-C hybrids (25–27 nm). In contrast,

the characteristic peak broadening per finite domain size was not present for  $(\text{Ti,Nb})\text{O}_2$  which corresponds with a coherence length of about 100 nm. TNO-1:2, TNO-1:5, TNO-OLC-1:2, and TNO-OLC-1:5 predominately are composed of  $\text{Ti}_2\text{Nb}_{10}\text{O}_{29}$  (87–95 mass%). In contrast, TNO hybridized with carbon nanohorns show a large amount of  $(\text{Ti,Nb})\text{O}_2$ , namely 70 mass% for TNO-NS-1:2 and 40 mass% for TNO-NS-1:5. For all samples, we also see an increased amount of the desired  $\text{Ti}_2\text{Nb}_{10}\text{O}_{29}$  phase for the initial 1 : 5 stoichiometry, which aligns with the corresponding Ti : Nb ratio.

We further characterized the nanoscale phases of TNO and carbon with scanning electron (SEM) and transmission electron microscopy (TEM). Scanning electron micrographs of TNO and TNO-C hybrid samples are presented in Fig. 4, and there are metal oxide agglomerates with a particle size ranging from *ca.* 10 nm to of about 100 nm for all materials. TNO-1:2 and TNO-1:5 (Fig. 4A and B) show a seemingly coarser texture, with the latter appearing slightly larger in agglomerate size

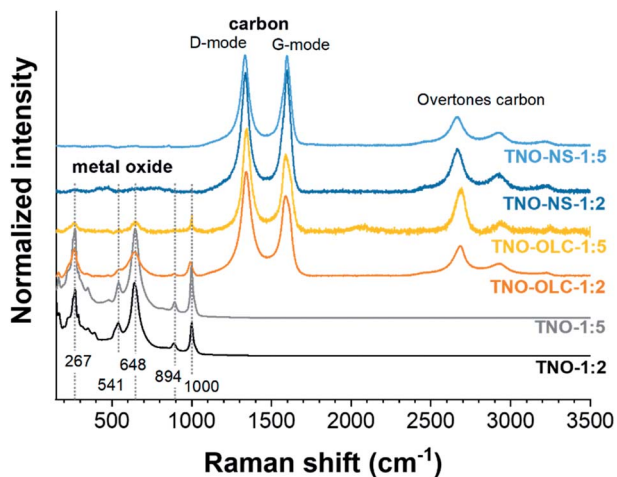


Fig. 6 Background-corrected Raman spectra of TNO-1:2, TNO-1:5, TNO-OLC-1:2, TNO-OLC-1:5, TNO-NS-1:2, and TNO-NS-1:5. All data were normalized to the intensity of the carbon D-mode as 100% and the intensity at  $3500\text{ cm}^{-1}$  as 0%.

Table 4 Results of the carbon-related Raman peak analysis

	D mode ( $\text{cm}^{-1}$ )		G mode ( $\text{cm}^{-1}$ )		$I_D/I_G$ ratio
	Position	FWHM	Position	FWHM	
OLC	1343	57	1594	57	1.6
TNO-OLC-1:2	1342	56	1596	56	1.9
TNO-OLC-1:5	1344	59	1597	57	1.8
NS	1333	54	1591	48	1.5
TNO-NS-1:2	1336	50	1599	45	1.2
TNO-NS-1:5	1334	52	1600	44	1.3

compared to the former. The TNO-OLC-1:2 and TNO-OLC-1:5 samples (Fig. 4C and D) show small agglomerates of carbon onions with small metal oxide clusters. As shown in Fig. 4E and F, carbon nanohorn agglomerates are distributed along with the metal oxide particles, and we locally can find metal oxide

particles larger than 100–200 nm. The formation of carbon onion agglomerates leads to abundant inter-particle pores, whereby the TNO growth was partially confined. Individual carbon nanohorn particles are 5- to 10-times larger than carbon onion which creates a significantly larger interparticle space.

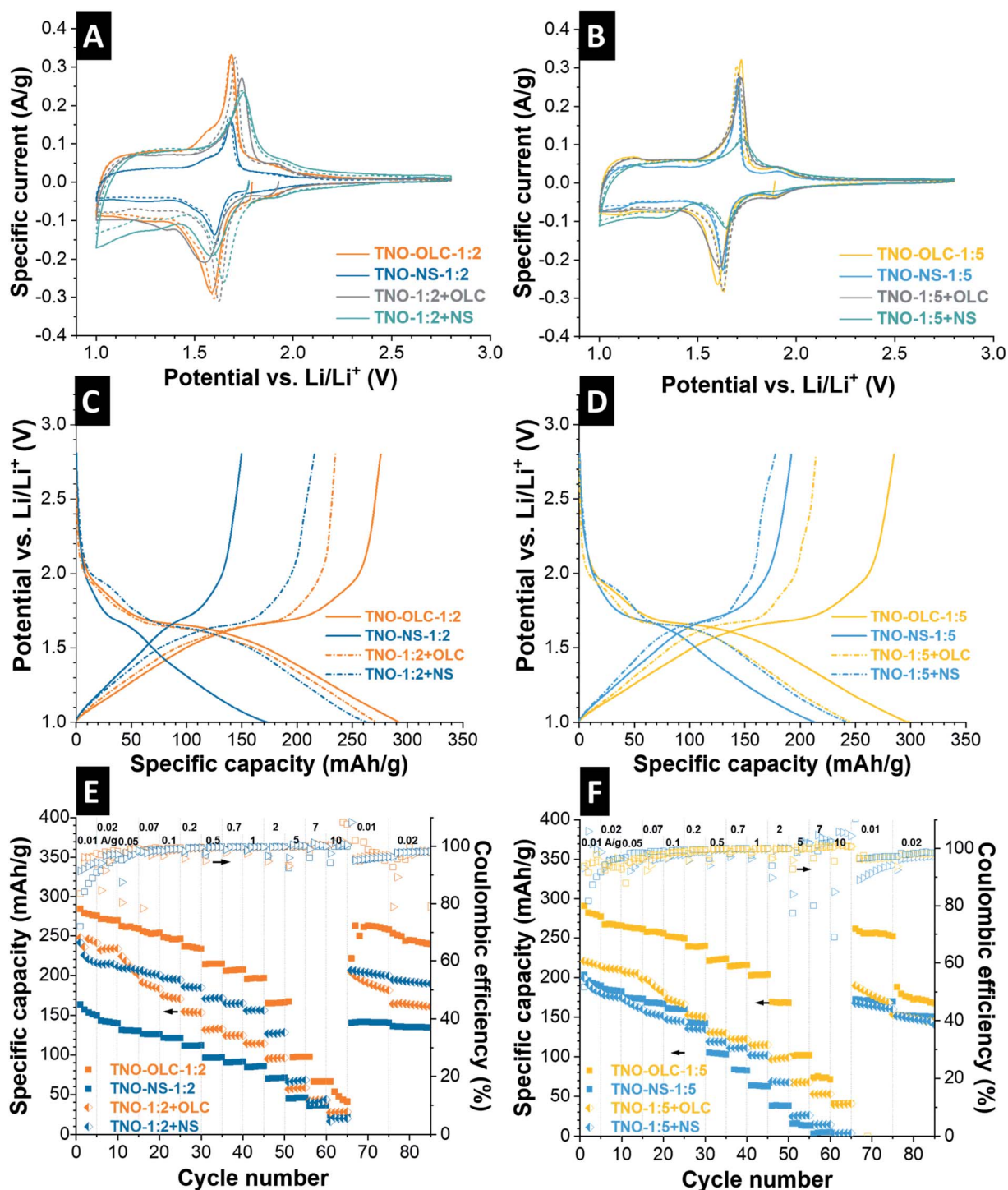


Fig. 7 (A, B) The 1<sup>st</sup> and 2<sup>nd</sup> cycles of cyclic voltammograms recorded at 0.1 mV s<sup>-1</sup> of TNO-C and TNO+ C materials with a molar (A) Ti : Nb ratio of 1 : 2 or (B) 1 : 5. The first-cycle data are presented by solid lines, the second-cycle data by dashed lines. (C, D) Galvanostatic charge/discharge profiles of the 5<sup>th</sup> cycle at 0.01 A g<sup>-1</sup> of samples with (C) Ti : Nb ratio of 1 : 2 and (D) 1 : 5 between 1.0 V and 2.8 V vs. Li/Li<sup>+</sup>. (E, F) The specific capacity of TNO-C and TNO+ C samples obtained from galvanostatic charge/discharge cycling at different specific current for rate capability and their Coulombic efficiency at a Ti : Nb molar ratio of (E) 1 : 2 or (F) 1 : 5.

Due to the dimensional difference, the metal oxide size and morphology of materials differ. These findings at higher resolution are confirmed by scanning electron micrographs recorded at lower magnification (ESI, Fig. S3†).

Transmission electron micrographs allow us to better characterize the nanocrystals contained within larger agglomerates. As seen in Fig. 5A and B, TNO-1:2 and TNO-1:5 show crystalline lattice spacings of 0.94 nm and 0.99 nm indicating (002)- and (102)-planes of  $\text{Ti}_2\text{Nb}_{10}\text{O}_{29}$ . Similar values are found for all other samples, too. The TEM images of TNO-OLC samples (Fig. 5C and D) show carbon onion agglomerates and the TNO nanoparticles located between single carbon onions. TNO-NS samples (Fig. 5E and F) also show well-hybridized and distributed metal oxide particles between the carbon nanohorn agglomerates.

Raman spectroscopy was performed for further phase analysis (Fig. 6). For TNO-1:2, TNO-1:5, TNO-OLC-1:2, and TNO-OLC-1:5 samples, the peaks at  $541\text{ cm}^{-1}$ ,  $648\text{ cm}^{-1}$ ,  $894\text{ cm}^{-1}$ , and  $1000\text{ cm}^{-1}$  are consistent with edge-shared and corner-shared  $\text{TiO}_6$ - and  $\text{NbO}_6$ -octahedra in alignment with previous reports on  $\text{Ti}_2\text{Nb}_{10}\text{O}_{29}$ .<sup>16,58–60</sup> The very small  $\text{Ti}_2\text{Nb}_{10}\text{O}_{29}$  signal intensity in hybrid samples based on carbon nanohorns results from the lower relative amount of this specific phase and the higher amount of weakly Raman-active  $(\text{Ti,Nb})\text{O}_2$ .<sup>61</sup>

The spectra of hybrid materials with either carbon onions or carbon nanohorns show the distinct peaks of incompletely graphitic carbon, namely the D-mode at  $1335\text{--}1345\text{ cm}^{-1}$  and the G-mode at  $1597\text{--}1599\text{ cm}^{-1}$ , and a pronounced range of overtones mode between  $2300\text{--}3400\text{ cm}^{-1}$ . The peak position and FWHM of each D- and G-mode and the integral of the  $I_D/I_G$  ratio are obtained by four Voigt peak fitting and presented in Table 4. The deconvolution results of the Raman spectra *via* Voigt peak fitting of carbon onion and nanohorns are presented in ESI, Fig. S4.† The D-mode relates to the ring-breathing modes of  $\text{sp}^2$ -hybridized carbon atoms due to the presence of defects, and the G-mode represents bond stretching of all pairs of  $\text{sp}^2$ -hybridized carbon.<sup>62,63</sup> The obtained  $I_D/I_G$  ratios and peak width values confirm that carbon onions and carbon nanohorns consist of nanocrystalline graphitic carbon with little difference between the two nanocarbon materials. After the hybridization of carbon onions and carbon nanohorns with TNO metal oxides, the  $I_D/I_G$  ratio, peak width, and peak position only slightly vary; this indicates that the degree of carbon ordering does not significantly change after the synthesis and hybridization.<sup>62</sup>

XPS was conducted to determine the chemical states of Ti and Nb in our TNO-C hybrid and TNO+C composite electrodes. The XPS results are depicted in Fig. S5 in ESI.† The resulting peaks at  $207.4\text{ eV}$  ( $\text{Nb } 3d_{5/2}$ ),  $210.2\text{ eV}$  ( $\text{Nb } 3d_{3/2}$ ),  $458.8\text{ eV}$  ( $\text{Ti } 2p_{3/2}$ ), and  $464.2\text{ eV}$  ( $\text{Ti } 2p_{1/2}$ ) show that the chemical state of Nb and Ti in our TNO samples consists of  $\text{Nb}^{5+}$  and  $\text{Ti}^{4+}$  in alignment with  $\text{Ti}_2\text{O}_{10}\text{Nb}_{29}$  and  $(\text{Ti,Nb})\text{O}_2$ .<sup>17,64</sup> Other oxidation states of Nb or Ti were not found despite the different synthesis conditions of Air and Ar.

### 3.3. Electrochemical performance

We tested the electrochemical performance using a lithium metal disc as the counter electrode and the reference electrode

and assembled CR2032 coin cells. As a first step towards the comprehensive electrochemical characterization, we have carried out cyclic voltammetry. Fig. 7A and B show the first and second voltammetric cycle of hybrid and composite TNO samples with Ti : Nb ratio of 1 : 2 and 1 : 5 at a scan rate of  $0.1\text{ mV s}^{-1}$  between  $1.0\text{ V}$  and  $2.8\text{ V vs. Li/Li}^+$ . The data of all samples show a cathodic (lithiation) peak at  $1.6\text{ V vs. Li/Li}^+$ , and an anodic (delithiation) peak at  $1.7\text{ V vs. Li/Li}^+$  which are related to the redox couple of  $\text{Nb}^{5+}/\text{Nb}^{4+}$ .<sup>65</sup> The broad peaks between  $1.0\text{ V}$  and  $1.4\text{ V vs. Li/Li}^+$  are commonly attributed to the  $\text{Nb}^{4+}/\text{Nb}^{3+}$  redox couple, and the peaks at  $1.75\text{ V}$  and  $2.0\text{ V vs. Li/Li}^+$  can be attributed to  $\text{Ti}^{4+}/\text{Ti}^{3+}$ .<sup>65,66</sup> After the first cycle, TNO-OLC-1:2 and TNO-NS-1:2 show distinctive change of the cathodic peaks, which is presumably related to the irreversible insertion of  $\text{Li}^+$  ions into the nanosized TNO crystal structure during the first lithiation–delithiation cycle.<sup>66</sup> TNO-NS-1:2 also displays low amplitude of redox peaks and larger anodic and cathodic peaks separation which relates to the presence of the rutile-type  $(\text{Ti,Nb})\text{O}_2$  phase which has a lower charge storage capacity.<sup>67</sup>

To quantify the charge/discharge kinetics (Table 5), we fitted the data by assuming:

$$i = av^b \quad (3)$$

where  $a$  and  $b$  are variables,  $i$  is the specific current ( $\text{mA g}^{-1}$ ), and  $v$  is the scan rate ( $\text{mV s}^{-1}$ ). From the analysis of the variable  $b$ , we can approximate the contribution of diffusion-controlled ( $b = 0.5$ ) and surface-controlled ( $b = 1$ ) processes to the overall measured current.<sup>68,69</sup> We used the cathodic peak currents for scan rates of  $0.1\text{--}2.0\text{ mV s}^{-1}$  to obtain  $b$ -values in the operating potential range of  $1.0\text{--}2.8\text{ V vs. Li/Li}^+$  (ESI, Fig. S6†). When testing the TNO+C composite electrodes, we obtained  $b$ -values of  $0.56$  (TNO-1:2+OLC),  $0.53$  (TNO-1:2+NS),  $0.56$  (TNO-1:5+OLC), and  $0.47$  (TNO-1:5+NS). The hybrid TNO samples showed  $b$ -values of  $0.68$  (TNO-OLC-1:2),  $0.71$  (TNO-OLC-1:5),  $0.81$  (TNO-NS-1:2), and  $0.69$  (TNO-NS-1:5). The higher  $b$ -values for hybrid TNO-OLC samples and TNO-NS samples than composite electrodes indicate less limitation of solid-state diffusion when carbon onions and carbon nanohorns are hybridized during synthesis.<sup>31</sup> It means that abundant electron pathways to TNO surface sites provided by carbon onions and carbon nanohorns

Table 5 Calculated  $b$ -values from cyclic voltammetry at different scan rates and specific capacities from galvanostatic charge/discharge cycling in the range of  $1.0\text{--}2.8\text{ V vs. Li/Li}^+$

	$b$ -value	Capacity ( $\text{mA h g}^{-1}$ )	
		$0.01\text{ A g}^{-1}$	$1\text{ A g}^{-1}$
TNO-OLC-1:2	0.68	286	198
TNO-OLC-1:5	0.71	290	197
TNO-NS-1:2	0.81	160	87
TNO-NS-1:5	0.69	187	40
TNO-1:2+OLC	0.56	259	123
TNO-1:2+NS	0.53	254	159
TNO-1:5+OLC	0.56	235	116
TNO-1:5+NS	0.47	243	102

in the hybrid materials are highly beneficial. This should translate to a faster charge/discharge process and more favorable cycling kinetics, as we will explore *via* galvanostatic charge/discharge cycling at different rates.

Before we further explore the galvanostatic rate handling, we first present data for the fifth galvanostatic charge/discharge cycle at  $0.01 \text{ A g}^{-1}$  for all the TNO-C hybrid and TNO+C composite in Fig. 7C and D. The lithiation profile of all hybrid and composite samples shows first lithiation regime from 2.0–1.7 V *vs.* Li/Li<sup>+</sup>, followed by a plateau around 1.7 V *vs.* Li/Li<sup>+</sup>, then linearly decreases after the plateau from 1.6–1.0 V *vs.* Li/Li<sup>+</sup>. These findings agree with the results from cyclic voltammetry. The delithiation profile of composite TNO-1:5+C samples present more distinctive plateau separations at 1.7 V *vs.* Li/Li<sup>+</sup> and the capacity increases between 1.7–2.0 V *vs.* Li/Li<sup>+</sup> than TNO-1:2 samples which can be ascribed to the existence of Ti<sup>4+</sup>/Ti<sup>3+</sup> peaks in TNO-1:5 samples at 1.7–2.0 V *vs.* Li/Li<sup>+</sup> in the corresponding cyclic voltammogram.

The galvanostatic rate capability was tested between  $0.01 \text{ A g}^{-1}$  and  $10 \text{ A g}^{-1}$  (Fig. 7E and F). The capacity values were normalized to the metal oxide mass of electrode to provide an easier comparison between TNO hybridized with carbon nanohorns and carbon onions and their mere physical mixture composites. As shown in ESI, Fig. S7,<sup>†</sup> the capacity obtained during galvanostatic rate capability tests in the potential range of 1.0–2.8 V *vs.* Li/Li<sup>+</sup> for carbon onions and carbon nanohorns are around 30–40 mA h g<sup>-1</sup> at low rates. With a mass content of about 15–20% in the hybrid and composite materials, the charge storage contribution of the carbon species is minor. For TNO materials obtained from a 1 : 2 molar ratio of Ti : Nb (Fig. 7E), we recorded during galvanostatic cycling at a specific current rate of  $0.01 \text{ A g}^{-1}$  in the potential range from 1.0–2.8 V *vs.* Li/Li<sup>+</sup> the lowest performance for TNO-NS-1:2, with an initial capacity of about 163 mA h g<sup>-1</sup>. This sample also showed the highest amount of the electrochemically less favorable niobian rutile phase (Ti,Nb)O<sub>2</sub> by XRD analysis. The importance of the crystal phase is revealed when comparing the hybrid (TNO-NS-1:2) and the composite (TNO-1:2+NS) electrode performance; here the initial TNO-1:2 grains were mostly composed of Ti<sub>2</sub>Nb<sub>10</sub>O<sub>29</sub> as found by XRD; only the presence of carbon

nanohorns during the TNO particle synthesis shifted the outcome in favor of (Ti,Nb)O<sub>2</sub>. Therefore, we obtained a much higher initial specific capacity for TNO-1:2+NS of 240 mA h g<sup>-1</sup> since carbon nanohorns only served as a conductive additive for Ti<sub>2</sub>Nb<sub>10</sub>O<sub>29</sub> in this case. TNO-OLC-1:2 provided the highest initial capacity of about 284 mA h g<sup>-1</sup>, which was higher than the composite TNO-1:2+OLC (*ca.* 247 mA h g<sup>-1</sup>). This may result from the overall small agglomerate size of TNO particles, as was seen from scanning electron micrographs (Fig. 4). Yet, as the specific current is increased, we see a much better rate handling ability of hybrid TNO-OLC-1:2 (165 mA h g<sup>-1</sup> at  $2 \text{ A g}^{-1}$ ; -42%) compared to composite TNO-1:2+OLC (94 mA h g<sup>-1</sup> at  $2 \text{ A g}^{-1}$ ; -62%) because of the better charge transport of the former. This aligns with the rather large capacity loss of about 20% with the capacity measured when returning to a specific current of  $0.01 \text{ A g}^{-1}$  after the rate handling testing. We also noticed a more unstable performance for TNO-OLC-1:2 at the 65<sup>th</sup> cycle when resuming low-rate operation.

For the set of samples obtained from a Ti : Nb ratio of 1 : 5 (Fig. 7F), we see again the poorest overall performance for TNO-NS-1:5 per the large amount of (Ti,Nb)O<sub>2</sub> with an initial capacity of 186 mA h g<sup>-1</sup>. This is about 20 mA h g<sup>-1</sup> higher than TNO-NS-1:2 because of the higher relative amount of the electrochemically more favorable phase Ti<sub>2</sub>Nb<sub>10</sub>O<sub>29</sub> (Table 3). Poorer rate capability is observed for TNO-NS-1:5, possibly due to less distribution of synthesized TNO phase within the hybrid material as seen from Fig. 4. The best initial charge storage capacity is found for TNO-OLC-1:5 (290 mA h g<sup>-1</sup>), which presents almost the same rate handling as TNO-OLC-1:2, but slightly higher absolute value than TNO-OLC-1:2 ascribed to the less content of (Ti,Nb)O<sub>2</sub> phase (Table 3). This aligns with the very similar particle morphology (Fig. 4) of both materials. TNO-OLC-1:5 hybrid material can also maintain a larger percentage of the initial capacity at a higher rate (169 mA h g<sup>-1</sup> at  $2 \text{ A g}^{-1}$ ; -42%) compared to composite TNO-1:5+OLC (220 mA h g<sup>-1</sup> at  $0.01 \text{ A g}^{-1}$ ; 96 mA h g<sup>-1</sup> at  $2 \text{ A g}^{-1}$ ; -56%). In alignment with the performance of TNO-OLC-1:2, we also see for TNO-OLC-1:5 a less stable performance after the resuming low-rate operation at the 65<sup>th</sup> cycle. The cycling operation did

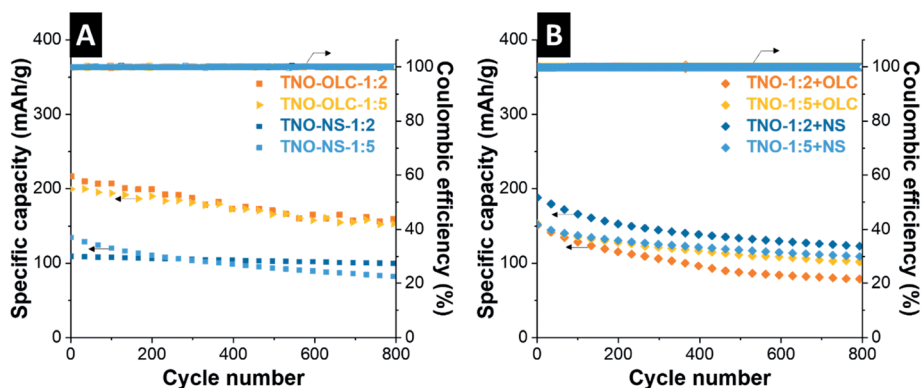


Fig. 8 Galvanostatic charge/discharge cycling performance stability at a specific current of  $1 \text{ A g}^{-1}$  for (A) TNO-C hybrid materials and (B) TNO+C composite materials for 800 cycles. In each case, we carried out a set of 10 initial cycles at  $0.05 \text{ A g}^{-1}$  for conditioning.

**Table 6** Comparison of electrochemical performance of previously reported TNO materials with various synthesis methods. We added only the highest performance data from our current work to the comparison table (TNO-OLC-1:5)

Material	Synthesis	Potential range	Specific capacity	Rate capability	Cycling stability	Ref.
Ti <sub>2</sub> Nb <sub>10</sub> O <sub>29</sub> /reduced graphene oxide	Solid-state reaction, ball milling	2.5–1.0 V	256 mA h g <sup>-1</sup> at 30 mA g <sup>-1</sup>	165 mA h g <sup>-1</sup> at 500 mA g <sup>-1</sup>	70% after 50 cycles	Ref. 33
Ti <sub>2</sub> Nb <sub>10</sub> O <sub>29</sub> /C	Solid-state reaction	2.5–1.0 V	296 mA h g <sup>-1</sup> at 1C	204 mA h g <sup>-1</sup> at 30C	95% after 100 cycles	Ref. 70
Ti <sub>2</sub> Nb <sub>10</sub> O <sub>29</sub> nanofibers	Electro-spinning	3.0–1.0 V	304 mA h g <sup>-1</sup> at 50 mA g <sup>-1</sup>	93 mA h g <sup>-1</sup> at 15 A g <sup>-1</sup>	50% after 2000 cycles	Ref. 28
Ti <sub>2</sub> Nb <sub>10</sub> O <sub>29</sub> porous nanospheres	Solvothermal synthesis	3.0–1.0 V	248 mA h g <sup>-1</sup> at 0.1C	95 mA h g <sup>-1</sup> at 20C	83% after 500 cycles	Ref. 26
Ti <sub>2</sub> Nb <sub>10</sub> O <sub>29</sub> porous nanospheres	Solvothermal synthesis	3.0–1.0 V	282 mA h g <sup>-1</sup> at 0.1C	215 mA h g <sup>-1</sup> at 10C	90% after 500 cycles	Ref. 71
TiNb <sub>2</sub> O <sub>7</sub> nanofibers	Electro-spinning	3.0–1.0 V	268 mA h g <sup>-1</sup> at 100 mA g <sup>-1</sup>	150 mA h g <sup>-1</sup> at 1 A g <sup>-1</sup>	91% after 250 cycles	Ref. 27
TiCr <sub>0.5</sub> Nb <sub>10.5</sub> O <sub>29</sub> /carbon nanotube nanocomposite	Direct hydrolysis	3.0–0.8 V	297 mA h g <sup>-1</sup> at 0.1C	206 mA h g <sup>-1</sup> at 20C	95% after 100 cycles	Ref. 72
Ti <sub>2</sub> Nb <sub>10</sub> O <sub>29</sub> hollow nanofibers	Electro-spinning	3.0–0.8 V	307 mA h g <sup>-1</sup> at 0.1C	136 mA h g <sup>-1</sup> at 20C	70% after 500 cycles	Ref. 29
TiNb <sub>2</sub> O <sub>7</sub> nanorods	Sol-gel synthesis	3.0–1.0 V	279 mA h g <sup>-1</sup> at 0.1C	122 mA h g <sup>-1</sup> at 20C	91% after 100 cycles	Ref. 73
Ti <sub>2</sub> Nb <sub>10</sub> O <sub>29</sub> /carbon onion nanohybrid	Sol-gel synthesis	2.8–1.0 V	290 mA h g <sup>-1</sup> at 10 mA g <sup>-1</sup> ( <i>ca.</i> 0.03C)	169 mA h g <sup>-1</sup> at 2 A g <sup>-1</sup> ( <i>ca.</i> 7C)	76% after 800 cycles (at 1 A g <sup>-1</sup> )	This work

not affect the structure of the samples evidenced by SEM analysis after cycling (ESI, Fig. S3†).

The comparison of TNO-1:2+OLC and TNO-1:2+NS (Fig. 7E) allows us to directly compare carbon onions and nanohorns as a conductive additive since the metal oxide phase structure is identical in both cases. Our data show a very similar initial performance at round 240 mA h g<sup>-1</sup> for both composite electrodes; yet, the rate handling and performance stability is higher when using carbon nanohorns compared to carbon onions. This may show the importance of local phase distribution of the metal oxide and carbon phases throughout the electrode which seems to be better for carbon nanohorns, at least for our electrode preparation protocol.<sup>13</sup> A contradictory pattern is seen when comparing TNO-1:5+OLC and TNO-1:5+NS (Fig. 7F): the initial capacity and the power performance of TNO-1:5+OLC is consistently higher to that of TNO-1:5+NS. Possibly, the slightly larger agglomerate size of TNO-1:5 compared to TNO-1:2 may favor carbon onions over carbon nanohorns as a better conductive additive.

As a final test for the electrochemical performance, we show in Fig. 8 the galvanostatic charge/discharge cycling stability. 800 cycles at a specific current of 1 A g<sup>-1</sup> were carried out after an initial 10 cycles at 0.05 A g<sup>-1</sup> for conditioning of the cells. Among the hybrid samples (Fig. 8A), TNO-C electrodes based on carbon nanohorns show the lowest absolute performance. TNO-OLC-1:2, TNO-OLC-1:5, and TNO-NS-1:5 show a similar decrease rate of about 80–100 μA h g<sup>-1</sup> per cycle, reaching 156 mA h g<sup>-1</sup> (–26%), 152 mA h g<sup>-1</sup> (–24%), and 83 mA h g<sup>-1</sup> (–39%), respectively, after 800 cycles. The only exception is TNO-NS-1:2, which was the sample dominated by (Ti,Nb)O<sub>2</sub>. This sample showed a rather stable electrochemical performance, reaching 100 mA h g<sup>-1</sup> after 800 cycles (–9%). The composite samples (Fig. 8B) show all a very similar trend with

a decrease in specific capacity of about 30–35 μA h g<sup>-1</sup> per cycle between the 400<sup>th</sup> and 800<sup>th</sup> cycle. Among these samples, TNO-1:2+OLC yielded the lowest capacity after 800 cycles (78 mA h g<sup>-1</sup>) while TNO-1:2+NS showed the highest capacity retention (123 mA h g<sup>-1</sup>).

As can be seen in Table 6, other works of Ti<sub>2</sub>Nb<sub>10</sub>O<sub>29</sub> in combination with carbon have reported values for the specific capacity from 248 mA h g<sup>-1</sup> (solvothermal synthesis; ref. 26) to 307 mA h g<sup>-1</sup> (electrospun; ref. 29). These data are consistent with the best-measured performance of our sample TNO-OLC-1:5 with an initial capacity of 290 mA h g<sup>-1</sup> at 0.01 A g<sup>-1</sup> (corresponding with a C-rate of about 0.03C). While difficult to compare with other works per differences in setup and operation condition, we also align with other reports for the rate handling. Previous works have shown a specific capacity of 93–212 mA h g<sup>-1</sup> at rates up to 20C compared to 169 mA h g<sup>-1</sup> at 2 A g<sup>-1</sup> (*ca.* 7C) for TNO-OLC-1:5. We also confirmed promising cycling stability since both TNO-OLC-1:2 and TNO-OLC-1:5 maintained about 75% of the capacity after 800 galvanostatic charge/discharge cycles at 1 A g<sup>-1</sup>.

### 3.4. Electrochemical performance of full-cells

To further explore the performance of TNO-hybrid materials in practical applications, we used a full-cell setup. The best performing TNO-OLC-1:5 was then employed as a negative electrode in full-cell and activated carbon (AC) electrode as a positive electrode. For the full-cell assembly, we chose a 1 : 3 ratio of the active mass when comparing the negative and positive electrode, considering the specific capacity and the rate capability of each electrode. The full-cell was then pre-cycled at 1 A g<sup>-1</sup> for 10 cycles then prior to the galvanostatic charge/discharge cycles at different specific currents from 0.025 A g<sup>-1</sup>

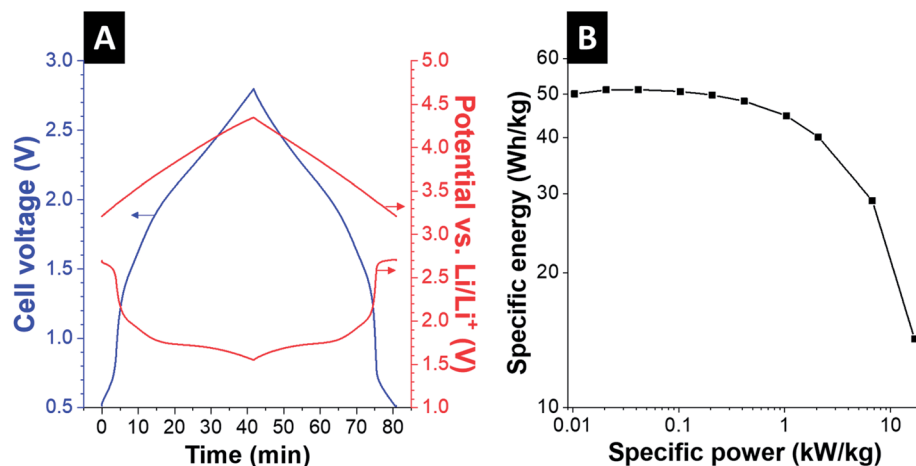


Fig. 9 (A) Galvanostatic charge/discharge profile of a full-cell with TNO-OLC-1:5 as a negative electrode and activated carbon (AC) as the positive electrode at  $0.05 \text{ A g}^{-1}$ . The potentials are plotted as cell voltage and as the corresponding electrode potentials. (B) Ragone chart of the corresponding cell.

to  $10 \text{ A g}^{-1}$ . The electrode potential profile during galvanostatic charge/discharge at a specific current of  $0.05 \text{ A g}^{-1}$  is depicted in Fig. 9A. The voltage profile of the positive electrode shows a linear increase to  $4.3 \text{ V vs. Li/Li}^+$  and decrease to  $3.2 \text{ V vs. Li/Li}^+$ , which is associated with ion electrosorption at the AC electrode surface. The charging profile of the negative TNO-OLC-1:5 electrode shows three regimes between  $2.3 \text{ V}$  and  $1.6 \text{ V vs. Li/Li}^+$  in agreement with the insertion potential shown in Fig. 7D; the discharge step also presents three regimes corresponding with the extraction of inserted  $\text{Li}^+$  ions. Fig. 9B presents the trade-off between specific power and specific energy (Ragone plot). The specific power and specific energy values were calculated using the total mass of the negative and the positive electrode. The full-cell configuration showed a performance of  $50 \text{ Wh kg}^{-1}$  at  $10 \text{ W kg}^{-1}$  and  $14 \text{ Wh kg}^{-1}$  at  $17 \text{ kW kg}^{-1}$ , with an energy efficiency of 89% and 52%, respectively.

## 4. Conclusions

We have synthesized nano-TNO hybridized either with carbon nanohorns or carbon onions by using a sol-gel method and subsequent heat treatment. The synthesis of TNO-C hybrid materials using carbon onions yielded predominately  $\text{Ti}_2\text{Nb}_{10}\text{O}_{29}$  with an average domain size of about 20–30 nm; the presence of carbon nanohorns shifted the synthesis product in favor of niobian rutile  $(\text{Ti,Nb})\text{O}_2$ . When synthesizing TNO particles without the presence of carbon, we obtained also nanoscale powder with average domain sizes of about 40 nm. Smaller domains of  $\text{Ti}_2\text{Nb}_{10}\text{O}_{29}$  below 30 nm were found in our hybrid samples; yet, the presence of carbon nanohorns modified the crystal structure and we found large amounts of niobian rutile  $(\text{Ti,Nb})\text{O}_2$  with larger domain sizes ( $>100 \text{ nm}$ ). The latter had a less favorable electrochemical energy storage capacity in  $1 \text{ M LiPF}_6$  in EC/DMC operated compared to  $\text{Ti}_2\text{Nb}_{10}\text{O}_{29}$ . The highest specific capacity values were afforded by hybrids of TNO and carbon onions with an initial capacity of  $284 \text{ mA h g}^{-1}$  for TNO-OLC-1:2 and  $290 \text{ mA h g}^{-1}$  for TNO-OLC-1:5. When using

carbon onions merely as a conductive additive in combination with TNO-1:2 or TNO-1:5, the resulting composite electrode also provided an initial specific capacity of about  $240 \text{ mA h g}^{-1}$ . This result clearly shows the strong influence of the carbon substrate on the crystal structure of TNO by hybridization. The selection of appropriate carbon substrates enables good electrochemical performance, but the difference in the crystal structure of the lithium-insertion compound may severely outweigh any influence of the hybrid-vs.-composite electrode design.

## Conflicts of interest

The authors state no conflict of interest.

## Acknowledgements

The authors thank Eduard Arzt (INM) for his continuing support. We acknowledge funding from the German Federal Ministry for Economic Affairs and Energy (BMWi) in support of the HyBaCap project (award number 03ET6113C). This work also received support *via* the Carbon Metal Oxide Nanohybrid project (CarMON) supported by the Leibniz Association (SAW-2017). We thank Pattarachai Srimuk (INM) for gas sorption analyses and helpful discussions and Andrea Jung (INM) for CHNS/O analysis.

## References

- 1 J. M. Tarascon and M. Armand, *Nature*, 2001, **414**, 359.
- 2 M. Armand and J. M. Tarascon, *Nature*, 2008, **451**, 652.
- 3 X. Zhu, J. Xu, Y. Luo, Q. Fu, G. Liang, L. Luo, Y. Chen, C. Lin and X. S. Zhao, *J. Mater. Chem. A*, 2019, **7**, 6522–6532.
- 4 X. Lou, R. Li, X. Zhu, L. Luo, Y. Chen, C. Lin, H. Li and X. S. Zhao, *ACS Appl. Mater. Interfaces*, 2019, **11**, 6089–6096.
- 5 R. Li, Y. Pu, J. Xu, Q. Fu, G. Liang, X. Zhu, L. Luo, Y. Chen and C. Lin, *Ceram. Int.*, 2019, **45**, 12211–12217.

- 6 J. Shim and K. A. Striebel, *J. Power Sources*, 2003, **119**–121, 955–958.
- 7 S. S. Zhang, *J. Power Sources*, 2006, **161**, 1385–1391.
- 8 M. V. Reddy, G. V. Subba Rao and B. V. R. Chowdari, *Chem. Rev.*, 2013, **113**, 5364–5457.
- 9 S. S. Zhang, K. Xu and T. R. Jow, *J. Power Sources*, 2004, **130**, 281–285.
- 10 Y. Zhao, X. F. Li, B. Yan, D. B. Xiong, D. J. Li, S. Lawes and X. L. Sun, *Adv. Energy Mater.*, 2016, **6**, 1502175.
- 11 A. Tolosa, B. Krüner, S. Fleischmann, N. Jäckel, M. Zeiger, M. Aslan, I. Grobelsek and V. Presser, *J. Mater. Chem. A*, 2016, **4**, 16003–16016.
- 12 J. Lee, Y. S. Jung, S. C. Warren, M. Kamperman, S. M. Oh, F. J. DiSalvo and U. Wiesner, *Macromol. Chem. Phys.*, 2011, **212**, 383–390.
- 13 M. Widmaier, N. Jäckel, M. Zeiger, M. Abuzarli, C. Engel, L. Bommer and V. Presser, *Electrochim. Acta*, 2017, **247**, 1006–1018.
- 14 L. Hu, L. J. Luo, L. F. Tang, C. F. Lin, R. J. Li and Y. J. Chen, *J. Mater. Chem. A*, 2018, **6**, 9799–9815.
- 15 X. Wu, J. Miao, W. Han, Y.-S. Hu, D. Chen, J.-S. Lee, J. Kim and L. Chen, *Electrochem. Commun.*, 2012, **25**, 39–42.
- 16 Q. Cheng, J. Liang, Y. Zhu, L. Si, C. Guo and Y. Qian, *J. Mater. Chem. A*, 2014, **2**, 17258–17262.
- 17 T. Takashima, T. Tojo, R. Inada and Y. Sakurai, *J. Power Sources*, 2015, **276**, 113–119.
- 18 J.-T. Han and J. B. Goodenough, *Chem. Mater.*, 2011, **23**, 3404–3407.
- 19 J.-T. Han, Y.-H. Huang and J. B. Goodenough, *Chem. Mater.*, 2011, **23**, 2027–2029.
- 20 A. Tolosa, S. Fleischmann, I. Grobelsek, A. Quade, E. Lim and V. Presser, *ChemSusChem*, 2018, **11**, 159–170.
- 21 R. Li, X. Zhu, Q. Fu, G. Liang, Y. Chen, L. Luo, M. Dong, Q. Shao, C. Lin, R. Wei and Z. Guo, *Chem. Commun.*, 2019, **55**, 2493–2496.
- 22 D. Pech, M. Brunet, H. Durou, P. Huang, V. Mochalin, Y. Gogotsi, P.-L. Taberna and P. Simon, *Nat. Nanotechnol.*, 2010, **5**, 651.
- 23 E. Lim, C. Jo, H. Kim, M. H. Kim, Y. Mun, J. Chun, Y. Ye, J. Hwang, K. S. Ha, K. C. Roh, K. Kang, S. Yoon and J. Lee, *ACS Nano*, 2015, **9**, 7497–7505.
- 24 M. H. Oh, T. Yu, S.-H. Yu, B. Lim, K.-T. Ko, M.-G. Willinger, D.-H. Seo, B. H. Kim, M. G. Cho, J.-H. Park, K. Kang, Y.-E. Sung, N. Pinna and T. Hyeon, *Science*, 2013, **340**, 964–968.
- 25 L. Fei, Y. Xu, X. Wu, Y. Li, P. Xie, S. Deng, S. Smirnov and H. Luo, *Nanoscale*, 2013, **5**, 11102–11107.
- 26 S. F. Lou, X. Q. Cheng, J. L. Gao, Q. Li, L. Wang, Y. Cao, Y. L. Ma, P. J. Zuo, Y. Z. Gao, C. Y. Du, H. Huo and G. P. Yin, *Energy Storage Materials*, 2018, **11**, 57–66.
- 27 V. Aravindan, J. Sundaramurthy, A. Jain, P. S. Kumar, W. C. Ling, S. Ramakrishna, M. P. Srinivasan and S. Madhavi, *ChemSusChem*, 2014, **7**, 1858–1863.
- 28 D. Pham-Cong, J. Kim, V. T. Tran, S. J. Kim, S.-Y. Jeong, J.-H. Choi and C. R. Cho, *Electrochim. Acta*, 2017, **236**, 451–459.
- 29 Q. Fu, J. Hou, R. Lu, C. Lin, Y. Ma, J. Li and Y. Chen, *Mater. Lett.*, 2018, **214**, 60–63.
- 30 S. Fleischmann, A. Tolosa and V. Presser, *Chem.–Eur. J.*, 2018, **24**, 12143–12153.
- 31 S. Fleischmann, M. Zeiger, N. Jäckel, B. Krüner, V. Lemkova, M. Widmaier and V. Presser, *J. Mater. Chem. A*, 2017, **5**, 13039–13051.
- 32 S. Li, X. Cao, C. N. Schmidt, Q. Xu, E. Uchaker, Y. Pei and G. Z. Cao, *J. Mater. Chem. A*, 2016, **4**, 4242–4251.
- 33 W. L. Wang, B.-Y. Oh, J.-Y. Park, H. Ki, J. Jang, G.-Y. Lee, H.-B. Gu and M.-H. Ham, *J. Power Sources*, 2015, **300**, 272–278.
- 34 S. Deng, D. Chao, Y. Zhong, Y. Zeng, Z. Yao, J. Zhan, Y. Wang, X. Wang, X. Lu, X. Xia and J. Tu, *Energy Storage Materials*, 2018, **12**, 137–144.
- 35 X. Zhang, S. Deng, Y. Zeng, M. Yu, Y. Zhong, X. Xia, Y. Tong and X. Lu, *Adv. Funct. Mater.*, 2018, **28**, 1805618.
- 36 Z. Yao, X. Xia, Y. Zhang, D. Xie, C. Ai, S. Lin, Y. Wang, S. Deng, S. Shen, X. Wang, Y. Yu and J. Tu, *Nano Energy*, 2018, **54**, 304–312.
- 37 S. Deng, Y. Zhang, D. Xie, L. Yang, G. Wang, X. Zheng, J. Zhu, X. Wang, Y. Yu, G. Pan, X. Xia and J. Tu, *Nano Energy*, 2019, **58**, 355–364.
- 38 K. Makgopa, P. M. Ejikeme, C. J. Jafta, K. Raju, M. Zeiger, V. Presser and K. I. Ozoemena, *J. Mater. Chem. A*, 2015, **3**, 3480–3490.
- 39 K. Makgopa, K. Raju, P. M. Ejikeme and K. I. Ozoemena, *Carbon*, 2017, **117**, 20–32.
- 40 M. E. Plonska-Brzezinska, D. M. Brus, A. Molina-Ontoria and L. Echegoyen, *RSC Adv.*, 2013, **3**, 25891–25901.
- 41 E. Lim, H. Shim, S. Fleischmann and V. Presser, *J. Mater. Chem. A*, 2018, **6**, 9480–9488.
- 42 S. Fleischmann, N. Jäckel, M. Zeiger, B. Krüner, I. Grobelsek, P. Formanek, S. Choudhury, D. Weingarth and V. Presser, *Chem. Mater.*, 2016, **28**, 2802–2813.
- 43 M. Choucair and J. A. Stride, *Carbon*, 2012, **50**, 1109–1115.
- 44 M. Zeiger, N. Jäckel, V. N. Mochalin and V. Presser, *J. Mater. Chem. A*, 2016, **4**, 3172–3196.
- 45 N. Karousis, I. Suarez-Martinez, C. P. Ewels and N. Tagmatarchis, *Chem. Rev.*, 2016, **116**, 4850–4883.
- 46 I. Suarez-Martinez, N. Grobert and C. P. Ewels, *Carbon*, 2012, **50**, 741–747.
- 47 P. J. F. Harris, S. C. Tsang, J. B. Claridge and M. L. H. Green, *J. Chem. Soc., Faraday Trans.*, 1994, **90**, 2799–2802.
- 48 S. Mauro, *US Pat.*, 7,125,525, 2006.
- 49 S. M. Unni, S. N. Bhange, R. Illathvalappil, N. Mutneja, K. R. Patil and S. Kurungot, *Small*, 2015, **11**, 352–360.
- 50 A. Tolosa, S. Fleischmann, I. Grobelsek and V. Presser, *ACS Appl. Energy Mater.*, 2018, **1**, 3790–3801.
- 51 G. Y. Gor, M. Thommes, K. A. Cychosz and A. V. Neimark, *Carbon*, 2012, **50**, 1583–1590.
- 52 M. Widmaier, B. Krüner, N. Jäckel, M. Aslan, S. Fleischmann, C. Engel and V. Presser, *J. Electrochem. Soc.*, 2016, **163**, A2956–A2964.
- 53 D. Weingarth, H. Noh, A. Foelske-Schmitz, A. Wokaun and R. Kötz, *Electrochim. Acta*, 2013, **103**, 119–124.
- 54 D. Weingarth, M. Zeiger, N. Jäckel, M. Aslan, G. Feng and V. Presser, *Adv. Energy Mater.*, 2014, **4**, 1400316.

- 55 C. Jo, Y. Kim, J. Hwang, J. Shim, J. Chun and J. Lee, *Chem. Mater.*, 2014, **26**, 3508–3514.
- 56 C. J. Brinker and G. W. Scherer, *Sol–Gel Science: The Physics and Chemistry of Sol–Gel Processing*, Academic Press, San Diego, 1990.
- 57 M. Thommes, K. Kaneko, A. V. Neimark, J. P. Olivier, F. Rodriguez-Reinoso, J. Rouquerol and K. S. W. Sing, *Pure Appl. Chem.*, 2015, **87**, 1051–1069.
- 58 A. A. McConnell, J. S. Anderson and C. N. R. Rao, *Spectrochim. Acta, Part A*, 1976, **32**, 1067–1076.
- 59 R. M. Pittman and A. T. Bell, *J. Phys. Chem.*, 1993, **97**, 12178–12185.
- 60 N. G. Eror and U. Balachandran, *J. Solid State Chem.*, 1982, **45**, 276–279.
- 61 B. X. Huang, K. Wang, J. S. Church and Y.-S. Li, *Electrochim. Acta*, 1999, **44**, 2571–2577.
- 62 A. C. Ferrari and J. Robertson, *Philos. Trans. R. Soc., A*, 2004, **362**, 2477.
- 63 A. C. Ferrari, *Solid State Commun.*, 2007, **143**, 47–57.
- 64 G. Wan, L. Yang, S. Shi, Y. Tang, X. Xu and G. Wang, *Chem. Commun.*, 2019, **55**, 517–520.
- 65 K. Tang, X. Mu, P. A. van Aken, Y. Yu and J. Maier, *Adv. Energy Mater.*, 2013, **3**, 49–53.
- 66 X. Lu, Z. L. Jian, Z. Fang, L. Gu, Y. S. Hu, W. Chen, Z. X. Wang and L. Q. Chen, *Energy Environ. Sci.*, 2011, **4**, 2638–2644.
- 67 H. Usui, S. Yoshioka, K. Wasada, M. Shimizu and H. Sakaguchi, *ACS Appl. Mater. Interfaces*, 2015, **7**, 6567–6573.
- 68 S. Ardizzone, G. Fregonara and S. Trasatti, *Electrochim. Acta*, 1990, **35**, 263–267.
- 69 M. Opitz, J. Yue, J. Wallauer, B. Smarsly and B. Roling, *Electrochim. Acta*, 2015, **168**, 125–132.
- 70 G. Y. Liu, B. Jin, R. X. Zhang, K. Y. Bao, H. Q. Xie, J. L. Guo, M. Wei and Q. Jiang, *Int. J. Hydrogen Energy*, 2016, **41**, 14807–14812.
- 71 X. Xia, S. Deng, S. Feng, J. Wu and J. Tu, *J. Mater. Chem. A*, 2017, **5**, 21134–21139.
- 72 L. Hu, R. Lu, L. Tang, R. Xia, C. Lin, Z. Luo, Y. Chen and J. Li, *J. Alloys Compd.*, 2018, **732**, 116–123.
- 73 L. Hu, C. Lin, C. Wang, C. Yang, J. Li, Y. Chen and S. Lin, *Funct. Mater. Lett.*, 2016, **09**, 1642004.

## **Supplementary Information**

# **Nanosized titanium niobium oxide/carbon electrodes for lithium-ion energy storage applications**

**Hwirim Shim,<sup>1,2</sup> Eunho Lim,<sup>1</sup> Simon Fleischmann,<sup>1</sup>**

**Antje Quade,<sup>3</sup> Aura Tolosa,<sup>1</sup> Volker Presser<sup>1,2,\*</sup>**

<sup>1</sup> INM - Leibniz Institute for New Materials, 66123 Saarbrücken, Germany

<sup>2</sup> Department of Materials Science and Engineering, Saarland University, 66123 Saarbrücken, Germany

<sup>3</sup> Leibniz Institute for Plasma Science and Technology, 17489 Greifswald, Germany

\* Corresponding author's eMail: [volker.presser@leibniz-inm.de](mailto:volker.presser@leibniz-inm.de)

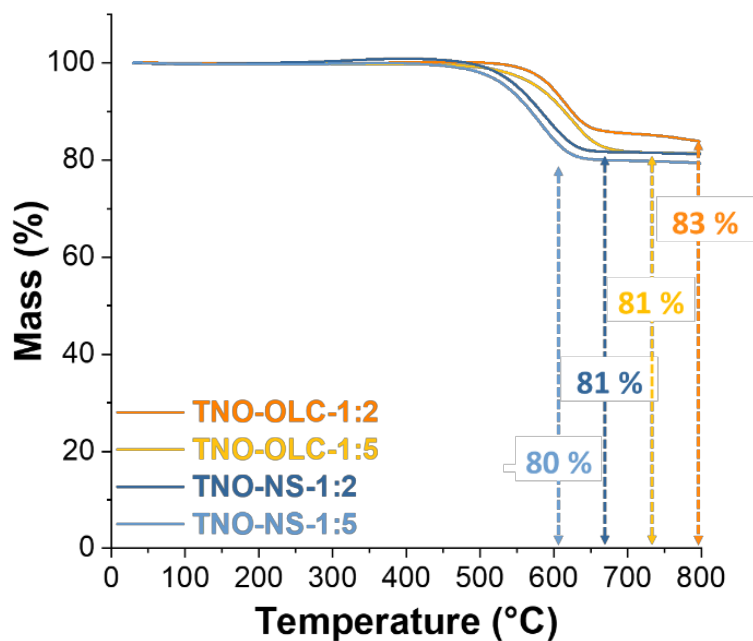


**Fig. S1:** Thermogravimetric analysis of samples under an air atmosphere for the characterization of the amount of carbon.

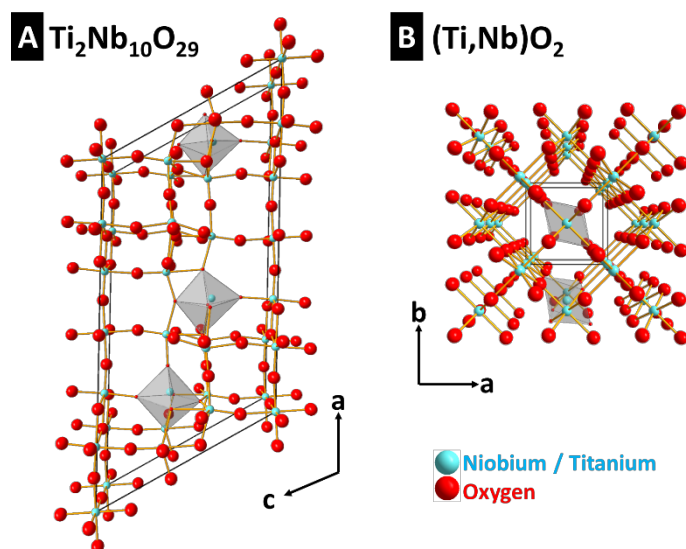


**Fig. S2:** Crystal structures of (A)  $\text{Ti}_2\text{Nb}_{10}\text{O}_{29}$  (PDF 72-0159) and (B) rutile-type  $(\text{Ti},\text{Nb})\text{O}_2$  (PDF 72-7371). Selected coordination octahedra of oxygen surrounding niobium / titanium are added for visualization purposes.

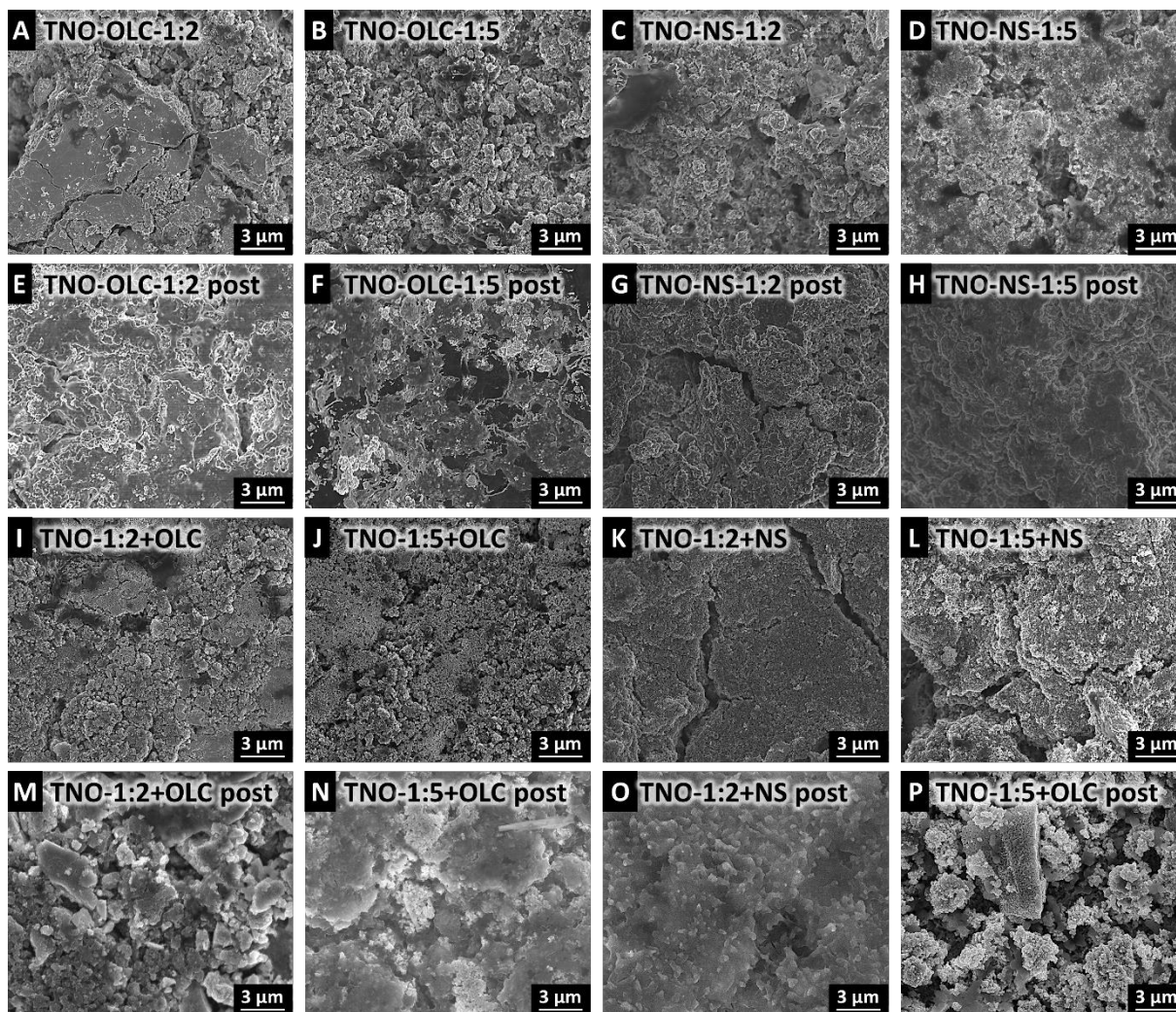


**Fig. S3:** Scanning electron micrographs of the hybrid and composite electrodes. The label “post” demarks samples that were investigated post-mortem, that is, after extended cycling.

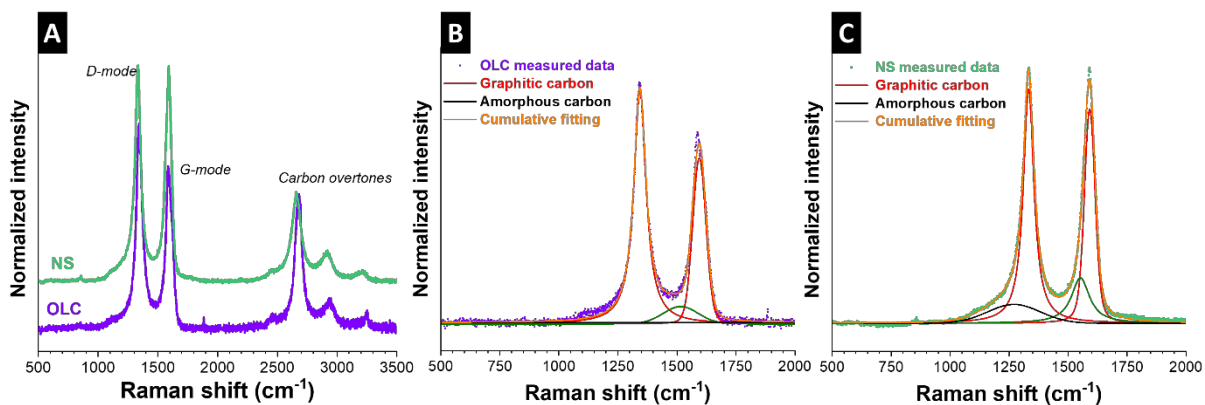


**Fig. S4:** (A) Raman spectra of carbon onions and carbon nanohorns. D- and G-mode peak fitting for (B) carbon onions and (C) carbon nanohorns.

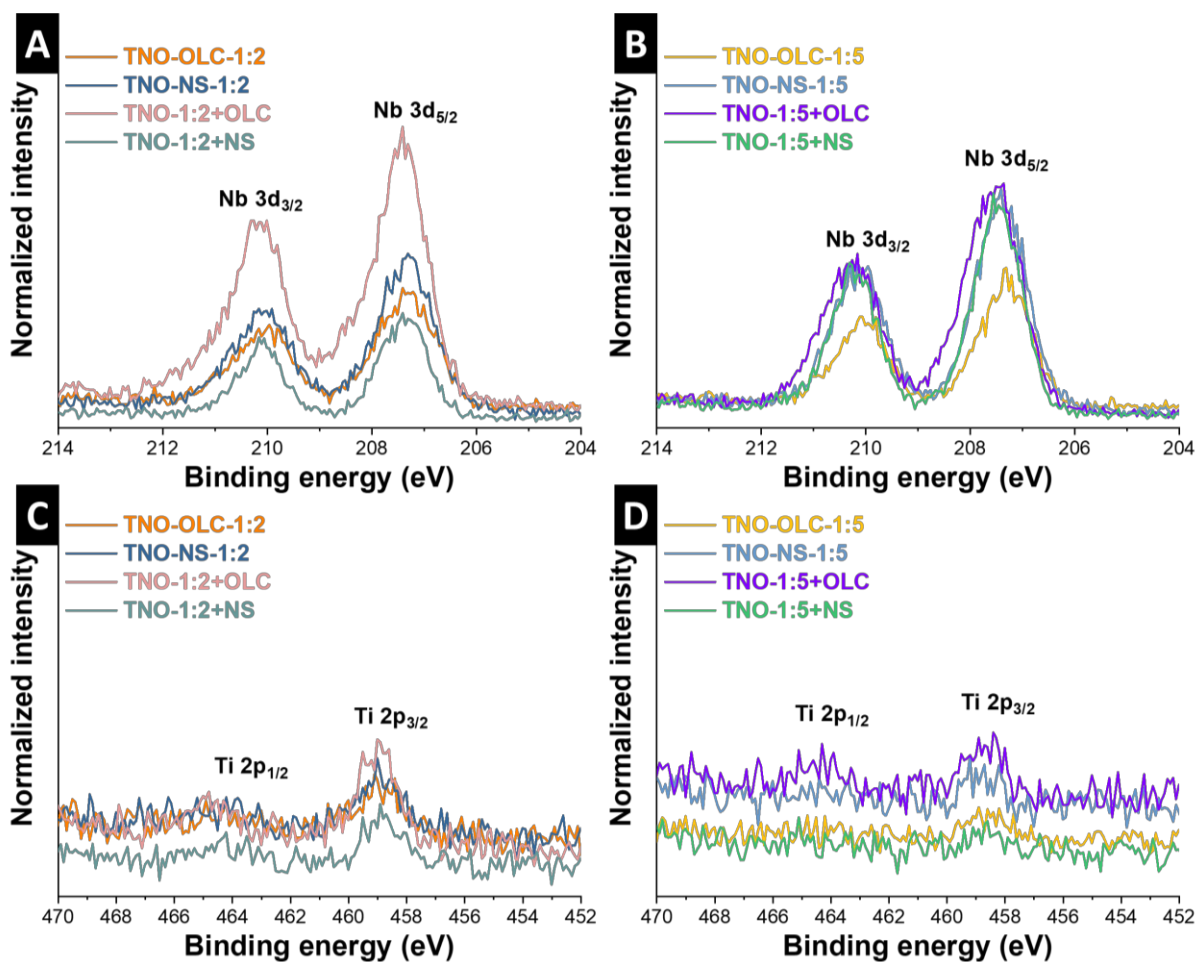


**Fig. S5:** The XPS spectra of (A-B) Nb 3d and (C-D) Ti 2p for TNO-C hybrid and TNO+C composite electrodes.

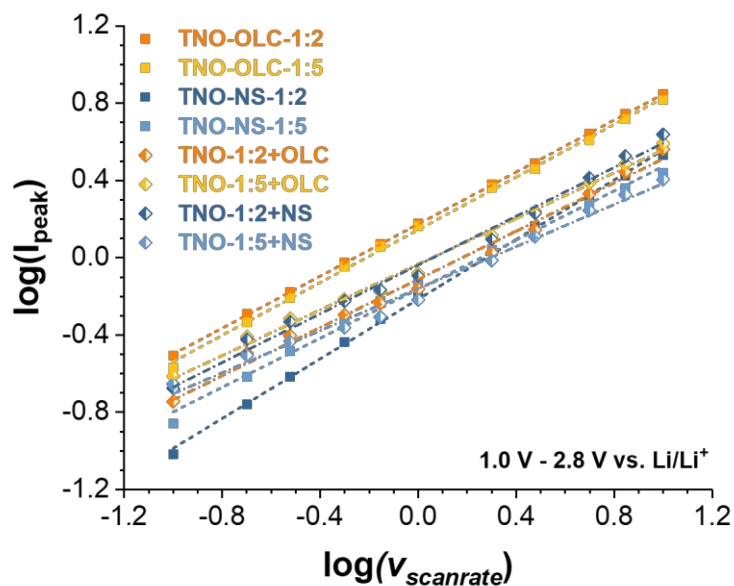


**Fig. S6:** Plot of  $\log(\text{scan rate})$  vs.  $\log(\text{peak current})$  of the lithiation (cathodic) in the potential range 1.0-2.8 V vs.  $\text{Li/Li}^+$  at scan rates of 0.1-2.0 mV/s and the linear fitting of each sample.

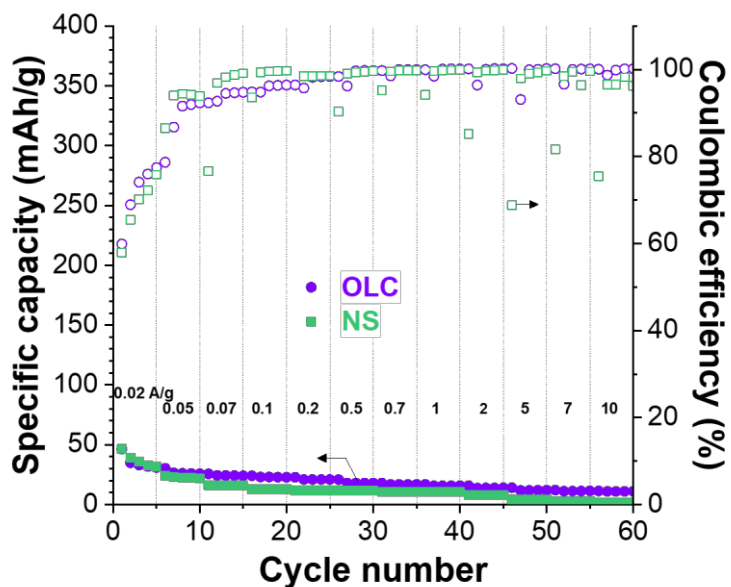


**Fig. S7:** The specific capacity of electrodes consisting of carbon onions (OLC) or carbon nanohorns (NS) obtained from galvanostatic charge/discharge cycling at different specific current for rate capability and their Coulombic efficiency between 1.0-2.8 V vs.  $\text{Li/Li}^+$ .

**Table S1:** List of the samples and their synthesis conditions according to hybridized carbon substrates.

<b>Carbon substrate</b>	<b>Ti:Nb ratio of precursor</b>	<b>Synthesis atmosphere</b>	<b>Sample name</b>
<b>Carbon onions</b>	1:2	Argon	TNO-OLC-1:2
	1:5	Argon	TNO-OLC-1:5
<b>Carbon nanohorns</b>	1:2	Argon	TNO-NS-1:2
	1:5	Argon	TNO-NS-1:5
<b>No carbon</b>	1:2	Air	TNO-1:2
	1:5	Air	TNO-1:5

# Fast and stable lithium-ion storage kinetics of anatase titanium dioxide/carbon onion hybrid electrodes

Eunho Lim<sup>1</sup>, Hwirim Shim<sup>1,2</sup>, Simon Fleischmann<sup>1,2</sup>, Volker Presser<sup>1,2</sup>

<sup>1</sup> INM - Leibniz Institute for New Materials, 66123 Saarbrücken, Germany

<sup>2</sup> Department of Materials Science and Engineering, Saarland University, 66123 Saarbrücken, Germany

## Citation:

E. Lim, H. Shim, S. Fleischmann, & V. Presser (2018). Fast and stable lithium-ion storage kinetics of anatase titanium dioxide/carbon onion hybrid electrodes. *Journal of Materials Chemistry A*, 6(20), 9480-9488.

## Own contributions:

Thermogravimetric analysis, transmission electron microscopy, critical discussion.

Cite this: *J. Mater. Chem. A*, 2018, 6, 9480Received 11th March 2018  
Accepted 2nd May 2018

DOI: 10.1039/c8ta02293c

rsc.li/materials-a

# Fast and stable lithium-ion storage kinetics of anatase titanium dioxide/carbon onion hybrid electrodes†

Eunho Lim,<sup>ID</sup><sup>a</sup> Hwirim Shim,<sup>ID</sup><sup>ab</sup> Simon Fleischmann<sup>ID</sup><sup>ab</sup> and Volker Presser<sup>ID</sup><sup>\*ab</sup>

Research on alternatives to replace conventional graphite anodes is needed to advance lithium-ion battery technology. In this work, an anatase nano-TiO<sub>2</sub>/carbon onion hybrid material (nano-TiO<sub>2</sub>-C) is introduced as a rapid and stable lithium storage anode material, synthesized by a simple synthetic route using tailored sol-gel chemistry. The nano-TiO<sub>2</sub>-C hybrid material provides highly reversible capacity (166 mA h g<sup>-1</sup> at 0.02 A g<sup>-1</sup>), promising rate capability (61 mA h g<sup>-1</sup> at 5 A g<sup>-1</sup>), and long-term cycle stability (capacity retention: 94% at 1 A g<sup>-1</sup> for 1000 cycles). We demonstrate that hybridization of nano-TiO<sub>2</sub> with carbon onions improves the high rate performance significantly.

## 1. Introduction

Li-ion batteries (LIBs) with graphite anodes are today the main energy storage device for portable electronics such as mobile phones and laptops.<sup>1,2</sup> The current research seeks to overcome the sluggish Li<sup>+</sup> insertion/extraction kinetics in graphite to meet the increasing demands for high power applications.<sup>3</sup> Also, the low Li<sup>+</sup> storage potential of graphite can cause safety problems because lithium-plating can occur at around 0 V vs. Li/Li<sup>+</sup>.<sup>4</sup> Therefore, alternative anode materials are explored. One promising candidate are polymorphs of TiO<sub>2</sub> such as anatase or rutile.<sup>5,6</sup> Among various TiO<sub>2</sub> phases, the anatase crystal structure offers a particularly beneficial Li<sup>+</sup> insertion/extraction behavior.<sup>7-10</sup> Firstly, the Li<sup>+</sup> insertion/extraction potential is located at around 1.7 V vs. Li/Li<sup>+</sup>, whereby anatase TiO<sub>2</sub> does not suffer from lithium-plating.<sup>11</sup> Secondly, the volume changes of anatase TiO<sub>2</sub> are very low during cycling (<4%).<sup>12</sup> These two properties imply that anatase TiO<sub>2</sub> may provide stable long-term performance. Thirdly, LIBs with anatase TiO<sub>2</sub> can use a cost-attractive and lightweight Al current collector for anode instead of expensive and heavy Cu. This replacement is possible because the alloying reaction between Li<sup>+</sup> and Al does not occur in the potential range for electrochemical reaction of anatase TiO<sub>2</sub> with Li<sup>+</sup> (1.0–3.0 V vs. Li/Li<sup>+</sup>).<sup>13</sup> However, the main drawback of anatase TiO<sub>2</sub> as an electrode material is its poor electrical conductivity and relatively low Li<sup>+</sup> diffusion rate.<sup>14-16</sup>

One effective strategy to enable fast charge/discharge kinetics is to reduce the particle size of anatase TiO<sub>2</sub> by use of nanoscale materials. Well-designed nanomaterial electrodes provide advantages such as a large electrode-electrolyte interface area and shortened lengths for Li<sup>+</sup> diffusion and electron transport.<sup>17,18</sup> Also, nanosizing the electrode material gives rise to pseudocapacitive reactions associated with surface or near-surface redox reactions with Li<sup>+</sup>, which are kinetically not limited by solid-state diffusion.<sup>19-22</sup> Therefore, the use of nanoscale particles improves the charge transfer kinetics of the system by reducing limitations posed by Li<sup>+</sup> diffusion in anatase TiO<sub>2</sub> and providing easier access to charge storage sites. Another effective strategy for enhanced energy storage kinetics is the hybridization of anatase TiO<sub>2</sub> with conductive carbon materials (e.g., graphene or carbon nanotubes).<sup>23-25</sup> The carbon materials create electronic pathways to compensate for the poor electronic conductivity of anatase TiO<sub>2</sub>. In a previous study, we introduced carbon onions as a substrate for atomic layer deposited metal oxide/carbon hybrids.<sup>26</sup> Capitalizing on the high intrinsic conductivity of carbon onions and small particle size of 5–10 nm with 0-D nanostructure, they are well-suited to form a homogeneously distributed conductive network throughout the electrode.<sup>27</sup> Carbon onions consist of several stacked spherical shells of graphitic carbon and can be obtained by thermal annealing of nanodiamonds in either an inert gas atmosphere or vacuum.<sup>28</sup> They form mostly mesopores in the voids between the spherical particles that are well-suited to promote the formation of homogeneously distributed, nano-sized anatase TiO<sub>2</sub> domains. They belong to the family of spherical, highly conductive carbon materials, and share structural similarities with other carbons like PUREBLACK carbon.<sup>29,30</sup> We believe that concurrent use of the two strategies (hybrid material with nano-engineering) will significantly enhance the electrochemical performance of anatase TiO<sub>2</sub>

<sup>a</sup>INM – Leibniz Institute for New Materials, 66123 Saarbrücken, Germany. E-mail: volker.presser@leibniz-inm.de

<sup>b</sup>Department of Materials Science and Engineering, Saarland University, 66123 Saarbrücken, Germany

† Electronic supplementary information (ESI) available. See DOI: 10.1039/c8ta02293c

because the intrinsic properties of anatase  $\text{TiO}_2$  highly depend on its morphology, crystallite size, and conductivity.<sup>31–33</sup>

In this work, we report on nanosized anatase  $\text{TiO}_2$ /carbon onion hybrid materials (nano- $\text{TiO}_2$ -C) as a rapid and stable  $\text{Li}^+$  insertion host easily synthesized by tailored sol-gel chemistry. The nano- $\text{TiO}_2$ -C electrodes delivered higher capacity and excellent rate capability as well as stable long-term cycling performance compared to nano- $\text{TiO}_2$  synthesized without carbon onions. We investigated the electrochemical performance of the nano- $\text{TiO}_2$ -C as LIB anode by using cyclic voltammetry analysis and galvanostatic intermittent titration technique. We demonstrate that hybridization with carbon onions significantly improves the electrochemical performance by enhancing the diffusion kinetics by shortened diffusion paths for  $\text{Li}^+$  and lowering the internal resistance of the material. Furthermore, we compare the power handling of the nano- $\text{TiO}_2$ -C hybrid material with commercial anatase  $\text{TiO}_2$  and commercial graphite. Our results will show the importance of rational design by hybridization for LIB electrode materials.

## 2. Experimental description

### 2.1. Materials

**2.1.1. Synthesis of nano- $\text{TiO}_2$ -C, nano- $\text{TiO}_2$ , com- $\text{TiO}_2$ , and com-graphite.** For the synthesis of an anatase nano- $\text{TiO}_2$ /carbon onion hybrid material (nano- $\text{TiO}_2$ -C), 1 mL of titanium isopropoxide (TTIP, Sigma Aldrich) was mixed with 5 mL of tetrahydrofuran (THF, Sigma Aldrich) with appropriate stirring at room temperature. Then, 0.36 mL of 35–37% hydrochloric acid (concentrated HCl, Sigma Aldrich) was added dropwise to the TTIP/THF mixture solution with continuous stirring for 1 h. To hybridize the synthesized  $\text{TiO}_x$  sols with carbon onions, the synthesized  $\text{TiO}_x$  sols were homogeneously mixed with carbon onion (0.05 g) by a wet impregnation method. Then, the prepared  $\text{TiO}_x$ /carbon onion hybrid material was dried at 40 °C overnight under a vacuum condition. Subsequently, the prepared  $\text{TiO}_x$ /carbon onion hybrid material was dried at 80 °C overnight. For crystallization of  $\text{TiO}_x$  to anatase  $\text{TiO}_2$ , the prepared  $\text{TiO}_x$ /carbon onion hybrid material was heat-treated in Ar atmosphere at 400 °C for 2 h with heating/cooling rate of 1 °C  $\text{min}^{-1}$ . The anatase nano- $\text{TiO}_2$  (nano- $\text{TiO}_2$ ) material without carbon onions was synthesized with the same method mentioned above, but just without the addition of carbon onions. And, commercial anatase  $\text{TiO}_2$  (com- $\text{TiO}_2$ ) and commercial graphite (com-graphite) were purchased from Sigma Aldrich and Graphite Kropfmühl, respectively.

**2.1.2. Synthesis of carbon onions.** Carbon onions were prepared using thermal annealing of a detonation nanodiamond precursor (average diameter *ca.* 5 nm, NaBond Technologies) in Ar atmosphere at 1700 °C for 1 h with heating/cooling rate of 20 °C  $\text{min}^{-1}$  in a high-temperature furnace (Thermal Technology Inc.).<sup>34</sup>

### 2.2. Materials characterization

**2.2.1. Structural and chemical characterization.** For X-ray diffraction (XRD) measurements, a D8 Discover (Bruker AXS)

diffractometer with a Cu X-ray source (Cu- $K_{\alpha}$ , 40 kV, 40 mA) and a two-dimensional detector (VANTEC-500) was employed. Transmission electron microscopy (TEM) was conducted using a 2100F system (JEOL) at an operating voltage of 200 kV. Elemental mappings were carried out by energy dispersive X-ray spectrometer (EDX) with a Thermo Fisher Scientific EDX detector (UltraDry). To obtain Raman spectra, a Renishaw inVia Raman Microscope was employed using an Nd:YAG laser with an excitation wavelength of 532 nm and a power of about 0.2 mW. A 50 $\times$  objective (numeric aperture: 0.9) and a 2400 lines per mm grating was used reaching a resolution of 1.2  $\text{cm}^{-1}$ . For thermogravimetric analysis (TGA), a TG 209 F1 Libra system (Netzsch) was employed.

**2.2.2. Electrochemical measurements.** For the preparation of  $\text{TiO}_2$  electrodes (nano- $\text{TiO}_2$ -C, nano- $\text{TiO}_2$ , and com- $\text{TiO}_2$ ) and the com-graphite electrode, the active materials (80 mass%), additive carbon (acetylene carbon black, 10 mass%, Alfa Aesar), and polyvinylidene fluoride (PVDF, 10 mass%, Alfa Aesar) binder were homogeneously mixed in a solution of *N*-methyl-2-pyrrolidone (NMP, Sigma Aldrich). The prepared slurries were casted on Cu collectors *via* doctor-blading. The prepared electrodes were dried at 60 °C for 6 h and afterward at 110 °C overnight under vacuum. The dried electrodes were roll-pressed, and the mass loading and thickness of the electrodes were controlled in the range of 1.4–1.6  $\text{mg cm}^{-2}$  and 35–40  $\mu\text{m}$ , respectively; the diameter of the electrode discs was 1.4 cm. Metallic lithium was employed as the counter electrode and as the reference electrode. We used 2032-type coin cells for all electrochemical tests. 1 M  $\text{LiPF}_6$  in ethylene carbonate (EC)/dimethyl carbonate (DMC; 1 : 1 by volume, purchased from BASF, battery grade) was employed as the electrolyte, and Whatman GF/F glass microfiber filters were used as the separator. The galvanostatic charge-discharge tests were conducted using an Arbin battery cycler, and the used currents for galvanostatic tests were based on the mass of active materials (*e.g.*, nano- $\text{TiO}_2$ -C). For the galvanostatic intermittent titration technique (GITT), we applied a specific current of 0.02 A  $\text{g}^{-1}$  for 30 min to confirm the closed-circuit voltage (CCV) and turned off for 10 h to characterize the quasi-open-circuit voltage (QOCV). Cyclic voltammetry was carried out with a potentiostat/galvanostat (VSP300, Bio-Logic). The potential range of all electrochemical tests was 1.0–3.0 V *vs.*  $\text{Li}/\text{Li}^+$ .

## 3. Results and discussion

### 3.1. Material characterization

The anatase nano- $\text{TiO}_2$ /carbon onion hybrid material (nano- $\text{TiO}_2$ -C) was synthesized by using tailored sol-gel chemistry. A schematic illustration of our synthesis approach is shown in Fig. 1A. Titanium isopropoxide (TTIP) is usually used as a  $\text{TiO}_2$  precursor, but its extreme hydrolysis and condensation under normal condition (pH  $\sim$ 7) would lead to highly aggregated  $\text{TiO}_x$  sols. To overcome this problem, we employed tailored sol-gel chemistry by using acidic conditions to synthesize nanosized anatase  $\text{TiO}_2$  particles. First, TTIP was mixed with tetrahydrofuran (THF), and then the concentrated hydrochloric acid (HCl) was injected into the solution. Concentrated HCl is employed as

both reactant ( $\text{H}_2\text{O}$ ) and acid catalyst to precisely tailor hydrolysis and condensation rate of TTIP. We did this to accelerate the hydrolysis of TTIP in acidic media with inhibited inorganic condensation, resulting in the synthesis of nanosized  $\text{TiO}_x$  sols.<sup>35,36</sup> Subsequently, the nanosized  $\text{TiO}_x$  sols were impregnated into the interparticle volume of the carbon onions *via* vacuum back-filing. Finally, for the conversion of  $\text{TiO}_x$  to anatase  $\text{TiO}_2$ , the  $\text{TiO}_x$ /carbon onion hybrid material was heat-treated in argon at 400 °C. It is expected that nanosized anatase  $\text{TiO}_2$  can be homogeneously distributed in mesopores between spherical carbon onion particles, which further prevent severe sintering during heat-treatment. It could result in improved electrochemical performance regarding rate capability and cycling stability. In addition, high intrinsic conductivity of carbon onions will be beneficial for providing electron pathways to the domains of anatase  $\text{TiO}_2$ . For comparison, we also synthesized nanosized anatase  $\text{TiO}_2$  (nano- $\text{TiO}_2$ ) by the same method mentioned above without introduction of carbon onions.

Structural characterization of  $\text{TiO}_2$  electrodes and commercial graphite (com-graphite) was performed using X-ray diffraction (XRD). The XRD patterns of  $\text{TiO}_2$  electrodes including nano- $\text{TiO}_2$ -C, nano- $\text{TiO}_2$ , and commercial anatase  $\text{TiO}_2$  (com- $\text{TiO}_2$ ) show diffraction peaks of the anatase  $\text{TiO}_2$  (JCPDS no. 21-1272) without impurities (Fig. 1B and ESI, Fig. S1A†). The XRD peaks of nano- $\text{TiO}_2$ -C and nano- $\text{TiO}_2$  are much broader than those of com- $\text{TiO}_2$  because of nanoscale of the former. We also provide the XRD pattern of graphite with the typical (002) and (004) plane reflections for comparison in ESI, Fig. S1B.†

The particle size and morphology of nano- $\text{TiO}_2$ -C and the control materials were characterized using transmission electron microscopy (TEM). As seen from the ESI, Fig. S2A–C† show that carbon onions before hybridization with nanosized anatase  $\text{TiO}_2$  have a small particle size of 5–10 nm with several stacked spherical shells of incompletely ordered graphitic carbon. The 0-D nanostructure of carbon onions seems to aid the hybridization with nanosized anatase  $\text{TiO}_2$ . In addition, their small particle size could promote the formation of effective electron

pathways to domains of anatase  $\text{TiO}_2$ . Similar effects may also be achieved by use of other nanocarbons, including optimized carbon black. Fig. 2A provides TEM micrographs of nano- $\text{TiO}_2$ -C comprising particles below 10 nm. As seen at higher magnification (Fig. 2B), nano- $\text{TiO}_2$  particles and carbon onions are well hybridized. Fig. 2C–F shows the elemental distribution of titanium, oxygen, and carbon obtained by energy dispersive X-ray spectroscopy (EDX). The data show the homogeneous hybridization between  $\text{TiO}_2$  and carbon onions. Like the TEM micrographs of nano- $\text{TiO}_2$ -C, the TEM images in ESI Fig. S2D and E† show that nano- $\text{TiO}_2$  consists of particles smaller than 10 nm. In contrast to the nanoscale  $\text{TiO}_2$  electrodes, the size and morphology of com- $\text{TiO}_2$  particles are much larger and irregular (ESI, Fig. S2F†).

The presence of carbon onions in the nano- $\text{TiO}_2$ -C hybrid material was confirmed by Raman spectroscopy and quantified by thermogravimetric analysis (TGA). The Raman spectrum in Fig. 3A exhibit two bands around 1350  $\text{cm}^{-1}$  and 1600  $\text{cm}^{-1}$  which are characteristic for the D-band and G-band of incompletely crystalline graphitic carbon, respectively. The Raman spectrum of carbon aligns with our previous work on carbon onions.<sup>28</sup> Raman peaks at 143  $\text{cm}^{-1}$ , 195  $\text{cm}^{-1}$ , 396  $\text{cm}^{-1}$ , 518  $\text{cm}^{-1}$ , and 639  $\text{cm}^{-1}$  are assigned as the  $E_g$ ,  $E_g$ ,  $B_{1g}$ ,  $A_{1g}$  or  $B_{1g}$ , and  $E_g$  modes of anatase  $\text{TiO}_2$ .<sup>37</sup> The thermogram depicted in Fig. 3B allows us to quantify the carbon content because  $\text{TiO}_2$  is non-combustible. We calculated a carbon content of the nano- $\text{TiO}_2$ -C material from the TGA data of 23 mass% (Fig. 3B).

### 3.2. General electrochemical performance

During the first galvanostatic cycle at a rate of 0.02 A  $\text{g}^{-1}$  in the potential range from 1.0–3.0 V *vs.* Li/Li<sup>+</sup>, the nano- $\text{TiO}_2$ -C material provides a specific capacity of 186 mA h  $\text{g}^{-1}$  and 158 mA h  $\text{g}^{-1}$  for lithiation and de-lithiation, respectively, with a coulombic efficiency of *ca.* 85% (ESI, Fig. S3A†). The irreversible capacity loss in the first cycle aligns with side reactions such as solid-electrolyte interphase (SEI) formation and irreversible reactions inside nanostructured materials.<sup>38–40</sup> After the

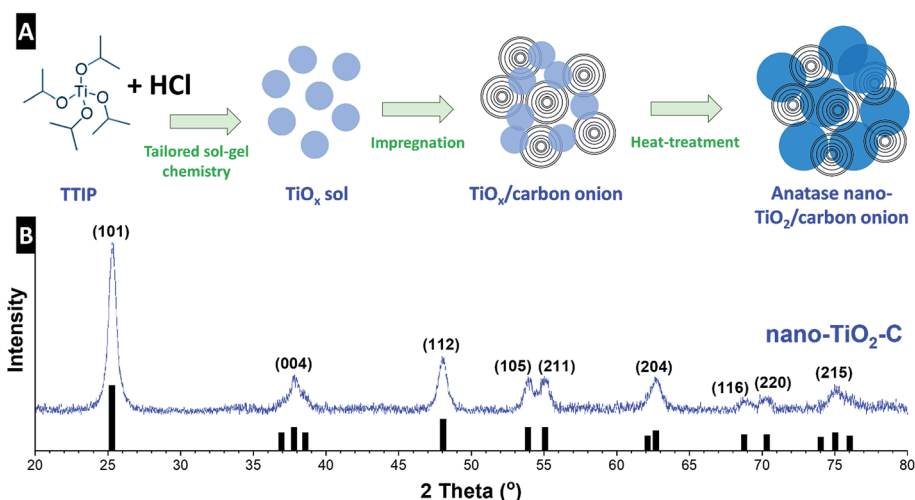


Fig. 1 (A) Schematic illustration of the synthesis of nano- $\text{TiO}_2$ -C. (B) XRD pattern of nano- $\text{TiO}_2$ -C.

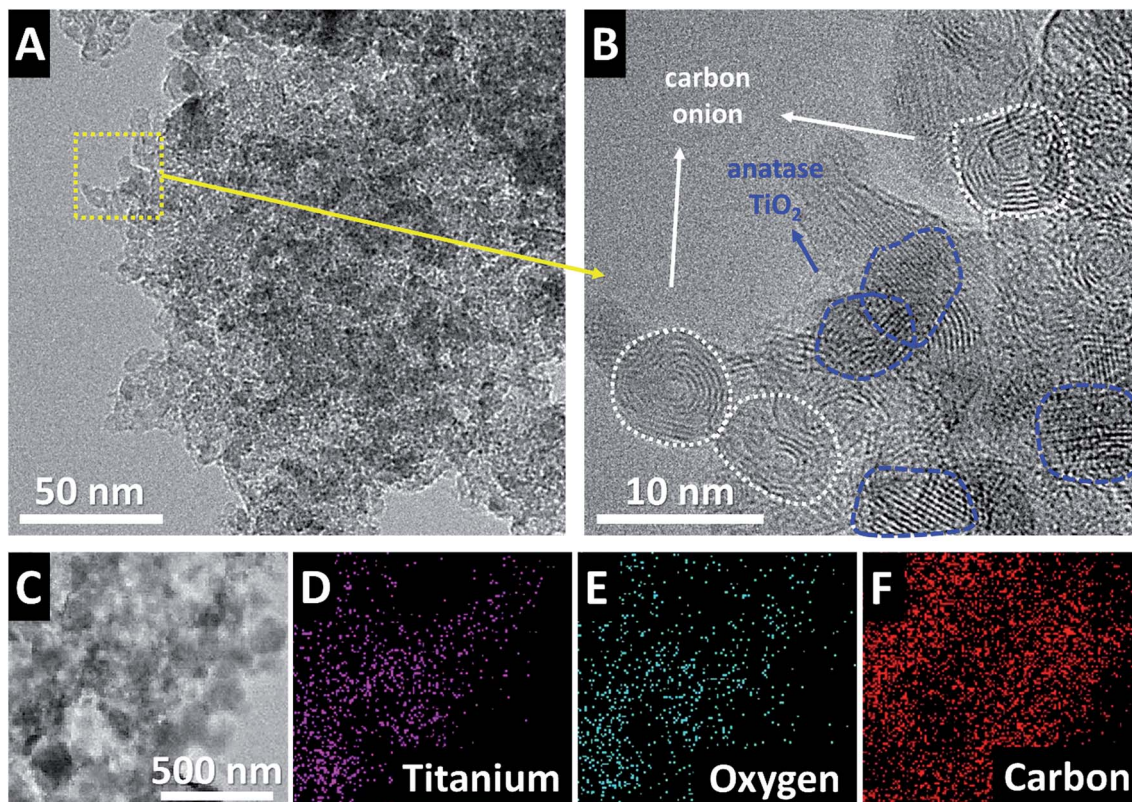


Fig. 2 (A and B) TEM images of nano-TiO<sub>2</sub>-C. (C-F) EDX elemental mappings of nano-TiO<sub>2</sub>-C.

first cycle, a reversible capacity of 166 mA h g<sup>-1</sup> is observed at 0.02 A g<sup>-1</sup> for nano-TiO<sub>2</sub>-C (Fig. 4A). The de-lithiation capacity of nano-TiO<sub>2</sub>-C was 166 mA h g<sup>-1</sup> at 0.02 A g<sup>-1</sup> and 61 mA h g<sup>-1</sup> at 5 A g<sup>-1</sup>, which indicates a rate capability superior to nano-TiO<sub>2</sub>. As shown in ESI, Fig. S3B,<sup>†</sup> the specific capacity of carbon onions is around 10–30 mA h g<sup>-1</sup> at various currents of 0.02–5 A g<sup>-1</sup> in the potential range of 1.0–3.0 V vs.

Li/Li<sup>+</sup>. These data indicate that carbon onions do not serve as Li<sup>+</sup> intercalation host materials but exhibit exclusively capacitive charge storage. The carbon onions are essential as electrical network to provide sufficient electron pathways to nanosized anatase TiO<sub>2</sub> domains. Therefore, even though the content of active materials in nano-TiO<sub>2</sub>-C is lower than that of nano-TiO<sub>2</sub>, nano-TiO<sub>2</sub>-C provides superior specific capacity

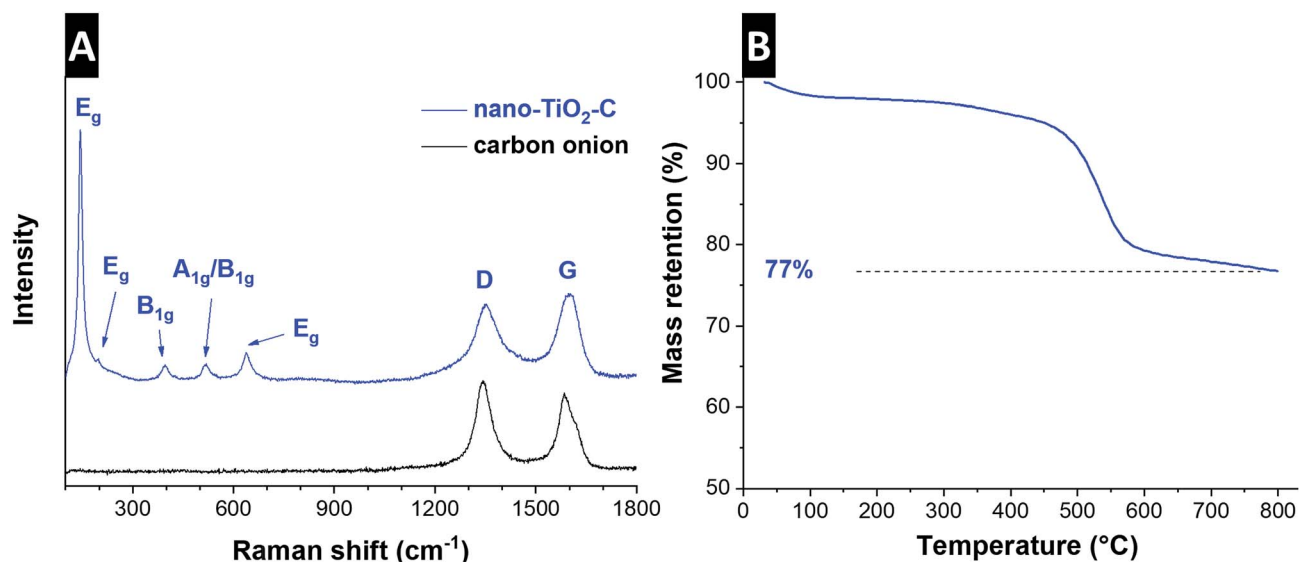


Fig. 3 (A) Raman spectra and (B) TGA profile of nano-TiO<sub>2</sub>-C.

and rate capability. Further detailed reason will be discussed in next section.

These values of nano-TiO<sub>2</sub>-C are considerably larger than commercial TiO<sub>2</sub> (com-TiO<sub>2</sub>), which yielded 72 mA h g<sup>-1</sup> at 0.02 A g<sup>-1</sup> and the capacity of the latter was completely lost at rates of 1 A g<sup>-1</sup> or higher. The power handling performance of nano-TiO<sub>2</sub>-C was also considerably higher than com-graphite above a specific current of 0.1 A g<sup>-1</sup> (Fig. S3C and D†).

### 3.3. Charge storage kinetics

We further explored the power performance of nano-TiO<sub>2</sub>-C *via* cyclic voltammetry (CV) at scan-rates from 0.1–1.0 mV s<sup>-1</sup>. Fig. 4B and C shows CV curves in the potential range of 1.0–3.0 V vs. Li/Li<sup>+</sup> of nano-TiO<sub>2</sub> and nano-TiO<sub>2</sub>-C. The pair of redox peaks at 1.7–2.0 V vs. Li/Li<sup>+</sup> corresponds with lithiation and delithiation. They are influenced by the diffusion-controlled process in anatase-type TiO<sub>2</sub> because the Li<sup>+</sup> intercalation into anatase TiO<sub>2</sub> obeys a two-phase process including a Li-poor (tetragonal, Li<sub>0.01</sub>TiO<sub>2</sub>) and Li-rich (orthorhombic, Li<sub>0.55</sub>TiO<sub>2</sub>)

phases.<sup>41–43</sup> In contrast to nano-TiO<sub>2</sub>, the hybrid material nano-TiO<sub>2</sub>-C shows two smaller peaks in the potential range of 1.5–1.6 V vs. Li/Li<sup>+</sup> which are related to a second phase transition from Li<sub>0.55</sub>TiO<sub>2</sub> to fully lithiated LiTiO<sub>2</sub> (Fig. 4C).<sup>44</sup> We attribute this to the improved surface-controlled reaction, suggesting that the carbon onions in nano-TiO<sub>2</sub>-C hybrids play an important role to provide pathways for electron transport to the surface of nano-sized anatase TiO<sub>2</sub>.<sup>42,45</sup> Therefore, nano-TiO<sub>2</sub>-C delivered a higher specific capacity than nano-TiO<sub>2</sub> at all currents, even though the content of anatase TiO<sub>2</sub> in nano-TiO<sub>2</sub>-C is smaller. We further employed a kinetic analysis *via* eqn (1):

$$i = av^b \quad (1)$$

where  $a$  and  $b$  are variables,  $i$  is current (A g<sup>-1</sup>), and  $v$  is the scan-rate (mV s<sup>-1</sup>). From the  $b$  values, one can separate the surface-controlled current ( $i = av^1$ ) and the diffusion-controlled current ( $i = av^{0.5}$ ) on first approximation.<sup>19,46–48</sup> We used the peak currents of the lithiation process at CV scan-rates of 0.1–1.0 mV

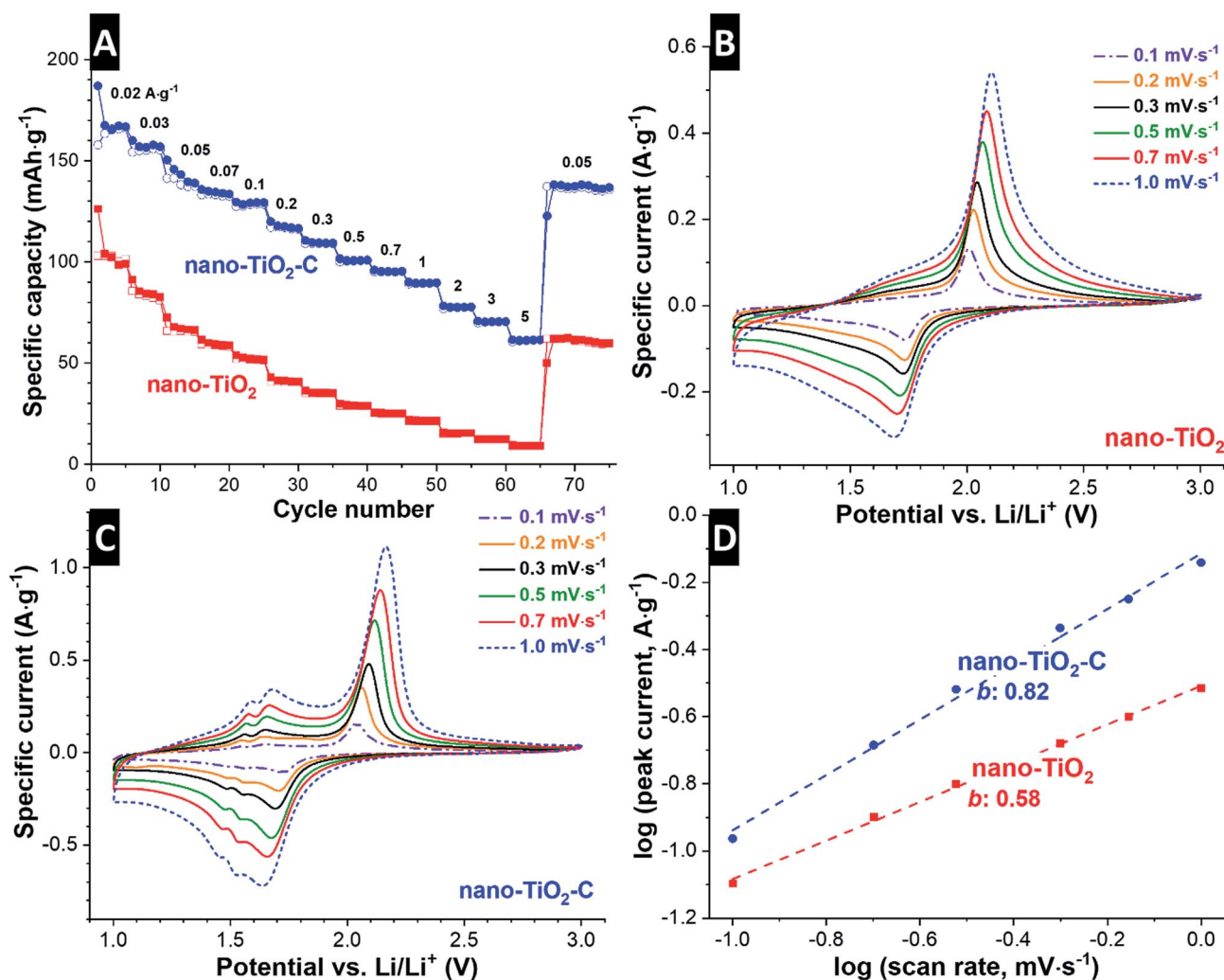


Fig. 4 (A) Comparison of rate performance of TiO<sub>2</sub> electrodes at various currents from 0.02–5 A g<sup>-1</sup>. (B and C) CV curves of nano-TiO<sub>2</sub> and nano-TiO<sub>2</sub>-C at scan-rates from 0.1–1.0 mV s<sup>-1</sup>. (D) log(scan-rate) vs. log(peak current) plots of cathodic current (lithiation process) on TiO<sub>2</sub> electrodes.

$s^{-1}$  and obtained  $b$  values for nano-TiO<sub>2</sub>-C and nano-TiO<sub>2</sub> of 0.82 and 0.58, respectively (Fig. 4D). The higher  $b$  value calculated for nano-TiO<sub>2</sub>-C implies that the hybrid system is much less limited by solid-state diffusion compared to nano-TiO<sub>2</sub> without carbon onions. This aligns with the experimental finding of a superior power handling ability when tested as LIB anode material.

We further separated the ideal surface-controlled ( $b = 1$ ) and ideal diffusion-controlled ( $b = 0.5$ ) contribution of the charge storage process *via* eqn (2):<sup>19,49</sup>

$$i = k_1 v + k_2 v^{0.5} \quad (2)$$

where  $k_1$  and  $k_2$  are suitable variables. By dividing both sides of eqn (2) by  $v^{0.5}$ , we obtain eqn (3):

$$\frac{i}{v^{0.5}} = k_1 v^{0.5} + k_2 \quad (3)$$

In eqn (2),  $k_1 v$  and  $k_2 v^{0.5}$  represent the current contributions from the surface-controlled and diffusion-controlled reactions, respectively. As seen in the ESI, Fig. S4† we can determine  $k_1$  values at each fixed potential for the so-called iso-potential analysis. According to this procedure, ESI, Fig. S5† displays the contribution of capacitor-like currents (shaded area) and the total measured currents in CVs recorded at scan-rates of 0.1–1.0 mV s<sup>-1</sup>. Larger capacitor-like currents in nano-TiO<sub>2</sub>-C (*e.g.*, 58% at 0.1 mV s<sup>-1</sup>) were observed compared to nano-TiO<sub>2</sub> (32% at 0.1 mV s<sup>-1</sup>). At higher scan-rates, the overall specific capacity decreases, but the relative contribution of capacitor-like currents increases (*e.g.*, at 1.0 mV s<sup>-1</sup>: 81% for nano-TiO<sub>2</sub>-C and 60% for nano-TiO<sub>2</sub>). We limited the scan-rates to 1 mV s<sup>-1</sup> in response to the issues of iso-potential analysis when quantifying the scan-rate dependency of measured electrochemical currents.<sup>50</sup> These issues occur because of the rate dependency of redox peaks and

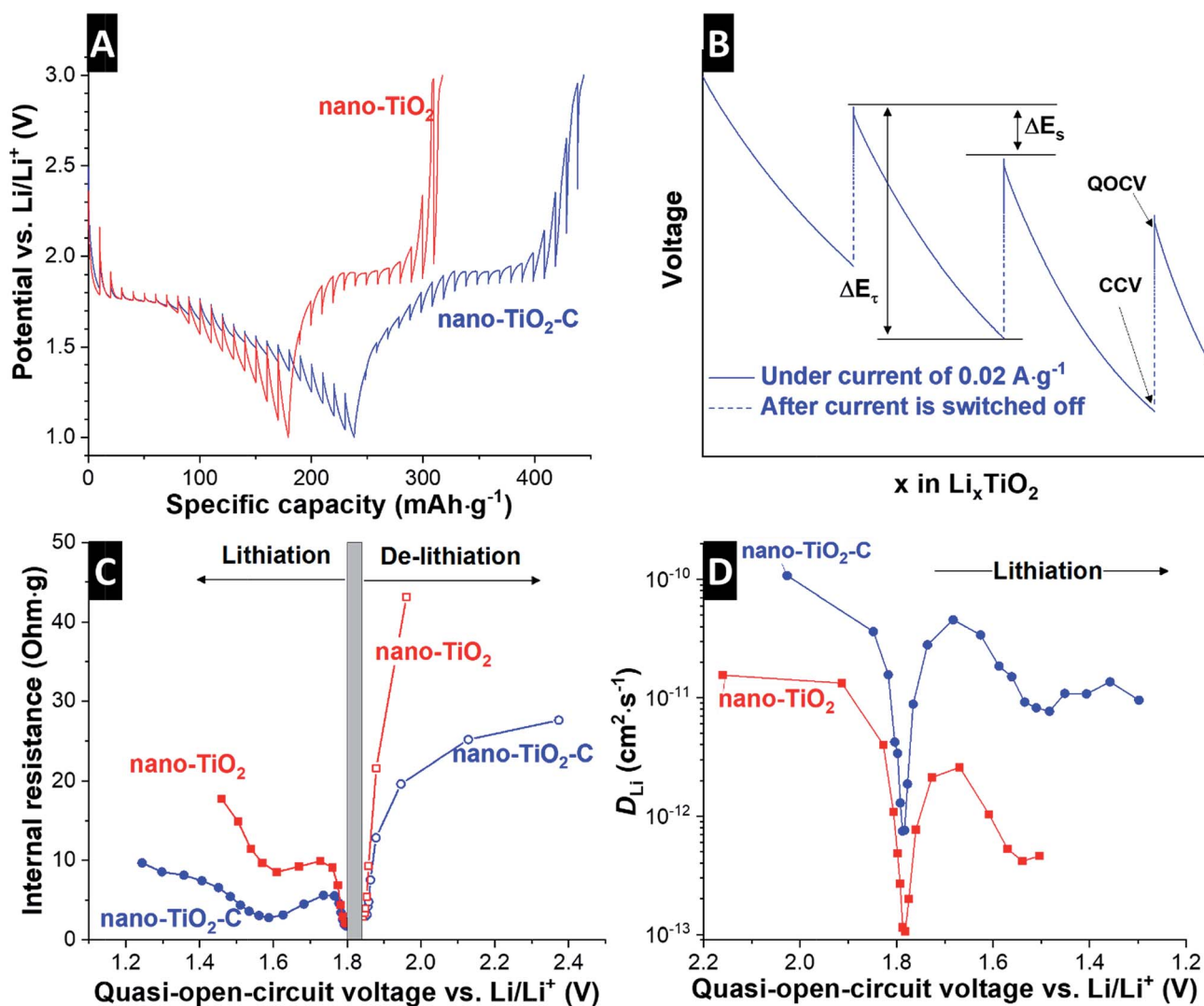


Fig. 5 (A) GITT profiles of TiO<sub>2</sub> electrodes at 0.02 A g<sup>-1</sup> (current on for 30 min, current off for 10 h). (B) Experimental scheme of GITT (current on: solid line and current off: dotted line) to define  $\Delta E_s$ ,  $\Delta E_t$ , QOCV, and OCV. (C) Evolution of the internal resistance of TiO<sub>2</sub> electrodes for the lithiation and the de-lithiation process. (D) Calculated  $D_{Li}$  from GITT for nano-TiO<sub>2</sub>-C and nano-TiO<sub>2</sub> during lithiation.

become prohibitive for quantitative analysis at high scan-rates. Albeit the limitations of iso-potential analysis of measured currents, our data clearly demonstrate the improved performance of anatase TiO<sub>2</sub> hybridized with carbon ions over conventional anatase TiO<sub>2</sub>.

### 3.4. GITT analysis

We used the galvanostatic intermittent titration technique (GITT) to further explore the effect of carbon ions on the electrochemical performance of the nano-TiO<sub>2</sub>-C hybrid material. This method is suitable to investigate the evolution of internal resistance during lithiation and de-lithiation. Fig. 5A displays the GITT voltage profiles of nano-TiO<sub>2</sub>-C and nano-TiO<sub>2</sub> at a current of 0.02 A g<sup>-1</sup> in the first cycle. As schematically exemplified in Fig. 5B, the voltage under a constant current for lithiation decreases to reach closed-circuit voltage (CCV); then, the voltage increases during the relaxation time when the current is turned off to reach quasi-open-circuit voltage (QOCV).

The internal resistances obtained from the difference between QOCV and CCV in each voltage transient for lithiation and de-lithiation (Fig. 5C) show that the nano-TiO<sub>2</sub>-C has a smaller internal resistance compared to the nano-TiO<sub>2</sub>. The internal resistance of the nano-TiO<sub>2</sub>-C electrode at a potential of ~1.7 V vs. Li/Li<sup>+</sup> for the two-phase reaction between Li<sup>+</sup> and anatase TiO<sub>2</sub> is significantly lower than that of nano-TiO<sub>2</sub>. This finding implies that the conductive carbon network provided by

carbon ions in nano-TiO<sub>2</sub>-C results in improved charge transfer.

Additionally, we used GITT to characterize the apparent Li<sup>+</sup> diffusion coefficient ( $D_{Li}$ ) by using the eqn (4) based on Fick's second law:<sup>51,52</sup>

$$D_{Li} = \frac{4}{\pi\tau} \left( \frac{m_B V_m}{M_B A} \right)^2 \left( \frac{\Delta E_s}{\Delta E_t} \right)^2 \quad (4)$$

where  $\tau$  is the constant current pulse time,  $M_B$  and  $m_B$  are the molar mass and the active material mass of the electrode, respectively,  $V_m$  and  $A$  are the molar volume and the electrode contact area, and  $\Delta E_s$  and  $\Delta E_t$  are the difference between the steady voltages and the total cell voltage change during the current pulse, respectively.

Fig. 5D compares the data for nano-TiO<sub>2</sub> and nano-TiO<sub>2</sub>-C, and the shape of the  $D_{Li}$  vs. potential plot follows the pattern reported for anatase TiO<sub>2</sub> by Zhang *et al.*<sup>53</sup> For our samples, we see that overall Li<sup>+</sup> diffusivity of nano-TiO<sub>2</sub>-C is significantly higher than that of nano-TiO<sub>2</sub>. For example, the minimum  $D_{Li}$  value at the voltage plateau region for nano-TiO<sub>2</sub> ( $1.2 \times 10^{-13}$  cm<sup>2</sup> s<sup>-1</sup> at 1.8 V vs. Li/Li<sup>+</sup>) is about 7-times smaller than for nano-TiO<sub>2</sub>-C ( $7.6 \times 10^{-13}$  cm<sup>2</sup> s<sup>-1</sup>). Considering the comparable size of the primary anatase particles in nano-TiO<sub>2</sub> and nano-TiO<sub>2</sub>-C (as indicated by TEM and XRD), we see that the homogeneous distribution of conductive pathways throughout the electrode is important to obtain enhanced rate handling performance with hybrid materials.

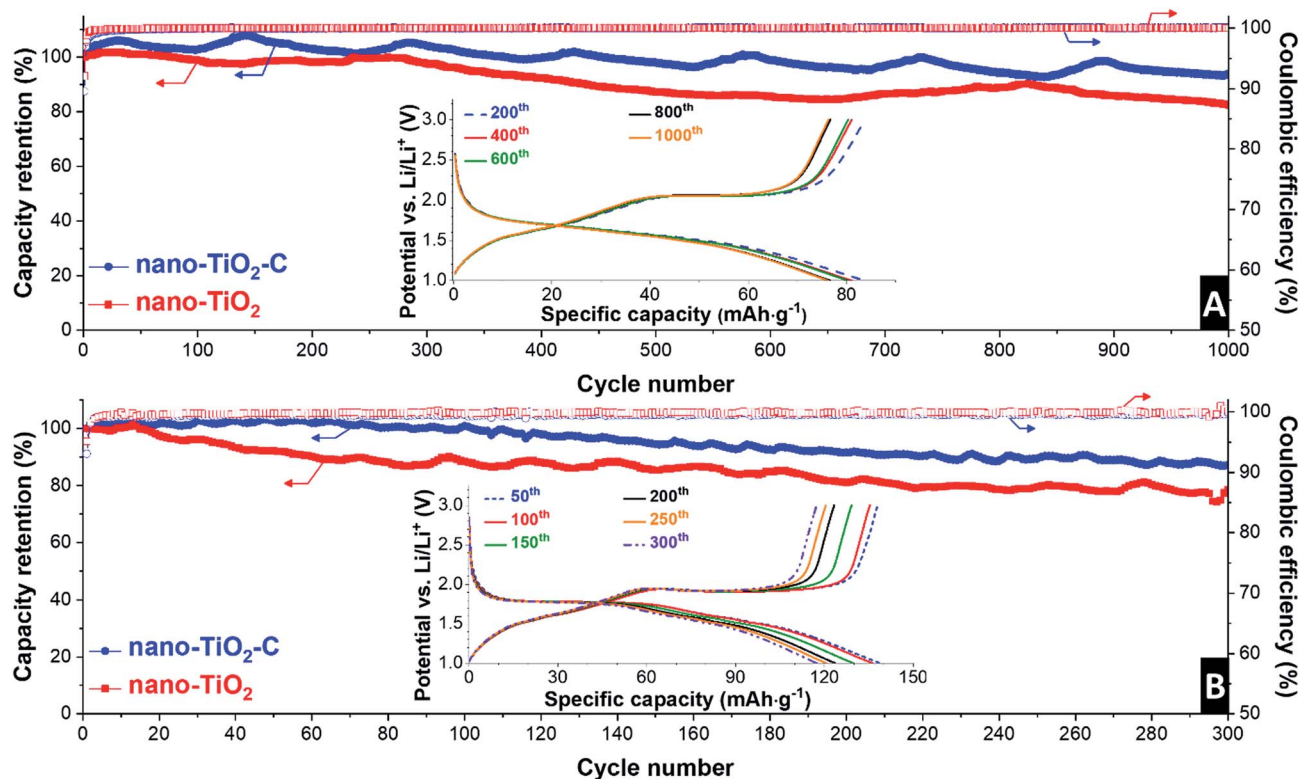


Fig. 6 Cycle stability of nano-TiO<sub>2</sub>-C and nano-TiO<sub>2</sub> at (A) 1 A g<sup>-1</sup> and at (B) 0.1 A g<sup>-1</sup>. Before the cycle stability test, pre-Cycling (10 cycles) was conducted at 0.05 A g<sup>-1</sup>. Inset: galvanostatic charge-discharge curves of nano-TiO<sub>2</sub>-C with increasing cycle number.

Table 1 Comparison of electrochemical performances of nano-TiO<sub>2</sub>-C and nano-TiO<sub>2</sub> with other results previously reported

Sample	Specific capacity	Cycle stability	Electrolyte	Reference
Nano-TiO <sub>2</sub> -C	~166 mA h g <sup>-1</sup> at 0.02 A g <sup>-1</sup>	~94% for 1000 cycles at 1 A g <sup>-1</sup>	1 M LiPF <sub>6</sub> in EC/DMC	This work
Nano-TiO <sub>2</sub>	~100 mA h g <sup>-1</sup> at 0.02 A g <sup>-1</sup>	~82% for 1000 cycles at 1 A g <sup>-1</sup>	1 M LiPF <sub>6</sub> in EC/DMC	This work
TiO <sub>2</sub> -graphene nanofibers	~145 mA h g <sup>-1</sup> at 0.15 A g <sup>-1</sup>	~84% for 300 cycles at 0.15 A g <sup>-1</sup>	1 M LiPF <sub>6</sub> in EC/DEC	Ref. 54
TiO <sub>2</sub> -N doped carbon	~175 mA h g <sup>-1</sup> at 0.168 A g <sup>-1</sup>	~89% for 170 cycles at 0.84 A g <sup>-1</sup>	1 M LiPF <sub>6</sub> in EC/DMC	Ref. 16
TiO <sub>2</sub> -graphene	~145 mA h g <sup>-1</sup> at 0.2 A g <sup>-1</sup>	~83% for 50 cycles at 0.2 A g <sup>-1</sup>	1 M LiPF <sub>6</sub> in EC/DMC	Ref. 56
TiO <sub>2</sub> mesocrystal	~175 mA h g <sup>-1</sup> at 0.034 A g <sup>-1</sup>	~74% for 60 cycles at 0.17 A g <sup>-1</sup>	1 M LiClO <sub>4</sub> in PC/DMC	Ref. 55
TiO <sub>2</sub> -functionalized graphene	~175 mA h g <sup>-1</sup> at 0.034 A g <sup>-1</sup>	~99% for 100 cycles at 0.168 A g <sup>-1</sup>	1 M LiPF <sub>6</sub> in EC/DMC	Ref. 24

### 3.5. Performance stability

Finally, we characterized long-term cycle stability of the nano-TiO<sub>2</sub>-C and the nano-TiO<sub>2</sub> materials. Fig. 6A and B show the cycling stability at a rate of 1 A g<sup>-1</sup> and 0.1 A g<sup>-1</sup>, respectively. Li<sup>+</sup> insertion/extraction reactions for nano-TiO<sub>2</sub>-C are more stable compared to nano-TiO<sub>2</sub>, and we see for the former capacity retention of ~94% and ~87% and coulombic efficiency of around 100% for 1000 and 300 cycles, respectively. In addition, the galvanostatic charge-discharge profiles of nano-TiO<sub>2</sub>-C during cycling are well maintained as confirmed in the insets of Fig. 6. The superior stability correlates with the confinement of nanosized TiO<sub>2</sub> in the mesopores volume of carbon onions, possibly benefitting the structural integrity of the electrode material during progressive cycling.<sup>17</sup> Additionally, we compare the electrochemical performance of the nano-TiO<sub>2</sub>-C and nano-TiO<sub>2</sub> electrodes with other anatase TiO<sub>2</sub> materials reported in previous works (Table 1).<sup>24,54-57</sup> As seen from the data, our nano-TiO<sub>2</sub>-C electrode delivers a promising specific capacity and long-term cycle stability.

## 4. Conclusions

The present work synthesized a hybrid material of anatase TiO<sub>2</sub> and carbon onions using tailored sol-gel chemistry. The nano-TiO<sub>2</sub>-C possessed excellent electrochemical behavior including a high specific capacity of ~166 mA h g<sup>-1</sup> at 0.02 A g<sup>-1</sup>, rapid charge storage kinetics of ~61 mA h g<sup>-1</sup> at 5 A g<sup>-1</sup>, and stable performance for 1000 cycles in the potential range from 1.0–3.0 V vs. Li/Li<sup>+</sup>. The performance was superior compared to non-hybridized nano-TiO<sub>2</sub>, synthesized with the same synthesis approach, commercial TiO<sub>2</sub>, and commercial graphite. Thereby, we demonstrated that the hybridization of anatase TiO<sub>2</sub> and carbon onions allows resulting electrodes to enhance the electrical conductivity *via* the presence of a conductive agent (carbon onions) and the fast lithiation/de-lithiation process enabled by nanosizing TiO<sub>2</sub>. Using detailed electrochemical analysis, we quantified the improvement of internal resistance and ion transport, which was linked to the presence of well distributed, electrically conductive carbon onions.

## Conflicts of interest

There are no conflicts to declare.

## Acknowledgements

This work was part of the Carbon Metal Oxide Nanohybrid project (CarMON) supported by the by the Leibniz Association (SAW-2017). The authors thank Prof. Eduard Arzt (INM) for his continuing support and thank Benjamin Krüner (INM) for his support.

## References

- 1 K. Kang, Y. S. Meng, J. Bréger, C. P. Grey and G. Ceder, *Science*, 2006, **311**, 977–980.
- 2 V. Etacheri, R. Marom, R. Elazari, G. Salitra and D. Aurbach, *Energy Environ. Sci.*, 2011, **4**, 3243–3262.
- 3 M. Pfanzelt, P. Kubiak, M. Fleischhammer and M. Wohlfahrt-Mehrens, *J. Power Sources*, 2011, **196**, 6815–6821.
- 4 T. Djenizian, I. Hanzu and P. Knauth, *J. Mater. Chem.*, 2011, **21**, 9925–9937.
- 5 K.-T. Kim, G. Ali, K. Y. Chung, C. S. Yoon, H. Yashiro, Y.-K. Sun, J. Lu, K. Amine and S.-T. Myung, *Nano Lett.*, 2014, **14**, 416–422.
- 6 P. Kubiak, M. Pfanzelt, J. Geserick, U. Hörmann, N. Hüsing, U. Kaiser and M. Wohlfahrt-Mehrens, *J. Power Sources*, 2009, **194**, 1099–1104.
- 7 J. Y. Shin, D. Samuelis and J. Maier, *Adv. Funct. Mater.*, 2011, **21**, 3464–3472.
- 8 E. Madej, F. La Mantia, W. Schuhmann and E. Ventosa, *Adv. Energy Mater.*, 2014, **4**, 1400829.
- 9 K. Hwang, H. Sohn and S. Yoon, *J. Power Sources*, 2018, **378**, 225–234.
- 10 G. Kim, C. Jo, W. Kim, J. Chun, S. Yoon, J. Lee and W. Choi, *Energy Environ. Sci.*, 2013, **6**, 2932–2938.
- 11 J. Lee, Y. S. Jung, S. C. Warren, M. Kamperman, S. M. Oh, F. J. DiSalvo and U. Wiesner, *Macromol. Chem. Phys.*, 2011, **212**, 383–390.
- 12 D. Deng, M. G. Kim, J. Y. Lee and J. Cho, *Energy Environ. Sci.*, 2009, **2**, 818–837.
- 13 M. Inaba, Y. Oba, F. Niina, Y. Murota, Y. Ogino, A. Tasaka and K. Hirota, *J. Power Sources*, 2009, **189**, 580–584.
- 14 J.-Y. Shin, J. H. Joo, D. Samuelis and J. Maier, *Chem. Mater.*, 2012, **24**, 543–551.
- 15 Y. G. Guo, Y. S. Hu, W. Sigle and J. Maier, *Adv. Mater.*, 2007, **19**, 2087–2091.

- 16 L. Tan, L. Pan, C. Cao, B. Wang and L. Li, *J. Power Sources*, 2014, **253**, 193–200.
- 17 S. Fleischmann, D. Leistenschneider, V. Lemkova, B. Krüner, M. Zeiger, L. Borchardt and V. Presser, *Chem. Mater.*, 2017, **29**, 8653–8662.
- 18 E. Lim, C. Jo, H. Kim, M.-H. Kim, Y. Mun, J. Chun, Y. Ye, J. Hwang, K.-S. Ha and K. C. Roh, *ACS Nano*, 2015, **9**, 7497–7505.
- 19 J. Wang, J. Polleux, J. Lim and B. Dunn, *J. Phys. Chem. C*, 2007, **111**, 14925–14931.
- 20 S. Fleischmann, M. Zeiger, N. Jäckel, B. Krüner, V. Lemkova, M. Widmaier and V. Presser, *J. Mater. Chem. A*, 2017, **5**, 13039–13051.
- 21 E. Lim, W.-G. Lim, C. Jo, J. Chun, M.-H. Kim, K. C. Roh and J. Lee, *J. Mater. Chem. A*, 2017, **5**, 20969–20977.
- 22 V. Augustyn, P. Simon and B. Dunn, *Energy Environ. Sci.*, 2014, **7**, 1597–1614.
- 23 I. Moriguchi, R. Hidaka, H. Yamada, T. Kudo, H. Murakami and N. Nakashima, *Adv. Mater.*, 2006, **18**, 69–73.
- 24 D. Wang, D. Choi, J. Li, Z. Yang, Z. Nie, R. Kou, D. Hu, C. Wang, L. V. Saraf, J. Zhang, I. A. Aksay and J. Liu, *ACS Nano*, 2009, **3**, 907–914.
- 25 S. Fleischmann, A. Tolosa and V. Presser, *Chem.–Eur. J.*, 2018, DOI: 10.1002/chem.201800772.
- 26 S. Fleischmann, A. Tolosa, M. Zeiger, B. Krüner, N. J. Peter, I. Grobelsek, A. Quade, A. Kruth and V. Presser, *J. Mater. Chem. A*, 2017, **5**, 2792–2801.
- 27 S. Fleischmann, N. Jäckel, M. Zeiger, B. Krüner, I. Grobelsek, P. Formanek, S. Choudhury, D. Weingarh and V. Presser, *Chem. Mater.*, 2016, **28**, 2802–2813.
- 28 M. Zeiger, N. Jäckel, V. N. Mochalin and V. Presser, *J. Mater. Chem. A*, 2016, **4**, 3172–3196.
- 29 M. Wissler, *J. Power Sources*, 2006, **156**, 142–150.
- 30 A. A. Deshmukh, S. D. Mhlanga and N. J. Coville, *Mater. Sci. Eng., R*, 2010, **70**, 1–28.
- 31 H. Liu, W. Li, D. Shen, D. Zhao and G. Wang, *J. Am. Chem. Soc.*, 2015, **137**, 13161–13166.
- 32 A. K. Rai, L. T. Anh, J. Gim, V. Mathew, J. Kang, B. J. Paul, J. Song and J. Kim, *Electrochim. Acta*, 2013, **90**, 112–118.
- 33 S.-J. Park, H. Kim, Y.-J. Kim and H. Lee, *Electrochim. Acta*, 2011, **56**, 5355–5362.
- 34 M. Zeiger, N. Jäckel, D. Weingarh and V. Presser, *Carbon*, 2015, **94**, 507–517.
- 35 C. J. Brinker and G. W. Scherer, *Sol-gel science: the physics and chemistry of sol-gel processing*, Academic press, 2013.
- 36 G. J. d. A. Soler-Illia, C. Sanchez, B. Lebeau and J. Patarin, *Chem. Rev.*, 2002, **102**, 4093–4138.
- 37 W. Zhang, Y. He, M. Zhang, Z. Yin and Q. Chen, *J. Phys. D: Appl. Phys.*, 2000, **33**, 912.
- 38 J. W. Kim, V. Augustyn and B. Dunn, *Adv. Energy Mater.*, 2012, **2**, 141–148.
- 39 Y.-B. He, M. Liu, Z.-D. Huang, B. Zhang, Y. Yu, B. Li, F. Kang and J.-K. Kim, *J. Power Sources*, 2013, **239**, 269–276.
- 40 M. S. Kim, E. Lim, S. Kim, C. Jo, J. Chun and J. Lee, *Adv. Funct. Mater.*, 2017, **27**, 1603921.
- 41 P. Zheng, T. Liu, Y. Su, L. Zhang and S. Guo, *Sci. Rep.*, 2016, **6**, 36580.
- 42 M. Wagemaker, W. J. Borghols and F. M. Mulder, *J. Am. Chem. Soc.*, 2007, **129**, 4323–4327.
- 43 M. Wagemaker, A. Kentgens and F. Mulder, *Nature*, 2002, **418**, 397.
- 44 J. Brumbarov, J. Vivek, S. Leonardi, C. Valero-Vidal, E. Portenkirchner and J. Kunze-Liebhäuser, *J. Mater. Chem. A*, 2015, **3**, 16469–16477.
- 45 W. J. Borghols, D. Lutzenkirchen-Hecht, U. Haake, E. R. van Eck, F. M. Mulder and M. Wagemaker, *Phys. Chem. Chem. Phys.*, 2009, **11**, 5742–5748.
- 46 V. Augustyn, J. Come, M. A. Lowe, J. W. Kim, P.-L. Taberna, S. H. Tolbert, H. D. Abruña, P. Simon and B. Dunn, *Nat. Mater.*, 2013, **12**, 518.
- 47 S. Ardizzone, G. Fregonara and S. Trasatti, *Electrochim. Acta*, 1990, **35**, 263–267.
- 48 T. C. Liu, W. G. Pell, B. E. Conway and S. L. Roberson, *J. Electrochem. Soc.*, 1998, **145**, 1882–1888.
- 49 E. Lim, C. Jo, M. S. Kim, M. H. Kim, J. Chun, H. Kim, J. Park, K. C. Roh, K. Kang and S. Yoon, *Adv. Funct. Mater.*, 2016, **26**, 3711–3719.
- 50 M. Opitz, J. Yue, J. Wallauer, B. Smarsly and B. Roling, *Electrochim. Acta*, 2015, **168**, 125–132.
- 51 X. Hao and B. M. Bartlett, *Adv. Energy Mater.*, 2013, **3**, 753–761.
- 52 H. Park, H. B. Wu, T. Song and U. Paik, *Adv. Energy Mater.*, 2015, **5**, 1401945.
- 53 Y. Zhang, F. Du, X. Yan, Y. Jin, K. Zhu, X. Wang, H. Li, G. Chen, C. Wang and Y. Wei, *ACS Appl. Mater. Interfaces*, 2014, **6**, 4458–4465.
- 54 X. Zhang, P. Suresh Kumar, V. Aravindan, H. H. Liu, J. Sundaramurthy, S. G. Mhaisalkar, H. M. Duong, S. Ramakrishna and S. Madhavi, *J. Phys. Chem. C*, 2012, **116**, 14780–14788.
- 55 J. Ye, W. Liu, J. Cai, S. Chen, X. Zhao, H. Zhou and L. Qi, *J. Am. Chem. Soc.*, 2011, **133**, 933–940.
- 56 H. Kim, M. Y. Cho, M. H. Kim, K. Y. Park, H. Gwon, Y. Lee, K. C. Roh and K. Kang, *Adv. Energy Mater.*, 2013, **3**, 1500–1506.
- 57 L. Tan, C. Cao, H. Yang, B. Wang and L. Li, *Mater. Lett.*, 2013, **109**, 195–198.

## **Supporting Information**

### **Fast and stable lithium-ion storage kinetics of anatase titanium dioxide/carbon onion hybrid electrodes**

*Eunho Lim,<sup>1</sup> Hwirim Shim,<sup>1,2</sup> Simon Flesichmann,<sup>1,2</sup> Volker Presser<sup>1,2,\*</sup>*

<sup>1</sup> INM - Leibniz Institute for New Materials, 66123 Saarbrücken, Germany

<sup>2</sup> Department of Materials Science and Engineering, Saarland University, 66123 Saarbrücken, Germany

\* Corresponding author's eMail: [volker.presser@leibniz-inm.de](mailto:volker.presser@leibniz-inm.de)

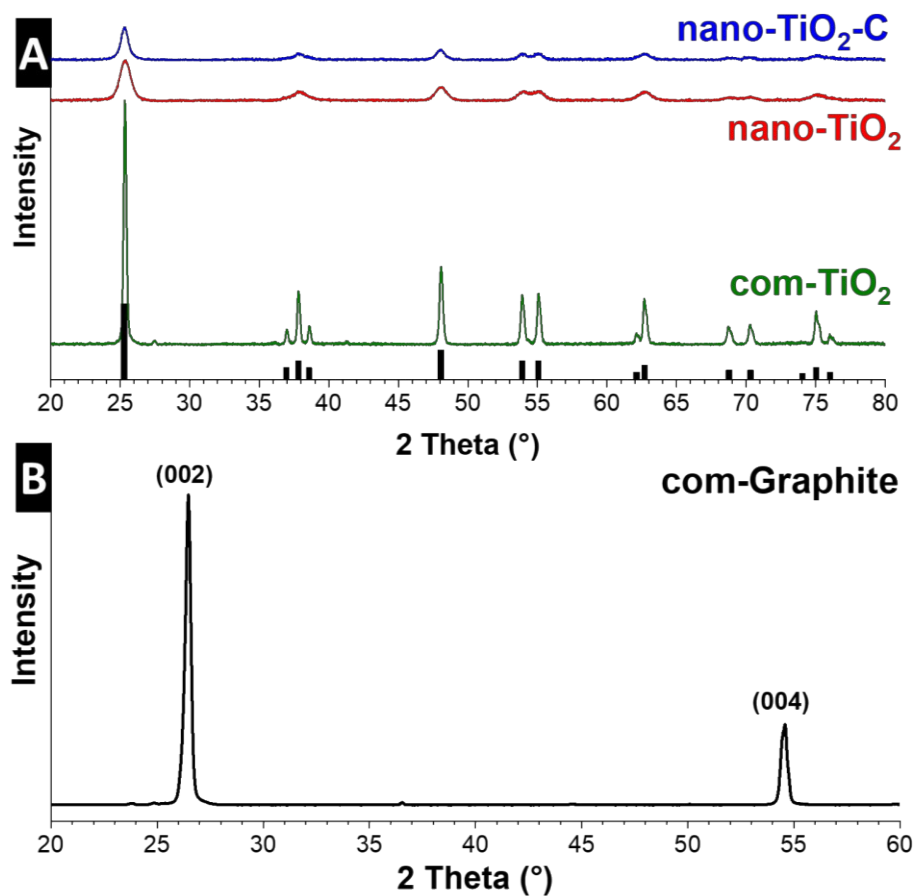


**Fig. S1:** XRD patterns of (A) nano-TiO<sub>2</sub>-C, nano-TiO<sub>2</sub>, and com-TiO<sub>2</sub> and (B) com-graphite.

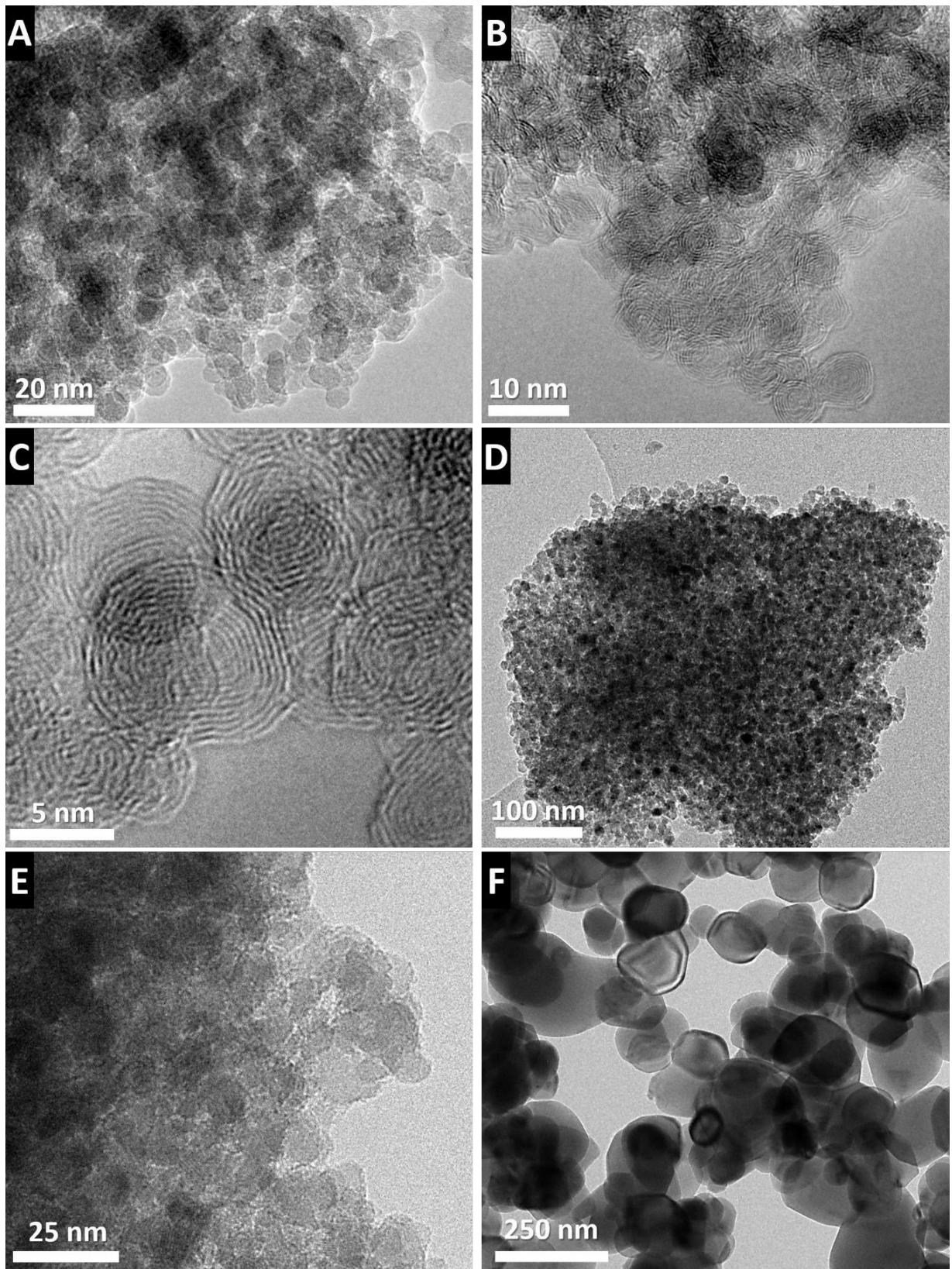


**Fig. S2:** TEM images of (A-C) carbon onions, (D-E) nano-TiO<sub>2</sub>, and (F) com-TiO<sub>2</sub>.

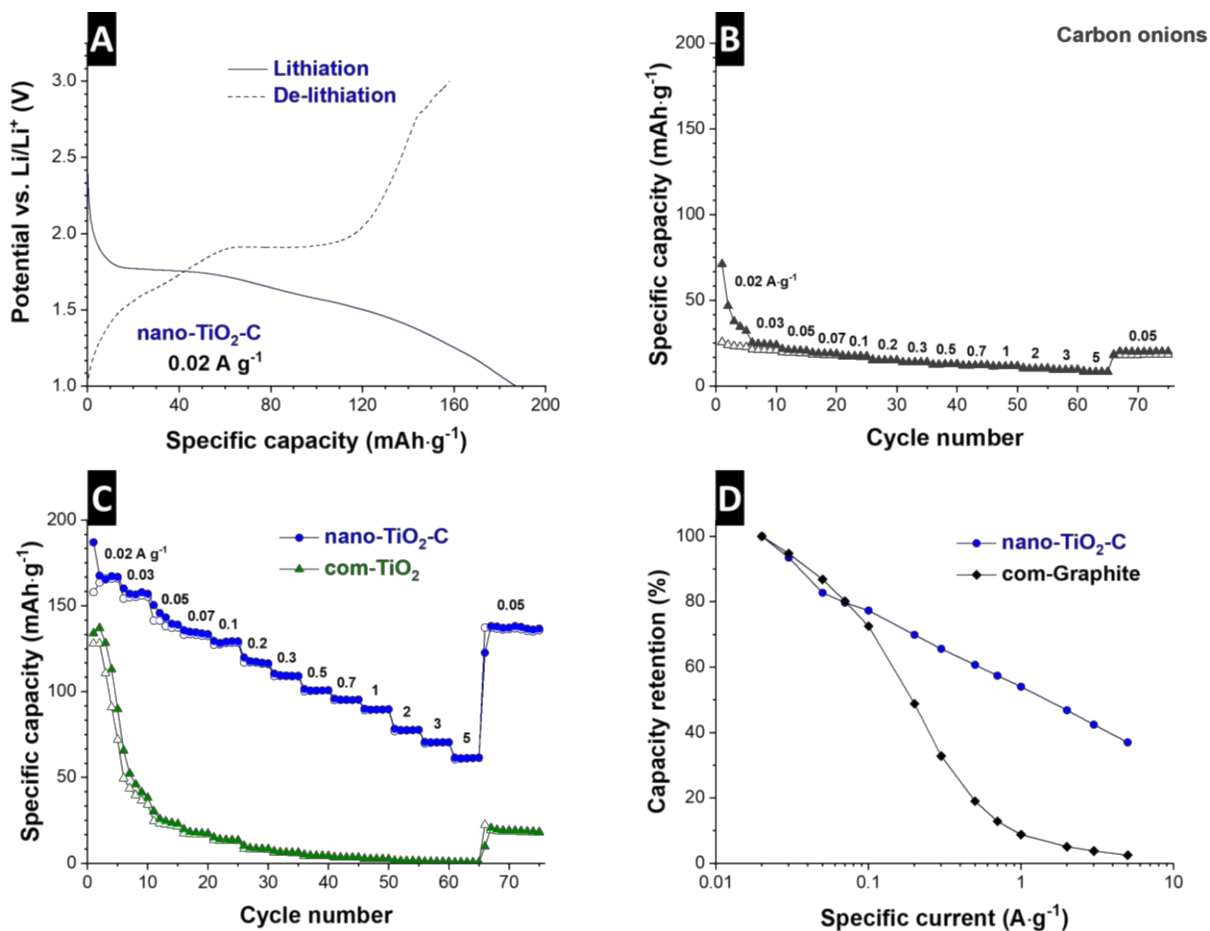


**Fig. S3:** (A) First-cycle galvanostatic charge-discharge curve of nano-TiO<sub>2</sub>-C at 0.02 A·g<sup>-1</sup>. (B) Rate performance of carbon onions at various currents of 0.02-5 A·g<sup>-1</sup> in the potential range of 1.0-3.0 V vs. Li/Li<sup>+</sup>. (C) Comparison of rate performance of nano-TiO<sub>2</sub>-C and com-TiO<sub>2</sub> at currents of 0.02-5 A·g<sup>-1</sup>. (D) Capacity retention of nano-TiO<sub>2</sub>-C and com-graphite at currents of 0.02-5 A·g<sup>-1</sup>.

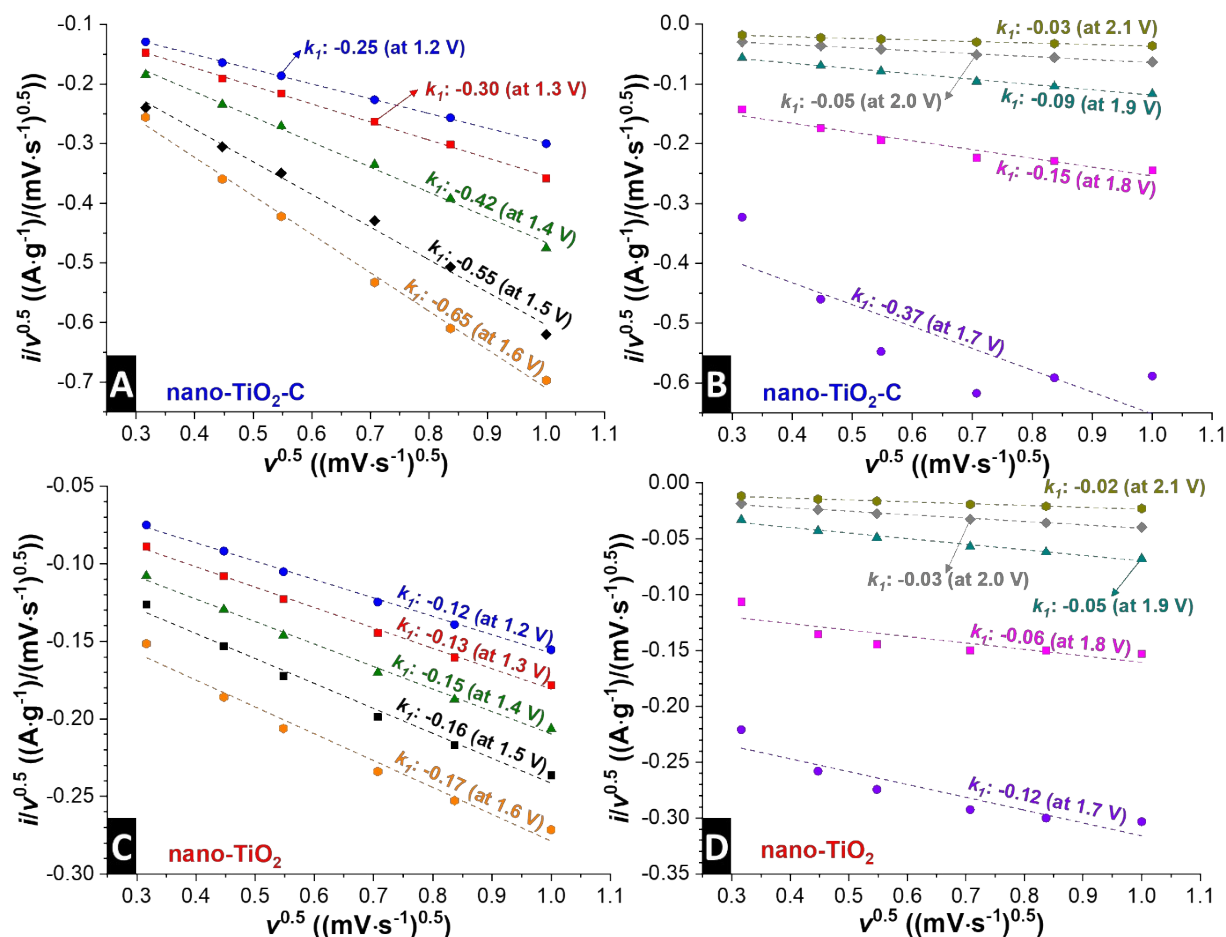


**Fig. S4:**  $v^{0.5}$  vs.  $i/v^{0.5}$  plots of cathodic current (lithiation) on nano-TiO<sub>2</sub>-C in the potential range of (A) 1.2-1.6 V and (B) 1.7-2.1 V vs. Li/Li<sup>+</sup>.  $v^{0.5}$  vs.  $i/v^{0.5}$  plots of cathodic current (lithiation) on nano-TiO<sub>2</sub> in the potential range of (C) 1.2-1.6 V vs. Li/Li<sup>+</sup> and (D) 1.7-2.1 V vs. Li/Li<sup>+</sup>.

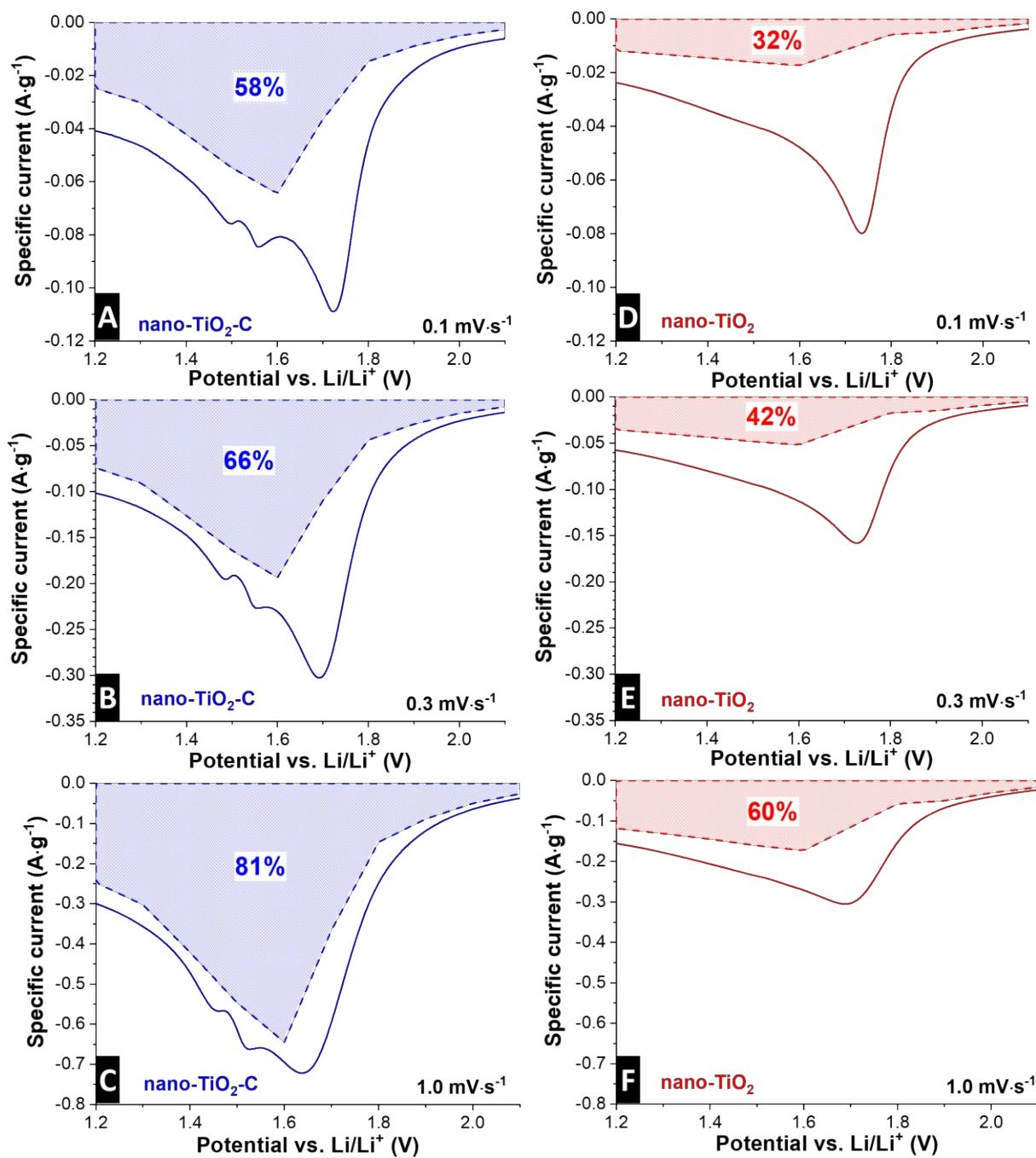


**Fig. S5:** CV data of (A-C) nano-TiO<sub>2</sub>-C and (D-F) nano-TiO<sub>2</sub> with separation between the total current (solid line) and capacitor-like current (shaded region) in the voltage range from 1.2-2.1 V vs. Li/Li<sup>+</sup> at three different scan-rates (0.1-1.0 mV·s<sup>-1</sup>) for lithiation.

# Hybrid anodes of lithium titanium oxide and carbon onions for lithium-ion and sodium-ion energy storage

**Hwirim Shim**,<sup>1,2</sup> **Stefanie Arnold**,<sup>1,2</sup> **Öznil Budak**,<sup>1,2</sup> **Maïke Ulbricht**,<sup>1,2</sup> **Volker Presser**<sup>1,2</sup>

<sup>1</sup> INM - Leibniz Institute for New Materials, 66123 Saarbrücken, Germany

<sup>2</sup> Department of Materials Science and Engineering, Saarland University, 66123 Saarbrücken, Germany

Citation: 10.1002/ente.202000679

## Own contributions:

Planning, synthesis, X-ray diffraction measurements, Raman measurements, thermogravimetric analysis, scanning electron microscopy, transmission electron microscopy, electrochemical measurements, writing.

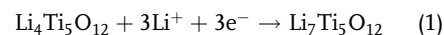


# Hybrid Anodes of Lithium Titanium Oxide and Carbon Onions for Lithium-Ion and Sodium-Ion Energy Storage

Hwirim Shim, Stefanie Arnold, Öznil Budak, Maike Ulbricht, Pattarachai Srimuk, and Volker Presser\*

This study demonstrates the hybridization of  $\text{Li}_4\text{Ti}_5\text{O}_{12}$  (LTO) with different types of carbon onions synthesized from nanodiamonds. The carbon onions mixed with a  $\text{Li}_4\text{Ti}_5\text{O}_x$  precursor for sol-gel synthesis. These hybrid materials are tested as anodes for both lithium-ion battery (LIB) and sodium-ion battery (SIB). Electrochemical characterization for LIB application is carried out using 1 M  $\text{LiPF}_6$  in a 1:1 (by volume) ethylene carbonate and dimethyl carbonate as the electrolyte. For lithium-ion intercalation, LTO hybridized with carbon onions from the inert-gas route achieves an excellent electrochemical performance of  $188 \text{ mAh g}^{-1}$  at  $10 \text{ mA g}^{-1}$ , which maintains  $100 \text{ mAh g}^{-1}$  at  $1 \text{ A g}^{-1}$  and has a cycling stability of 96% of initial capacity after 400 cycles, thereby outperforming both neat LTO and LTO with onions obtained via vacuum treatment. The performance of the best-performing hybrid material (LTO with carbon onions from argon annealing) in an SIB is tested, using 1 M  $\text{NaClO}_4$  in ethylene/dimethyl/fluoroethylene carbonate (19:19:2 by mass) as the electrolyte. A maximum capacity of  $102 \text{ mAh g}^{-1}$  for the SIB system is obtained, with a capacity retention of 96% after 500 cycles.

and natural abundance.<sup>[2]</sup> However, graphite electrodes experience major safety issues, because their operation potential is near to the lithium electroplating potential of 0.1 V versus  $\text{Li}/\text{Li}^+$ , which leads to a high risk of penetrable dendrite formation.<sup>[3,4]</sup> An alternative to graphite anodes is lithium titanium oxide ( $\text{Li}_4\text{Ti}_5\text{O}_{12}$ , LTO), for which good structural stability during lithiation/delithiation and safety due to its high operation potential have been reported.<sup>[5]</sup> The theoretical capacity of LTO is  $175 \text{ mAh g}^{-1}$ , utilizing three  $\text{Li}^+$  ions via Equation (1)<sup>[6]</sup>



The operation potential of the LTO range of around 1.55 V versus  $\text{Li}/\text{Li}^+$  for  $\text{Li}^+$  intercalation and deintercalation prevents solid electrolyte interface (SEI) formation.<sup>[7,8]</sup> In addition, LTO exhibits minor to zero volume change during operation,

yielding good cycling performance, and high coulombic efficiency.<sup>[7,9]</sup> However, LTO is known for its low  $\text{Li}^+$  ion diffusion ( $10^{-13}$ – $10^{-9} \text{ cm}^2 \text{ s}^{-1}$ )<sup>[10]</sup> and low electrical conductivity of  $10^{-8}$ – $10^{-13} \text{ S cm}^{-1}$ , which limits the achievable rate capability.<sup>[11–14]</sup> The performance of LTO can be enhanced by improving the intrinsic conductivity, which can be done by the introduction of oxygen deficiencies; however, this approach requires an extra step of thermal treatment of the active material.<sup>[15]</sup> Therefore, the mechanical or chemical implementation of carbon as a conductive additive is more preferred.<sup>[16]</sup> Much work has addressed the performance by forming nanocomposite or hybridizing conductive carbon materials to LTO. The former, nanocomposites, is the most common way of producing LTO-based electrodes, usually by the use of carbon black, carbon nanotubes, or graphene.<sup>[17–20]</sup> Hybrid materials can be obtained by methods, such as surface modification of LTO by carbon coating using carbon sources, such as sucrose, glucose, solvents, acids, or gases, which have resulted in enhanced electrochemical performance.<sup>[21–25]</sup> These works document the great importance of achieving a homogenous distribution of conductive and active material on a sub-100 nm length scale.<sup>[26]</sup> Therefore, the use of synthesis methods capable of yielding nanoscale hybridization is important, especially when using nanoscale carbon additive particles.

In addition to the ability to reversibly intercalate lithium, LTO has also been demonstrated to be suitable anode in sodium-ion

## 1. Introduction

The increased demand for energy storage applications in daily life necessitates the development of faster and more long-lasting energy storage devices. Lithium-ion batteries (LIBs) have been widely explored and implemented for mobile or stationary devices owing to their lightweight and high energy and power density.<sup>[1]</sup> Conventional LIBs use graphite as an anode due to its high theoretical capacity ( $372 \text{ mAh g}^{-1}$ ), good cycling stability,

H. Shim, S. Arnold, Ö. Budak, M. Ulbricht, Dr. P. Srimuk, Prof. V. Presser  
Program Division Energy Materials  
INM—Leibniz Institute for New Materials  
Saarbrücken 66123, Germany  
E-mail: volker.presser@leibniz-inm.de

H. Shim, S. Arnold, Ö. Budak, M. Ulbricht, Prof. V. Presser  
Department of Materials Science and Engineering  
Saarland University  
Saarbrücken 66123, Germany

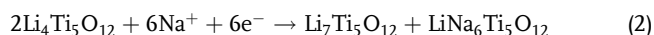
The ORCID identification number(s) for the author(s) of this article can be found under <https://doi.org/10.1002/ente.202000679>.

© 2020 The Authors. Published by Wiley-VCH GmbH. This is an open access article under the terms of the Creative Commons Attribution License, which permits use, distribution and reproduction in any medium, provided the original work is properly cited.

DOI: 10.1002/ente.202000679

batteries (SIBs).<sup>[27–34]</sup> Interest in SIBs is based on the high natural abundance of sodium and associated reduced costs.<sup>[33]</sup> The insertion–extraction potential of sodium into LTO is reported to be around 0.9 V versus Na/Na<sup>+</sup> without sodium metal plating on the electrode surface.<sup>[27,29,32]</sup>

The low intrinsic conductivity issue remains and possibly relates to the high overpotential or poor rate capability.<sup>[33,35]</sup> The theoretical Na<sup>+</sup> ion uptake capacity of LTO is also 175 mAh g<sup>−1</sup>, assuming the insertion of three Na<sup>+</sup> ions, according to Equation (2)<sup>[27]</sup>



In this study, we explore hybrid materials composed of sol–gel-derived LTO and nanoscale carbon onions (OLC) for use as LIB and SIB anode material. To obtain carbon onions, we used thermal annealing of nanodiamond precursors in an inert atmosphere or under vacuum to yield carbon onions with a primary particle size of 5–10 nm.<sup>[36,37]</sup> We chose carbon onions, because the absence of inner porosity and the mesopore-dominated interparticle pore space allows a highly favorable nanoscale implementation of metal oxides.<sup>[38,39]</sup> The resulting hybrid materials were electrochemically surveyed for charge storage capacity, rate capability, and cycling stability for the reversible intercalation of lithium and sodium.

## 2. Experimental Section

### 2.1. Material Preparation

Two types of carbon onions were synthesized by thermal annealing of nanodiamond powder (ND; NaBond Technologies) at 1700 °C for 1 h under Ar atmosphere, noted OLCa, or at 1300 °C for 4 h under vacuum, labeled OLCv, using high-temperature graphite furnace (Carbolite).

For the synthesis of the hybrid LTO, we used sol–gel synthesis. Lithium ethoxide dissolved in tetrahydrofuran (LiOEt, THF; Sigma Aldrich) and titanium isopropoxide (TTIP; Sigma Aldrich) were used as lithium and titanium sources, respectively. LiOEt (4 mL) was added to 5 mL of THF with vigorous stirring; then, 1.48 mL of TTIP was added dropwise to the stirring solution. Subsequently, 0.45 g of oxalic acid was added, and then, the precursor solution was stirred for 2 h at 50 °C. Appropriate amounts of OLCa or OLCv powders were added by wet impregnation into prepared sol. The carbon content was 15 mass% of the final hybrid material. The impregnated mixtures were dried at 50 °C under vacuum for overnight, followed by further drying at 80 °C for 12 h.

In addition to LTO-carbon hybrids, we also synthesized neat LTO. The latter was prepared by following the same synthesis protocol but without the addition of carbon onions. The well-dried materials were then annealed at 700 °C for 2 h (heating rate 1 °C min<sup>−1</sup>) under Ar atmosphere.

The resulting materials are named “LTO” = neat LTO, “LTO-OLCa” = LTO with the addition of argon-annealed carbon onions, and “LTO-OLCv” = LTO with the addition of vacuum-treated carbon onions.

### 2.2. Material Characterization

#### 2.2.1. Structural Characterization

X-ray diffraction (XRD) was carried out in a D8 Discover Diffractometer (Bruker AXS) with a copper X-ray source (Cu-K<sub>α</sub> radiation, 40 kV, 40 mA). We used a Göbel mirror with a 1 mm point focus and a 2D X-ray detector (VANTEC-500) for the measurements. The samples were placed on a sapphire single crystal and measured with the detector being placed at angles from 20θ to 80θ with a step width of 20θ and a measuring time of 1000 s per step.

The carbon content of the hybrid materials was determined with thermogravimetric analysis (TGA), performed with a TG-209-1 Libra (Netzsch). For each TGA measurement, the samples were heated to 1000 °C under synthetic air condition (80 vol% N<sub>2</sub>, 20 vol% O<sub>2</sub>) with a flow rate of 20 sccm at a heating rate of 5 °C min<sup>−1</sup>.

Raman spectroscopy was performed with a Renishaw inVia Raman Microscope using an neodymium-doped yttrium aluminum garnet laser with an excitation wavelength of 532 nm and a power of about 0.5 mW at the focal point. The acquisition time for each spectrum was 30 s with ten accumulations to enhance the signal-to-noise ratio. Peak fitting of the measured spectra was accomplished, assuming two Voigt peaks for the D- and G-modes individually.

Transmission electron microscopy (TEM) was performed using a JEOL 2100F system at an operating voltage at 200 kV. Samples for TEM imaging were prepared by dispersion and tip-sonication of the hybrid materials in ethanol and subsequent drop-casting of the dispersion on a copper grid with a lacey carbon film.

Scanning electron microscopy (SEM) of the prepared electrodes was conducted with a JEOL JSM-7500F system at an acceleration voltage of 3 kV and an emission current of 10 μA. The energy-dispersive X-ray spectroscopy (EDX) was carried out using an X-Max-150 detector (Oxford Instruments) attached to the SEM system. The spectra were obtained at an acceleration voltage of 15 kV and an emission current of 10 μA. Before the spectral acquisition of each sample, calibration was conducted with a silicon wafer.

The porosity of the powder materials was analyzed by the use of nitrogen gas sorption at −196 °C with an Autosorb iQ system from Quantachrome (now: Anton-Paar). The powder samples were outgassed at 300 °C for 20 h before the measurement, and the recorded gas sorption isotherms along with the calculated Brunauer–Emmett–Teller (BET) surface area values are provided in Figure S1, Supporting Information.

#### 2.2.2. Electrochemical Characterization

For the preparation of the anode, the synthesized LTO and the hybrid materials were mixed with polyvinylidene fluoride (PVDF; Alfa Aesar) binder with a 9:1 mass ratio without any further conductivity additive, followed by the addition of *N*-methyl-2-pyrrolidone (NMP; Sigma Aldrich) solvent. The mixed slurry was coated on a copper foil (25 μm, MTI) using a 200 μm doctor blade. The coated electrode was dried overnight in a fume hood at room temperature, then transferred to a vacuum oven, and dried

at 110 °C overnight. The dried coating was pressed in a hot roll press machine (MTI), and then punched to 10 mm discs using press punch (EL-CELL) for electrochemical benchmarking. The mass loadings of each electrode were  $5.5 \pm 0.4 \text{ mg cm}^{-2}$  for neat LTO  $3.7 \pm 0.2 \text{ mg cm}^{-2}$  for LTO-OLCa, and  $3.7 \pm 0.4 \text{ mg cm}^{-2}$  for LTO-OLCv. The dry thickness of the prepared electrode was 36  $\mu\text{m}$  for neat LTO and 39  $\mu\text{m}$  for the two hybrid samples. The electrode density was  $1.48 \text{ g cm}^{-3}$  for neat LTO,  $0.94 \text{ g cm}^{-3}$  for LTO-OLCa, and  $0.93 \text{ g cm}^{-3}$  for LTO-OLCv.

For half-cell measurements, an LTO containing working electrode and lithium or a sodium disc counter and reference electrodes were assembled into CR2032 coin cells. We used a Whatman GF/F glass fiber separator and 1 M LiPF<sub>6</sub> salt in a mixture of ethylene carbonate and dimethyl carbonate (EC:DMC; 1:1 by volume, Sigma Aldrich) or 1 M NaClO<sub>4</sub> in a mixture of EC:DMC with 5 mass% fluoroethylene carbonate (FEC) as the electrolyte.<sup>[40]</sup>

Cyclic voltammetry was carried out with a Biologic VMP300 potentiostat/galvanostat and performed in a potential window from 1.0 to 2.8 V versus Li/Li<sup>+</sup> and 0.3 to 2.5 V versus Na/Na<sup>+</sup> at the scan rates of 0.1–10 mV s<sup>-1</sup>. Electrochemical impedance spectroscopy (EIS) was measured at an applied AC voltage amplitude of 10 mV from the frequency range of 10<sup>6</sup>–10<sup>-2</sup> Hz. For quantifying the rate handling capability, galvanostatic charge/discharge with potential limitation (GCPL) measurement was carried out at an Arbin Battery Cycler in a potential range of 1.0–2.8 V versus Li/Li<sup>+</sup> and 0.3–2.5 V versus Na/Na<sup>+</sup> using specific currents ranging from 0.01 to 10 A g<sup>-1</sup> and 0.025 to 5 A g<sup>-1</sup>, respectively. The cycling stability was quantified using GCPL at a specific current of 0.1 A g<sup>-1</sup> for both LIB and SIB testing. All the measurements were carried out in climate chambers (Binder) set to 25 ± 1 °C.

The specific capacity  $C_{\text{sp}}$  of the hybrid material was calculated by integration of the applied lithium or sodium extraction current  $I$  over the extraction time  $t$  accounting for the deintercalation

step from 1.0 to 2.8 V versus Li/Li<sup>+</sup> and 0.3 to 2.5 V versus Na/Na<sup>+</sup>, as in Equation (3)

$$C_{\text{sp}} = \frac{\int_{t_0}^t I dt}{m} \quad (3)$$

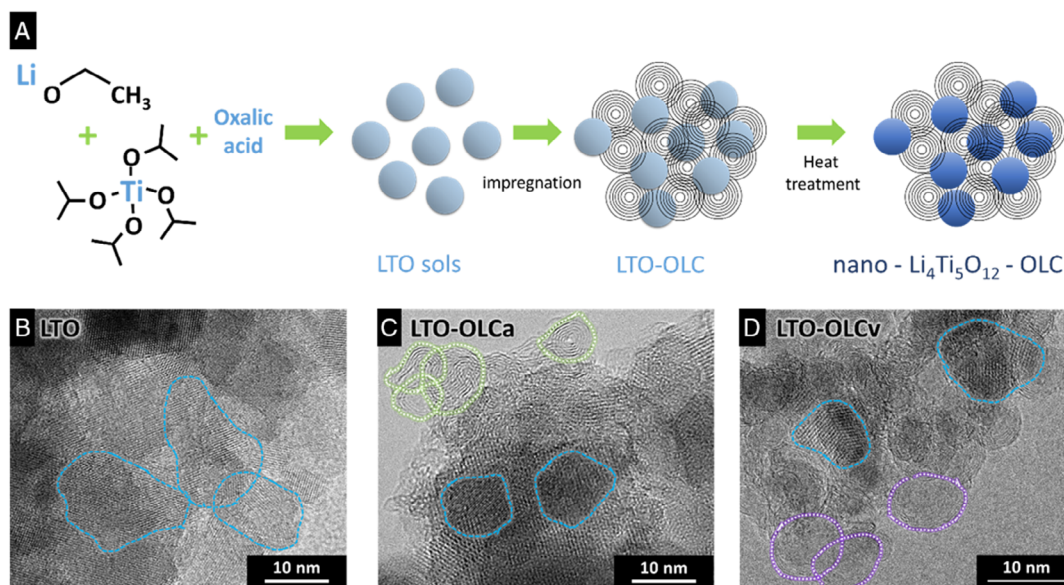
The specific capacity was normalized to the total mass of the hybrid material  $m$  in the electrode without the polymer binder.

## 3. Results and Discussion

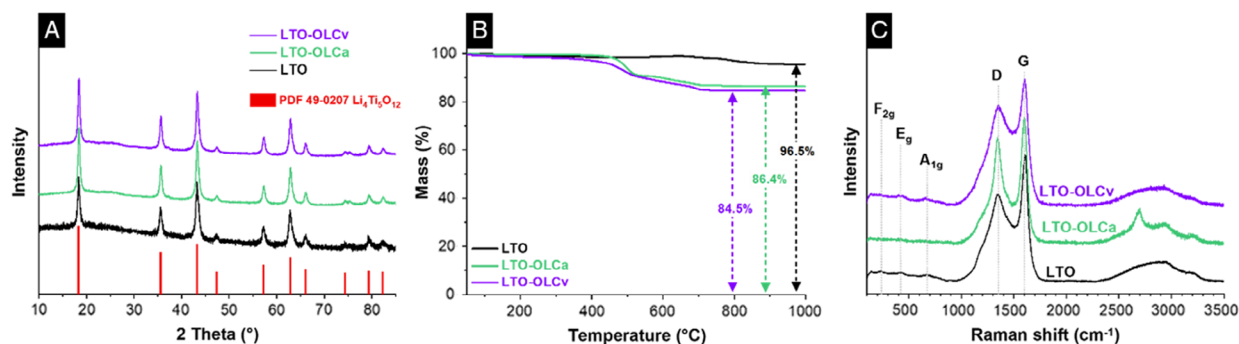
### 3.1. Hybrid Material Synthesis

Figure 1A presents the schematic illustration of the LTO-OLC hybrid. The preparation of LTO sols and wet impregnation of two different types of carbon onions synthesized under different conditions lead to a synthesis of the hybrid material LTO-OLCa and LTO-OLCv by thermal annealing. As shown in TEM images (Figure 1B–D), LTO, LTO-OLCa, and LTO-OLCv show nanoscale crystalline domains related to lithium-titanium oxide. For better comparison, TEM images of carbon onions (OLCa and OLCv) are presented in Figure S2A,B, Supporting Information.

XRD was used to determine and study the crystal structure of the prepared pristine and hybrid materials. The data of all X-ray diffractograms (Figure 2A) match very well to cubic spinel lithium titanium oxide (LTO, PDF 49-0207,  $a = 8.359 \text{ \AA}$ ). The measurement data are dominated by signals from the crystalline LTO phase, whereas the contribution of the incompletely graphitic carbon is mostly lost in the background; more information on the carbon structure can be inferred from the Raman spectra (later paragraph). We used Rietveld refinement to calculate the average coherence length (roughly corresponding with the domain size) of LTO (Table S1, Supporting Information). All sample materials, that is, LTO and the two types of LTO-carbon



**Figure 1.** A) Schematic illustration of preparation for hybrid nano-LTO-OLC. The transmission micrograms of B) LTO, C) LTO-OLCa, and D) LTO-OLCv hybrid material. LTO domains are marked by blue dashed lines and carbon onions with C) green and D) purple dotted lines.



**Figure 2.** A) XRD patterns of LTO, LTO-OLCa, and LTO-OLCv. B) TGA of samples under synthetic air atmosphere for the characterization of the amount of carbon. C) Background-corrected Raman spectra of LTO, LTO-OLCa, and LTO-OLCv. All data were normalized to the intensity of the carbon G-mode as 100% and the intensity at  $3500\text{ cm}^{-1}$  as 0%.

hybrids, have a highly comparable domain size of about  $30 \pm 2\text{ nm}$  and a unit cell constant of  $a = 8.366 \pm 0.002\text{ \AA}$ .

The carbon content of the synthesized LTO hybrid materials was determined by TGA (recorded in synthetic air) and elemental (CHNS/O) analysis. As displayed in Figure 2B, LTO without carbon onions showed 3.5 mass% carbon content, which is the carbon formed during the thermal annealing of the as-prepared oxide sols from the residual chains from metal alkoxide precursors. LTO-OLCa and LTO-OLCv showed 14 and 15.5 mass% carbon content, respectively. These data agree with the carbon amount introduced during the synthesis step, and the elemental analysis results in Table S2, Supporting Information.

We characterized the carbon structure of the samples with Raman spectroscopy. The resulting spectra are presented in Figure 2C for LTO and the hybrid materials, and in Figure S2D, Supporting Information, for carbon onions. For comparison, the peak position and full-width at half-maximum (FWHM) of each D- and G-modes and the  $I_D/I_G$  ratio by use of four Voigt peak fitting are provided in Table S3, Supporting Information. The individual deconvolution of the Voigt peak fitting is presented in Figure S3, Supporting Information. The Raman spectra of all carbon onions and hybrid materials show the characteristic D-mode and G-mode of incompletely graphitized carbon (nanocrystalline carbon) and the corresponding overtones.<sup>[41]</sup> Carbon onions synthesized under argon atmosphere and vacuum show very different Raman spectra in agreement with previous studies.<sup>[36,37]</sup> Specifically, we see narrower D- and G-modes in the case of OLCa (D-mode:  $71\text{ cm}^{-1}$ ; G-mode:  $70\text{ cm}^{-1}$ ) compared with OLCv (D-mode:  $176\text{ cm}^{-1}$ ; G-mode:  $90\text{ cm}^{-1}$ ); this aligns with the much lower synthesis temperature during vacuum annealing ( $1300\text{ }^\circ\text{C}$ ) compared with the thermal treatment in argon ( $1700\text{ }^\circ\text{C}$ ). Higher synthesis temperatures are known to result in a higher order of structural ordering of the carbon phase.<sup>[42]</sup>

In Figure 2C, at lower Raman shift, characteristic vibration bands at  $243$ ,  $431$ , and  $670\text{ cm}^{-1}$  for LTO are observed for LTO, LTO-OLCa, and LTO-OLCv.<sup>[43–45]</sup> At first, it may be surprising to see carbon-related Raman signals for the LTO sample where no carbon onions were introduced during the synthesis. Still, we see clearly, for LTO, a D-band at  $1345\text{ cm}^{-1}$  and a G-band at  $1607\text{ cm}^{-1}$ . In addition, there is also the transpolyacetylene (TPA) peak in the range of  $1150\text{--}1200\text{ cm}^{-1}$ , which indicates the highly disordered nature of carbon.<sup>[41]</sup> This carbon

species is related to the carbonization of the metal alkoxide residues used for the synthesis. A small amount of carbon also aligns with the thermogram (Figure 2B), as indicated by the mass loss of about 3.5 mass% when heating above  $600\text{ }^\circ\text{C}$ . The presence of incompletely graphitic carbon in LTO-OLCa and LTO-OLCv is associated mostly with the carbon onions type OLCa and OLCv, respectively. We can understand the Raman spectra of LTO-OLCv and LTO-OLCa as a superimposition of the carbon seen already in the LTO sample in addition to carbon from the carbon onion structure (Figure S3D,E, Supporting Information). LTO-OLCa, compared with the other materials, shows a sharper D-mode ( $92\text{ cm}^{-1}$ ) and a sharper peak of the carbon-related combination and overtone modes between  $2300$  and  $3400\text{ cm}^{-1}$ . This suggests that the carbon network in LTO-OLCa, in general, possesses a higher degree of graphitic ordering compared with that of the other materials.

### 3.2. Lithium-Ion Intercalation Behavior and Performance

The synthesized LTO and hybrid materials were prepared to electrodes and tested with a CR2032 coin cell for electrochemical benchmarking of LIB systems. The SEM images of the prepared electrodes are found in Figure S4, Supporting Information. For an overview of the electrochemical performance, the prepared cells were first tested for cyclic voltammetry (CV) in the potential range of  $1.0\text{--}2.8\text{ V}$  versus  $\text{Li}/\text{Li}^+$  at various scan rates of  $0.1\text{--}10\text{ mV s}^{-1}$ . The resulting cyclic voltammograms of LTO-OLCa are shown in Figure 3A, and voltammograms of LTO and LTO-OLCv are shown in Figure S5A,B, Supporting Information. For comparison, the cyclic voltammograms, which were normalized to the conducted scan rates, are also prepared and presented in Figure 3B for LTO-OLCa, and in Figure S5C,D, Supporting Information, for LTO and LTO-OLCv. In Figure 3A, the lithiation peak starts from  $1.55\text{ V}$  versus  $\text{Li}/\text{Li}^+$ , and the delithiation peak at  $1.6\text{ V}$  versus  $\text{Li}/\text{Li}^+$ . The peak separation is larger for faster scan rates due to the overpotential caused by kinetic limitation (Figure 3B).

For a better understanding of the charge transfer kinetics, we used Equation (4)<sup>[46–48]</sup>

$$i = av^b \quad (4)$$

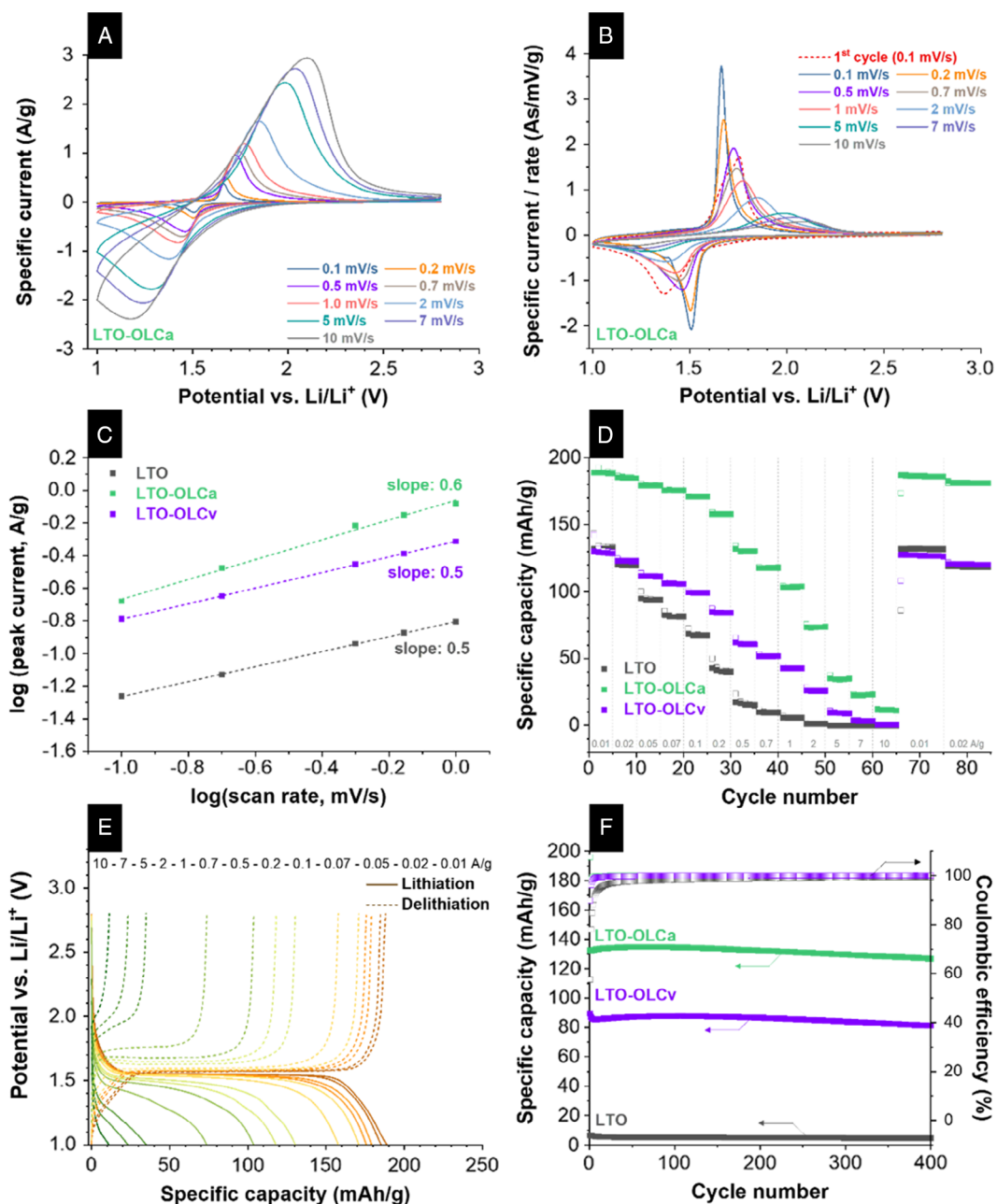


**Figure 3.** Lithium-ion intercalation behavior of LTO and LTO/carbon onium hybrid materials. A) Cyclic voltammograms recorded at 0.1–10 mV s<sup>-1</sup> of LTO-OLCa and B) the cyclic voltammograms normalized to the recorded scan rate. C) Plot of  $\log(\text{scan rate})$  versus  $\log(\text{peak current})$  of the lithiation (cathodic) in the potential range of 1.0–2.8 V versus Li/Li<sup>+</sup> and the linear fitting of each sample. D) The lithiation and delithiation specific capacity of LTO, LTO-OLCa, and LTO-OLCv from galvanostatic charge/discharge cycling at different specific current for rate capability. E) Galvanostatic charge–discharge profiles of the fifth cycle at 0.01–10 A g<sup>-1</sup> of sample LTO-OLCa between 1.0 and 2.8 V versus Li/Li<sup>+</sup>. F) Galvanostatic charge/discharge cycling performance stability at a specific current of 0.1 A g<sup>-1</sup> for LTO, LTO-OLCa, and LTO-OLCv.

where  $a$  and  $b$  are the variables,  $i$  is the peak specific current (A/g), and  $\nu$  is the scan rate (mV s<sup>-1</sup>). From the obtained  $b$  value, the process kinetics fall between the boundary set by diffusion control ( $b = 0.5$ ) or surface control ( $b = 1$ ).<sup>[48]</sup> Figure 3C is obtained using CV data and the (shift-adjusted) peak currents of the hybrid materials at the scan rates of 0.1–1 mV s<sup>-1</sup>. Thereby, we observed the  $b$  values of LTO (0.5),

LTO-OLCa (0.6), and LTO-OLCv (0.5). These values are all close to the ideal case of diffusion-controlled kinetics.

To further understand the behavior of the LTO-OLC hybrids, the electrochemical impedance was measured from the prepared cells before the CV measurement, and the corresponding Nyquist plot is shown in Figure S6, Supporting Information. The spectra before the CV of LTO-OLCa and

LTO-OLCv are similar, and the spectrum of LTO is shifted toward larger resistance values. To quantify the resistance dependency on the surface reaction or charge transfer, we used the equivalent circuit of  $(R_s + CPE1/R_{int} + CPE2/(R_{ct} + W))$ , as summarized in Table S4, Supporting Information. Therein,  $R_s$  stands for the electrolyte and cell component resistance,  $R_{int}$  stands for the film formation on the interface of electrode–electrolyte, and  $R_{ct}$  stands for the charge-transfer resistance;  $W$  demarks the Warburg impedance, and CPE is a constant phase element. The high-frequency region is known to represent the contributions of the electronic resistance of the cell.<sup>[49]</sup> The charge transfer resistance of LTO before the CV (3871  $\Omega$ ) is higher than the hybrid LTO-OLCa (736  $\Omega$ ) and LTO-OLCv (1607  $\Omega$ ), which aligns with the superior rate capability of LTO-OLCa. The contribution of  $R_s$  is negligible for LTO-OLCa (4.6  $\Omega$ ) and LTO-OLCv (2.2  $\Omega$ ), but very high for LTO (84.0  $\Omega$ ) before CV. The integrated semi-circles indicate the resistance of surface reactions, including the electrode–electrolyte interface and the ionic mobility at the surface of the electrode.<sup>[49,50]</sup>

The rate capability of the LTO-OLC hybrid materials was tested with the GCPL technique applying specific currents between 0.01 and 10 A g<sup>-1</sup> at an operational potential of 1.0–2.8 V versus Li/Li<sup>+</sup> (Figure 3D). The highest specific capacity of 188 mAh g<sup>-1</sup> was obtained from LTO-OLCa, with a coulombic efficiency of 92%, followed by  $\approx$ 130 mAh g<sup>-1</sup> for LTO and LTO-OLCv, with a coulombic efficiency of  $\approx$ 92%. The coulombic efficiency of LTO-OLCa further increased to  $\approx$ 100% by the third cycle and maintained over 98% during the rate capability testing sequence. As the applied specific current increases above 0.5 A g<sup>-1</sup>, the specific capacity of LTO-OLCa decreased with a greater margin than at smaller specific currents. The specific capacity was 11 mAh g<sup>-1</sup> at a specific current of 10 A g<sup>-1</sup>, and the material recovered 98.9% of the initial capacity (corresponding with 186 mAh g<sup>-1</sup>) when returning to a rate of 0.01 A g<sup>-1</sup>.

The LTO and LTO-OLCa displayed the same initial capacity. LTO without carbon showed a low rate capability, enabling a charge storage of only 13 mAh g<sup>-1</sup> at 0.7 A g<sup>-1</sup>. Furthermore, LTO recovered 99% of the initial capacity, which corresponds with 127 mAh g<sup>-1</sup> when returning to a rate of 0.01 mA g<sup>-1</sup>. With only 3 mass% carbon content of the LTO electrode, the electron transfer might have enough time to establish the diffusion pathway at a low current of 0.01 mA g<sup>-1</sup> to obtain the specific capacity of 130 mAh g<sup>-1</sup>. However, at higher specific currents that require faster transport, the LTO only demonstrated inferior

rate capability. Although LTO-OLCv had the same initial capacity as the LTO, whereby LTO-OLCv showed better rate handling performance, which we ascribe to the higher carbon content of LTO-OLCv. Figure 3E shows the corresponding specific capacity and potential profile of LTO-OLCa. In good agreement with the cyclic voltammogram, the difference in the plateau between the lithiation and de-lithiation is small at low specific current (0.01–0.05 A g<sup>-1</sup>). As the specific current increases, such a difference in lithiation and de-lithiation potential increases.

For comparison, the capacity and potential plot of LTO and LTO-OLCv are shown in Figure S5E,F, Supporting Information. We observed the same behavior of potential separation that the pristine LTO exhibits large potential separation already at 0.1 A g<sup>-1</sup>, whereas LTO-OLCa and LTO-OLCv exhibit a large potential separation at 0.5 A g<sup>-1</sup>. As the kinetic analysis suggests that diffusion is the limiting factor, the different rate handling performance (Figure 3D) must be the influence of the added OLC. Yet, the degree of graphitization carbon in LTO-OLCa is significantly better than LTO-OLCv (confirmed by Raman result, Table S3, Supporting Information). Also, the impedance data indicate better charge transport in LTO-OLCa compared with LTO-OLCv, which supports the higher lithium storage performance of LTO-OLCa. Thus, charge transfer in LTO-OLCa is faster than LTO-OLCv. The cycling performance of the LTO and LTO-OLC hybrid materials was carried out at 0.1 A g<sup>-1</sup>, and the results are presented in Figure 3F, including their coulombic efficiencies. LTO-OLCa exhibits an initial capacity of 132 mAh g<sup>-1</sup>, and 95.8% of the capacity remained after 400 cycles, losing only 0.013 mAh g<sup>-1</sup> per cycle. Similarly, LTO-OLCv showed a slight decrease of 3 mAh g<sup>-1</sup> after the initial capacity of 98 mAh g<sup>-1</sup>, and then maintained 90.8% of the initial capacity.

Table 1 presents previously reported performance values of LTO/C composite and hybrid materials in comparison with data from this study. The best-performing material from our present study was LTO-OLCa material with a specific capacity of 184 mAh g<sup>-1</sup> at 0.11C. The capacity retention is comparable to the state-of-the-art performance, which shows its potential as anode material for LIBs.

### 3.3. Sodium-Ion Intercalation Behavior and Performance

For testing the electrochemical performance for sodium-ion intercalation, we selected only LTO-OLCa due to its best

**Table 1.** Comparison of electrochemical performance of previously reported LTO materials with various synthesis methods and our LTO-OLCa hybrid material for LIBs.

Material	Synthesis	Specific capacity	Rate capability	Cycling stability	Reference
LTO-carbon onion	Sol–gel 700 °C, 2 h	184 mAh g <sup>-1</sup> at 0.11 C	74 mAh g <sup>-1</sup> at 11 C	95.8% after 400 cycles	This work
Li <sub>4</sub> T <sub>5</sub> O <sub>12</sub> /C	Solid state 900 °C, 20 h	165 mAh g <sup>-1</sup> at 0.2 C	–	–	[24]
Mesoporous Li <sub>4</sub> T <sub>5</sub> O <sub>12</sub> /C	Self-assembly 700 °C, 2 h	144 mAh g <sup>-1</sup> at 1 C	90 mAh g <sup>-1</sup> at 5 C	90% after 500 cycles	[51]
Li <sub>4</sub> T <sub>5</sub> O <sub>12</sub> /graphene oxide	Solid-state ball milling 500 °C, 4 h	170 mAh g <sup>-1</sup> at 1 C	122 mAh g <sup>-1</sup> at 30 C	94.8% after 300 cycles	[52]
Li <sub>4</sub> T <sub>5</sub> O <sub>12</sub> -AC nanotubes	Electrospinning 800 °C, 3 h	120 mAh g <sup>-1</sup> at 100 mA g <sup>-1</sup>	84 mAh g <sup>-1</sup> at 4 A g <sup>-1</sup>	67% after 100 cycles	[17]
Li <sub>4</sub> T <sub>5</sub> O <sub>12</sub> porous monolith	Sol–gel, hydrothermal 700 °C, 2 h	165 mAh g <sup>-1</sup> at 0.1 C	105 mAh g <sup>-1</sup> at 30 C	98% after 500 cycles	[53]
Li <sub>4</sub> T <sub>5</sub> O <sub>12</sub> thin nanosheet	Hydrothermal, 600 °C, 3 h	168 mAh g <sup>-1</sup> at 0.2 C	130 mAh g <sup>-1</sup> at 64 C	96% after 400 cycles	[33]

performance and stability based on the LIB data. We prepared CR2032 coin cells using sodium metal as a counter and reference electrode for the electrochemical testing. Cyclic voltammetry was conducted in a potential range of 0.3–2.5 V versus Na/Na<sup>+</sup>. **Figure 4A** presents the first and fifth voltammetric cycles at the scan rates of 0.1–10 mV s<sup>-1</sup>. The first cycle shows sodiation peaks alongside the FEC redox activity starting from 0.6 V versus Na/Na<sup>+</sup>, and the lowest current was observed at ≈0.3 V versus Na/Na<sup>+</sup> (Figure S7, Supporting Information). This can be ascribed to the structural change of the LTO spinel from

intercalating the larger sized Na<sup>+</sup> ions into the interstitial sites.<sup>[29]</sup> From the next cycle, the paired sodiation/desodiation peak is observed at 0.7 and 1.05 V versus Na/Na<sup>+</sup>, and the peak separation is enhanced, as the scan rate increases;  $\Delta V$  was 0.35 V at the initial scan rate of 0.1 mV s<sup>-1</sup>, 0.65 V with 0.5 mV s<sup>-1</sup>, and more than 0.9 V at 1 mV s<sup>-1</sup>. The higher peak separation indicates the need for higher overpotential or energy to insert/extract Na<sup>+</sup> ion into or out of the structure.<sup>[20]</sup>

The sodiation regime from voltammetry starts to deteriorate above with a scan rate of 2 mV s<sup>-1</sup>, and at 5 mV s<sup>-1</sup> and higher

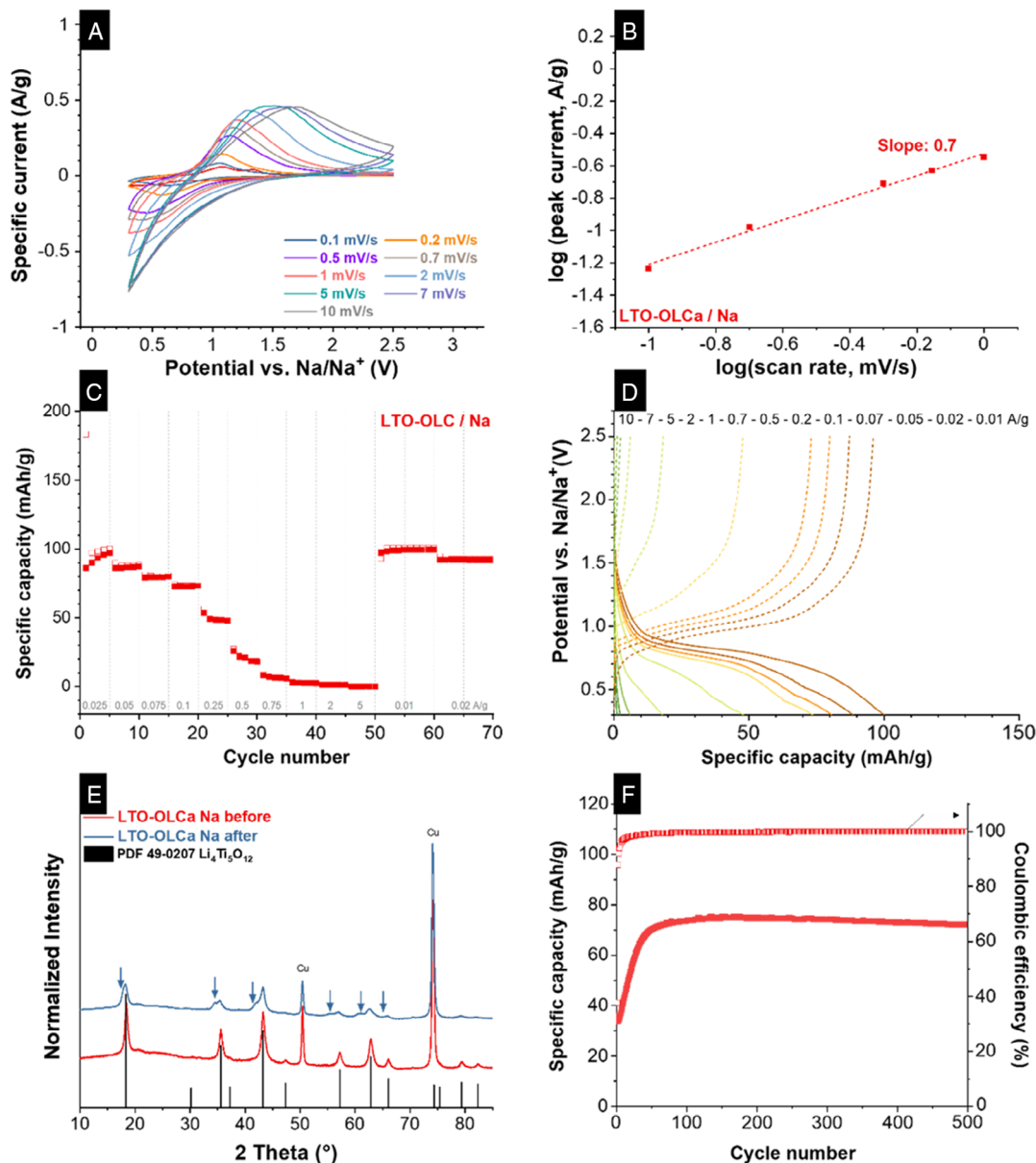


**Figure 4.** Sodium-ion intercalation performance of LTO-OLCa. A) Cyclic voltammograms recorded at 0.1–10 mV s<sup>-1</sup> in the potential range of 0.3–2.5 V versus Na/Na<sup>+</sup>. B) Plot of  $\log(\text{scan rate})$  versus  $\log(\text{peak current})$  of the sodiation (cathodic) in the potential range of 0.3–2.5 V versus Na/Na<sup>+</sup> and the linear fitting of LTO-OLCa. C) The sodiation and desodiation specific capacity of LTO-OLCa sample obtained from galvanostatic charge/discharge cycling at different specific current for rate capability. D) Galvanostatic charge–discharge profiles of the fifth cycle at 0.025–5 A g<sup>-1</sup> of sample LTO-OLCa between 0.3 and 2.5 V versus Na/Na<sup>+</sup>. E) The X-ray diffractograms of LTO-OLCa electrodes, before and after the galvanostatic charge–discharge process. F) Galvanostatic charge/discharge cycling performance stability at a specific current of 0.1 A g<sup>-1</sup> for LTO-OLCa.

scan rates, the cyclic voltammograms do not show a further change in current reflex with changing scan rate. This implies that the insertion of Na<sup>+</sup> ion into the sites is kinetically hindered.<sup>[20]</sup> Just like for the Li-containing electrolyte, we calculated *b* values for SIB data (Figure 4B). The *b* value of LTO-OLCa tested against sodium was 0.7, which is higher than the values obtained from the lithium intercalation testing. The lowest peak current at 0.1 mV s<sup>-1</sup> scan demonstrates a significant influence on the reconstruction of the LTO structure with sodiation. The *b* value of the sodium intercalation, excluding the peak current at 0.1 mV s<sup>-1</sup>, was 0.6, which is close to the value found from LIB testing.

The GCPL of the LTO-OLCa hybrid material was tested in the specific current range of 0.025–5 A g<sup>-1</sup> to quantify the rate capability. Figure 4C displays both sodiation and desodiation capacities of LTO-OLCa. The capacity values were normalized to the metal oxide mass for a better comparison with the literature. At 0.025 A g<sup>-1</sup>, the initial desodiation capacity reaches 87 mAh g<sup>-1</sup> at a low coulombic efficiency of 47%. Such a low coulombic efficiency might result from the irreversible sodiation in the first cycle and the side reactions regarding SEI formation.<sup>[54]</sup> However, the desodiation capacity increases slightly from the first cycle to the fifth, which may be due to the reconstruction of the LTO structure during the insertion/extraction of the sodium ions. Accordingly, the coulombic efficiency further enhances as the cell continues being tested. Above a specific current of 0.25 A g<sup>-1</sup>, the capacity decreases severely, leading to no significant insertion/extraction capacity of Na<sup>+</sup> above 1 A g<sup>-1</sup>. To distinguish the contribution of the carbon onion, an electrode of only carbon onion annealed in Ar (OLCa) was prepared and tested with GCPL at the same operational potential and specific current. The sodiation capacity values of OLCa are presented in Figure S8B, Supporting Information, with the highest capacity of 14 mAh g<sup>-1</sup>; in addition, Figure S8A, Supporting Information, displays the capacity values of OLCa when used as an LIB anode. Figure 4D shows the corresponding potential profiles of the GCPL results at the fifth cycles of each applied specific currents tested in the potential range of 0.3–2.5 V versus Na/Na<sup>+</sup>. At lower specific currents, the Na<sup>+</sup> insertion into LTO begins from 0.9 V versus Na/Na<sup>+</sup> to 0.6 V versus Na/Na<sup>+</sup> with the first slope, and then continues with a different slope to 0.3 V versus Na/Na<sup>+</sup>. When comparing the GCPL result of LTO-OLCa between lithium-ion and sodium-ion cells, one can observe the difference between the slope of the plateau (Figure 3E and 4D) suggesting higher overpotential.

To characterize possible structural change that we suspect from the first voltammetric cycles and very low coulombic efficiency of GCPL at the first cycle, we carried out post-mortem XRD analysis of the tested electrodes. The diffractograms of the electrodes before and after GCPL testing are presented in Figure 4E. The diffractogram of LTO-OLCa before cycling matches the peak position of cubic LTO, which has *a* = 8.366 ± 0.002 Å. In addition to the set of reflection peaks inherent to LTO, we also see the emergence of another set of the same number of reflections shifted toward larger *d* values (i.e., lower scattering angles) for the LTO-OLCa after cycling. We also see sharp and intense peaks relating to the current collector material (i.e., copper). After electrochemical testing, there is a significant increase in the unit cell dimension to *a* = 8.4677 Å and a decrease in the domain size to about 10 nm. We see double peaks for the main reflections of LTO-OLCa, which indicate the coexistence of a population of LTO domains with increased unit cell volume and one close to the initial value (*a* = 8.3608 Å). This phase also has a domain size of about 10 nm, and the mass ratio between both crystallographically distinct LTO phases is about 1:1 (46:54; i.e., there is slightly less expanded LTO). The presence of about 54 mass% of residual Na<sub>6</sub>LiTi<sub>5</sub>O<sub>12</sub> is in contrast to the full electrochemical desodiation treatment of the post-mortem electrode. In agreement with previous work, when inserting Na<sup>+</sup> into the LTO structure, Na<sup>+</sup> substitutes Li in the LTO lattice. Subsequently, Na<sub>6</sub>LiTi<sub>5</sub>O<sub>12</sub> heterogeneously emerges from the LTO phase.<sup>[55]</sup> Therefore, the inability to revert all of the sodiated materials to the initial crystal structure aligns with the reduced achievable charge storage capacity of about 100 mAh g<sup>-1</sup> and the low initial coulombic efficiency of ≈50%. The disassembly of the cell was done after the desodiation step of the GCPL test; therefore, it is evident that the permanent transformation of the Na-containing phase occurs during the first cycles, as CV and GCPL profiles indicate.<sup>[34]</sup>

The size difference of Na<sup>+</sup> and Li<sup>+</sup> ions (ionic radius, Na<sup>+</sup> = 102 pm, Li<sup>+</sup> = 76 pm) is expected to trigger the poor rate performance of LTO as an anode in SIB than LIB. This size difference is initiated by the structural change, leading to more reduced cycling stability of the SIB.<sup>[29,33]</sup> Moreover, the dependency of SIB performance on the size of LTO was reported by Yu et al.,<sup>[30]</sup> which showed that smaller LTO particles enhance the rate and cycling performance of SIB. As our LTO-OLCa has a crystalline size of around 30 nm, the higher performance was expected. As presented in Table 2, the rate performance of LTO-OLCa in the SIB setup was not comparable to the

**Table 2.** Comparison of electrochemical performance of previously reported LTO materials with various synthesis methods and our LTO-OLCa hybrid material for SIBs, normalized to metal oxide mass. “rGO” means “reduced graphene oxide”.

Material	Synthesis	Potential range	Specific capacity	Rate capability	Cycling stability	Reference
LTO-carbon onion	Sol-gel 700 °C, 2 h	2.5–0.3 V	97 mAh g <sup>-1</sup> at 0.15 C	27 mAh g <sup>-1</sup> at 2.8 C	95.6% after 500 cycles	This work
Li <sub>4</sub> Ti <sub>5</sub> O <sub>12</sub>	Solid state 800 °C, 20 h	3.0–0.3 V	187 mAh g <sup>-1</sup> at 0.1 C	–	–	[27]
Porous Li <sub>4</sub> Ti <sub>5</sub> O <sub>12</sub> /C	Spray drying 950 °C, 24 h	3.0–0.5 V	155 mAh g <sup>-1</sup> at 0.1 C	90 mAh g <sup>-1</sup> at 5 C	95% after 20 cycles	[29]
Li <sub>4</sub> Ti <sub>5</sub> O <sub>12</sub> /C nanowire	Hydrothermal 750 °C, 6 h	2.5–0.3 V	168 mAh g <sup>-1</sup> at 0.2 C	38 mAh g <sup>-1</sup> at 100 C	97% after 50 cycles	[31]
Li <sub>4</sub> Ti <sub>5</sub> O <sub>12</sub> porous monolith	Sol-gel, hydrothermal 700 °C, 2 h	1.5–0.5 V	127 mAh g <sup>-1</sup> at 1 C	63 mAh g <sup>-1</sup> at 30 C	70% after 100 cycles	[53]
Li <sub>4</sub> Ti <sub>5</sub> O <sub>12</sub> thin nanosheet	Hydrothermal, 600 °C, 3 h	2.5–0.5 V	170 mAh g <sup>-1</sup> at 0.2 C	115 mAh g <sup>-1</sup> at 30 C	92% after 150 cycles	[33]
Li <sub>4</sub> Ti <sub>5</sub> O <sub>12</sub> -TiO <sub>2</sub> /rGO aerogel	Hydrothermal 700 °C, 6 h	2.5–0.3 V	184 mAh g <sup>-1</sup> at 0.5 C	77 mAh g <sup>-1</sup> at 20 C	64% after 700 cycle	[56]

reported state of the art. Yet, around 96% capacity retention after 500 cycles compared with the maximum capacity is superior to the cycling performance in the reported literature, which reports very low counts of cycles. This suggests that the hybridization of LTO with carbon onion benefits the longevity of SIB (Figure 4F). Recently, Pfeifer et al. reported the importance of the appropriate selection of electrolytes for SIB application using sodium metal.<sup>[57]</sup> To enhance the performance and stability of hard carbon or sodium metal anodes for SIB, FEC was introduced to the electrolyte system additives.<sup>[54]</sup> Some have reported LTO as an anode for SIB using FEC-containing electrolytes, such as NaClO<sub>4</sub> in ethylene carbonate:diethyl carbonate:fluoroethylene carbonate (50:50:1 by volume)<sup>[58]</sup> or NaClO<sub>4</sub> in propylene carbonate:fluoroethylene carbonate (98:2 by volume),<sup>[31]</sup> which showed enhanced stability performance.

#### 4. Conclusion

In conclusion, we synthesized nano-sized LTO and carbon onion hybrid materials and applied them, for the first time, as an anode in LIBs and SIBs. The LTO-OLCa successfully demonstrated its excellent performance with a high specific capacity of 188 mAh g<sup>-1</sup> and a favorable rate capability of 74 mAh g<sup>-1</sup> at 2 A g<sup>-1</sup>, with 99% retention of its initial capacity after the testing to 10 A g<sup>-1</sup>. The longevity test of LTO-OLCa yielded 95.8% of initial capacity, superior to both LTO synthesized without carbon onions with inferior performance, or LTO hybridized with OLCv, which only performed 91% recovery in both capacity and the retention for LIB. The LTO-OLCa, which had excellent performance in the LIB system, exhibited unsatisfactory performance when applied as anode for SIB with a specific capacity of only 102 mAh g<sup>-1</sup>. Nevertheless, the longevity of LTO-OLCa with sodium showed 96% of the maximum capacity retention after 500 cycles using 1 M NaClO<sub>4</sub> in EC:DMC (1:1 by mass) containing 5 mass% FEC as the electrolyte. This work demonstrates carbon onion as a preferable hybridization substance. We believe that our LTO and carbon onion hybrid material has a potential for further improvement, for example, by the implementation of a different electrode design or a different electrolyte system to increase performance or longevity.

#### Supporting Information

Supporting Information is available from the Wiley Online Library or from the author.

#### Acknowledgements

The authors acknowledge funding from the German Federal Ministry for Economic Affairs and Energy (BMWi) in support of the HyBaCap project (award number 03ET6113C). They thank Eduard Arzt (INM) for his continuing support and Roland Bennewitz (INM) & Wiebke Buhrow (INM) for discussions and additional experimentation. Open access funding enabled and organized by Projekt DEAL.

#### Conflict of Interest

The authors declare no conflict of interest.

#### Keywords

lithium titanate, lithium titanium oxide, lithium-ion batteries, Li<sub>4</sub>Ti<sub>5</sub>O<sub>12</sub>, sodium-ion batteries

Received: July 24, 2020

Revised: August 30, 2020

Published online:

- [1] M. Armand, J. M. Tarascon, *Nature* **2008**, 451, 652.
- [2] J. Shim, K. A. Striebel, *J. Power Sources* **2003**, 119–121, 955.
- [3] R. Yazami, P. Touzain, *J. Power Sources* **1983**, 9, 365.
- [4] R. Yazami, *Electrochim. Acta* **1999**, 45, 87.
- [5] P. Cicconi, L. Postacchini, E. Pallotta, A. Monteriù, M. Prist, M. Bevilacqua, M. Germani, *J. Power Sources* **2019**, 436, 226837.
- [6] L. Kavan, M. Grätzel, *Solid State Lett.* **2002**, 5, A39.
- [7] T. Ohzuku, A. Ueda, N. Yamamoto, *J. Electrochem. Soc.* **1995**, 142, 1431.
- [8] S. S. Zhang, K. Xu, T. R. Jow, *J. Power Sources* **2004**, 130, 281.
- [9] W. J. H. Borghols, M. Wagemaker, U. Lafont, E. M. Kelder, F. M. Mulder, *J. Am. Chem. Soc.* **2009**, 131, 17786.
- [10] B.-N. Yun, H. L. Du, J.-Y. Hwang, H.-G. Jung, Y.-K. Sun, *J. Mater. Chem.* **2017**, 5, 2802.
- [11] K. Zaghib, M. Simoneau, M. Armand, M. Gauthier, *J. Power Sources* **1999**, 81–82, 300.
- [12] S. Bach, J. P. Pereira-Ramos, N. Baffier, *J. Power Sources* **1999**, 81–82, 273.
- [13] Y. H. Rho, K. Kanamura, *J. Solid State Chem.* **2004**, 177, 2094.
- [14] B. Yan, M. Li, X. Li, Z. Bai, J. Yang, D. Xiong, D. Li, *J. Mater. Chem. A* **2015**, 3, 11773.
- [15] M. Widmaier, K. Pfeifer, L. Bommer, V. Presser, *Batteries Supercaps* **2018**, 1, 11.
- [16] S. Fleischmann, A. Tolosa, V. Presser, *Chem. Eur. J.* **2018**, 24, 12143.
- [17] H. S. Choi, J. H. Im, T. Kim, J. H. Park, C. R. Park, *J. Mater. Chem.* **2012**, 22, 16986.
- [18] A. Nugroho, W. Chang, S. J. Kim, K. Y. Chung, J. Kim, *RSC Adv.* **2012**, 2, 10805.
- [19] H. Kim, K.-Y. Park, M.-Y. Cho, M.-H. Kim, J. Hong, S.-K. Jung, K. C. Roh, K. Kang, *ChemElectroChem* **2014**, 1, 125.
- [20] C. Chen, H. Xu, T. Zhou, Z. Guo, L. Chen, M. Yan, L. Mai, P. Hu, S. Cheng, Y. Huang, J. Xie, *Adv. Energy Mater.* **2016**, 6, 1600322.
- [21] L. Cheng, X.-L. Li, H.-J. Liu, H.-M. Xiong, P.-W. Zhang, Y.-Y. Xia, *J. Electrochem. Soc.* **2007**, 154, A692.
- [22] T. Yuan, X. Yu, R. Cai, Y. Zhou, Z. Shao, *J. Power Sources* **2010**, 195, 4997.
- [23] Y.-B. He, F. Ning, B. Li, Q.-S. Song, W. Lv, H. Du, D. Zhai, F. Su, Q.-H. Yang, F. Kang, *J. Power Sources* **2012**, 202, 253.
- [24] H.-G. Jung, S.-T. Myung, C. S. Yoon, S.-B. Son, K. H. Oh, K. Amine, B. Scrosati, Y.-K. Sun, *Energy Environ. Sci.* **2011**, 4, 1345.
- [25] H. Li, L. Shen, X. Zhang, J. Wang, P. Nie, Q. Che, B. Ding, *J. Power Sources* **2013**, 221, 122.
- [26] M. Widmaier, N. Jäckel, M. Zeiger, M. Abuzarli, C. Engel, L. Bommer, V. Presser, *Electrochim. Acta* **2017**, 247, 1006.
- [27] L. Zhao, H.-L. Pan, Y.-S. Hu, H. Li, L.-Q. Chen, *Chin. Phys. B* **2012**, 21, 028201.
- [28] Y. Wang, X. Yu, S. Xu, J. Bai, R. Xiao, Y. S. Hu, H. Li, X. Q. Yang, L. Chen, X. Huang, *Nat. Commun.* **2013**, 4, 2365.

- [29] Y. Sun, L. Zhao, H. Pan, X. Lu, L. Gu, Y.-S. Hu, H. Li, M. Armand, Y. Ikuhara, L. Chen, X. Huang, *Nat. Commun.* **2013**, *4*, 1870.
- [30] X. Yu, H. Pan, W. Wan, C. Ma, J. Bai, Q. Meng, S. N. Ehrlich, Y.-S. Hu, X.-Q. Yang, *Nano Lett.* **2013**, *13*, 4721.
- [31] K.-T. Kim, C.-Y. Yu, C. S. Yoon, S.-J. Kim, Y.-K. Sun, S.-T. Myung, *Nano Energy* **2015**, *12*, 725.
- [32] M. Kitta, R. Kataoka, M. Kohyama, *Phys. Chem. Chem. Phys.* **2016**, *18*, 19888.
- [33] X. Feng, H. Zou, H. Xiang, X. Guo, T. Zhou, Y. Wu, W. Xu, P. Yan, C. Wang, J.-G. Zhang, Y. Yu, *ACS Appl. Mater. Interfaces* **2016**, *8*, 16718.
- [34] M. Kitta, R. Kataoka, S. Tanaka, N. Takeichi, M. Kohyama, *ACS Appl. Energy Mater.* **2019**, *2*, 4345.
- [35] Y. Liu, J. Liu, M. Hou, L. Fan, Y. Wang, Y. Xia, *J. Mater. Chem. A* **2017**, *5*, 10902.
- [36] M. Zeiger, N. Jäckel, M. Aslan, D. Weingarth, V. Presser, *Carbon* **2015**, *84*, 584.
- [37] M. Zeiger, N. Jäckel, D. Weingarth, V. Presser, *Carbon* **2015**, *94*, 507.
- [38] S. Fleischmann, A. Tolosa, M. Zeiger, B. Krüner, N. J. Peter, I. Grobelsek, A. Quade, A. Kruth, V. Presser, *J. Mater. Chem. A* **2017**, *5*, 2792.
- [39] N. Jäckel, D. Weingarth, M. Zeiger, M. Aslan, I. Grobelsek, V. Presser, *J. Power Sources* **2014**, *272*, 1122.
- [40] K. Pfeifer, S. Arnold, Ö. Budak, X. Luo, V. Presser, H. Ehrenberg, S. Dsoke, *J. Mater. Chem. A* **2020**, *8*, 6092.
- [41] D. B. Schuepfer, F. Badaczewski, J. M. Guerra-Castro, D. M. Hofmann, C. Heiliger, B. Smarsly, P. J. Klar, *Carbon* **2020**, *161*, 359.
- [42] G. A. Zickler, B. Smarsly, N. Gierlinger, H. Peterlik, O. Paris, *Carbon* **2006**, *44*, 3239.
- [43] N. C. Saha, H. G. Tompkins, *J. Appl. Phys.* **1992**, *72*, 3072.
- [44] Y. Tang, F. Huang, W. Zhao, Z. Liu, D. Wan, *J. Mater. Chem.* **2012**, *22*, 11257.
- [45] C.-K. Lan, S.-I. Chuang, Q. Bao, Y.-T. Liao, J.-G. Duh, *J. Power Sources* **2015**, *275*, 660.
- [46] S. Ardizzone, G. Fregonara, S. Trasatti, *Electrochim. Acta* **1990**, *35*, 263.
- [47] M. Hillert, *Metall. Trans. A* **1975**, *6*, 5.
- [48] M. Opitz, J. Yue, J. Wallauer, B. Smarsly, B. Roling, *Electrochim. Acta* **2015**, *168*, 125.
- [49] J. Landesfeind, D. Pritzl, H. A. Gasteiger, *J. Electrochem. Soc.* **2017**, *164*, A1773.
- [50] F. J. Günter, J. B. Habedank, D. Schreiner, T. Neuwirth, R. Gilles, G. Reinhart, *J. Electrochem. Soc.* **2018**, *165*, A3249.
- [51] E. Kang, Y. S. Jung, G. H. Kim, J. Chun, U. Wiesner, A. C. Dillon, J. K. Kim, J. Lee, *Adv. Funct. Mater.* **2011**, *21*, 4349.
- [52] Y. Shi, L. Wen, F. Li, H.-M. Cheng, *J. Power Sources* **2011**, *196*, 8610.
- [53] G. Hasegawa, K. Kanamori, T. Kiyomura, H. Kurata, K. Nakanishi, T. Abe, *Adv. Energy Mater.* **2015**, *5*, 1400730.
- [54] S. Komaba, T. Ishikawa, N. Yabuuchi, W. Murata, A. Ito, Y. Ohsawa, *ACS Appl. Mater. Interfaces* **2011**, *3*, 4165.
- [55] M. Kitta, K. Kuratani, M. Tabuchi, N. Takeichi, T. Akita, T. Kiyobayashi, M. Kohyama, *Electrochim. Acta* **2014**, *148*, 175.
- [56] Y. Tian, G. Xu, Z. Wu, J. Zhong, L. Yang, *RSC Adv.* **2017**, *7*, 52702.
- [57] K. Pfeifer, S. Arnold, J. Becherer, C. Das, J. Maibach, H. Ehrenberg, S. Dsoke, *ChemSusChem* **2019**, *12*, 3312.
- [58] L. Y. Yang, H. Z. Li, J. Liu, S. S. Tang, Y. K. Lu, S. T. Li, J. Min, N. Yan, M. Lei, *J. Mater. Chem.* **2015**, *3*, 24446.

## Supplementary Information

# **Hybrid anodes of lithium titanium oxide and carbon onions for lithium-ion and sodium-ion energy storage**

**Hwirim Shim,<sup>1,2</sup> Stefanie Arnold,<sup>1,2</sup> Öznil Budak,<sup>1,2</sup>  
Maik Ulbricht,<sup>1,2</sup> Pattarachai Srimuk,<sup>1</sup> Volker Presser<sup>1,2,\*</sup>**

<sup>1</sup> INM - Leibniz Institute for New Materials, 66123 Saarbrücken, Germany

<sup>2</sup> Department of Materials Science and Engineering, Saarland University, 66123 Saarbrücken, Germany

\* Corresponding author's eMail: [volker.presser@leibniz-inm.de](mailto:volker.presser@leibniz-inm.de)

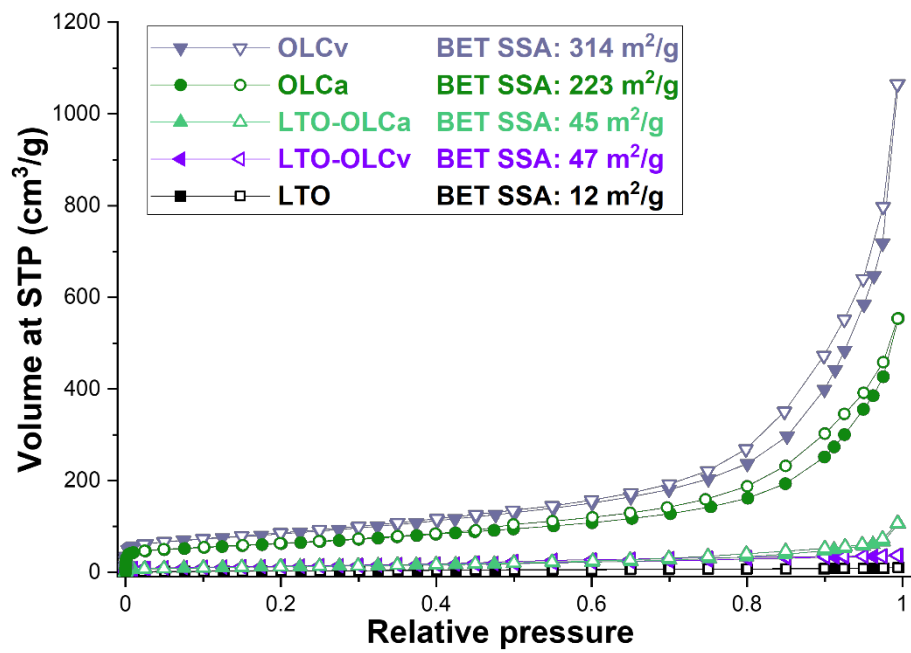


**Fig. S1:** Nitrogen gas sorption isotherms with volumes at standard-temperature-pressure (STP) as a function of relative pressure for LTO, OLCa, OLCv, LTO-OLCv, and LTO-OLCa powders.

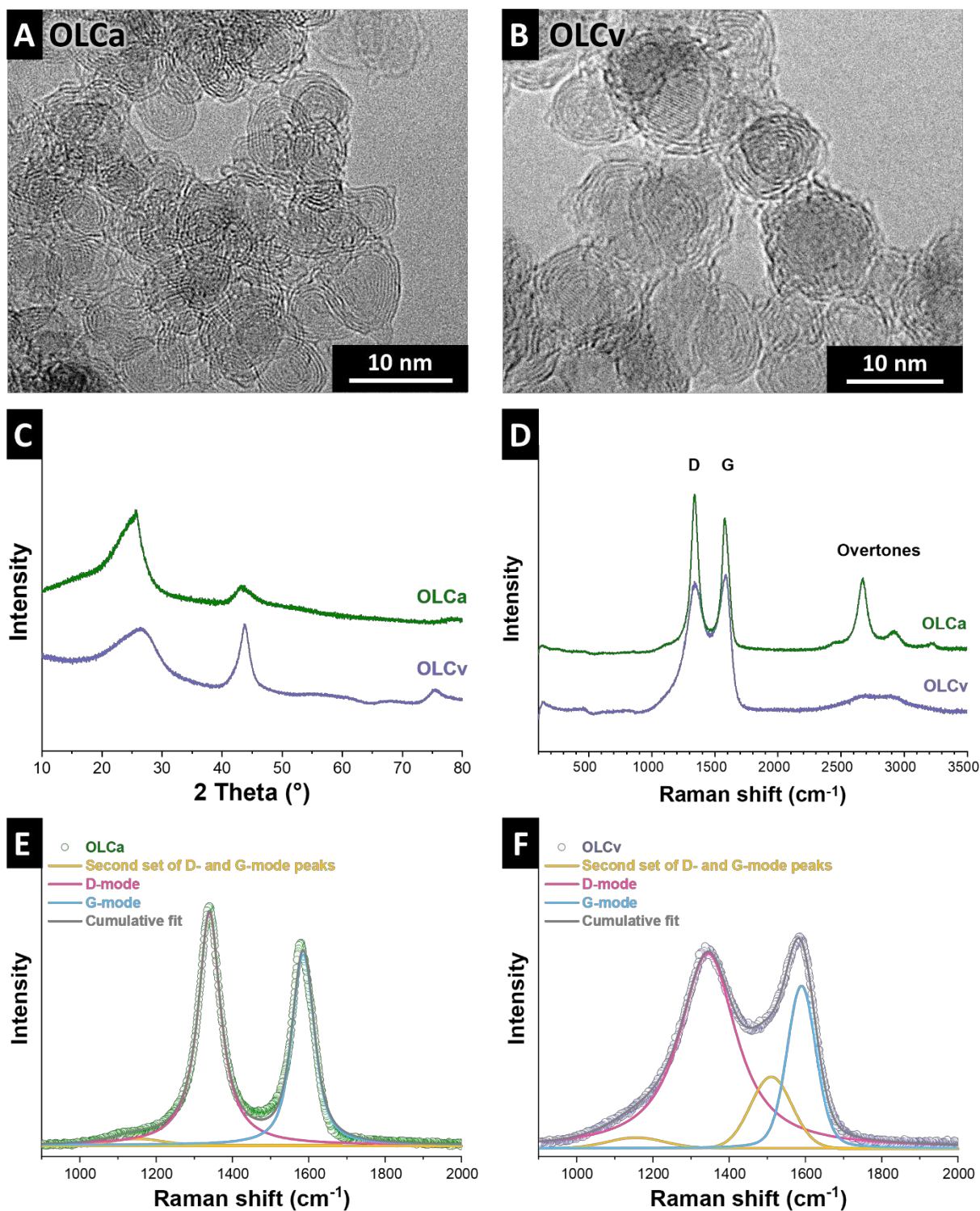


**Fig. S2:** The transmission micrograms of (A)OLCa and (B) OLCv. (C) X-ray diffractograms and (D) Raman spectra of OLCa and OLCv. D-mode and G-mode fitting of (E) OLCa, and (F) OLCv.

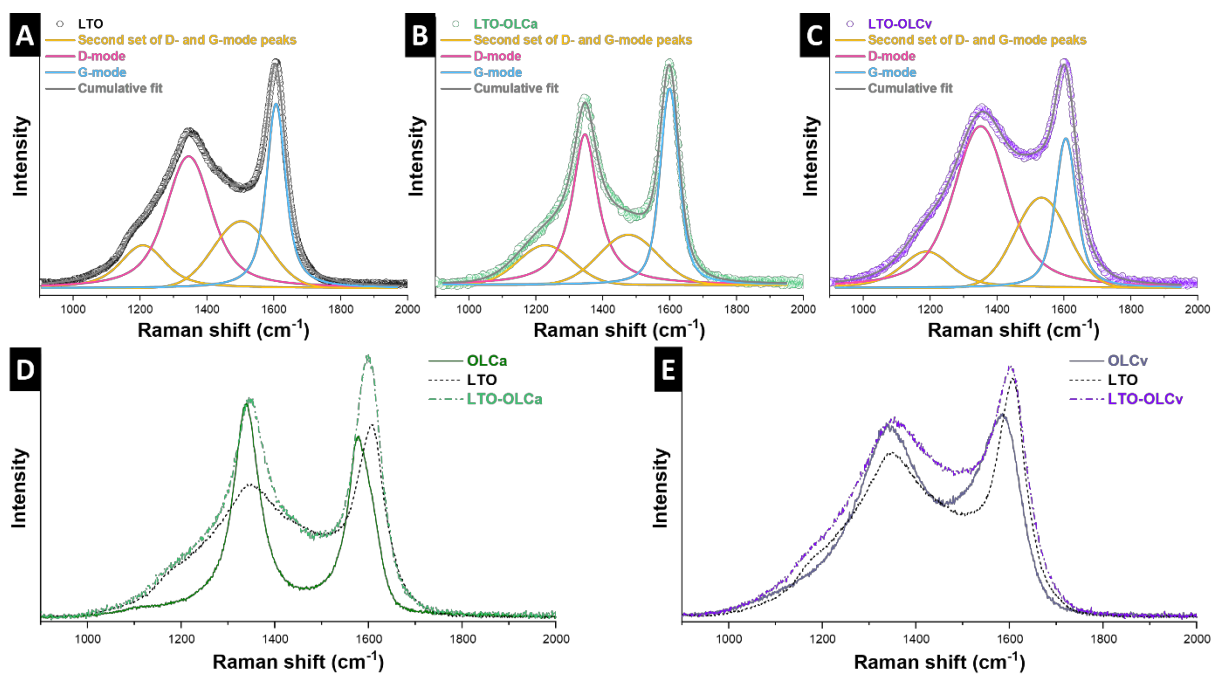


**Fig. S3:** Raman spectra: D- and G-mode peak fitting for (A) LTO, (B) LTO-OLCa, and (C) LTO-OLCv. Overlaid Raman spectra of (D) LTO, OLCa, and LTO-OLCa, and (E) LTO, OLCv, and LTO-OLCv; the relative intensities were adjusted to improve visibility of the individual carbon species.

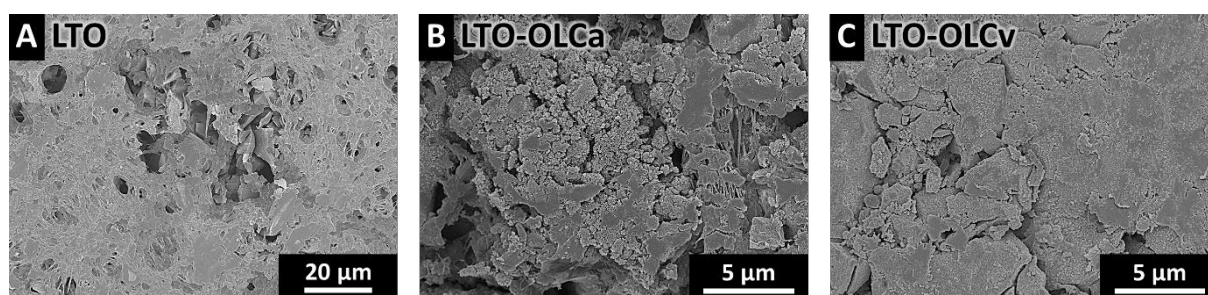


**Fig. S4:** Scanning electron micrographs of (A) LTO, (B) LTO-OLCa, and (C) LTO-OLCv electrodes.

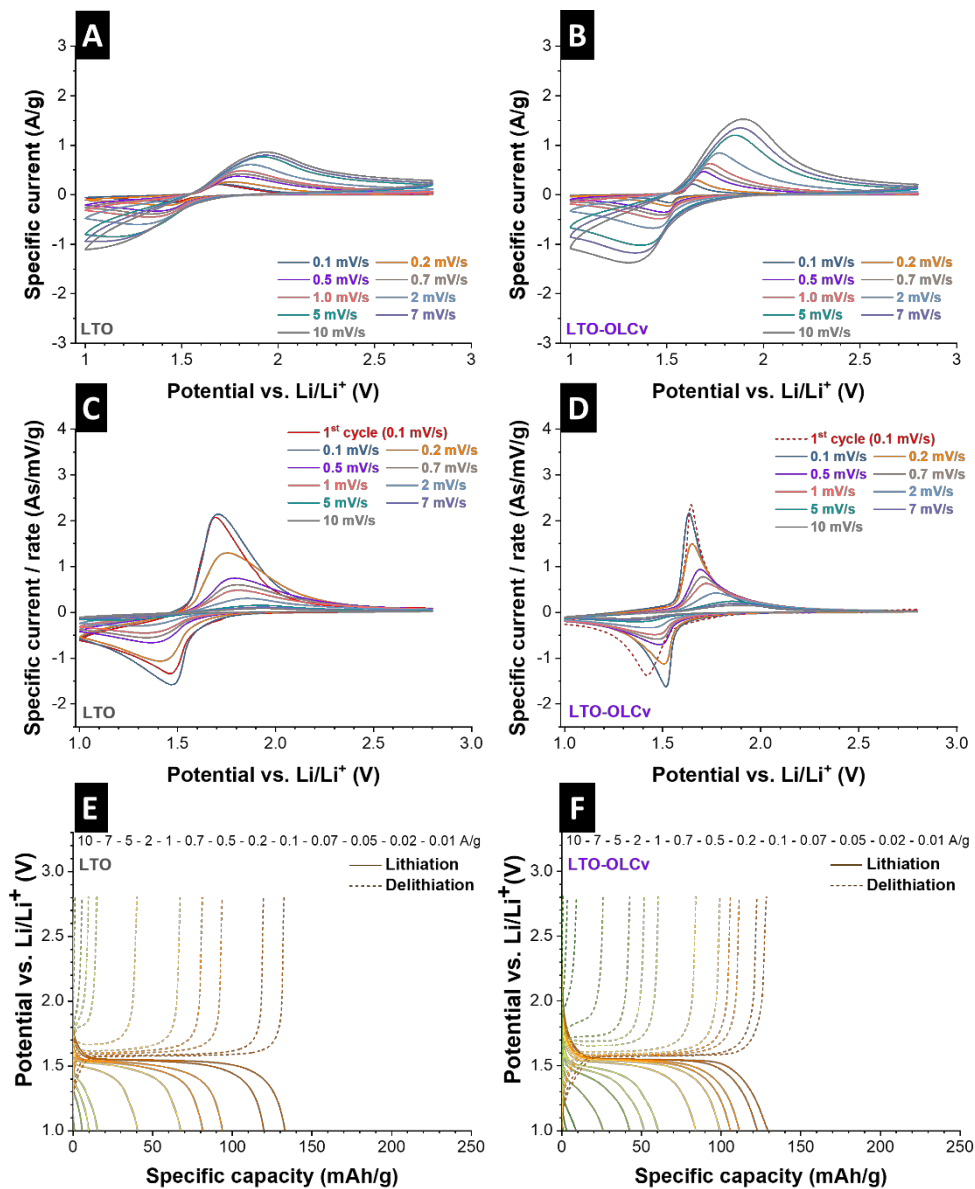


**Fig. S5:** (A-B) Cyclic voltammograms recorded at 0.1-10 mV/s for (A) LTO and (B) LTO-OLCv normalized by scan rates. (C-D) Cyclic voltammograms normalized by scan rates recorded at 0.1-10 mV/s and for (C) LTO and (D) LTO-OLCv. (E-F) Galvanostatic charge-discharge profiles of the 5<sup>th</sup> cycle at 0.01-10 A/g of samples (E) LTO and (F) LTO-OLCv.

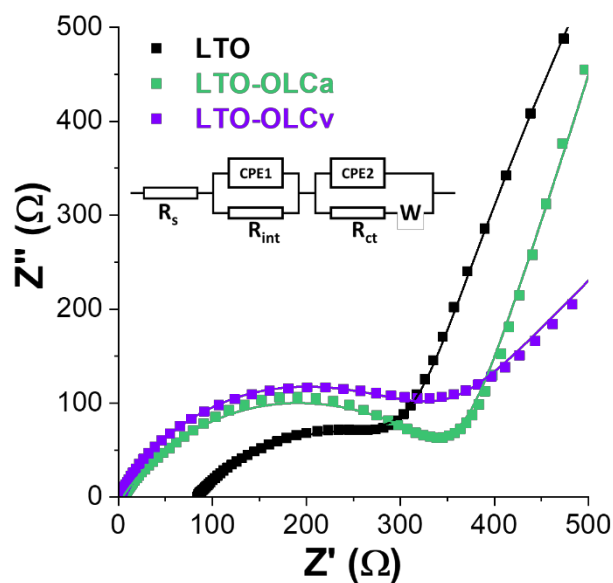


**Fig. S6:** Electrochemical impedance spectra of LTO, LTO-OLCa, and LTO-OLCv (dotted) and the fitting results (lined).

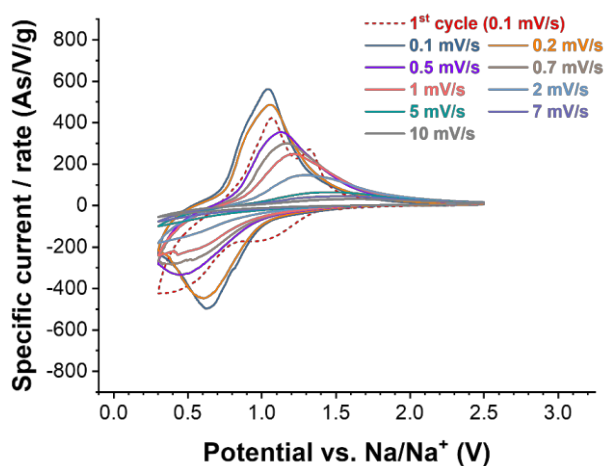


**Fig. S7:** Cyclic voltammograms displayed in Fig. 4a recorded at 0.1-10 mV/s for LTO-OLCa normalized by scan rates between 0.01-2.5 V vs. Na/Na<sup>+</sup>.

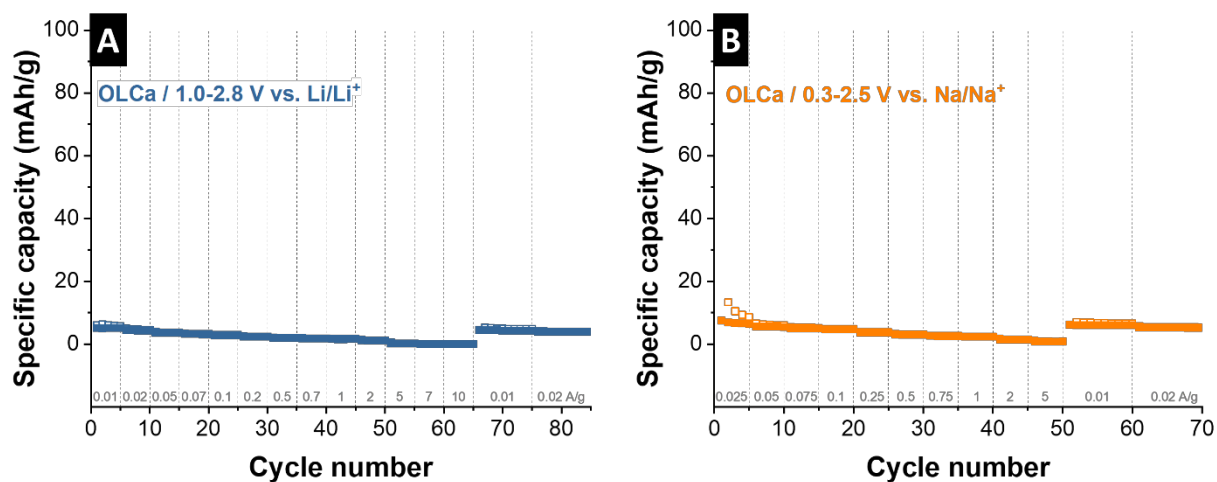


**Fig. S8:** (A) The lithiation and delithiation specific capacity of OLCa obtained from galvanostatic charge/discharge cycling at different specific current for rate capability in the range of 1.0-2.8 V vs. Li/Li<sup>+</sup>. (B) The sodiation and desodiation specific capacity of OLCa obtained from galvanostatic charge/discharge cycling at different specific current for rate capability in the range of 0.3-2.5 V vs. Na/Na<sup>+</sup>. Open symbols: charging; filled symbols: discharging.

**Table S1:** Crystal phases, lattice constants, and domain sizes obtained from Rietveld-fitting based on the X-ray diffractograms seen in Fig. 2.

Material	Crystal phase, space group, and PDF number	Fitted lattice parameters (Å)	Domain size (nm)
LTO	Li <sub>4</sub> Ti <sub>5</sub> O <sub>12</sub> cubic Fd-3m (PDF 49-0207)	a= 8.36384	30
LTO-OLCa	Li <sub>4</sub> Ti <sub>5</sub> O <sub>12</sub> cubic Fd-3m (PDF 49-0207)	a= 8.36655	31
LTO-OLCv	Li <sub>4</sub> Ti <sub>5</sub> O <sub>12</sub> cubic Fd-3m (PDF 49-0207)	a= 8.36577	30

**Table S2:** Results of the elemental analysis. All values in mass%. b.d.l.: below detection limit.

Material	C	H	N	S	O
OLCa	98.76±0.25	b.d.l.	b.d.l.	b.d.l.	1.90±0.48
OLCv	95.91±0.53	b.d.l.	1.67±0.01	b.d.l.	2.99±0.87
LTO	3.08±0.03	0.19±0.01	0.07±0.02	b.d.l.	20.53±0.28
LTO-OLCa	13.12±0.36	b.d.l.	0.15±0.06	b.d.l.	29.17±1.75
LTO-OLCv	13.72±0.25	0.21±0.02	0.22±0.04	b.d.l.	23.35±1.59

**Table S3:** Results of the carbon-related Raman peak analysis. Position and FWHM-values in units of cm<sup>-1</sup>.

Material	D-mode		G-mode		I <sub>D</sub> /I <sub>G</sub> ratio
	position (cm <sup>-1</sup> )	FWHM (cm <sup>-1</sup> )	position (cm <sup>-1</sup> )	FWHM (cm <sup>-1</sup> )	
OLCa	1340	71	1585	70	1.3
OLCv	1344	176	1589	90	3.1
LTO	1345	162	1607	68	1.7
LTO-OLCa	1347	92	1600	67	1.3
LTO-OLCv	1351	193	1585	70	2.8

**Table S4:** Results of the R<sub>s</sub>, R<sub>int</sub>, and R<sub>ct</sub> obtained by fitting the data in Fig S6.

Material	R <sub>s</sub> (Ω)	CPE1 (F·s)	R <sub>int</sub> (Ω)	CPE2 (F·s)	R <sub>ct</sub> (Ω)	W
LTO	84.05	9.7e-05	247.3	5.5e-04	3871	1974
LTO-OLCa	4.6	6.0e-05	359.2	2.8e-03	736	1384
LTO-OLCv	2.2	3.4e-05	9333.5	1.1e-03	1607	911

# Comparison of organic electrolytes at various temperatures for 2.8 V-Li-ion hybrid supercapacitors

**Hwirim Shim**,<sup>1,2</sup> **Öznil Budak**,<sup>1,2</sup> **Veronika Haug**,<sup>3</sup> **Matthias Widmaier**,<sup>2</sup> **Volker Presser**<sup>1,2</sup>

<sup>1</sup> INM - Leibniz Institute for New Materials, 66123 Saarbrücken, Germany

<sup>2</sup> Department of Materials Science and Engineering, Saarland University, 66123 Saarbrücken, Germany

<sup>3</sup> Robert Bosch GmbH, Robert-Bosch-Campus 1, 71272 Renningen, Germany

## Citation:

H. Shim, Ö. Budak, V. Haug, M. Widmaier, & V. Presser (2020). Comparison of organic electrolytes at various temperatures for 2.8 V-Li-ion hybrid supercapacitors. *Electrochimica Acta*, 337, 135760.

## Own contributions:

Planning, conductivity measurement, X-ray diffraction measurements, scanning electron microscopy, electrochemical measurements, writing.



# Comparison of organic electrolytes at various temperatures for 2.8 V–Li-ion hybrid supercapacitors



H. Shim <sup>a, b</sup>, Ö. Budak <sup>a, b</sup>, V. Haug <sup>c</sup>, M. Widmaier <sup>b</sup>, V. Presser <sup>a, b, \*</sup>

<sup>a</sup> INM - Leibniz Institute for New Materials, 66123, Saarbrücken, Germany

<sup>b</sup> Department of Materials Science and Engineering, Saarland University, 66123, Saarbrücken, Germany

<sup>c</sup> Robert Bosch GmbH, Robert-Bosch-Campus 1, 71272, Renningen, Germany

## ARTICLE INFO

### Article history:

Received 20 December 2019

Received in revised form

18 January 2020

Accepted 21 January 2020

Available online 22 January 2020

### Keywords:

Hybrid supercapacitor

Electrolytes

Electrochemical energy storage

## ABSTRACT

We explore different electrolytes containing lithium perchlorate (LiClO<sub>4</sub>) and lithium bis(tri-fluoromethylsulfonyl)imide (LiTFSI) salts in various solvents at different temperatures to associate the electrochemical stability of lithium titanium oxide (LTO)/lithium manganese oxide (LMO)-activated carbon (AC) composite Li-ion hybrid supercapacitors. By varying the solvents and operation temperature, we were able to detect a correlation between the electrochemical performance and the conductivity of each electrolyte. To test the electrochemical stability and longevity of the electrolytes in such a system, full-cells were analyzed via a voltage floating for 10 h at charged state (2.8 V) of the full-cell. Energy and power performance were the highest for acetonitrile (ACN) containing electrolytes due to their high lithium-ion conductivity. Additionally, the longevity of LiClO<sub>4</sub> in 3-methoxypropionitrile (3-MPN) was superior to all tested electrolytes at ambient temperature with 97% capacity retention and energy efficiency of about 86% after 500 h of voltage floating. LiClO<sub>4</sub> in a mixture of ACN and ethylene carbonate (EC) was the most stable electrolyte at high temperatures with 70% capacity retention after 500 h voltage floating at 60 °C and 50% capacity retention after 250 h voltage floating. The longevity of LiTFSI in ACN and LiClO<sub>4</sub> in 3-MPN electrolyte demonstrated a capacity retention of 97% and 92% after 500 h voltage floating, respectively, at low temperature (−10 °C).

© 2020 Elsevier Ltd. All rights reserved.

## 1. Introduction

Growing demand in long-lasting, fast-charging, or high-power energy storage for portable electrical applications motivates the worldwide investigation on devices such as lithium-ion batteries (LIBs) and supercapacitors (Fig. 1) [1,2]. While both of these two energy storage technologies employ a pair of electrodes immersed in an electrolyte, they employ different charge storage mechanisms and different electrode materials [3]. Lithium-ion batteries are based on materials with Faradaic charge-transfer reactions to store and release energy by insertion, conversion, or alloying of lithium-ions [4]. In most present-day lithium-ion batteries, lithium is inserted into the anode while it extracted from the cathode and vice versa during charging and discharging. Thereby, charge storage and recovery are enabled via cation-specific processes. Typically

Faradaic materials exhibit non-linear voltage profiles with plateaus indicating the redox-active reactions that enable high specific energy but low specific power due to the relatively slow diffusion process (Fig. 1A) [5,6]. In contrast, supercapacitors show a linear capacitor-like voltage profile, achieving high specific power but low specific energy (Fig. 1A) [7,8]. This electrochemical signature can be achieved either by ion electroadsorption at the fluid/solid interface (electrical double-layer capacitors) or by fast redox-processes (pseudocapacitors) [9]. Commonly, high surface area electrodes such as activated carbon are employed for electrical double-layer capacitors [10,11]. In the latter case, during charging, electroadsorption of cations at the negatively polarized electrode and anions at the positively polarized is observed; thereby, most present-day electrical double-layer capacitors (also known as supercapacitors or ultracapacitors) employ cation- and concurrent anion-specific adsorption processes.

To overcome the limitations of the individual devices and utilize the distinct electrochemical features of each system, many researchers have investigated hybrid supercapacitors (HSC) [12,13]. These devices can be constructed by combining a Faradaic electrode

\* Corresponding author. INM - Leibniz Institute for New Materials, 66123, Saarbrücken, Germany

E-mail address: [volker.presser@leibniz-inm.de](mailto:volker.presser@leibniz-inm.de) (V. Presser).

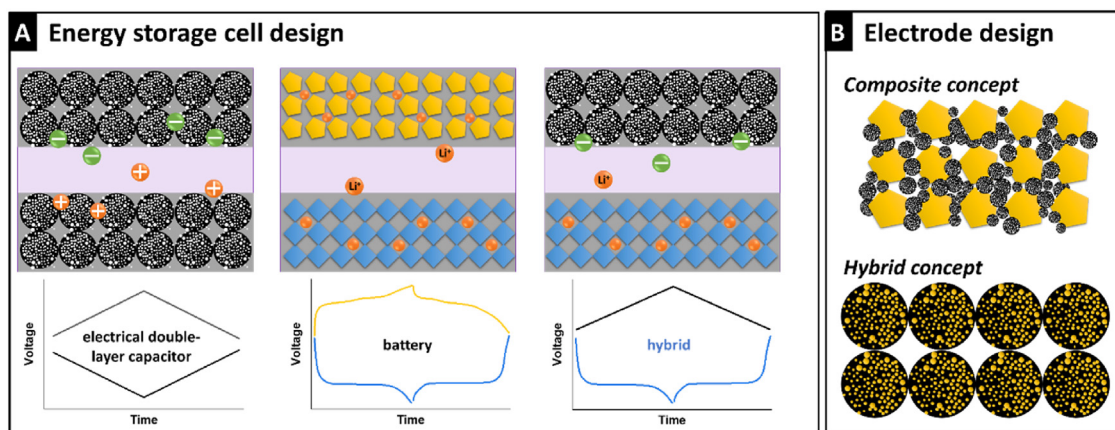


**Fig. 1.** (A) Cell concept of a supercapacitor, a Li-ion battery, and a resulting hybrid device. (B) Composite vs. hybrid concept to combine within one electrode features of a supercapacitor (via ion electrosorption in nanoporous carbon) and a Li-ion battery (via an ion insertion electrode material).

as the negative electrode (anode), such as lithium titanium oxide, and an electrode composed of highly porous carbon as the positive electrode (cathode), and a Li-containing electrolyte [4,14–20]. Therefore, the voltage profile of each electrode exhibits distinctive electrochemical behavior of Faradaic and non-Faradaic materials (Fig. 1A). Another approach is to combine materials for ion electrosorption and Faradaic materials within the electrode (Fig. 1B). Since Faradaic charge storage materials are often intrinsic insulators, research and commercial approaches add a conductive additive during the electrode preparation. This physical add-mixing of a Faradaic material and carbons yields composite electrodes, and numerous such material combinations have been reported [4,21]. Other variations implement a combination of a Faradaic material and nanoporous carbon on a nanoscopic level, which yields hybrid materials [4,22]. Examples include the nanoscale implementation of an intercalation material into carbon nanotubes via ultracentrifugation [18], atomic layer decoration of carbon surfaces with metal oxides [23,24], or metal oxide/carbon core/shell architectures [25,26].

Most present-day lithium-ion batteries use carbonate-based electrolytes with dissolved Li-containing salts [27,28]. We also find organic electrolytes in supercapacitors, in particular, acetonitrile, because of its high ion mobility [29]. There is a large number of other organic-solvent electrolytes (including mixtures of different organic solvents) along with alternative electrolytes based on aqueous media or ionic liquids [30–33]. Most works in the literature have adapted conventional lithium-ion battery electrolytes to hybrid systems due to their high conductivity and wide operating potential [17,32,34–37]. Still, the safety and longevity of the conventional electrolyte can hinder the hybrid supercapacitor system in some applications. Therefore, the hybrid supercapacitor concept necessitates optimal salt and solvent combination to achieve a good performance, especially for non-ambient temperature applications [18,22,33,38,39]. Lithium-containing inorganic salts used for lithium-ion battery electrolytes are also employed for hybrid supercapacitors such as lithium perchlorate (LiClO<sub>4</sub>), Lithium tetrafluoroborate (LiBF<sub>4</sub>), lithium hexafluorophosphate (LiPF<sub>6</sub>), or lithium hexafluoroarsenate (LiAsF<sub>6</sub>). LiClO<sub>4</sub> is characterized by a high solubility and conductivity, wide anodic limit, and more stable SEI formation from lack of an F<sup>-</sup> ion [27,40–42]. The high reactivity of the oxidation state of the perchlorate ion and thermal instability is the main drawback of LiClO<sub>4</sub>. Lithium bis(trifluoromethylsulfonyl)imide (LiTFSI) is an attractive alternative to LiClO<sub>4</sub> due to its high chemical and thermal stability [43–45]. However, LiTFSI has been reported to corrode aluminum current

collectors within the operation potential of LIBs [46–48].

Commonly used solvents for hybrid supercapacitor electrolytes are based on propylene carbonate (PC), mixtures of ethylene carbonate (EC) with linear carbonates (e.g., dimethyl carbonate), and acetonitrile (ACN) [30,44]. However, the high viscosity of the carbonates and the reduced stability of ACN at elevated temperatures necessitate the exploration of suitable alternatives [39,44]. In our work, we investigate ACN mixed with EC to reduce the volatility and increase the thermal stability of the electrolyte. Furthermore, among nitrile-based solvents with a relatively low melting point, flammability, and volatility, 3-methoxypropionitrile (3-MPN) was reported first in 2004 by Wang et al. as a solvent for lithium titanate based lithium-ion batteries [49]. Our work explores 3-MPN for the first time in the context of a hybrid supercapacitor. Additionally, we study a Li-salt containing ionic liquid for its supposed good stability at room temperature and higher temperatures and wider operation voltage [30,33,39]. With a focus on the electrolyte, we chose the well-established lithium titanium oxide and lithium manganese oxide/activated carbon system for the electrodes [16,17,20,50]. Our data include energy and power ratings along with performance stability tests via voltage floating at different temperatures (–10 °C to +75 °C).

## 2. Experimental description

### 2.1. Materials

As seen from Table 1, all electrolytes were based on lithium perchlorate (LiClO<sub>4</sub>, Sigma Aldrich) or lithium bis(trifluoromethylsulfonyl)imide (LiTFSI, Iolitec). The electrolytes were prepared by dissolving of these lithium salts in different solvents or ionic liquid: acetonitrile (ACN, BASF SelectiLyte), a 1:1 (by volume) mixture of acetonitrile and ethylene carbonate (ACN:EC, Sigma

**Table 1**  
Electrolyte conductivity at selected temperatures.

Solvate	Solvent	Conductivity (mS/cm)			
		at –10 °C	at +25 °C	at +60 °C	at +70 °C
1 M LiClO <sub>4</sub>	ACN	9.5	30.8	38.1	39.3
1 M LiClO <sub>4</sub>	ACN:EC	10.8	18.1	25.6	27.6
1 M LiClO <sub>4</sub>	PC	1.9	5.0	9.4	10.7
1 M LiClO <sub>4</sub>	3-MPN	3.4	6.8	10.4	11.4
1 M LiTFSI	ACN	23.8	34.3	43.5	45.3
1 M LiTFSI	PMPyrrTFSI	0.1	1.1	4.0	5.4

Aldrich; labeled in our work as ACN:EC (1:1)), propylene carbonate (PC, Sigma Aldrich), 3-methoxypropionitrile (3-MPN, Sigma Aldrich), and 1-methyl-1-propylpyrrolidinium bis(trifluoromethylsulfonyl)imide (PMPyrrTFSI, Iolitec). The chemical structures of all electrolytes are displayed in *Supporting Information, Fig. S1*.

Coconut-derived activated carbon (AC) powders YP-50F and YP-80F were purchased from Kuraray chemicals. Carbon black (Denka Black) was purchased from Denka, lithium titanium oxide (LTO) from Sigma Aldrich, and lithium manganese oxide (LMO) from Toda Kogyo. The X-ray diffraction pattern of the initial materials along with the crystal structures of LMO and LTO are shown in *Supporting Information, Fig. S2*.

## 2.2. Working electrode preparation

For the LTO electrodes, LTO powder was mixed with 20 mass% carbon black and 5 mass% carboxymethyl cellulose (CMC) dissolved in water and ethanol mixture in a DAC400 FVZ speed-mixer. The electrode slurry was subsequently doctor-bladed on a carbon-coated aluminum foil current collector (Ranafoil, Toyo Aluminum). The casted electrode sheets were dried in a fume hood for two days, followed by drying in a vacuum oven at +120 °C for 12 h.

LMO-AC electrodes were prepared by mixing 58 mass% AC YP-80F powder, 32 mass% LMO powder, 5 mass% carbon black, and 5 mass% polyvinylidene fluoride (PVdF, Sigma Aldrich) dissolved in dimethyl sulfoxide following the same electrode preparation step as for LTO electrodes.

Scanning electron micrographs of the as-prepared cathodes and anodes are shown in *Supporting Information, Fig. S3*.

Activated carbon type YP-50F was employed for the preparation of the quasi-reference electrode (QRE). Detailed information on the chemical composition, structure, and porosity of this carbon is found in our previous work [50]. YP-50F powder was treated in nitric acid at +95 °C for 5 h, followed by thorough washing and drying as described elsewhere [50]. For convenience and comparability to literature, all QRE potentials stated in this work were calculated to Li potential. The activated carbon powder was dispersed in ethanol in an agate mortar, and 10 mass% of polytetrafluoroethylene (PTFE, 60 mass% solution in water; Sigma Aldrich) was admixed to the dispersion. Dispersions were mixed well until a rubber-like texture was obtained, then transferred to hot-roll press to prepare a film with 500 μm wet thickness. The paste was dried in a vacuum oven at +120 °C overnight.

## 2.3. Material characterization

### 2.3.1. Electrolyte conductivity measurements

We measured the ionic conductivity of each electrolyte using a Microcell HC electrochemical cell with Pt electrodes (RHD Instruments) and a Modulab electrochemical workstation with ESC software (Solartron Analytical). With a syringe, 0.9 mL of each electrolyte was transported into the measuring cup, and the Pt electrode crucible was screwed closed. The closed-cell was mounted on the Peltier element of temperature-controlled base unit (Eurotherm 2000) using heat sink paste to improve the heat transfer between the Peltier element and the crucible. Potentiostatic impedance at each temperature was measured after temperature-stabilized for 10 min. The impedance was measured from 1 Hz to 700 kHz at open circuit potential (OCV), in steps of different temperature from -20 °C to +80 °C, in steps of Δ10 °C, including +25 °C. The cell constant was calculated by using the conductance obtained from 0.1 M KCl aqueous standard (VWR) with a conductivity of 12.880 mS/cm at +25 °C using Eq. (1).

$$G = \frac{1}{R} = \frac{A}{l \cdot \rho} = \frac{A \cdot \sigma}{l} \quad (1)$$

where  $G$  is conductance,  $R$  is resistance,  $A$  is the area,  $l$  is the length,  $\rho$  is the resistivity, and  $\sigma$  is the conductivity. The obtained impedance admittance data for each electrolyte was fitted to obtain the resistivity value of the cell. Using Eq. (1), and the calculated cell constant, the ionic conductivity of the electrolytes at different temperatures were obtained.

### 2.3.2. Electrochemical characterization

For all the electrochemical measurements, we used custom-built polyether ether ketone (PEEK) cells. Specifications of the PEEK cells can be found in Ref. [51].

For full-cell measurements, an LTO electrode disk of 12 mm and an LMO electrode disk of 12 mm was employed as the negative and positive electrode, respectively. A surface-functionalized YP-50F electrode served as QRE. The prepared cells were pre-cycled from 0.8 to 2.8 V at 10C for 20 cycles, followed by galvanostatic charge/discharge cycling with potential limitation (GCPL) measurements using different C-rate of 1C–250C in the cell voltage range of 0.8–2.8 V to obtain a Ragone plot. The specific energy of the full-cells was calculated by integrating the voltage behavior over the discharging time as in (Eq. (2)):

$$E_{sp} = \frac{I \int_{t_0}^t U(t) dt}{m} \quad (2)$$

where  $I$  is the applied current,  $t$  is the time,  $U$  is the time-dependent cell voltage, and  $m$  is the total mass of both positive and negative electrode, including binder and additives. The specific power is calculated from specific energy divided by discharging time. The IR drop values of the discharge process are included in the calculation of the specific power and energy.

For measurements at higher or lower temperatures, the galvanostatic measurements to obtain Ragone plots were first done at +25 °C for comparison. To ensure temperature stabilization, the climate chamber was then heated or cooled to either +60 °C, +75 °C, or -10 °C, and the cells were stored at 0.8 V for 10 h at the respective temperature. After this resting period, the GCPL measurement at elevated or decreased temperature was conducted. After sets of GCPL measurements, the cells were cycled three times with 5C, followed by charging at 5C and continued with voltage floating at 2.8 V for 10 h [15]. After 10 h of floating, the cells were discharged with 5C and charge-discharged three times again with 5C. This voltage floating process was repeated 50 times. The internal resistance of the charge/discharge process was calculated from the IR drop using Ohm's law.

## 3. Results and discussion

### 3.1. Temperature-dependent electrolyte conductivity

To establish a physicochemical baseline for the electrochemical testing, we first quantified the conductivity of each electrolyte via potentiostatic impedance within the temperature range of -20 °C to +80 °C. The impedance results yield the resistance of the electrolyte, which is then converted into the conductivity (Table 1). For each electrolyte, the measurement was started at +25 °C then decreased to -20 °C and subsequently increased to +20 °C to prevent the remains of frozen electrolytes for higher temperature measurement. Fig. 2 illustrates the temperature dependence of the prepared electrolytes. The conductivities of LiTFSI in ACN

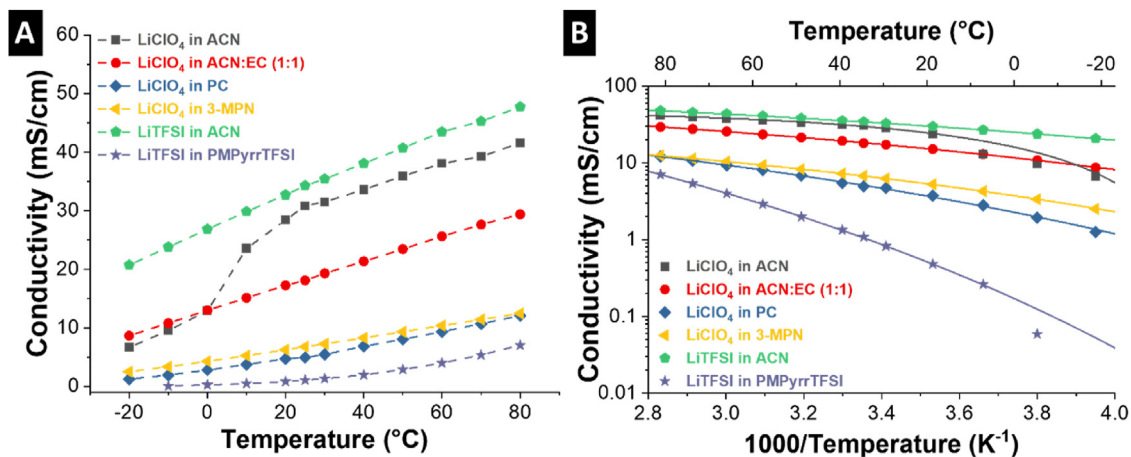


Fig. 2. (A) The temperature dependence of the conductivity of different electrolytes from -20 °C to +80 °C. The dashed lines are added to guide the eye. (B) Measured conductivity data and the results of Vogel-Tammann-Fulcher fitting (solid lines).

electrolyte display the highest values, even though it possesses a larger anion size when compared to LiClO<sub>4</sub>. This is expected to originate from the higher ion dissociation of LiTFSI than LiClO<sub>4</sub> in ACN as the solvent [45,52]. The rapid drop of the conductivity for LiClO<sub>4</sub> in ACN at a lower temperature is due to the crystallization of the solvate in the mixture, as identified by Seo et al. (Ref. [53]).

At temperatures above 0 °C, the conductivity of LiClO<sub>4</sub> in ACN:EC (1:1) is lower than LiClO<sub>4</sub> in ACN due to the addition of more viscous EC; however, the conductivity is higher than LiClO<sub>4</sub> in ACN at temperatures below 0 °C per the suppressed solvate crystallization. Cyclic carbonates provide better Li<sup>+</sup> solvation because they have higher permittivity and dipole moment [27]. Also, at room temperature, the dielectric constant of EC (97) is higher than ACN (37), which favors Li<sup>+</sup> coordination leading to improved ion transport [54,55]. This indicates the solubility of the LiClO<sub>4</sub> salt changes with the introduction of EC to the ACN. The temperature dependence was followed the Arrhenius behavior; therefore, the solvate crystallization does not occur for LiClO<sub>4</sub> in ACN:EC (1:1), which is in stark contrast to pure ACN.

The conductivity of LiClO<sub>4</sub> in PC is comparable to the data obtained in 3-MPN, with a slightly lower slope than ACN containing electrolytes. The lowest conductivity is observed for LiTFSI dissolved in an ionic liquid, which shows its highest conductivity of 7 mS/cm at +80 °C. To describe the temperature dependence of the conductivity, the Arrhenius equation and Vogel-Tammann-Fulcher (VTF) equation (Eq. (3)) are being used [56–59].

$$\sigma = AT^{-0.5} \exp(-B / (T - T_0)) \quad (3)$$

where *A* and *B* are generally related to the carrier number and configurational entropy, respectively, and *T*<sub>0</sub> is the theoretical glass transition temperature [53,56]. The conductivity values in Fig. 2A were used to determine the parameter *A*, *B*, and *T*<sub>0</sub> (Supporting Information, Table S1). As seen in Fig. 2B, the VTF equation fits the measured data very well, including the behavior of LiClO<sub>4</sub> in ACN, which is influenced by solvate crystallization at lower temperatures [53].

### 3.2. Electrochemical performance at ambient temperature

In our full-cell setup, we used an LTO anode and an LMO-AC cathode, as proposed by Cericola et al. [16] and optimized by Widmaier et al. [20,60] for high-performance hybrid supercapacitors. The LMO-AC electrode consists of 58 mass% AC to

maintain good rate handling performance against the LTO anode. The latter did not contain AC but 20 mass% carbon black (CB) in electrode preparation. This choice was motivated as previous works did not show a significant advantage when combining LTO with AC considering the fast lithiation/delithiation process of LTO [20,60,61]. The mass balancing of LTO and LMO-AC electrodes was 1:2 with respect to the total electrode mass of each electrode. The used mass ratio and amount of electrode material components allows us to calculate the theoretical, maximum specific capacity (41.5 mAh/g) and corresponding specific energy (116 Wh/kg) at a cut-off voltage of 2.8 V.

The full-cells were first cycled with galvanostatic cycling with potential limitation (GCPL) at +25 °C, with a cut-off voltage of 2.8 V using C-rates from 1C to 250C to obtain the Ragone plot (Fig. 3A). The specific energy and specific power of the hybrid supercapacitor were calculated from the discharge data at each C-rate and normalized to the total mass of both positive and negative electrodes. Table 2 presents the electrochemical performance of each electrolyte shown in specific energy (Wh/kg) at 1 kW/kg of specific power performed at different temperatures.

Among our set of electrolytes, we identified the highest specific energy at a low rate to be 85 Wh/kg and 81 Wh/kg of LiTFSI in ACN and LiClO<sub>4</sub> in ACN, respectively. This is comparable to our previous work [20]. The energy efficiencies of LiTFSI and LiClO<sub>4</sub> in ACN at the lower C-rate were 90.7% and 92.6%, respectively. LiClO<sub>4</sub> in ACN, ACN:EC (1:1), and 3-MPN at lower C-rates exhibit very similar specific energy and power of ~70 Wh/kg and 0.35 kW/kg, respectively. At rates exceeding 25C, both the specific energy and power of LiClO<sub>4</sub> in 3-MPN decrease faster than the LiClO<sub>4</sub> in ACN:EC (1:1). About 50% of the low-rate specific energy was maintained at 10 kW/kg for LiTFSI and LiClO<sub>4</sub> in ACN electrolytes. LiClO<sub>4</sub> in PC shows a lower energy performance of 50 Wh/kg at low rates; however, at higher rates, the specific energy, and the power was comparable to LiClO<sub>4</sub> in 3-MPN, which we expect to have similar electrochemical performance due to comparable ionic conductivity. LiTFSI in ionic liquid displays the lowest energy and power performance with 20 Wh/kg and 2 kW/kg, respectively, with 85% of energy efficiency. This agrees with its low conductivity and hence, its low diffusion coefficient seen in Fig. 2 [62]. The overall electrochemical performance of the full-cells is proportional to the conductivities at +25 °C, and we see larger specific energy for systems with a higher diffusion coefficient at the same rate. Our data also indicates a convergence of all energy values towards an equilibrium value of 100 Wh/kg at very low rates.

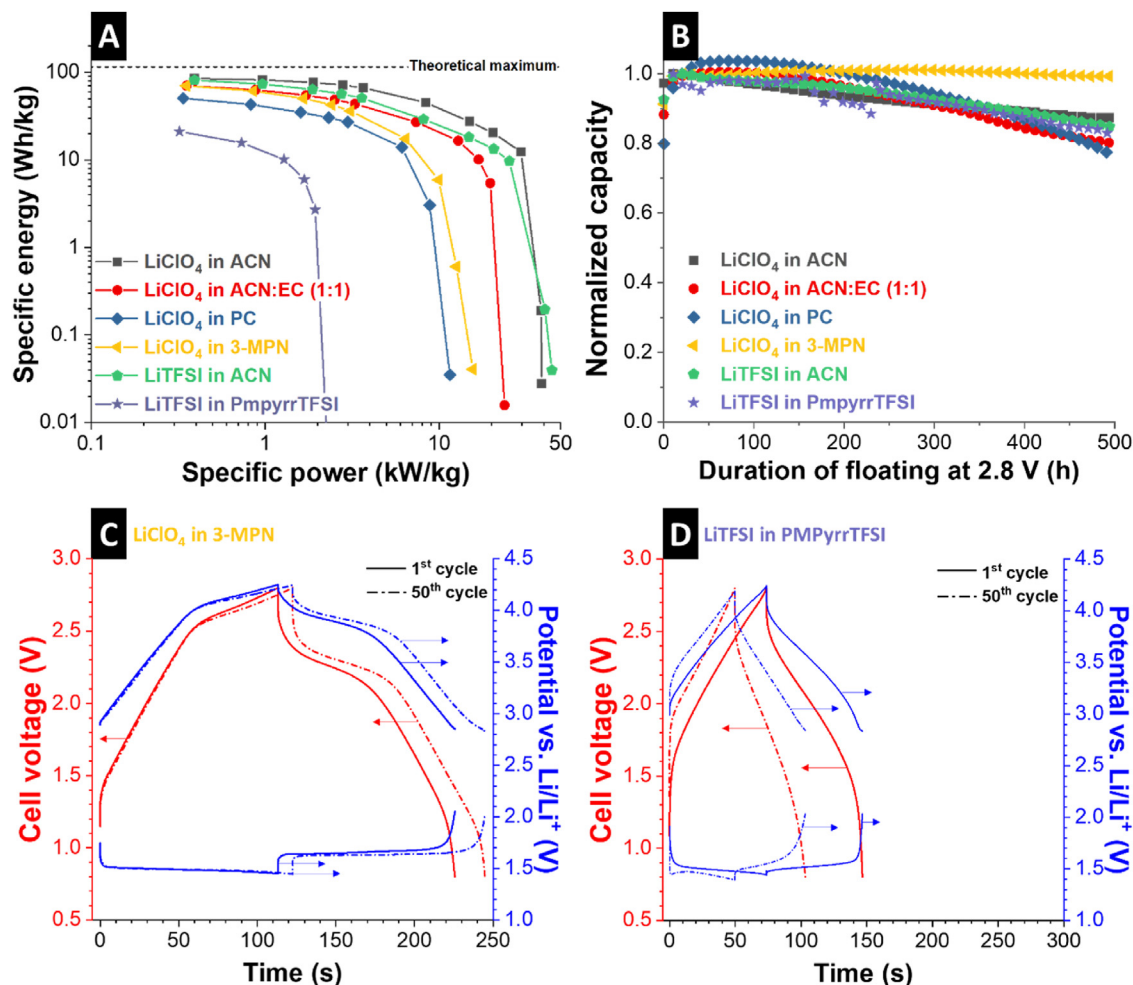


**Fig. 3.** The electrochemical characterization of the hybrid supercapacitors at +25 °C (A) Ragone chart of HSC cycled at 1–250C at 0.8–2.8 V cell voltage. (B) The stability testing of 10 h voltage floating at charged state (2.8 V). The capacity values are obtained from the 3<sup>rd</sup> discharge step after the 10 h floating is finished. Voltage profile of the full-cell with (C) LiClO<sub>4</sub> in 3-MPN (D) LiTFSI in PMPyrrTFSI electrolytes after the 1<sup>st</sup> voltage floating cycle (solid line), and the 50<sup>th</sup> of voltage floating. The potential development of LTO and LMO-AC electrodes was monitored via a carbon quasi-reference electrode.

**Table 2**

Specific energy obtained from electrochemical testing at 1 kW/kg of each electrolyte at different temperatures.

Solvate	Solvent	Specific energy at 1 kW/kg (Wh/kg)			
		at -10 °C	at +25 °C	at +60 °C	at +75 °C
1 M LiClO <sub>4</sub>	ACN	44	81	81	–
1 M LiClO <sub>4</sub>	ACN:EC	28	61	77	64
1 M LiClO <sub>4</sub>	PC	22	41	46	–
1 M LiClO <sub>4</sub>	3-MPN	22	58	76	67
1 M LiTFSI	ACN	36	72	76	–
1 M LiTFSI	PMPyrrTFSI	–	12	28	–

Subsequently, the voltage floating at a cell voltage of 2.8 V was carried out to characterize the electrochemical stability of the cells. We chose this method to provide a more stressful test to survey the electrolyte stability rather than the cycling stability of the electrode material [63]. After 10 h of voltage floating at a cell voltage of 2.8 V, we carried out three galvanostatic discharge-charge cycles at 5C to quantify the capacity, and this procedure was repeated every 10 h. The normalized capacity is shown in Fig. 3B, where most of the electrolytes maintained over 80% of the initial capacity after 500 h (= 50 × 10 h intervals). The most stable electrolyte was LiClO<sub>4</sub> in 3-MPN with energy efficiency maintained about 83–85% and

maintained 97% of the maximum capacity.

The voltage profile of the full-cell with LiClO<sub>4</sub> in 3-MPN is displayed in Fig. 3C with the cell voltage, negative and positive electrode potential profiles at the first cycle before the voltage floating, and the last cycle after voltage floating for 500 h. The LTO electrode shows a voltage plateau at 1.5 V and 1.7 V vs. Li/Li<sup>+</sup> in alignment with the insertion and extraction of Lithium. For the LMO-AC electrode, there are two different regimes, which can be distinguished by their different slopes: A first region ranging from 3.0 to 3.9 V and a second region with a lower slope from 3.9 to 4.2 V vs. Li/Li<sup>+</sup>. The electrochemical signal in the first region is caused by electrosorption on the surface of AC particles, whereas the second region is associated with lithiation/delithiation of LMO and simultaneous ion electrosorption [20]. LiClO<sub>4</sub> in ACN and LiTFSI in ACN maintained 87% and 84% of the maximum capacity, respectively, after 500 h voltage floating. The energy efficiencies decrease from 93% to 91% and 92%–86.5% for LiClO<sub>4</sub> and LiTFSI in ACN, respectively. The higher efficiency decrease of LiTFSI in ACN indicates a higher internal resistance increase. This is in line with the aging behavior when comparing the capacity decline. LiTFSI in the ionic liquid maintained 82% of the capacity retention compared to the initial capacity with energy efficiency degradation from 88% to 83%.

Further galvanostatic charge/discharge profiles of the samples

not part of Fig. 3C and D are displayed in *Supporting Information, Fig. S4*. The calculated resistance values of the cells during voltage floating experiments are presented in *Supporting Information, Table S2*. The initial and final resistance values of the cells with each electrolyte show only a small resistance increase. For cells using LiTFSI in ionic liquid, a slightly higher increase of the resistance was observed after the voltage floating experiments.

3.3. *Electrochemical performance at above-ambient temperature (+60 °C and +75 °C)*

In the next step, we quantified the electrochemical energy storage performance of the full-cells at +60 °C. The comparison of the Ragone plot at +25 °C (Fig. 3A) and +60 °C (Fig. 4A) shows the overall enhancement of the energy and power performance of the full-cells at a higher temperature. The most significant difference is observed for LiTFSI in ionic liquid with a specific energy of 42 Wh/kg and specific power of 12 kW/kg. LiClO<sub>4</sub> and LiTFSI in ACN did not show significant enhancement; however, the specific energy of LiClO<sub>4</sub> in ACN:EC (1:1), PC, and 3-MPN at 1C increased to above 75 Wh/g. The performance of all the electrolytes at higher C-rates beyond 10C was enhanced both in specific energy and power. The energy efficiency of all full-cells also increased at C-rates beyond

10C. The increase in power and energy performance relate to the enhanced ion mobility at higher temperatures as presented in the conductivity data in Fig. 2.

Next, we carried out voltage floating at a cell voltage of 2.8 V with intermittent GCPL to quantify the charge storage capacity. As seen from the data shown in Fig. 4B, there is a sharp decrease in the performance stability of the ACN-based electrolytes, when compared to the performance at room temperature. The cell with LiClO<sub>4</sub> in ACN electrolyte achieved an initial capacity of 34 mAh/g before the first voltage-floating and started a continuous decrease. After the 100 h floating sequence, the capacity decrease was accelerated with more than 2 mAh/g of decrease per 10 h floating, and after the 16th voltage floating step, the cell had lost all available capacity. LiClO<sub>4</sub> in ACN:EC (1:1) maintains its capacity like the results from the ambient temperature. The initial capacity and specific energy were 29 mAh/g and 68 Wh/kg, respectively, with a constant increase to 34 mAh/g and 74 Wh/kg, respectively. This performance can be attributed to the possible rearrangement of LTO structure during insertion as a change in the voltage profile of LTO [13,64–66]. Subsequently, the capacity began to decrease with an average of 0.2 mAh/g per 10 h floating cycle, yielding the best performance with 70% of the initial capacity at +60 °C. The corresponding energy efficiency was 92% in the first cycle and 82% after

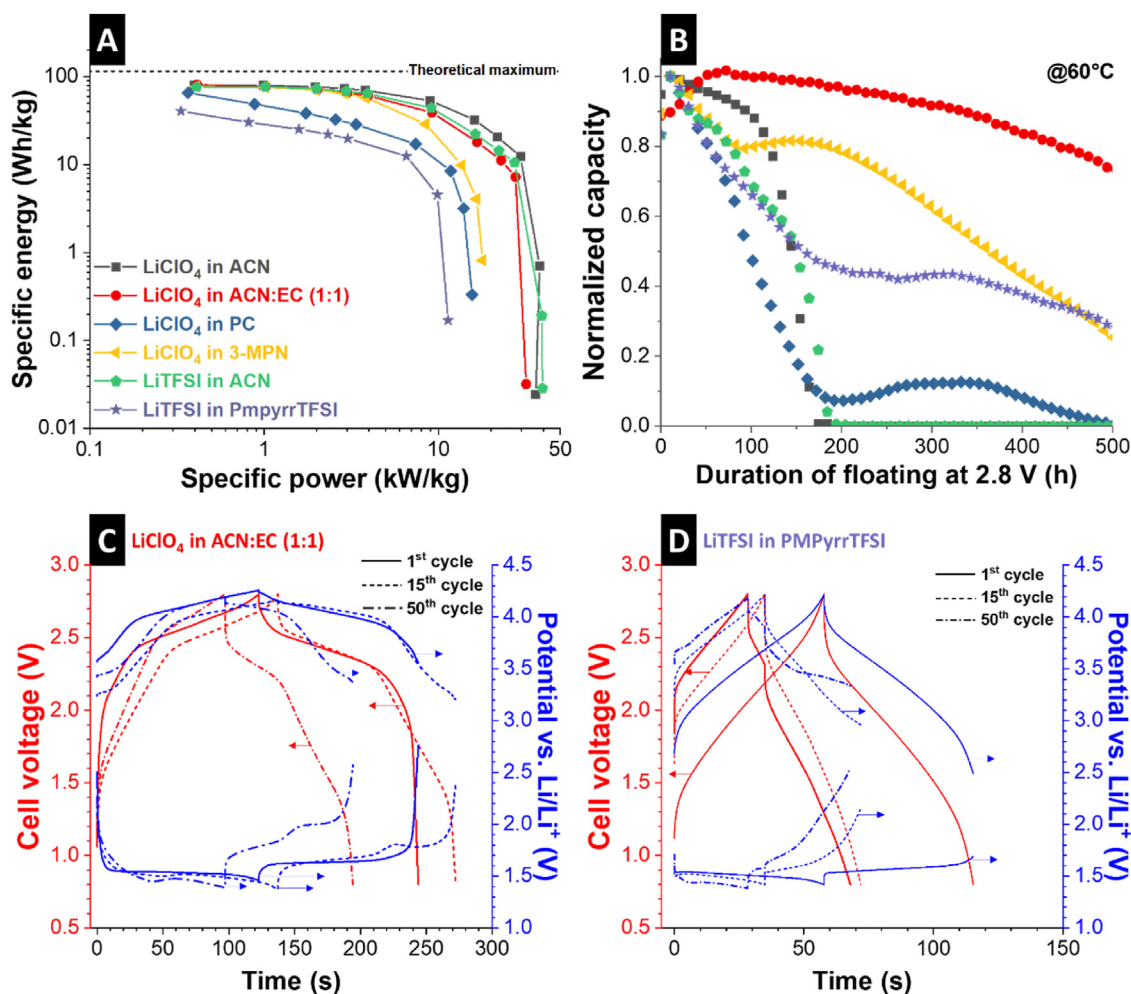


Fig. 4. The electrochemical characterization of the hybrid supercapacitors at +60 °C (A) Ragone chart of HSC cycled at 1C–250C between 0.8 and 2.8 V cell voltage. (B) The stability testing of 10 h voltage floating at charged state (2.8 V). The capacity values are obtained from the 3<sup>rd</sup> discharge step after the 10 h floating is finished. Voltage profile of HSC with (C) LiClO<sub>4</sub> in ACN:EC (1:1 by volume) and (D) LiTFSI in PMPyrrTFSI electrolytes after the 1<sup>st</sup> (solid line), the 15<sup>th</sup> (dashed line), and the 50<sup>th</sup> (dashed-dotted line) voltage floating cycle. The potential development of LTO and LMO-AC electrodes was monitored via a carbon quasi-reference electrode.

500 h voltage floating.

In Fig. 4C and D and Supporting Information, Fig. S5, the voltage profiles of the corresponding full-cell after 10 h, 150 h, and 500 h of voltage floating at 2.8 V is shown. As the voltage profiles of cathode and anode agree with the data at ambient temperature for the first cycle; however, after 150 h of voltage floating, the lithium insertion/extraction plateau for LTO starts to deviate with an increasing potential difference between lithiation and delithiation. The voltage profile of the LMO-AC cathode maintains the charge/discharge features very similar to what was observed in the test at +25 °C. Furthermore, significant changes in IR drop are observed for all cells as the voltage floating proceeds, concluding an increased resistance of the full-cells. The calculated resistances of ACN based electrolytes increased severely by two orders of magnitude as the capacity performances decay. LiClO<sub>4</sub> in ACN:EC (1:1) maintained the lowest resistance after the voltage floating which supports its promising performance. Despite the poor electrochemical stability of LiTFSI in ionic liquid, the resistance after 500 h of voltage floating only increased slightly compared to the initial value, which might be ascribed to the enhanced mobility at elevated temperature.

While being very promising for voltage floating at 2.8 V at room temperature, LiClO<sub>4</sub> in 3-MPN tested at +60 °C maintained only 25% of the initial capacity after 500 h of voltage floating (Supporting Information, Fig. S5C). The anode and cathode voltage profile of 3-MPN maintain the initial behavior. However, the voltage profile of the LTO electrode has changed over the voltage floating cycles, which was not observed at +75 °C. The capacity of electrolytes with PC decrease, like in the case of the ACN-based electrolytes.

Fig. 4D depicts the voltage profile of the full-cell with LiTFSI in PMPyrrTFSI electrolytes. Contradictory to the trend, the potential behavior of the LMO-AC electrode does not exhibit a normal two-slopes regime, but the presence of a single slope is indicating that LMO is electrochemically inactive for LiTFSI in PMPyrrTFSI. Therefore, the cell performance decreases significantly because of the imbalance in charge and potential distribution at each electrode. Seemingly, LMO is insufficiently stable in the chosen ionic liquid in general, but this issue most evidently manifests at elevated temperatures [67–70]. The structural degradation of LMO is also confirmed by post-mortem X-ray diffraction (Supporting Information, Fig. S6). Compared to the initial state, the cell constant *a* of LMO shifts from 0.821 nm to 0.811 nm after cycling at either +25 °C or +60 °C, with a lowered domain size from about 180 nm to 45–60 nm after cycling.

From the voltage floating performance of all the electrolytes at +60 °C, the best capacity retention after 50th cycles was found for LiClO<sub>4</sub> in ACN:EC (1:1) and LiClO<sub>4</sub> in 3-MPN. These two systems were then continued to be tested at +75 °C. As presented in Table 2, smaller energy performance is witnessed than compared to the measurement at +60 °C. The energy storage performance of the corresponding full-cells is depicted in Fig. 5A. The initial specific energy of both LiClO<sub>4</sub> in ACN:EC (1:1) and LiClO<sub>4</sub> in 3-MPN achieved ~71 Wh/kg with 81% energy efficiency. The corresponding specific capacity was 33 mAh/g, which is comparable to values obtained from the experiment at +60 °C. Despite the higher ionic conductivity at higher temperatures, the electrochemical performance diminishes, which aligns with the known high-temperature complications of LMO (such as Mn-ion dissolution above +55 °C) [70–72].

The voltage floating at a cell voltage of 2.8 V was subsequently conducted, and the results are presented in Fig. 5B. The initial increase in capacity is more pronounced when compared to +25 °C or +60 °C measurements for LiClO<sub>4</sub> in ACN:EC (1:1) electrolyte and the maximum capacity of 31 mAh/g is about 20% higher than the initial capacity of 26 mAh/g. The initial cathode voltage profile of

the cell with LiClO<sub>4</sub> in ACN:EC (1:1) electrolyte clearly consists of two regions originating from AC and LMO charge storage (Fig. 5C). After 150 h of voltage floating, the voltage profile assigned to lithium insertion into LMO decreases. After 250 h, the voltage pattern changes to display a trigonal shape not typical for LMO, but characteristic of the electrical double-layer formation. At a value of about 43% compared to the maximum capacity, we see the loss of charge storage contribution from LMO and dominance of just the AC component (which only provided charge storage via ion electrosorption).

LiClO<sub>4</sub> in 3-MPN achieved an initial capacity of 29 mAh/g with an energy efficiency of 72%, then continually decrease until 8% of the initial capacity after 250 h of voltage floating at 2.8 V. The voltage profile of LiClO<sub>4</sub> is shown in Fig. 5D, which is comparable to LiClO<sub>4</sub> in ACN:EC (1:1). After 250 h voltage floating, the profiles of both anode and cathode are different from its original voltage profiles. This finding indicates the loss of the cells' charge storage capacity.

### 3.4. Electrochemical performance at below-ambient temperature (−10 °C)

We quantified the electrochemical energy storage performance of the full-cells at −10 °C. The direct comparison of the Ragone plot at +25 °C (Fig. 3A) and −10 °C (Fig. 6A) shows the low energy and power performance of the full-cells at below ambient temperature. An electrochemical operation of the cell containing LiTFSI in PMPyrrTFSI was not possible due to its low ionic conductivity at −10 °C. The conductivity data (Fig. 2, Table 2) show the conductivities of electrolytes at −10 °C are 1–20 mS/cm lower than at +25 °C. This indicates the lower mobility of ions at −10 °C, which is in line with the measured energy storage performance. At 1C, LiClO<sub>4</sub> in ACN achieved the best specific energy of ~59 Wh/kg with a Coulombic efficiency and energy efficiency of 98% and 88%, respectively. At a higher rate of 10C, the specific energy remains lower than LiTFSI in ACN, which aligns with the non-linear drop of conductivity of LiClO<sub>4</sub> in ACN at below 0 °C (Fig. 2), due to the solvation of the solvent molecules and the solubility of the salt. Meanwhile, LiTFSI in ACN maintained a high power performance of 36 kW/kg at 250C.

The voltage floating test was conducted subsequently and depicted in Fig. 6B. Compared to the initial capacity before the 10 h voltage floating, all the electrolytes maintained more than 50% of the capacity (excluding LiClO<sub>4</sub> in ACN). LiClO<sub>4</sub> in 3-MPN and ACN:EC (1:1), as well as LiTFSI in ACN, showed an increase of capacity during the early cycles of 10 h voltage floating before the capacity starts to decay. During the voltage floating test at +25 °C and +60 °C, LiTFSI in ACN did not follow this trend. After reaching the maximum capacity, the cell provided high capacity retention (97%) after 500 h voltage floating compared to the maximum capacity. Coulombic and energy efficiency maintained a level of 98% and 80%, respectively. We expect this stability attributes from the suppression of an increase in internal resistance at low temperature (Supporting Information, Fig. S8). The overall initial resistance for cells tested at −10 °C were larger than ones at +25 °C as presented in Table S2 in Supporting Information. This agrees with the suppressed mobility, therefore lower conductivity compared to higher temperatures. However, the increase in resistance after the 500 h voltage floating test is negligible at −10 °C for LiTFSI in ACN, LiClO<sub>4</sub> in ACN:EC (1:1), and LiClO<sub>4</sub> in 3-MPN, which achieved the highest capacity retention.

The voltage profiles of the full-cell and the electrodes after 10 h, 150 h, and 500 h of voltage floating are presented in Fig. 6C and D and Supporting Information, Fig. S7. The duration of the charge/discharge reaction is shortened due to the decreased ion

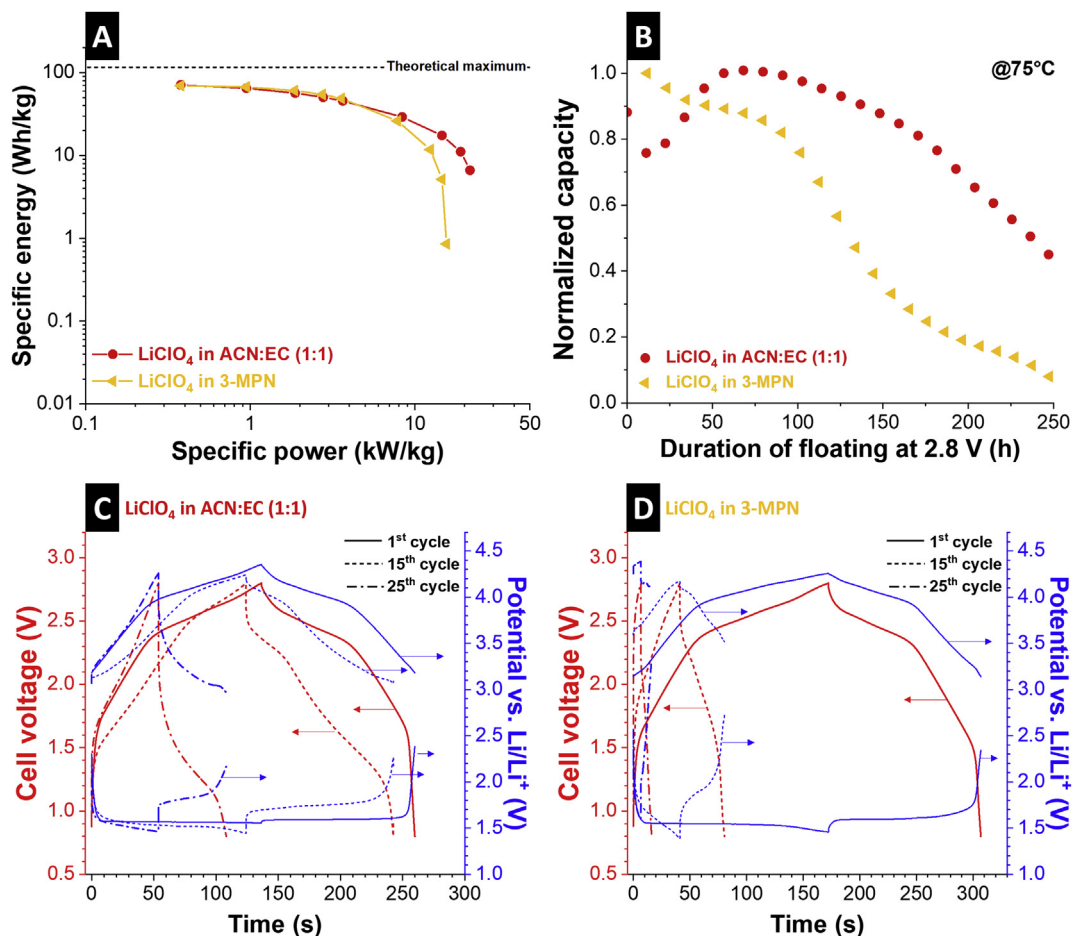


**Fig. 5.** The electrochemical characterization of the hybrid supercapacitors at +75 °C (A) Ragone chart at 1C–250C between 0.8 and 2.8 V cell voltage. (B) The stability testing of 10 h voltage floating at charged state (2.8 V). The capacity values are obtained from the 3<sup>rd</sup> discharge step after the 10 h floating is finished. Voltage profile of HSC with (C) LiClO<sub>4</sub> in ACN:EC (1:1 by volume) and (D) LiClO<sub>4</sub> in 3-MPN electrolytes after the 1<sup>st</sup> (solid line), the 15<sup>th</sup> (dashed line), and the 25<sup>th</sup> (dashed-dotted line) voltage floating cycle. The potential development of LTO and LMO-AC electrodes was monitored via a quasi-reference electrode.

conductivity at lower temperatures, but the overall shape of the initial voltage profiles maintained as comparable to +25 °C. LiClO<sub>4</sub> in 3-MPN achieved with 92% capacity retention after 500 h of voltage floating. Although the capacity retention was very high, the voltage profile depicted in Fig. 6D show distorted LMO-AC electrode behavior. The lithium insertion/extraction reaction hysteresis of the LTO electrode is also very broad, indicating overpotential. The diffusion of the Li<sup>+</sup> ion is significantly decreased at the LTO structure, resulting in increased polarization at a lower temperature [73]. Combination of hindered Li<sup>+</sup> diffusion at the electrode and low conductivity of the electrolyte, the overpotential shift at LTO is also significant for the cells showing rather poor stability with LiClO<sub>4</sub> in PC and LiClO<sub>4</sub> in ACN (*Supporting Information, Fig. S7*).

#### 4. Conclusions

In this study, we investigated the stability of different electrolytes for hybrid supercapacitor applications at ambient, above-ambient, and below-ambient temperatures. The nitrile and carbonate-based organic solvents and ionic liquid were employed for hybrid supercapacitors with a promising combination of anode and cathode materials, LTO and LMO [16,17,60]. LiClO<sub>4</sub> in ACN:EC (1:1) and 3-MPN achieved a stable performance during floating at

both above and below ambient temperature. At ambient temperature, LiClO<sub>4</sub> in 3-MPN showed an excellent electrochemical stability and remained 97% of its initial capacity after 500 h voltage floating at 2.8 V. LiClO<sub>4</sub> in ACN:EC (1:1) is superior at above ambient temperatures with 70% and 43% capacity retention at +60 °C and +75 °C after 500 h and 250 h of voltage floating, respectively, at 2.8 V. The use of only ACN as the solvent, at elevated potentials like 2.8 V is not preferred in this temperature range, considering the limited electrochemical stability.

An appropriate selection of lithium-containing salt and solvent can enhance the longevity of Li-ion hybrid supercapacitors. At high temperatures, there is the key issue of LMO degradation to be considered. The loss of charge storage capacity of the LMO cannot be compensated by the AC component in the hybrid cathode so that the overall cell degradation progresses. This issue is not remedied using an ionic liquid, which, itself, would provide excellent high-temperature stability. Instead, the best high-temperature performance stability was provided by LiClO<sub>4</sub> in ACN:EC (1:1), which shows the great potential of mixed solvents. At low temperatures, after several conditioning cycles, the best performance regarding energy, power, and stability, is obtained in LiTFSI in ACN. This aligns with the much higher ion mobility, which, at -10 °C, is the strongest limiting factor for the cell performance. LiClO<sub>4</sub> in ACN is to be

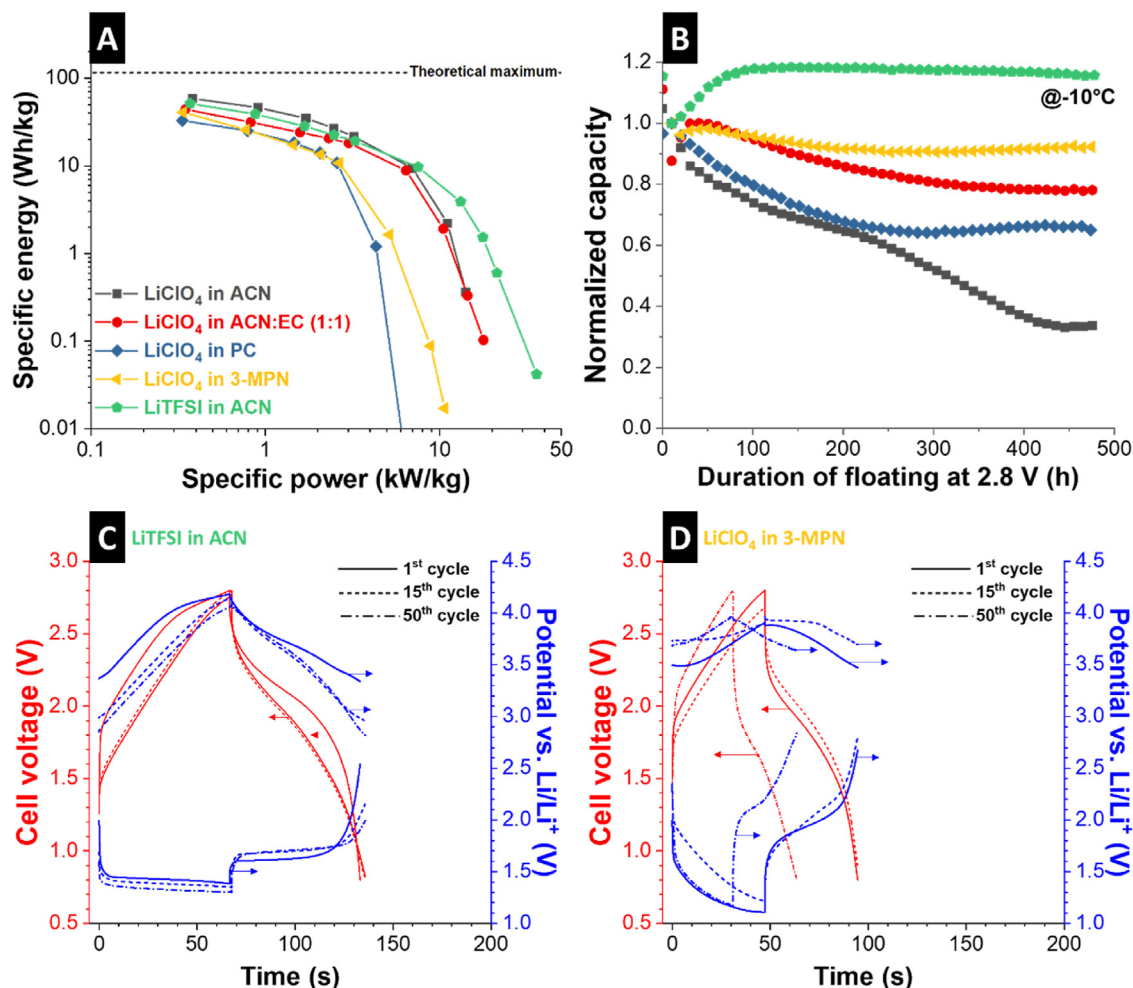


**Fig. 6.** The electrochemical characterization of the hybrid supercapacitors at  $-10\text{ }^{\circ}\text{C}$  (A) Ragone chart at 1C–250C between 0.8 and 2.8 V cell voltage. (B) The stability testing of 10 h voltage floating at charged state (2.8 V). The capacity values are obtained from the 3<sup>rd</sup> discharge step after the 10 h floating is finished. Voltage profile of HSC with (C) LiTFSI in ACN and (D) LiClO<sub>4</sub> in 3-MPN electrolytes before the 1<sup>st</sup> voltage floating cycle (solid line), and after the 15<sup>th</sup> (dashed line) and the 50<sup>th</sup> (dashed-dotted line) voltage floating. The potential development of LTO and LMO-AC electrodes was monitored via a quasi-reference electrode.

avoided at low temperatures because of the well-known solubility issues and solvate crystallization; these effects yield poor performance stability over time.

#### Declaration of competing interest

The authors declare that they have no known competing financial interests or personal relationships that could have appeared to influence the work reported in this paper.

#### CRediT authorship contribution statement

**H. Shim:** Investigation, Data curation, Visualization, Writing - original draft. **Ö. Budak:** Investigation, Data curation. **V. Haug:** Conceptualization, Writing - review & editing. **M. Widmaier:** Data curation, Writing - review & editing. **V. Presser:** Conceptualization, Data curation, Visualization, Writing - review & editing, Supervision.

#### Acknowledgments

The work at INM was part of the HyBaCap project supported by the German Federal Ministry for Economic Affairs and Energy

(BMW; award number 03 ET6113C). We thank Eduard Arzt (INM) for his continuing support. The authors thank D. Weirather-Köstner and M. Marinaro (ZSW) for support and access to conductivity measurements.

#### Appendix A. Supplementary data

Supplementary data to this article can be found online at <https://doi.org/10.1016/j.electacta.2020.135760>.

#### References

- [1] Z. Yang, J. Zhang, M.C.W. Kintner-Meyer, X. Lu, D. Choi, J.P. Lemmon, J. Liu, Electrochemical energy storage for green grid, *Chem. Rev.* 111 (2011) 3577–3613.
- [2] J.M. Tarascon, M. Armand, Issues and challenges facing rechargeable lithium batteries, *Nature* 414 (2001) 359.
- [3] P. Simon, Y. Gogotsi, B. Dunn, Where do batteries end and supercapacitors begin? *Science* 343 (2014) 1210–1211.
- [4] S. Fleischmann, A. Tolosa, V. Presser, Design of carbon/metal oxide hybrids for electrochemical energy storage, *Chem. Eur J.* 24 (2018) 12143–12153.
- [5] B. Dunn, H. Kamath, J.-M. Tarascon, Electrical energy storage for the grid: a battery of choices, *Science* 334 (2011) 928–935.
- [6] M. Armand, J.M. Tarascon, Building better batteries, *Nature* 451 (2008) 652–657.
- [7] P. Simon, Y. Gogotsi, Materials for electrochemical capacitors, *Nat. Mater.* 7 (2008) 845.

- [8] T. Brousse, D. Bélanger, J.W. Long, To be or not to be pseudocapacitive? *J. Electrochem. Soc.* 162 (2015) A5185–A5189.
- [9] M. Salanne, B. Rotenberg, K. Naoi, K. Kaneko, P.L. Taberna, C.P. Grey, B. Dunn, P. Simon, Efficient storage mechanisms for building better supercapacitors, *Nat. Energy* 1 (2016) 16070.
- [10] H. Shi, Activated carbons and double layer capacitance, *Electrochim. Acta* 41 (1996) 1633–1639.
- [11] D. Qu, H. Shi, Studies of activated carbons used in double-layer capacitors, *J. Power Sources* 74 (1998) 99–107.
- [12] A. Muzaffar, M.B. Ahamed, K. Deshmukh, J. Thirumalai, A review on recent advances in hybrid supercapacitors: design, fabrication and applications, *Renew. Sustain. Energy Rev.* 101 (2019) 123–145.
- [13] S. Fleischmann, M. Widmaier, A. Schreiber, H. Shim, F.M. Stiemke, T.J.S. Schubert, V. Presser, High voltage asymmetric hybrid supercapacitors using lithium- and sodium-containing ionic liquids, *Energy Storage Mater.* 16 (2019) 391–399.
- [14] G.G. Amatucci, F. Badway, A. Du Pasquier, T. Zheng, An asymmetric hybrid nonaqueous energy storage cell, *J. Electrochem. Soc.* 148 (2001) A930–A939.
- [15] P.W. Ruch, D. Cericola, A. Foelske-Schmitz, R. Kötz, A. Wokaun, Aging of electrochemical double layer capacitors with acetonitrile-based electrolyte at elevated voltages, *Electrochim. Acta* 55 (2010) 4412–4420.
- [16] D. Cericola, P. Novák, A. Wokaun, R. Kötz, Hybridization of electrochemical capacitors and rechargeable batteries: an experimental analysis of the different possible approaches utilizing activated carbon,  $\text{Li}_4\text{Ti}_5\text{O}_{12}$  and  $\text{LiMn}_2\text{O}_4$ , *J. Power Sources* 196 (2011) 10305–10313.
- [17] D. Cericola, R. Kötz, Hybridization of rechargeable batteries and electrochemical capacitors: principles and limits, *Electrochim. Acta* 72 (2012) 1–17.
- [18] K. Naoi, W. Naoi, S. Aoyagi, J.-i. Miyamoto, T. Kamino, New generation “nanohybrid supercapacitor”, *Acc. Chem. Res.* 46 (2013) 1075–1083.
- [19] E. Lim, C. Jo, J. Lee, A mini review of designed mesoporous materials for energy-storage applications: from electric double-layer capacitors to hybrid supercapacitors, *Nanoscale* 8 (2016) 7827–7833.
- [20] M. Widmaier, K. Pfeifer, L. Bommer, V. Presser, Valence-tuned lithium titanate nanopowder for high-rate electrochemical energy storage, *Batter. Supercaps* 1 (2018) 11–26.
- [21] M. Kerlau, M. Marcinek, V. Srinivasan, R.M. Kostecki, Studies of local degradation phenomena in composite cathodes for lithium-ion batteries, *Electrochim. Acta* 52 (2007) 5422–5429.
- [22] K. Naoi, S. Ishimoto, J.-i. Miyamoto, W. Naoi, Second generation ‘nanohybrid supercapacitor’: evolution of capacitive energy storage devices, *Energy Environ. Sci.* 5 (2012) 9363–9373.
- [23] J.S. Daubert, N.P. Lewis, H.N. Gotsch, J.Z. Mundy, D.N. Monroe, E.C. Dickey, M.D. Losego, G.N. Parsons, Effect of meso- and micro-porosity in carbon electrodes on atomic layer deposition of pseudocapacitive  $\text{V}_2\text{O}_5$  for high performance supercapacitors, *Chem. Mater.* 27 (2015) 6524–6534.
- [24] S. Fleischmann, A. Tolosa, M. Zeiger, B. Krüner, N.J. Peter, I. Grobelsek, A. Quade, A. Kruth, V. Presser, Vanadia-titania multilayer nanodecoration of carbon onions via atomic layer deposition for high performance electrochemical energy storage, *J. Mater. Chem.* 5 (2017) 2792–2801.
- [25] G. Li, X. Wang, X. Ma,  $\text{Nb}_2\text{O}_5$ -carbon core-shell nanocomposite as anode material for lithium ion battery, *J. Energy Chem.* 22 (2013) 357–362.
- [26] Ö. Budak, P. Srimuk, A. Tolosa, S. Fleischmann, J. Lee, S.W. Hieke, A. Frank, C. Scheu, V. Presser, Vanadium (III) oxide/carbon core/shell hybrids as an anode for lithium-ion batteries, *Batter. Supercaps* 2 (2019) 74–82.
- [27] K. Xu, Nonaqueous liquid electrolytes for lithium-based rechargeable batteries, *Chem. Rev.* 104 (2004) 4303–4418.
- [28] D. Aurbach, Y. Talyosef, B. Markovsky, E. Markevich, E. Zinigrad, L. Asraf, J.S. Gnanaraj, H.-J. Kim, Design of electrolyte solutions for Li and Li-ion batteries: a review, *Electrochim. Acta* 50 (2004) 247–254.
- [29] C. Zhong, Y. Deng, W. Hu, J. Qiao, L. Zhang, J. Zhang, A review of electrolyte materials and compositions for electrochemical supercapacitors, *Chem. Soc. Rev.* 44 (2015) 7484–7539.
- [30] F. Béguin, V. Presser, A. Balducci, E. Frackowiak, Carbons and electrolytes for advanced supercapacitors, *Adv. Mater.* 26 (2014) 2219–2251.
- [31] C. Schütter, S. Pohlmann, A. Balducci, Industrial requirements of materials for electrical double layer capacitors: impact on current and future applications, *Adv. Energy Mater.* 9 (2019), 1900334.
- [32] C. Schütter, T. Husch, V. Viswanathan, S. Passerini, A. Balducci, M. Korth, Rational design of new electrolyte materials for electrochemical double layer capacitors, *J. Power Sources* 326 (2016) 541–548.
- [33] A. Balducci, U. Bardi, S. Caporali, M. Mastragostino, F. Soavi, Ionic liquids for hybrid supercapacitors, *Electrochem. Commun.* 6 (2004) 566–570.
- [34] M. Schroeder, M. Winter, S. Passerini, A. Balducci, On the use of soft carbon and propylene carbonate-based electrolytes in lithium-ion capacitors, *J. Electrochem. Soc.* 159 (2012) A1240–A1245.
- [35] V. Khomenko, E. Raymundo-Piñero, F. Béguin, High-energy density graphite/AC capacitor in organic electrolyte, *J. Power Sources* 177 (2008) 643–651.
- [36] K. Xu, Electrolytes and interphases in Li-ion batteries and beyond, *Chem. Rev.* 114 (2014) 11503–11618.
- [37] A. Vlad, N. Singh, J. Rolland, S. Melinte, P.M. Ajayan, J.F. Gohy, Hybrid supercapacitor-battery materials for fast electrochemical charge storage, *Sci. Rep.* 4 (2014) 4315.
- [38] P.H. Smith, T.N. Tran, T.L. Jiang, J. Chung, Lithium-ion capacitors: electrochemical performance and thermal behavior, *J. Power Sources* 243 (2013) 982–992.
- [39] H. Wang, C. Zhu, D. Chao, Q. Yan, H.J. Fan, Nonaqueous hybrid lithium-ion and sodium-ion capacitors, *Adv. Mater.* 29 (2017), 1702093.
- [40] D. Aurbach, Y. Ein-Eli, B. Markovsky, A. Zaban, S. Luski, Y. Carmeli, H. Yamin, The study of electrolyte solutions based on ethylene and diethyl carbonates for rechargeable Li batteries: II. Graphite electrodes, *J. Electrochem. Soc.* 142 (1995) 2882–2890.
- [41] J.M. Tarascon, D. Guyomard, New electrolyte compositions stable over the 0 to 5 V voltage range and compatible with the  $\text{Li}_{1-x}\text{Mn}_2\text{O}_4$ /carbon Li-ion cells, *Solid State Ionics* 69 (1994) 293–305.
- [42] R. Jasinski, S. Carroll, Thermal stability of a propylene carbonate electrolyte, *J. Electrochem. Soc.* 117 (1970) 218–219.
- [43] B. Li, J. Zheng, H. Zhang, L. Jin, D. Yang, H. Lv, C. Shen, A. Shellikeri, Y. Zheng, R. Gong, J.P. Zheng, C. Zhang, Electrode materials, electrolytes, and challenges in nonaqueous lithium-ion capacitors, *Adv. Mater.* 30 (2018), 1705670.
- [44] B. Lee, J.R. Yoon, Influence of mixed solvent on the electrochemical property of hybrid capacitor, *J. Nanosci. Nanotechnol.* 15 (2015) 8849–8853.
- [45] D.M. Seo, O. Borodin, S.-D. Han, Q. Ly, P.D. Boyle, W.A. Henderson, Electrolyte solvation and ionic association, *J. Electrochem. Soc.* 159 (2012) A553–A565.
- [46] H. Yang, K. Kwon, T.M. Devine, J.W. Evans, Aluminum corrosion in lithium batteries an investigation using the electrochemical quartz crystal microbalance, *J. Electrochem. Soc.* 147 (2000) 4399–4407.
- [47] L.J. Krause, W. Lamanna, J. Summerfield, M. Engle, G. Korba, R. Loch, R. Atanasoski, Corrosion of aluminum at high voltages in non-aqueous electrolytes containing perfluoroalkylsulfonate imides; new lithium salts for lithium-ion cells, *J. Power Sources* 68 (1997) 320–325.
- [48] K. Matsumoto, K. Inoue, K. Nakahara, R. Yuge, T. Noguchi, K. Utsugi, Suppression of aluminum corrosion by using high concentration LiTFSI electrolyte, *J. Power Sources* 231 (2013) 234–238.
- [49] Q. Wang, S.M. Zakeeruddin, I. Exnar, M. Grätzel, 3-Methoxypropionitrile-based novel electrolytes for high-power Li-ion batteries with nanocrystalline  $\text{Li}_4\text{Ti}_5\text{O}_{12}$  anode, *J. Electrochem. Soc.* 151 (2004) A1598–A1603.
- [50] M. Widmaier, B. Krüner, N. Jäckel, M. Aslan, S. Fleischmann, C. Engel, V. Presser, Carbon as quasi-reference electrode in unconventional lithium-salt containing electrolytes for hybrid battery/supercapacitor devices, *J. Electrochem. Soc.* 163 (2016) A2956–A2964.
- [51] D. Weingarth, M. Zeiger, N. Jäckel, M. Aslan, G. Feng, V. Presser, Graphitization as a universal tool to tailor the potential-dependent capacitance of carbon supercapacitors, *Adv. Energy Mater.* 4 (2014), 1400316.
- [52] D.M. Seo, O. Borodin, S.-D. Han, P.D. Boyle, W.A. Henderson, Electrolyte solvation and ionic association II. Acetonitrile-lithium salt mixtures: highly dissociated salts, *J. Electrochem. Soc.* 159 (2012) A1489–A1500.
- [53] D.M. Seo, O. Borodin, D. Balogh, M. O’Connell, Q. Ly, S.-D. Han, S. Passerini, W.A. Henderson, Electrolyte solvation and ionic association III. Acetonitrile-lithium salt mixtures—transport properties, *J. Electrochem. Soc.* 160 (2013) A1061–A1070.
- [54] R.P. Seward, E.C. Vieira, The dielectric constants of ethylene carbonate and of solutions of ethylene carbonate in water, methanol, benzene and propylene carbonate, *J. Phys. Chem.* 62 (1958) 127–128.
- [55] D.M. Seo, S. Reininger, M. Kutcher, K. Redmond, W.B. Euler, B.L. Lucht, Role of mixed solvation and ion pairing in the solution structure of lithium ion battery electrolytes, *J. Phys. Chem. C* 119 (2015) 14038–14046.
- [56] C.A. Angell, D.L. Smith, Test of the entropy basis of the Vogel-Tammann-Fulcher equation. Dielectric relaxation of polyalcohols near  $T_g$ , *J. Phys. Chem.* 86 (1982) 3845–3852.
- [57] G. Tammann, W. Hesse, Die Abhängigkeit der Viskosität von der Temperatur bei unterkühlten Flüssigkeiten, *Z. Anorg. Allg. Chem.* 156 (1926) 245–257.
- [58] H. Vogel, Das temperaturabhängigkeitsgesetz der Viskosität von Flüssigkeiten, *Phys. Z.* 22 (1921) 645.
- [59] G.S. Fulcher, Analysis of recent measurements of the viscosity of glasses, *J. Am. Ceram. Soc.* 75 (1992) 1043–1055.
- [60] M. Widmaier, N. Jäckel, M. Zeiger, M. Abuzarli, C. Engel, L. Bommer, V. Presser, Influence of carbon distribution on the electrochemical performance and stability of lithium titanate based energy storage devices, *Electrochim. Acta* 247 (2017) 1006–1018.
- [61] Y. Li, F. El Gabaly, T.R. Ferguson, R.B. Smith, N.C. Bartelt, J.D. Sugar, K.R. Fenton, D.A. Cogswell, A.L.D. Kilcoyne, T. Tylliszczak, M.Z. Bazant, W.C. Chueh, Current-induced transition from particle-by-particle to concurrent intercalation in phase-separating battery electrodes, *Nat. Mater.* 13 (2014) 1149.
- [62] J.P. Southall, H.V.S.A. Hubbard, S.F. Johnston, V. Rogers, G.R. Davies, J.E. McIntyre, I.M. Ward, Ionic conductivity and viscosity correlations in liquid electrolytes for incorporation into PVDF gel electrolytes, *Solid State Ionics* 85 (1996) 51–60.
- [63] D. Weingarth, A. Foelske-Schmitz, R. Kötz, Cycle versus voltage hold – which is the better stability test for electrochemical double layer capacitors? *J. Power Sources* 225 (2013) 84–88.
- [64] T. Zhang, B. Fuchs, M. Secchiaroli, M. Wohlfahrt-Mehrens, S. Dsoke, Electrochemical behavior and stability of a commercial activated carbon in various organic electrolyte combinations containing Li-salts, *Electrochim. Acta* 218 (2016) 163–173.
- [65] S. Dsoke, B. Fuchs, E. Gucciardi, M. Wohlfahrt-Mehrens, The importance of the electrode mass ratio in a Li-ion capacitor based on activated carbon and  $\text{Li}_4\text{Ti}_5\text{O}_{12}$ , *J. Power Sources* 282 (2015) 385–393.
- [66] G. Hasegawa, K. Kanamori, T. Kiyomura, H. Kurata, K. Nakanishi, T. Abe, Hierarchically porous  $\text{Li}_4\text{Ti}_5\text{O}_{12}$  anode materials for Li- and Na-ion batteries: effects of nanoarchitectural design and temperature dependence of the rate

- capability, *Adv. Energy Mater.* 5 (2015), 1400730.
- [67] M. Egashira, A. Kanetomo, N. Yoshimoto, M. Morita, Charge-discharge rate of spinel lithium manganese oxide and olivine lithium iron phosphate in ionic liquid-based electrolytes, *J. Power Sources* 196 (2011) 6419–6424.
- [68] S. Seki, Y. Kobayashi, H. Miyashiro, Y. Ohno, A. Usami, Y. Mita, N. Kihira, M. Watanabe, N. Terada, Lithium secondary batteries using modified-imidazolium room-temperature ionic liquid, *J. Phys. Chem. B* 110 (2006) 10228–10230.
- [69] H. Seo, S. Na, B. Lee, T. Yim, S.H. Oh, Enhancement of surface stability of lithium manganese oxide spinel by silyl-group functionalized fluoride-responsive ionic liquid additives, *J. Ind. Eng. Chem.* 64 (2018) 311–317.
- [70] H. Zheng, H. Zhang, Y. Fu, T. Abe, Z. Ogumi, Temperature effects on the electrochemical behavior of spinel  $\text{LiMn}_2\text{O}_4$  in quaternary ammonium-based ionic liquid electrolyte, *J. Phys. Chem. B* 109 (2005) 13676–13684.
- [71] A. Bhandari, J. Bhattacharya, Review - manganese dissolution from spinel cathode: few unanswered questions, *J. Electrochem. Soc.* 164 (2017) A106–A127.
- [72] C. Zhan, J. Lu, A. Jeremy Kropf, T. Wu, A.N. Jansen, Y.-K. Sun, X. Qiu, K. Amine, Mn(II) deposition on anodes and its effects on capacity fade in spinel lithium manganate-carbon systems, *Nat. Commun.* 4 (2013) 2437.
- [73] T. Yuan, X. Yu, R. Cai, Y. Zhou, Z. Shao, Synthesis of pristine and carbon-coated  $\text{Li}_4\text{Ti}_5\text{O}_{12}$  and their low-temperature electrochemical performance, *J. Power Sources* 195 (2010) 4997–5004.

## Supporting Information

### **Comparison of organic electrolytes at various temperatures for 2.8 V-Li-ion hybrid supercapacitors**

**H. Shim,<sup>1,2</sup> Ö. Budak,<sup>1,2</sup> V. Haug,<sup>3</sup> M. Widmaier,<sup>2</sup> V. Presser<sup>1,2,\*</sup>**

<sup>1</sup> INM - Leibniz Institute for New Materials, 66123 Saarbrücken, Germany

<sup>2</sup> Department of Materials Science and Engineering, Saarland University, 66123 Saarbrücken, Germany

<sup>3</sup> Robert Bosch GmbH, Robert-Bosch-Campus 1, 71272 Renningen, Germany

\* Corresponding author's eMail: [volker.presser@leibniz-inm.de](mailto:volker.presser@leibniz-inm.de)

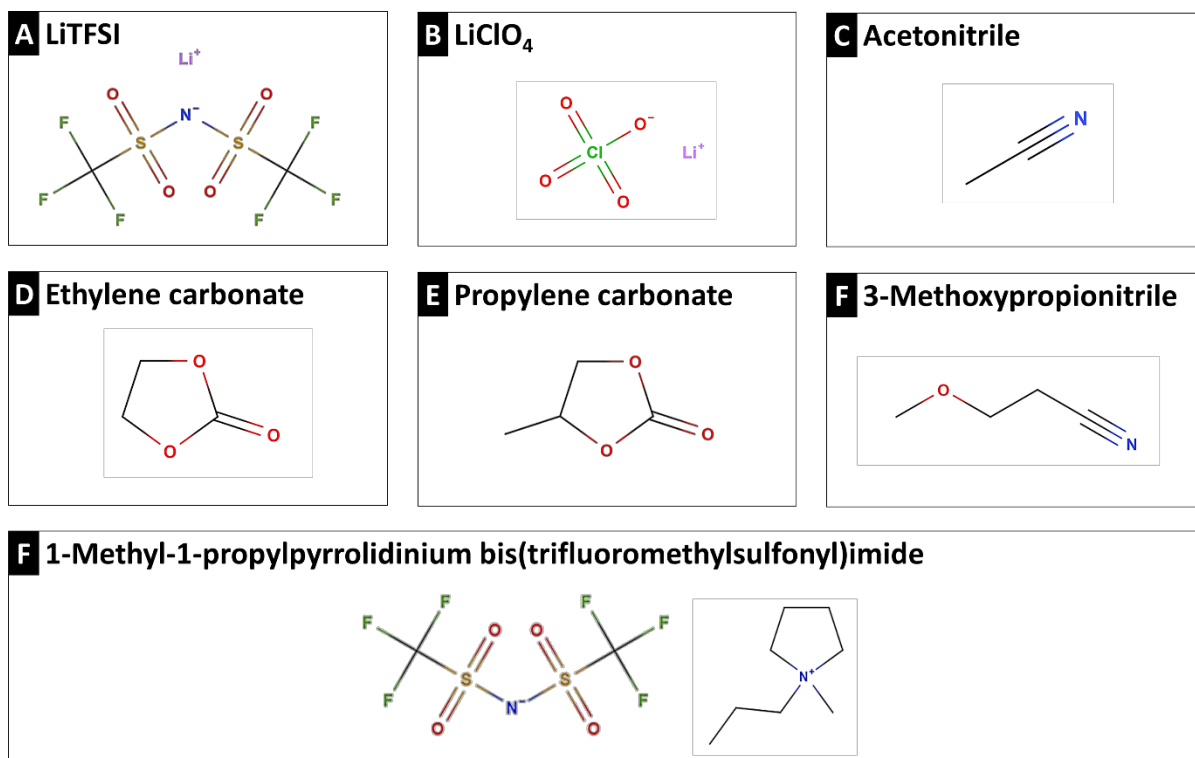


**Figure S1:** Chemical structures of the electrolytes and salts used in our work.

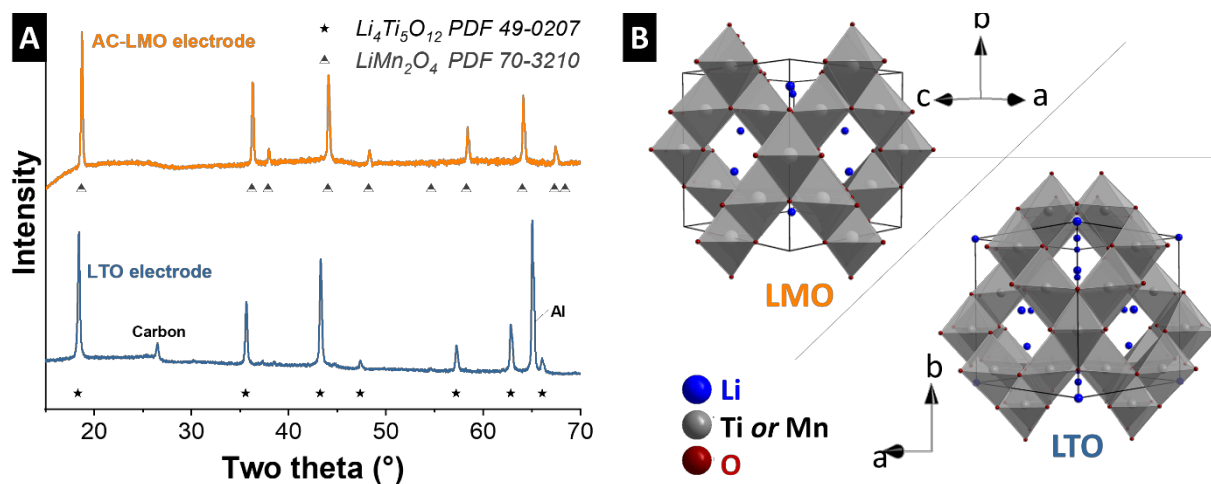


**Figure S2:** (A) X-ray diffraction pattern of the AC-LMO and LTO electrodes. The diffractograms were recorded with a Bruker AXS D8 Discover using Cu-K $\alpha$  radiation and a VANTEC detector. (B) Crystal structures of LMO and LTO per the PDF numbers given in panel A.

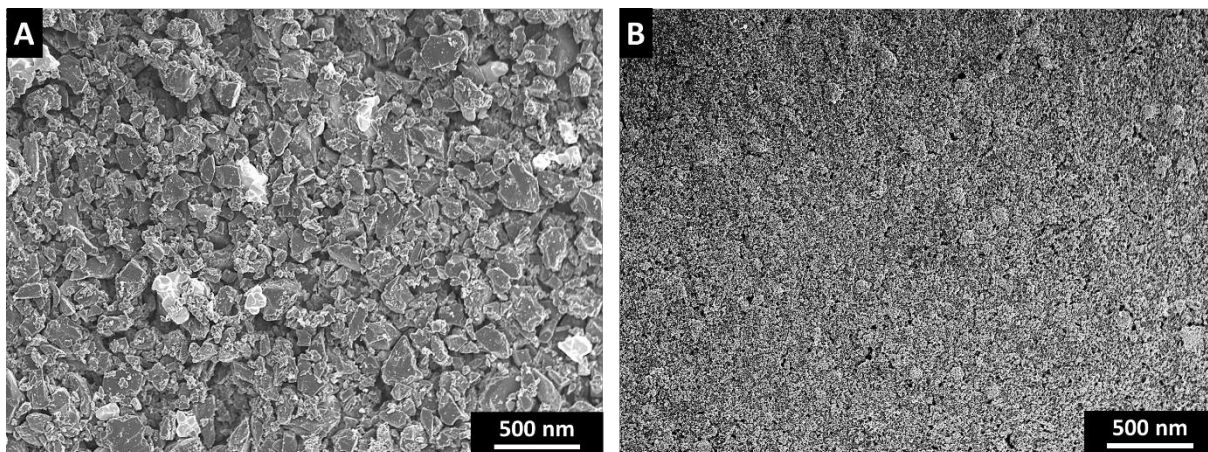


**Figure S3:** (A) Scanning electron micrograph of the AC-LMO electrode. (B) Scanning electron micrograph of the LTO electrode. Electron micrographs were recorded with a JEOL JSM-7500F at an acceleration voltage of 3 kV.

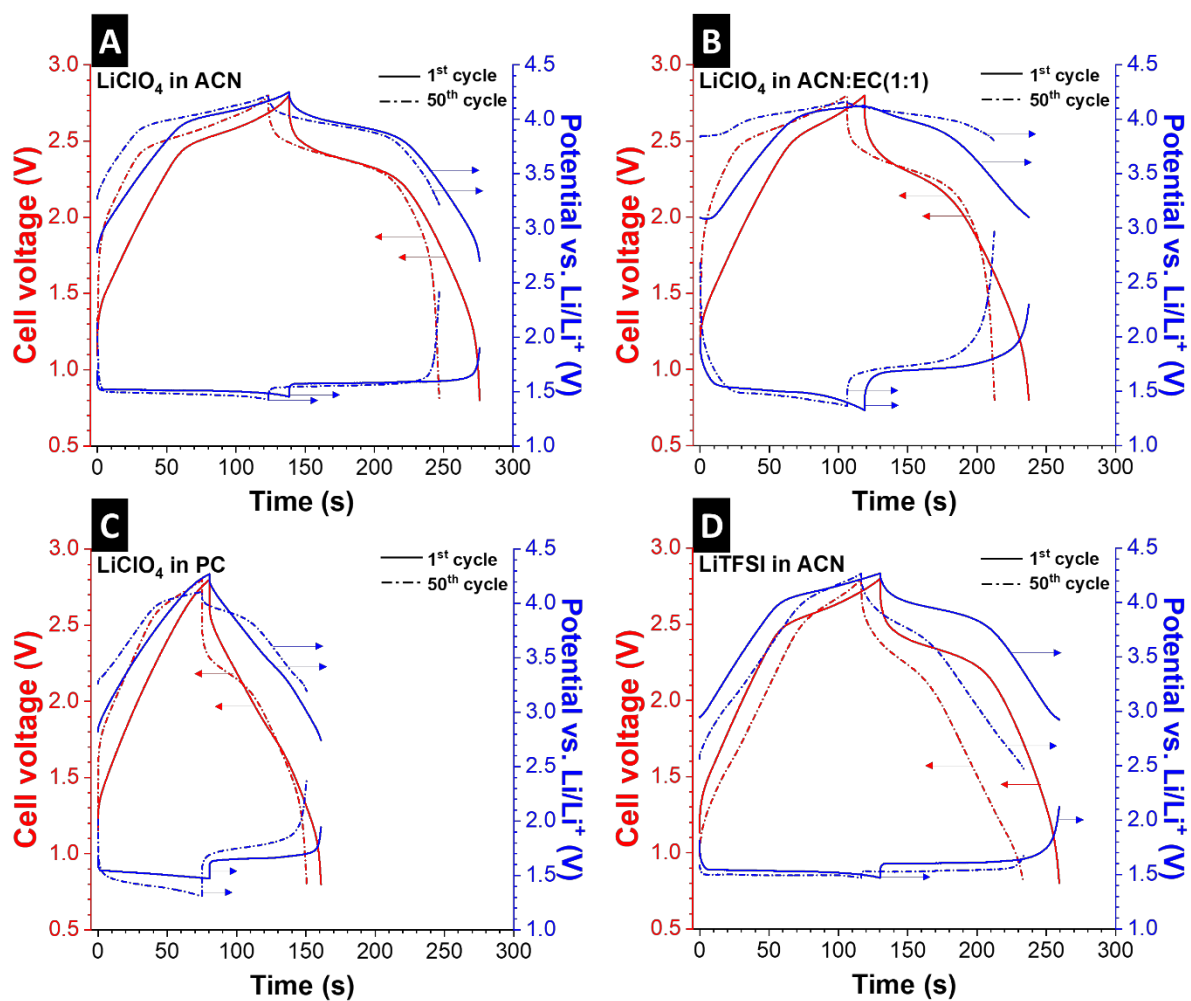


**Figure S4:** Galvanostatic charge/discharge profiles up to a cell voltage of 2.8 V at +25 °C after the 1<sup>st</sup> (solid line), and 50<sup>th</sup> (dashed-dotted line) voltage floating cycle. The potential development of LTO and LMO-AC electrodes were monitored via a carbon quasi-reference electrode.

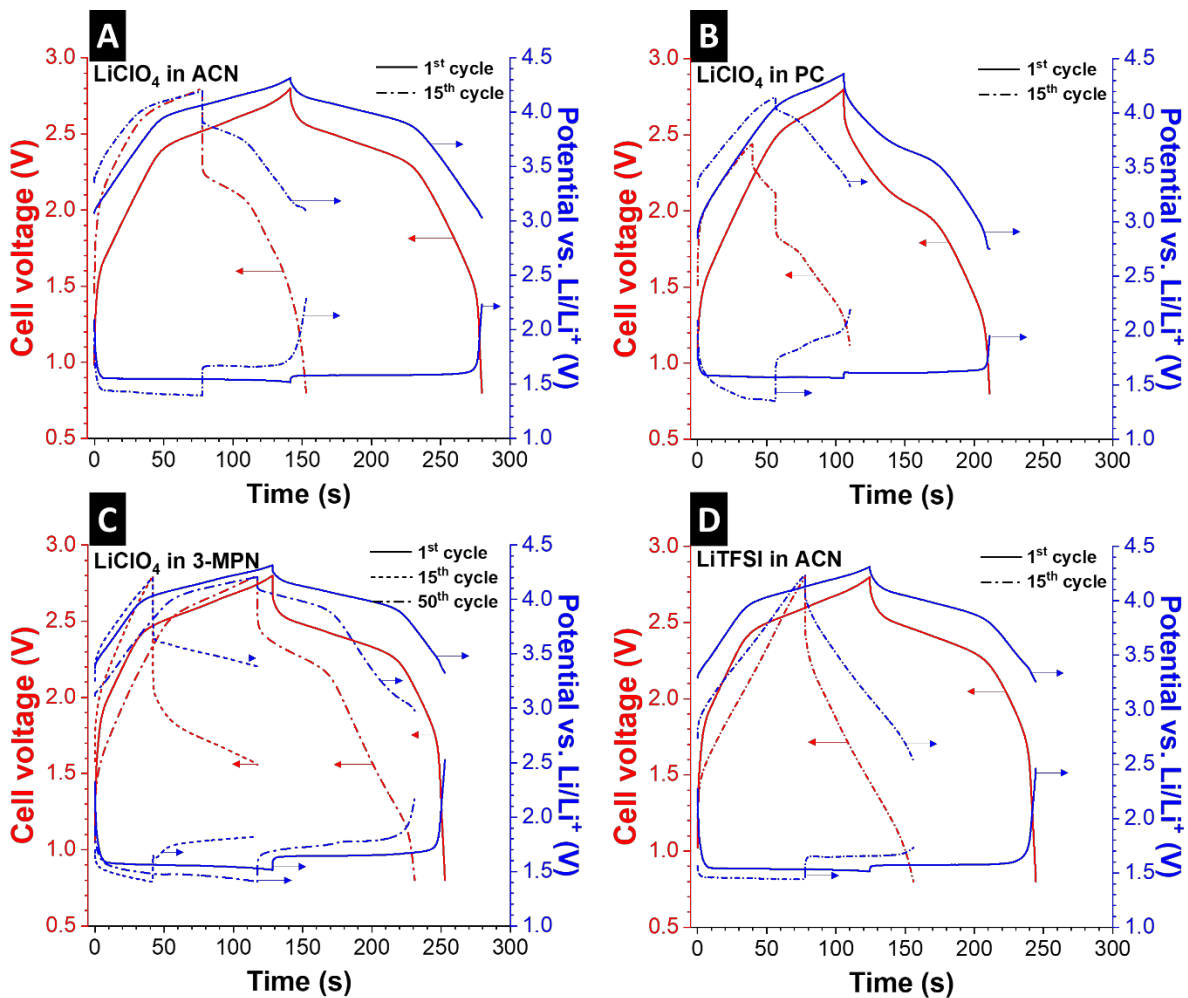


**Figure S5:** Galvanostatic charge/discharge profiles up to a cell voltage of 2.8 V at +60°C after the 1<sup>st</sup> (solid line), 15<sup>th</sup> (dashed line), and 50<sup>th</sup> (dashed-dotted line) voltage floating cycle. The potential development of LTO and LMO-AC electrodes were monitored via a carbon quasi-reference electrode.

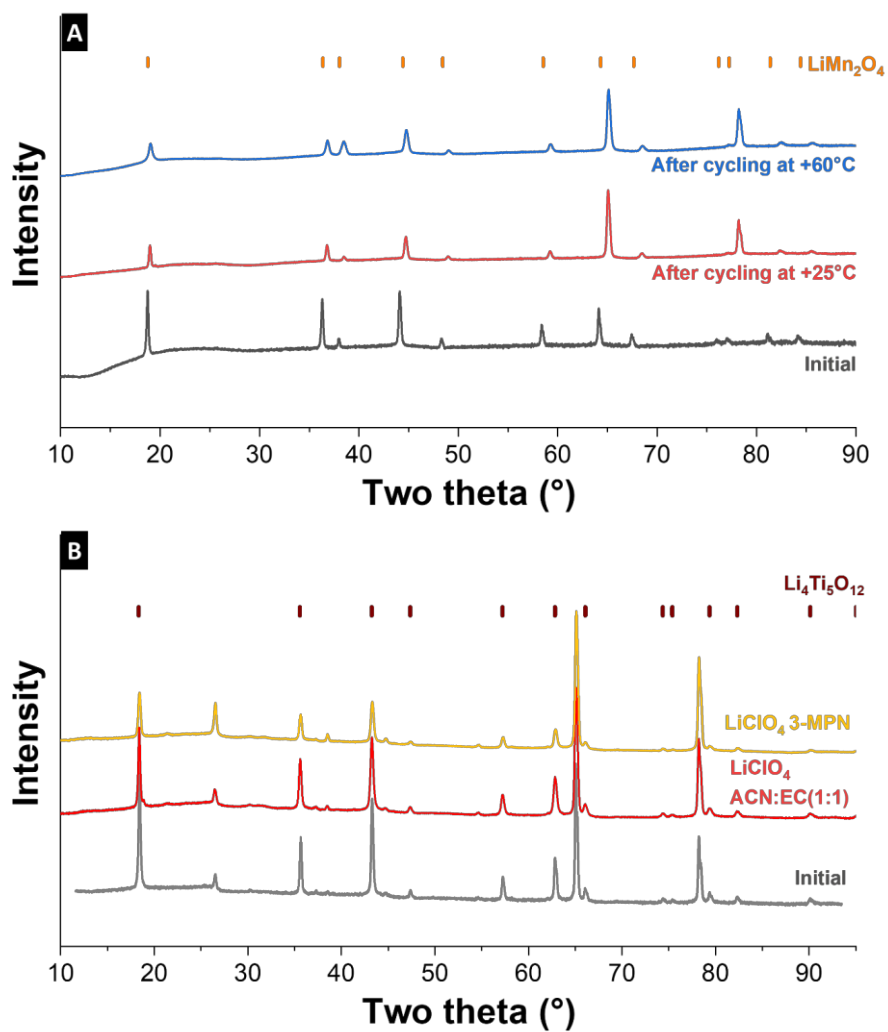


**Figure S6:** (A) X-ray diffraction pattern of the LMO electrode prior to testing and after cycling at +25 °C and at +60 °C (2.8 V cell voltage) using LiTFSI in PMPyrrTFSI. (B) X-ray diffraction pattern of the LMO electrode prior to testing and after cycling at +60 °C using LiClO<sub>4</sub> in 3-MPN and LiClO<sub>4</sub> in ACN:EC(1:1).

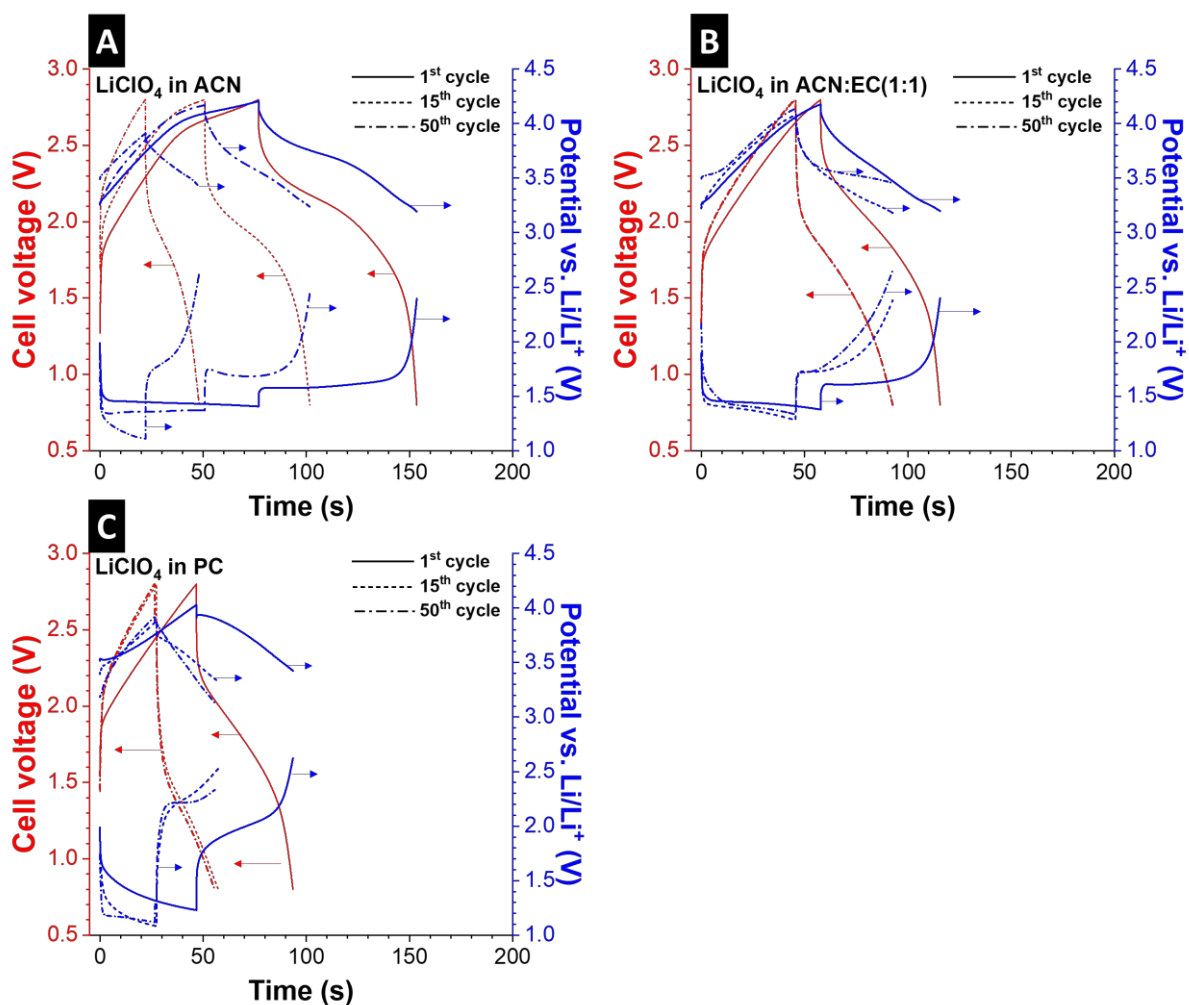


**Figure S7:** Galvanostatic charge/discharge profiles up to a cell voltage of 2.8 V at -10°C after the 1<sup>st</sup> (solid line), 15<sup>th</sup> (dashed line), and 50<sup>th</sup> (dashed-dotted line) voltage floating cycle. The potential development of LTO and LMO-AC electrodes were monitored via a carbon quasi-reference electrode.

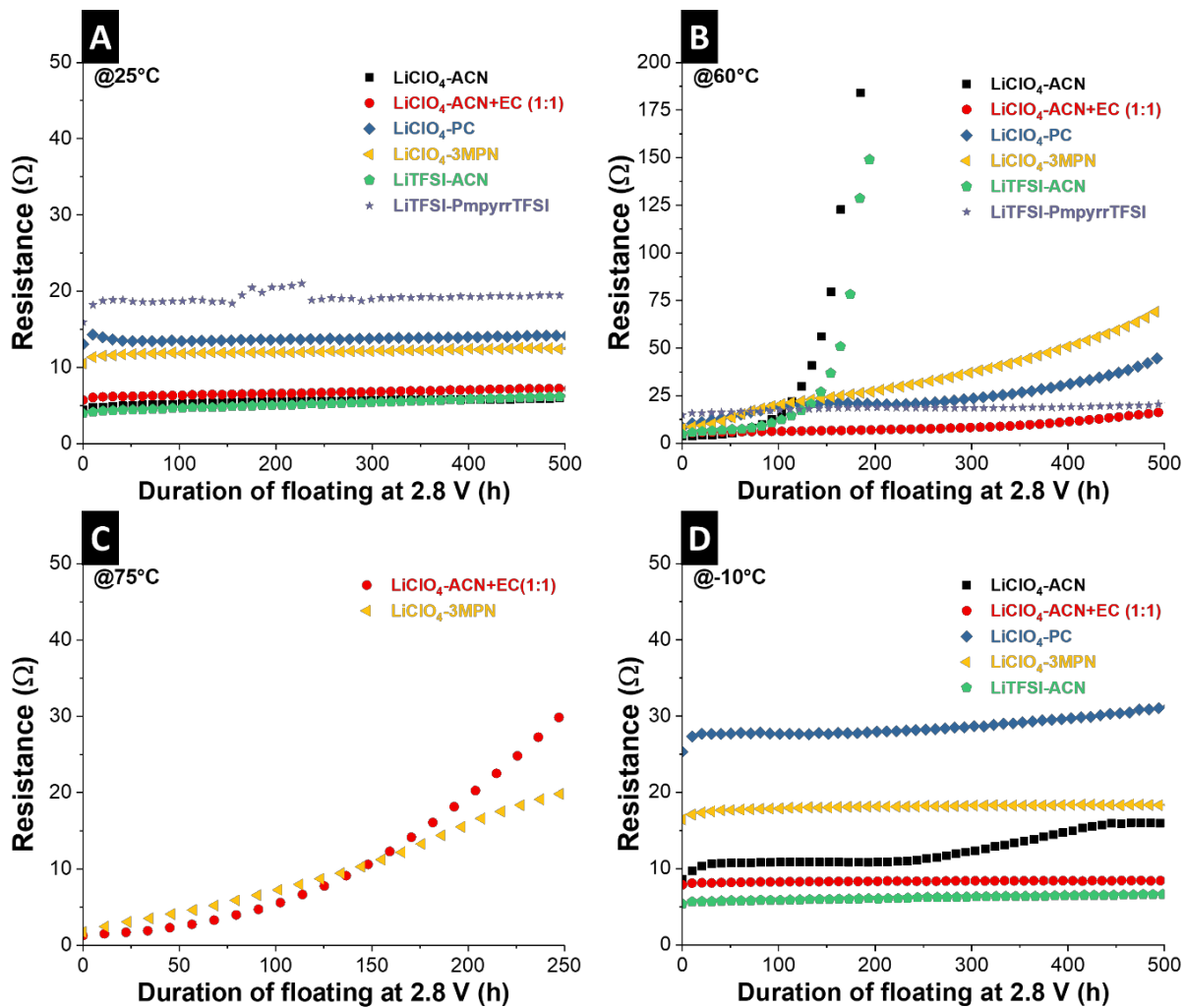


**Figure S8:** Resistance values calculated from the IR drop of galvanostatic charge/discharge from 10 h voltage floating test at (A) +25 °C, (B) +60 °C, (C) +75 °C, and (D) -10 °C. The resistance values are derived from the IR drop values of the 3<sup>rd</sup> discharge step after the 10 h floating is finished.

**Table S1:** The fitting constants obtained for the conductivity measurements.

Solvate	Solvent	A	B	T <sub>0</sub>	R <sup>2</sup>
1 M LiClO <sub>4</sub>	ACN	1311.2	68.5	224.7	>0.99
1 M LiClO <sub>4</sub>	ACN:EC	3286.5	408.9	123.7	>0.99
1 M LiClO <sub>4</sub>	PC	4129.7	647.8	129.8	>0.99
1 M LiClO <sub>4</sub>	3MPN	1821.4	445.5	136.1	>0.99
1 M LiTFSI	ACN	3781.8	351.3	109.2	>0.99
1 M LiTFSI	PMPyrrTFSI	37762.6	1197.1	141.4	>0.99

**Table S2:** The initial and the final resistance values ( $\Omega$ ) obtained from IR drop.

Solvate	Solvent	+25 °C		+60 °C		+75 °C		-10 °C	
1 M LiClO <sub>4</sub>	ACN	4.4	6.0	3.7	184	-	-	8.6	16.0
1 M LiClO <sub>4</sub>	ACN:EC	5.7	7.2	4.9	16.2	1.3	29.8	7.9	8.4
1 M LiClO <sub>4</sub>	PC	13.1	14.1	8.4	44.6	-	-	25.3	31.0
1 M LiClO <sub>4</sub>	3MPN	10.5	12.4	7.7	70.0	1.7	19.8	16.4	18.3
1 M LiTFSI	ACN	4.0	6.0	4.9	149	-	-	5.4	6.6
1 M LiTFSI	PMPyrrTFSI	15.9	19.4	14.8	20.53	-	-	-	-

# High voltage asymmetric hybrid supercapacitors using lithium-and sodium-containing ionic liquids

Simon Fleischmann,<sup>1,2</sup> Mathias Widmaier,<sup>2,3</sup> Anna Schreiber,<sup>1</sup> Hwirim Shim,<sup>1,2</sup>  
Frank M. Stiemke,<sup>4</sup> Thomas J. S. Schubert,<sup>4</sup> Volker Presser<sup>1,2</sup>

<sup>1</sup> INM - Leibniz Institute for New Materials, 66123 Saarbrücken, Germany

<sup>2</sup> Department of Materials Science and Engineering, Saarland University, 66123 Saarbrücken, Germany

<sup>3</sup> Robert Bosch GmbH, Robert-Bosch-Campus 1, 71272 Renningen, Germany

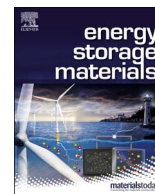
<sup>4</sup> IOLITEC Ionic Liquids Technologies GmbH, 74076 Heilbronn, Germany

## Citation:

S. Fleischmann, M. Widmaier, A. Schreiber, H. Shim, F. M. Stiemke, T. J. Schubert, & V. Presser. (2019). High voltage asymmetric hybrid supercapacitors using lithium- and sodium-containing ionic liquids. *Energy Storage Materials*, 16, 391-399.

## Own contributions:

Support with electrochemical measurements, critical discussion.



# High voltage asymmetric hybrid supercapacitors using lithium- and sodium-containing ionic liquids



Simon Fleischmann<sup>a,b</sup>, Mathias Widmaier<sup>b,c</sup>, Anna Schreiber<sup>a</sup>, Hwirim Shim<sup>a,b</sup>,  
Frank M. Stiemke<sup>d</sup>, Thomas J.S. Schubert<sup>d</sup>, Volker Presser<sup>a,b,\*</sup>

<sup>a</sup> INM - Leibniz Institute for New Materials, 66123 Saarbrücken, Germany

<sup>b</sup> Department of Materials Science and Engineering, Saarland University, 66123 Saarbrücken, Germany

<sup>c</sup> Robert Bosch GmbH, Robert-Bosch-Campus 1, 71272 Renningen, Germany

<sup>d</sup> IOLITEC Ionic Liquids Technologies GmbH, 74076 Heilbronn, Germany

## ARTICLE INFO

### Keywords:

Asymmetric hybrid supercapacitor  
lithium-ion capacitor  
sodium-ion capacitor  
lithium titanate  
ionic liquid  
battery-supercapacitor hybrid

## ABSTRACT

Asymmetric hybrid supercapacitors (AHSCs) combine high specific energy and power by merging two electrodes with capacitive and Faradaic charge storage mechanisms. In this study, we introduce AHSC cells that use lithium titanate and activated carbon electrodes in an alkali-ion containing ionic liquid electrolyte. With this cell concept, it is possible to operate the activated carbon electrode in a higher potential window. Consequently, higher cell voltages and a reduced carbon electrode mass can be used, resulting in significantly increased energy compared to aqueous or organic electrolytes. We demonstrate the feasibility of this cell concept for both lithium- and sodium-ion intercalation, underlining the general validity of our approach. Our prototype cells already reach high specific energies of 100 Wh/kg, while maintaining a specific power of up to 2 kW/kg and cycling stability of over 1500 cycles. Owing to the IL electrolyte, stable cycling of an AHSC at 80 °C is demonstrated for the first time.

## 1. Introduction

Electrical double-layer capacitors (EDLCs) are electrochemical energy storage devices that store charge by electrosorption of ions at high surface area carbon electrodes [1]. Despite their high specific power and longevity, the widespread use of EDLCs is limited by the low specific energy, owing to the purely physical charge storage mechanism. Many efforts to increase the specific energy of supercapacitors have focused on novel materials and innovative cell design by introducing Faradaic charge transfer to the capacitive system [2]. These approaches include the decoration of high surface area carbons with thin layers of Faradaic material [3–5], the use of redox-active electrolytes [6–8], composite electrodes combining these two charge storage mechanisms [9–11], or the utilization of an asymmetric hybrid supercapacitor cell design [12,13].

Asymmetric hybrid supercapacitors (AHSCs) employ one electrode storing charge by Faradaic reactions and another by capacitive double-layer formation. The aim is to synergistically combine the merits of battery and supercapacitor technologies, to produce cells that show higher specific energy than supercapacitors and higher specific power and longevity than batteries [14]. The most common types use a Li-ion

intercalating negative electrode material and an activated carbon positive electrode [14]. More recent studies also investigated sodium intercalating negative electrode materials, creating so-called sodium-ion capacitors [15–17]. Most commonly, the negative electrode of AHSCs shows a relatively constant operation potential at which intercalation occurs, whereas the positive electrode shows a linear, capacitor-like potential development. Consequently, the maximum cell voltage is determined by the difference between the intercalation potential of the negative electrode and the anodic stability limit of the electrolyte at the positive electrode.

Using organic electrolytes like Li-ion containing acetonitrile or carbonate mixtures, the anodic limit at the positive electrode is mostly found at around 4 V vs. Li<sup>+</sup>/Li [18–20]. The most frequently chosen negative electrode material for AHSCs is graphite due to its low Li-ion intercalation potential of around 0.2 V vs. Li<sup>+</sup>/Li [18]. This low intercalation potential is beyond the stability boundary of most electrolytes and requires the formation of the so-called solid electrolyte interphase (SEI) for stable cell operation [21]. Since SEI formation consumes Li-ions from the electrolyte, a prelithiation of the graphite electrode is required in a conventional AHSC cell due to the absence of a Li-containing positive electrode [18,22]. Further, the SEI layer limits

\* Corresponding author at: INM - Leibniz Institute for New Materials, 66123 Saarbrücken, Germany.  
E-mail address: [volker.presser@leibniz-inm.de](mailto:volker.presser@leibniz-inm.de) (V. Presser).

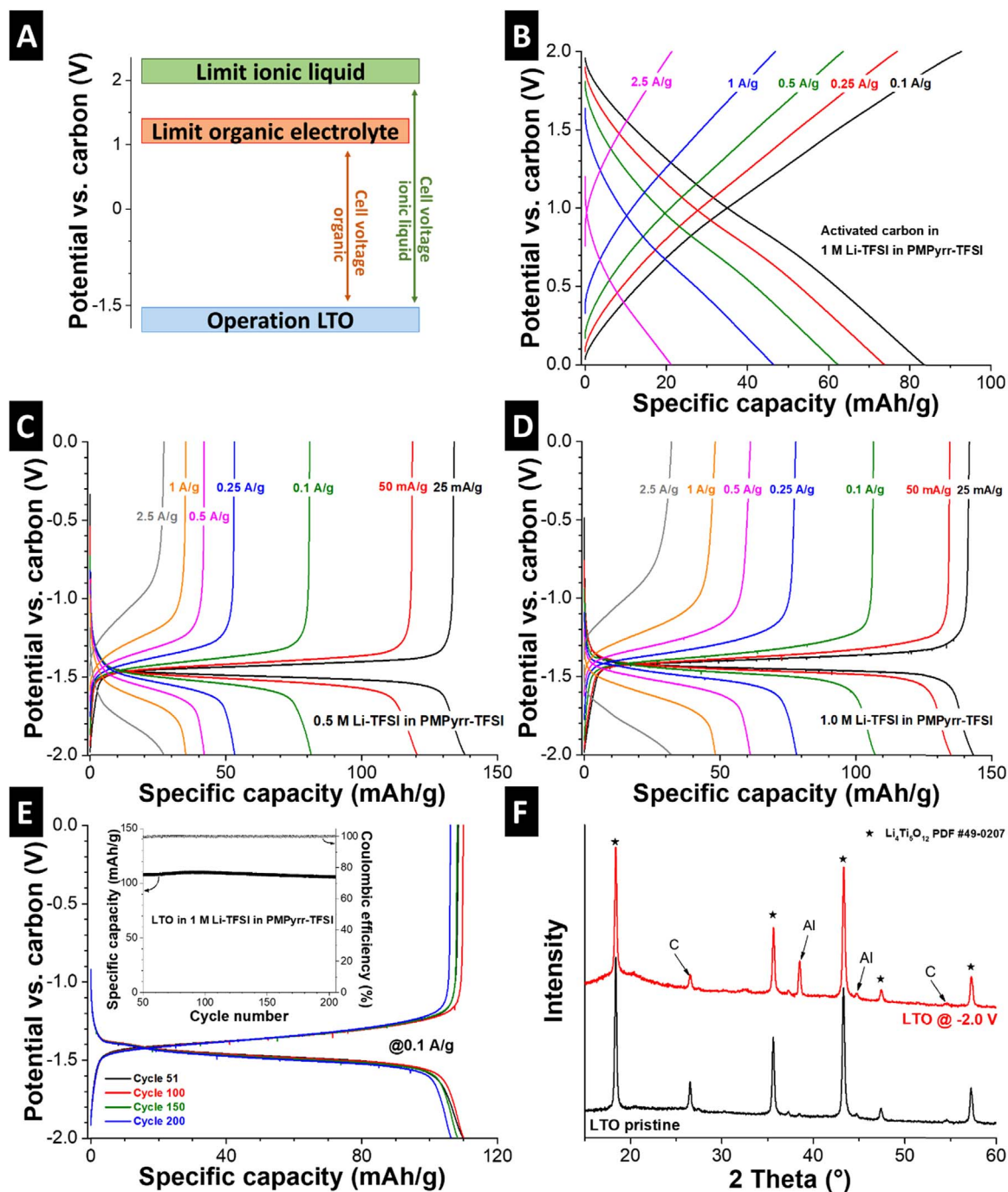


**Fig. 1.** Electrochemical and structural characterization of lithium half-cells. (A) Schematic representation of electrode potentials in an AHSC cell setup and the resulting maximum cell voltages depending on the electrolyte. Charge/discharge profiles of (B) activated carbon in 1 M Li-TFSI, (C) LTO in 0.5 M Li-TFSI, and (D) LTO in 1 M Li-TFSI electrolyte at different rates. (E) Charge/discharge profiles from the 51st to the 200th cycle of LTO in 1 M Li-TFSI at 0.1 A/g including specific capacity and Coulombic efficiency of every cycle in the inset. (F) X-ray diffractograms of pristine LTO electrode and ex situ measurement of fully lithiated LTO electrode in 1 M Li-TFSI electrolyte at -2.0 V vs. carbon.  $\text{Li}_4\text{Ti}_5\text{O}_{12}/\text{Li}_7\text{Ti}_5\text{O}_{12}$  signals are indicated by a star (PDF 49–0207), graphite- and Al-peaks originate from the current collector.

the power performance of the cell and can lead to dendrite formation at low operating temperatures or high charging rates [23]. The use of a negative electrode with a higher intercalation potential, like spinel lithium titanate (LTO,  $\text{Li}_4\text{Ti}_5\text{O}_{12}$ ), can effectively circumvent the necessity of SEI formation. Also, LTO is an attractive anode material for AHSCs because of its high rate capability, negligible volume change during intercalation and an intercalation potential of 1.55 V vs.  $\text{Li}/\text{Li}^+$  [24–26]. However, these advantages come at the cost of a drastic reduction of AHSC cell voltage to about 2.5 V in organic electrolytes (Fig. 1A), thereby exhibiting much smaller specific energies as comparable AHSCs using graphite as negative electrodes [18,27].

A well-known strategy to increase the specific energy of EDLCs is the use of ionic liquids (IL) as an electrolyte, as they offer larger stable potential windows compared to organic electrolytes [1,14]. Furthermore, their non-flammability, low volatility, and broad liquid temperature range greatly enhance the safety of the respective devices [28,29], and allow for stable cycling at elevated temperatures up to 100 °C [28,30]. ILs have also been employed as battery electrolytes to capitalize on their distinct temperature and safety features. Therefore, they employ either an alkali metal electrode as ion-source [31] or a dissolved alkali salt [32–34].

In this study, we employ such an IL electrolyte with dissolved

alkali-ions for an AHSC with a negative intercalation electrode for the first time. By synergistically combining the distinct virtues of ILs, a significant advance to state-of-the-art AHSC technology is achieved: (1) The anodic stability at the positive electrode is expanded, thereby increasing the maximum accessible cell voltage and, in turn, the specific energy of the AHSC (Fig. 1A). (2) Higher operation temperatures are enabled, which is important to applications in the mobility sector where elevated temperatures are encountered. (3) The cell safety is improved because of the non-flammability and low vapor pressure of the ionic liquid. We explore this strategy for AHSCs, using a positive activated carbon electrode and a negative lithium titanate electrode. We demonstrate 4 V AHSC devices with high electrochemical cycling stability using both lithium- or sodium-containing ILs. These cells also function at an elevated temperature of 80 °C, which is the first report of the stable high-temperature operation of any AHSC device employing intercalation reactions. Our proof-of-concept study employs solely commercially available materials, underlining the possibility of straightforward application and large innovation potential of this cell concept by use of improved electrode materials or electrolyte mixtures.

## 2. Materials and methods

### 2.1. Electrode and electrolyte preparation

Activated carbon (type YP-80F, Kuraray) was admixed with 5 mass % polytetrafluoroethylene (60 mass% aqueous solution, Sigma Aldrich) and ethanol in a pestle and mortar until a dough-like paste is obtained. The mass was formed in a hot-rolling machine to  $70 \pm 10 \mu\text{m}$  thick electrodes and dried in a vacuum oven overnight at 120 °C and 20 mbar. The material loading was  $2.5 \pm 0.5 \text{ mg/cm}^2$ . Additional information on the properties of the AC electrodes of type YP-80F is provided in Fig. S1.

For the preparation of LTO electrodes, lithium titanate (spinel  $\text{Li}_4\text{Ti}_5\text{O}_{12}$ , < 200 nm, Sigma Aldrich), carbon black (C-NERGY C65, Imerys Graphite & Carbon), and polyvinylidene fluoride (Solvay) were dissolved in dimethyl sulfoxide (Merck) with a mass ratio of 8:1:1 (dry mass) in a DAC400 FVZ speedmixer. Subsequently, the electrode slurry was doctor-bladed on a carbon-coated aluminum foil current collector (Ranafoil, Toyo Aluminium). The electrode sheets were dried for two days at ambient conditions in a fume hood, followed by drying in a vacuum oven at 120 °C and 20 mbar for 12 h. Dried electrodes typically possessed a thickness of  $25 \pm 5 \mu\text{m}$  with a material loading of  $3 \pm 1 \text{ mg/cm}^2$ .

All electrolytes used are based on the ionic liquid 1-methyl-1-propylpyrrolidinium bis(trifluoromethylsulfonyl)imide (PMPyrr-TFSA, Iolitec,  $\text{H}_2\text{O} < 10 \text{ ppm}$ ) which was dried with molecular sieves. For lithium-containing IL mixtures, lithium bis(trifluoromethylsulfonyl)imide (Li-TFSA, 99.9% purity, Iolitec) was used and for sodium-containing ILs, sodium bis(trifluoromethylsulfonyl)imide (Na-TFSA, 99.9% purity, Iolitec) was used. All reagents were transferred into an argon-filled glovebox (MBraun,  $\text{O}_2/\text{H}_2\text{O} < 1 \text{ ppm}$ ) through a connected vacuum furnace, where they were dried at 120 °C and 20 mbar for 24 h. Properties of the electrolyte as given by the supplier are listed in Table S1.

### 2.2. Materials characterization

X-ray diffraction was carried out with a D8 Discover (Bruker AXS) with a copper X-ray source, a Göbel mirror, a 0.5 mm point focus, and a 2-dimensional VANTEC500 detector that was placed at 20°, 40°, and 60°  $2\theta$  for 17 min at each measurement step.

### 2.3. Electrochemical characterization

All electrochemical measurements were conducted in custom-build three-electrode cells with a polyether ether ketone body and titanium

pistons, more information on these cells is given in Ref. [35]. In half-cell measurements, 12 mm discs of AC or LTO were used as working electrodes and an at least 15-times mass-oversized activated carbon (type YP-80F, Kuraray, 5 mass% PTFE-bound) was used as a counter electrode. In full-cells, we used 12 mm discs of activated carbon and 10 mm discs of LTO. To achieve the exact mass ratio needed, small pieces of the 12 mm activated carbon electrodes were removed. As a quasi-reference electrode, activated carbon (type YP-50F, Kuraray, 5 mass% PTFE-bound) was used, which is highly reliable in ionic liquid electrolytes [36]. It was beneficial to use the same quasi-reference for all cells to provide easier comparability between lithium- and sodium-containing cells. The potential difference between the used YP-50F quasi-reference and metallic lithium is determined to 3.09 V. As current collector, we used 12 mm discs of carbon-coated aluminum foil (type EQ-CC-Al-18u-260, MTI Corporation) for all activated carbon electrodes and the separator was a 13 mm glass-fiber mat (GF/D, Whatman). After cell assembly, they were dried in a vacuum oven at 120 °C overnight and transferred to an argon filled glovebox (MBraun,  $\text{O}_2/\text{H}_2\text{O} < 1 \text{ ppm}$ ), where they were filled with electrolyte.

Electrochemical measurements were carried out with a potentiostat/galvanostat (VMP-300, Bio-Logic) in a climate chamber at 25 °C or at 80 °C. Galvanostatic charge/discharge experiments were carried out at varying specific currents between 10 mA/g and 2.5 A/g, with 10 s resting after each half-cycle. The values are normalized to the active electrode mass, i.e., neglecting the PTFE binder in AC electrodes and neglecting carbon black and PVDF binder in LTO electrodes. AC half-cells with Li-TFSA electrolyte were first cycled at 0.1 A/g from 0 V to 1.2 V, 1.4 V, 1.6 V, 1.8 V, and 2.0 V vs. carbon, each step for 5 times, before being cycled between 0 V and 2.0 V vs. carbon at varying rates between 0.1 A/g and 2.5 A/g, 5 times for each rate. LTO half-cells with Li-TFSA electrolyte were cycled from 0 V to -2.0 V vs. carbon at rates of 25 mA/g to 2.5 A/g, each step for 5 times, before being cycled for 200 times in the same range at 0.1 A/g. LTO half-cells with Na-TFSA electrolyte were cycled from 0 V to -2.4 V vs. carbon at rates of 10 mA/g to 1 A/g, each step for 5 times, before being cycled for 200 times in the same range at 0.1 A/g.

The specific capacity  $C_{sp}$  in all half-cells was calculated according to Eq. (1):

$$C_{sp} = \frac{\int_{t_0}^t I dt}{m} \quad (1)$$

with current  $I$ , duration of the delithiation/desodiation/desorption step  $t-t_0$ , and  $m$  the active electrode mass as defined above.

Li-AHSC cells were assembled with an AC: $\text{Li}_4\text{Ti}_5\text{O}_{12}$  active mass ratio of 1.5:1. Galvanostatic cycling was carried out by charge/discharge at different rates between 10 mA/g to 1 A/g between 1 V and 4 V. Each charging/discharging step was repeated 5 times, with 10 s resting after each half-cycle. Na-AHSC cells employed an active mass ratio AC: $\text{Li}_4\text{Ti}_5\text{O}_{12}$  of 1.2:1 and were cycled at the same rates as Li-AHSCs. Cycling stability was tested by galvanostatic cycling at 0.1 A/g for Na-AHSC cells and at 0.2 A/g for Li-AHSC cells, since they initially exhibited about the same specific energy at these rates. All normalizations are calculated with respect to the sum of active masses of both electrodes, i.e., of activated carbon and  $\text{Li}_4\text{Ti}_5\text{O}_{12}$  masses, excluding PTFE, PVDF and carbon black in the LTO electrode. The specific energy  $E_{sp}$  of the cells was calculated by numeric integration according to Eq. (2):

$$E_{sp} = \frac{I \int_{t_0}^t U(t) dt}{M} \quad (2)$$

where  $I$  is the current,  $U(t)$  the voltage profile during the discharge step,  $t-t_0$  the discharge time and  $M$  the sum of active masses of both electrodes. The specific power was calculated by dividing  $E_{sp}$  by the discharge time, the energy efficiency by dividing  $E_{sp}$  by the energy spent in the charging step, and the Coulombic efficiency by dividing the charge delivered in the discharge step by the charge spent in the charging step.

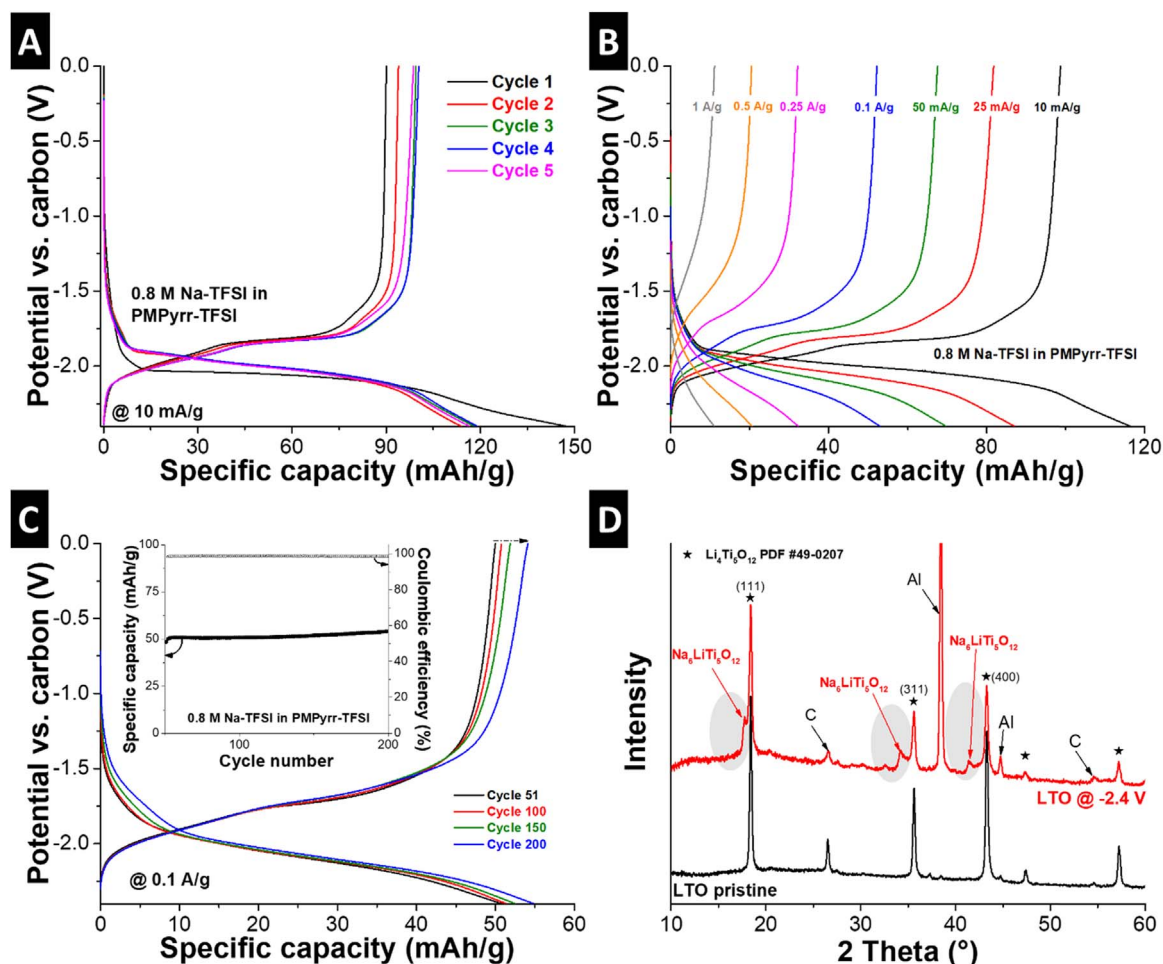


**Fig. 2.** Electrochemical and structural characterization of sodium half-cells. Charge/discharge profiles of LTO in 0.8 M Na-TFSI in PMPyrr-TFSI electrolyte (A) for the first five cycles at 10 mA/g, (B) at different rates and (C) from the 51th to 200th cycle at 0.1 A/g, including specific capacity and Coulombic efficiency of every cycle in the inset. (D) X-ray diffractograms of pristine LTO electrode and ex situ measurement of the fully sodiated LTO electrode in 0.8 M Na-TFSI electrolyte at  $-2.4$  V vs. carbon.  $\text{Li}_4\text{Ti}_5\text{O}_{12}$ / $\text{Li}_7\text{Ti}_5\text{O}_{12}$  signals are indicated by a star (PDF 49–0207), the  $\text{Na}_6\text{LiTi}_5\text{O}_{12}$  phase developed as a shoulder towards lower  $2\theta$  is highlighted; graphite- and Al-signals labeled accordingly originate from the current collector.

### 3. Results and discussion

#### 3.1. Lithium half-cells

Lithium-containing electrolytes were prepared by dissolving lithium bis(trifluoromethylsulfonyl)imide (Li-TFSI) in 1-methyl-1-propylpyrrolidinium bis(trifluoromethylsulfonyl)imide (PMPyrr-TFSI) to obtain 0.5 M and 1 M solutions. The anodic stability limits of the lithium-containing electrolytes with activated carbon electrodes (AC) were evaluated in a half-cell setup. The 1 M IL mixture still showed 90% Coulombic efficiency at 2.0 V vs. carbon (equal to 5.09 V vs.  $\text{Li}^+/\text{Li}$ ), which enables stable cycling for EDLCs [37,38]. The potential profiles of AC in 1 M Li-TFSI electrolyte show a linear, capacitor-like behavior between 0 V and 2.0 V vs. carbon, with a capacity of around 80 mAh/g at 0.1 A/g (Fig. 1B). Further details of AC performance can be found in Supplemental Information (Fig. S2 and Fig. S3).

LTO electrodes were employed and the lithium intercalation behavior was evaluated as a function of the Li-TFSI concentration. In 0.5 M Li-TFSI electrolyte, a maximum specific capacity of 138 mAh/g is measured at a rate of 25 mA/g and 81 mAh/g at 0.1 A/g (Fig. 1C). In 1 M Li-TFSI electrolyte, a similar maximum capacity of 143 mAh/g is exhibited, while the rate handling with 108 mAh/g at 0.1 A/g is far superior compared to 0.5 M Li-TFSI electrolyte (Fig. 1D, Fig. S4A). The hysteresis between lithiation and delithiation reactions is extremely narrow and remains below 100 mV at a rate of 25 mA/g. A narrow hysteresis is important to achieve high energy efficiency on an AHSC

device level [39,40]. Both electrolyte mixtures show a maximum capacity that is similar to comparable literature [41] and close to the theoretical capacity of LTO (175 mAh/g for fully lithiated  $\text{Li}_7\text{Ti}_5\text{O}_{12}$ ) [42] with a high Coulombic efficiency of 99.0% at 25 mA/g, suggesting high compatibility of the IL electrolytes with LTO. The superior rate handling of 1 M Li-TFSI electrolyte implies that the Li-ion conductivity in the 1 M mixture is higher compared to 0.5 M. Higher Li-TFSI concentration increases the viscosity of the electrolyte mixture, leading to lower overall ion mobility. However, Li-ion mobility has a much greater impact on the rate performance of the LTO electrode. Further optimization work for the electrolyte formulation to achieve a perfect balance between general conductivity and Li-ion mobility, possibly with other ILs or mixtures thereof, should be conducted in the future. The cycling stability of LTO electrodes in 1 M Li-TFSI electrolyte was tested by galvanostatic cycling at 0.1 A/g (Fig. 1E). The shape of the voltage profiles remains unchanged, and the specific capacity only shows a minor fading from initially 108 mAh/g to 106 mAh/g after 200 cycles. The Coulombic efficiency remains at 99.8%, underlining high stability of the system in 1 M Li-TFSI electrolyte.

To study the intercalation mechanism of lithium ions from the IL electrolyte, XRD measurements were conducted to compare a fully charged with a pristine LTO electrode (Fig. 1F). A comparison of both diffractograms reveals signals at identical positions, where spinel  $\text{Li}_4\text{Ti}_5\text{O}_{12}$  can be identified according to PDF 49–0207. LTO is known as a so-called zero-strain material, and the transformation from  $\text{Li}_4\text{Ti}_5\text{O}_{12}$  to  $\text{Li}_7\text{Ti}_5\text{O}_{12}$  during lithiation occurs with only 0.2% volume

change [42]. Our XRD data with unchanged LTO peak positions and the straight voltage profile suggest that the lithiation mechanism does not change in Li-ion containing IL as compared to the conventional organic electrolytes. Undesired co-intercalation of IL cations into the LTO crystal structure is therefore unlikely.

### 3.2. Sodium half-cells

An emerging alternative to lithium-ion technology is the use of sodium-ion intercalating materials [43]. This motivated us to expand our AHSC cell concept to sodium-containing IL by replacing Li-TFSI with sodium bis(trifluoromethylsulfonyl)imide (Na-TFSI). We use a 0.8 M solution of Na-TFSI in PMPyrr-TFSI, which we determined to be the maximum soluble Na-TFSI concentration in the IL at ambient conditions. LTO has been employed as anode material in sodium-ion batteries with organic carbonate electrolytes and showed a sodiation potential of around 0.9 V vs. Na<sup>+</sup>/Na [44–46]. This relatively high sodiation potential might circumvent SEI formation compared to other typical sodium-ion anode materials like hard carbon [47]. So far, sodium-ion intercalation in LTO from an IL electrolyte has not been reported. Using a 0.8 M Na-TFSI electrolyte, we observed an initial intercalation potential of around –2.0 V vs. carbon at a rate of 10 mA/g with a maximum specific capacity of 100 mAh/g, showing a relatively flat plateau and a first cycle Coulombic efficiency of 61.2% (Fig. 2A, Fig. S4B).

Sodium-ion intercalation in Li<sub>4</sub>Ti<sub>5</sub>O<sub>12</sub> from organic electrolytes is expected to follow a three-phase mechanism with the formation of a lithium-rich phase Li<sub>7</sub>Ti<sub>5</sub>O<sub>12</sub> and a sodium-rich phase Na<sub>6</sub>LiTi<sub>5</sub>O<sub>12</sub> during sodiation [44]. Low efficiency in the first cycle is known from organic electrolytes and was linked to structural rearrangements of the LTO crystal structure [46,48]. Over the next cycles, the onset of sodiation slightly shifts to a more positive potential of –1.85 V vs. carbon and the specific capacity increases, indicating that initial conditioning facilitates further sodiation reactions (Fig. 2A) [46]. The increased sodiation potential of the second cycle and subsequent cycles indicates the absence of SEI formation since the charge transfer resistance of the SEI would have shifted the sodiation towards more negative potentials. Rate handling tests at increased currents showed a capacity of 53 mA h/g at 0.1 A/g with a Coulombic efficiency of 98.5% (Fig. 2B). LTO showed stable cycling performance in the sodium-containing IL, exhibiting a slightly increased capacity of 54 mA h/g after 200 cycles at 0.1 A/g with a Coulombic efficiency over 98% (Fig. 2C).

We used XRD to examine the intercalation mechanism of sodium from IL electrolyte into LTO (Fig. 2D). The diffractogram of sodiated LTO confirms the formation of the sodium-rich Na<sub>6</sub>LiTi<sub>5</sub>O<sub>12</sub> phase by broad reflections located at slightly lower 2θ than the Li<sub>4</sub>Ti<sub>5</sub>O<sub>12</sub>/Li<sub>7</sub>Ti<sub>5</sub>O<sub>12</sub> signals. These shoulders are visible below the (111), (311), and (400) reflections at around 18.4°, 35.6°, and 43.2° 2θ, respectively. At the same time, the main reflections of the Li<sub>4</sub>Ti<sub>5</sub>O<sub>12</sub>/Li<sub>7</sub>Ti<sub>5</sub>O<sub>12</sub> phase are observed, confirming the presence of at least two separate phases in the sodiated state. This behavior aligns with sodium-ion intercalation in LTO in organic electrolytes [44,45] and shows that sodiation occurs according to the same mechanism for IL electrolyte.

### 3.3. AHSC full-cells

AHSC full-cells were assembled with LTO as a negative electrode and activated carbon as a positive electrode. For AHSCs employing lithium intercalation (Li-AHSC), we chose 1 M Li-TFSI in PMPyrr-TFSI electrolyte, sodium-AHSCs (Na-AHSC) used 0.8 M Na-TFSI in PMPyrr-TFSI electrolyte. The voltage profile of a Li-AHSC cell cycled between 1.0 V and 4.0 V at 50 mA/g is shown in Fig. 3A. The cell exhibits very small overpotential of the lithiation reaction and efficient utilization of the charge distributed to the two electrodes, resulting in the high energy efficiency of 74%. This performance demonstrates that the

promising electrochemical properties measured in half-cells can successfully be transferred to a Li-AHSC full cell employing IL electrolyte (further characterization in Supplemental Information, Fig. S6).

In Fig. 3B, the voltage profile of a Na-AHSC cell cycled between 1.0 V and 4.0 V cell voltage range at 25 mA/g is provided, also showing a symmetric profile with high energy efficiency of 75%. In case of the Na-AHSC cell, special consideration has to be paid to the structural rearrangements in LTO during the first cycles (Fig. S6B). The irreversible charge consumed during this process at the negative electrode must be balanced at the positive activated carbon electrode. Therefore, in the following cycles, the maximum accessible potential window of 2 V vs. carbon is not fully used.

We tested the galvanostatic cycling stability of Li-AHSCs between 1.0 V and 4.0 V cell voltage at a rate of 0.2 A/g (Fig. 3C). During the first cycles, a slight drop from about 36 Wh/kg to 32.5 Wh/kg is observed, before a continuing recovery over the next about 800 cycles back to 36 Wh/kg is exhibited. The fluctuations during the first cycles are associated with common side-reactions, which originate from impurities of electrode materials or IL electrolyte, leading to shifting operation potentials of the electrodes relative to each other. The Li-AHSC cell provides performance stability over 1,500 cycles, with only minor fading to 32.9 Wh/kg (91% retention). Cycling stability of the Na-AHSC cell (Fig. 3C) showed a significant increase in specific energy from about 35 Wh/kg to 44 Wh/kg during the first 50 cycles. Similar to half-cells, we expect the initial rearrangements inside the LTO particles during the three-phase intercalation reaction being the main cause for the increased capacity [46]. During subsequent cycles, the specific energy of Na-AHSC cells slowly decreases to about 24 Wh/kg after 1,500 cycles, corresponding to a retention of 69% of the initial energy. The lower stability compared to Li-AHSCs can be related to the increased mechanical stresses during sodiation and desodiation, owing to the high ionic radius of sodium ions (1.06 Å) [49]. Considering the use of commercially available LTO particles as an electrode material, the observed stability of our novel cell concept is very promising. By use of further optimized electrode materials, for example, by use of nanohybrid electrode materials [4,50], we expect a further improved stability.

The performance metrics of the AHSC cells are shown in a Ragone plot comparing specific energy and specific power (Fig. 3D), with the corresponding energy efficiency and Coulombic efficiency given in Fig. 3E. The specific energy of the Li-AHSC cell ranges from 98 Wh/kg to 10 Wh/kg at specific powers between 23 W/kg and 1.93 kW/kg. The Na-AHSC cell shows comparable results with a specific energy between 90 Wh/kg and 5.4 Wh/kg at a specific power of 26 W/kg and 1.78 kW/kg. The corresponding energy efficiencies reach 78% with the most efficient operation of both devices at a current between 50 mA/g and 0.25 A/g, where Coulombic efficiencies are nearly 100%, demonstrating high reversibility. Comparison with the state-of-the-art literature on AHSCs using AC as a positive electrode and a titanate-based negative electrode with organic electrolytes, it is confirmed that our cell concept significantly increases the energy of devices using both lithium- or sodium-intercalation (Fig. 3D, Table 1) [17,19,51,52]. We also provide a comparison using our Li-AHSC cell with 1 M LiClO<sub>4</sub> in acetonitrile electrolyte (Fig. 3D, Fig. S7, Table 1). The specific energy can be increased by more than a factor of three by use of IL electrolytes compared to the same electrodes in an organic electrolyte. However, the rather large viscosity of IL electrolytes at room temperature limits the resulting power performance. A cell employing acetonitrile at room temperature can deliver higher power.

### 3.4. High-temperature operation

IL electrolytes offer high safety because of their non-flammability and enable operation at elevated temperatures [53]. We demonstrate that these features can be transferred to our IL AHSC cell concept. Therefore, Li-AHSC cells are evaluated at a temperature of 80 °C. The

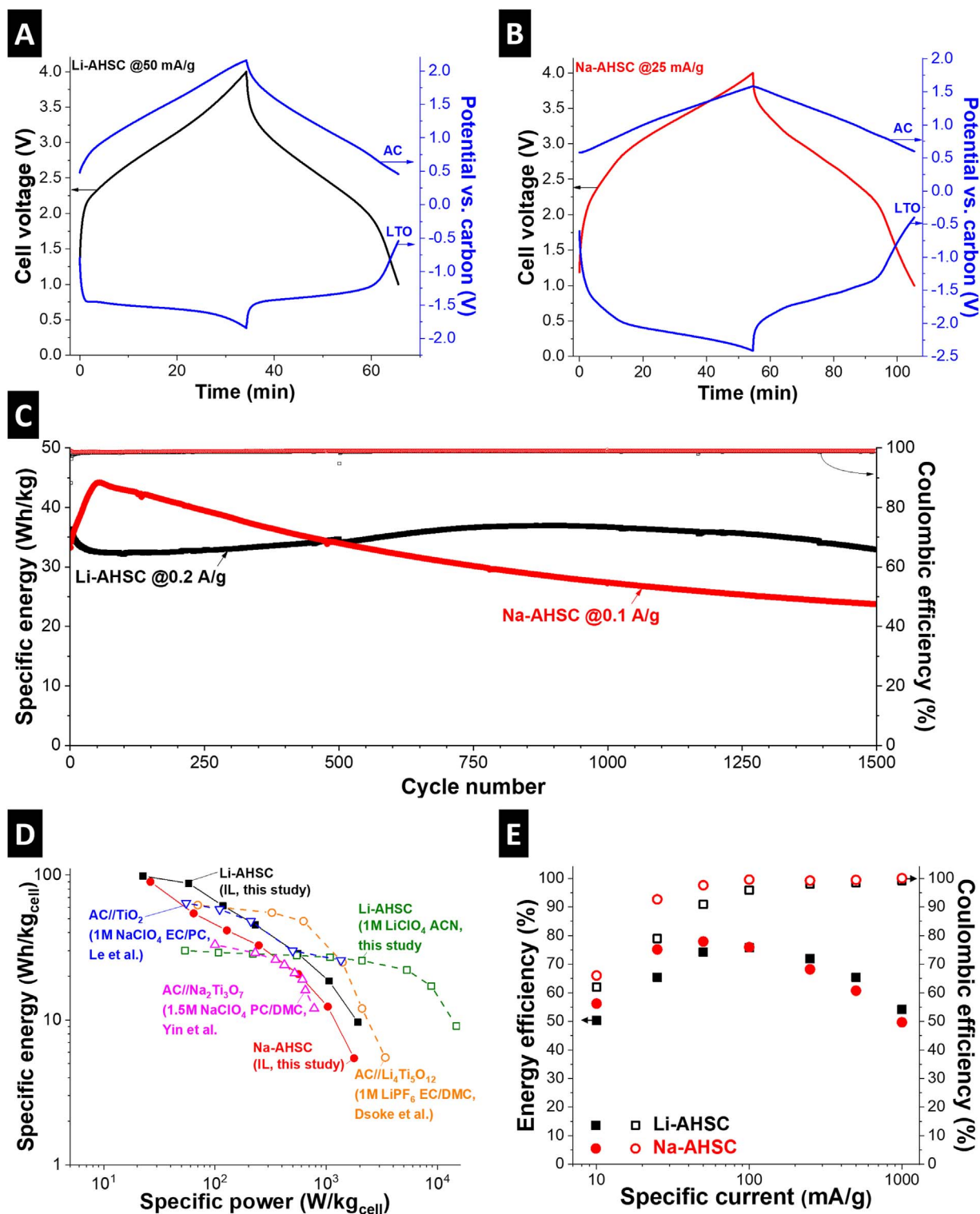


**Fig. 3.** Electrochemical characterization of AHSC full-cells. Voltage profiles of (A) Li-AHSC cell cycled at 50 mA/g and (B) Na-AHSC cell cycled at 25 mA/g, including potential development at negative LTO electrode and positive AC electrode monitored via quasi-reference spectator electrode. (C) Cycling stability of Li-AHSC cell cycled at 0.2 A/g, and Na-AHSC cell cycled at 0.1 A/g over 1500 cycles between 1 V and 4 V cell voltage. (D) Ragone chart of Li-AHSC and Na-AHSC cells cycled at rates between 10 mA/g and 1 A/g between 1 V and 4 V cell voltage with a comparison to literature (Refs [17,19,51].) and Li-AHSC cell with the same electrode materials filled with 1 M LiClO<sub>4</sub> in acetonitrile (ACN) electrolyte. (E) Energy efficiency and Coulombic efficiency of Li-AHSC and Na-AHSC cells.

power of the cells is highly increased because of the enhanced mobility of ions in the electrolyte. The voltage profile of a Li-AHSC cell cycled at 2.5 A/g is shown in Fig. 4A. With a limitation of the maximum cell voltage to 3.2 V, the positive electrode showed stable, linear potential development between 0 V and 1.2 V vs. carbon. At the same time, the

negative LTO electrode showed relatively constant lithiation plateaus around  $-1.4$  V vs. carbon. The latter value is 50 mV above the onset of lithiation at 25 °C, indicating a reduced barrier for intercalation at 80 °C (in agreement with Nernst equation). At this rate and temperature, the specific energy reached 37.5 Wh/kg at a high specific power of

**Table 1**

Comparison of AHSC cell performance with IL electrolytes and organic electrolytes, including comparable literature employing titanate-based anodes for lithium- or sodium-intercalation.

Negative electrode	Positive electrode	Electrolyte	Specific energy (Wh kg <sup>-1</sup> )	Specific power (kW kg <sup>-1</sup> )	Maximum cell voltage (V)	References
Li <sub>4</sub> Ti <sub>5</sub> O <sub>12</sub>	AC	1 M Li-TFSI in PMPyrr-TFSI	98	1.9	4.0	This work
Li <sub>4</sub> Ti <sub>5</sub> O <sub>12</sub>	AC	0.8 M Na-TFSI in PMPyrr-TFSI	90	1.8	4.0	This work
Li <sub>4</sub> Ti <sub>5</sub> O <sub>12</sub>	AC	1 M LiClO <sub>4</sub> in ACN	30	14.8	2.5	This work
Li <sub>4</sub> Ti <sub>5</sub> O <sub>12</sub>	AC	1 M LiPF <sub>6</sub> in EC/DMC	62	3.4	2.8	[19]
Li <sub>4</sub> Ti <sub>5</sub> O <sub>12</sub>	AC	1.5 M NaClO <sub>4</sub> in PC/DMC	33	0.78	3.0	[17]
Li <sub>4</sub> Ti <sub>5</sub> O <sub>12</sub>	AC	1 M NaClO <sub>4</sub> in EC/PC	64	1.36	3.8	[51]

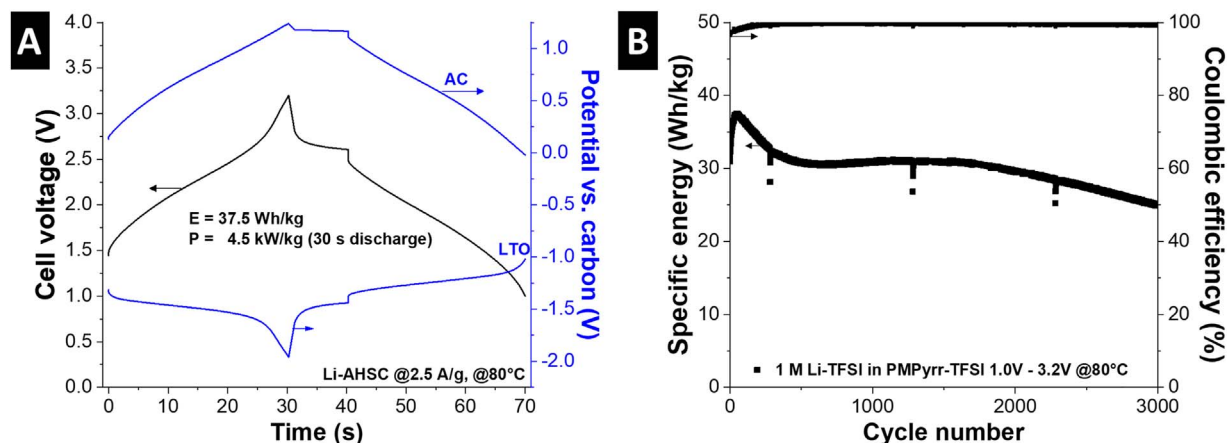


**Fig. 4.** High temperature operation. (A) Voltage profile of 50th cycle of a Li-AHSC cell cycled between 3.2 V and 1 V cell voltage at 2.5 A/g at a temperature of 80 °C. (B) Corresponding specific energy and Coulombic efficiency over 3000 cycles under these conditions.

4.5 kW/kg, corresponding to a discharge time of 30 s, with an energy efficiency of 77.4% and Coulombic efficiency of 98.2% (Fig. 4A). Stability testing was carried out at the same rate and in the same voltage window for over 3000 cycles, with a retention of 80% of the initial value (Fig. 4B, Fig. S8A). When cycling at a lower rate of 0.1 A/g, the cell voltage is reduced to 2.8 V, resulting in a specific energy of 71 Wh/kg at a power of 190 W/kg (Fig. S8B-C). To the best of our knowledge, no comparable hybrid supercapacitor cell that combines a Faradaic intercalation electrode with a capacitive electrode was shown to exhibit stable behavior at such a high temperature. The performance stability further underlines the promising performance of the Li-AHSC cell at elevated temperatures. By further improvement of the electrolyte formulation, for example, by creation of eutectic mixtures of ionic liquids [54,55] or mixing with organic solvent [56], even low temperature operation could be enabled for this AHSC cell concept in the future.

#### 4. Conclusions

In conclusion, we prepared ionic liquid electrolytes with dissolved lithium- and sodium-salt, respectively, and applied them for the first time in an asymmetric hybrid supercapacitor cell employing ion intercalation at the negative electrode (LTO) and double-layer formation at the positive electrode (AC). After evaluation of half-cell performance, a successful transfer to full-cells was achieved and both the lithium- and the sodium-ion AHSC cells were operated at 4 V up to 1500 cycles with only minor capacity fading. The maximum specific energy of Li-AHSC cells was about 100 Wh/kg, while the maximum specific power was about 2 kW/kg. Na-AHSC cells showed similar values with slightly reduced specific energy. Finally, Li-AHSC cells were shown for the first time to exhibit stable behavior at a high temperature of 80 °C for more than 3000 cycles at a high rate, exhibiting up to 38 Wh/kg at high power of 4.5 kW/kg.

We believe that the presented approach is particularly promising as it combines all virtues of ILs synergistically in one cell concept. ILs expand the stability window for the positive electrode, giving access to larger cell voltages, as we showed by enabling 4 V for LTO-based AHSC devices. The demonstrated possibility of high-temperature operation in combination with the non-flammability of the device is important for many applications including the mobility sector, where mass, volume, and cost of cooling systems and impact-safe housing could be reduced. The viability of this novel cell concept was demonstrated for different alkali ion systems by using only commercially available materials. Thus, there is great potential for further improvement, for example, by use of more advanced electrode materials that can increase energy, power, and longevity, or the exploration of further ILs or their mixtures with organic solvents or further additives.

#### Acknowledgments

We acknowledge funding from the German Federal Ministry for Economic Affairs and Energy (BMWi) in support of the HyBaCap project (award number 03ET6113C). We thank Eduard Arzt for his continuing support, and Mesut Aslan and Pattarachai Srimuk (all INM) for discussions and technical support.

#### Declaration of interests

The authors declare no competing interests.

#### Supplemental information

The supplemental information includes supplemental materials characterization, Supplemental electrochemical characterization and supplemental experimental procedures.

## Appendix A. Supporting information

Supplementary data associated with this article can be found in the online version at doi:10.1016/j.ensm.2018.06.011.

## References

- [1] P. Simon, Y. Gogotsi, Materials for electrochemical capacitors, *Nat. Mater.* 7 (2008) 845–854.
- [2] S. Fleischmann, A. Tolosa, V. Presser, Design of carbon/metal oxide hybrids for electrochemical energy storage, *Chem. - Eur. J.* (2018). <http://dx.doi.org/10.1002/chem.201800772>.
- [3] S. Fleischmann, N. Jäckel, M. Zeiger, B. Krüner, I. Grobelsek, P. Formanek, S. Choudhury, D. Weingarth, V. Presser, Enhanced electrochemical energy storage by nanoscopic decoration of endohedral and exohedral carbon with vanadium oxide via atomic layer deposition, *Chem. Mater.* 28 (2016) 2802–2813.
- [4] S. Fleischmann, D. Leistenschneider, V. Lemkova, B. Krüner, M. Zeiger, L. Borchardt, V. Presser, Tailored mesoporous carbon/vanadium pentoxide hybrid electrodes for high power pseudocapacitive lithium and sodium intercalation, *Chem. Mater.* 29 (2017) 8653–8662.
- [5] S. Boukhalfa, K. Evanoff, G. Yushin, Atomic layer deposition of vanadium oxide on carbon nanotubes for high-power supercapacitor electrodes, *Energy Environ. Sci.* 5 (2012) 6872–6879.
- [6] J. Lee, B. Krüner, A. Tolosa, S. Sathyamoorthi, D. Kim, S. Choudhury, K.H. Seo, V. Presser, Tin/vanadium redox electrolyte for battery-like energy storage capacity combined with supercapacitor-like power handling, *Energy Environ. Sci.* 9 (2016) 3392–3398.
- [7] J. Lee, A. Tolosa, B. Krüner, N. Jäckel, S. Fleischmann, M. Zeiger, D. Kim, V. Presser, Asymmetric tin-vanadium redox electrolyte for hybrid energy storage with nanoporous carbon electrodes, *Sustain. Energy Fuels* 1 (2017) 299–307.
- [8] E. Mourad, L. Coustan, P. Lannelongue, D. Zigah, A. Mehdi, A. Vioux, S.A. Freunberger, F. Favier, O. Fontaine, Biredox ionic liquids with solid-like redox density in the liquid state for high-energy supercapacitors, *Nat. Mater.* 16 (2017) 446.
- [9] N. Böckenfeld, R.-S. Kühnel, S. Passerini, M. Winter, A. Balducci, Composite LiFePO<sub>4</sub>/AC high rate performance electrodes for Li-ion capacitors, *J. Power Sources* 196 (2011) 4136–4142.
- [10] D. Cericola, P. Novák, A. Wokaun, R. Kötz, Hybridization of electrochemical capacitors and rechargeable batteries: an experimental analysis of the different possible approaches utilizing activated carbon, Li<sub>4</sub>Ti<sub>5</sub>O<sub>12</sub> and LiMn<sub>2</sub>O<sub>4</sub>, *J. Power Sources* 196 (2011) 10305–10313.
- [11] M. Widmaier, N. Jäckel, M. Zeiger, M. Abuzarli, C. Engel, L. Bommer, V. Presser, Influence of carbon distribution on the electrochemical performance and stability of lithium titanate based energy storage devices, *Electrochim. Acta* 247 (2017) 1006–1018.
- [12] G.G. Amatucci, F. Badway, A. Du Pasquier, T. Zheng, An asymmetric hybrid nonaqueous energy storage cell, *J. Electrochem. Soc.* 148 (2001) A930–A939.
- [13] W. Zuo, R. Li, C. Zhou, Y. Li, J. Xia, J. Liu, Battery-supercapacitor hybrid devices: recent progress and future prospects, *Adv. Sci.* 4 (2017) 1600539.
- [14] F. Béguin, V. Presser, A. Balducci, E. Frackowiak, Carbons and electrolytes for advanced supercapacitors, *Adv. Mater.* 26 (2014) 2219–2251.
- [15] J. Ding, H. Wang, Z. Li, K. Cui, D. Karpuzov, X. Tan, A. Kohandehghan, D. Mitlin, Peanut shell hybrid sodium ion capacitor with extreme energy–power rivals lithium ion capacitors, *Energy Environ. Sci.* 8 (2015) 941–955.
- [16] X. Wang, S. Kajiyama, H. Iinuma, E. Hosono, S. Oro, I. Moriguchi, M. Okubo, A. Yamada, Pseudocapacitance of MXene nanosheets for high-power sodium-ion hybrid capacitors, *Nat. Commun.* 6 (2015) 6544.
- [17] J. Yin, L. Qi, H. Wang, Sodium titanate nanotubes as negative electrode materials for sodium-ion capacitors, *ACS Appl. Mater. Interfaces* 4 (2012) 2762–2768.
- [18] P. Jeżowski, O. Crosnier, E. Deunf, P. Poizot, F. Béguin, T. Brousse, Safe and recyclable lithium-ion capacitors using sacrificial organic lithium salt, *Nat. Mater.* 17 (2017) 167.
- [19] S. Dsoke, B. Fuchs, E. Gucciardi, M. Wohlfahrt-Mehrens, The importance of the electrode mass ratio in a Li-ion capacitor based on activated carbon and Li<sub>4</sub>Ti<sub>5</sub>O<sub>12</sub>, *J. Power Sources* 282 (2015) 385–393.
- [20] T. Zhang, B. Fuchs, M. Secchiarioli, M. Wohlfahrt-Mehrens, S. Dsoke, Electrochemical behavior and stability of a commercial activated carbon in various organic electrolyte combinations containing Li-salts, *Electrochim. Acta* 218 (2016) 163–173.
- [21] P. Verma, P. Maire, P. Novák, A review of the features and analyses of the solid electrolyte interphase in Li-ion batteries, *Electrochim. Acta* 55 (2010) 6332–6341.
- [22] S. Sivakumar, A. Pandolfo, Evaluation of lithium-ion capacitors assembled with pre-lithiated graphite anode and activated carbon cathode, *Electrochim. Acta* 65 (2012) 280–287.
- [23] K. Xu, Nonaqueous liquid electrolytes for lithium-based rechargeable batteries, *Chem. Rev.* 104 (2004) 4303–4418.
- [24] K. Naoi, S. Ishimoto, Y. Isobe, S. Aoyagi, High-rate nano-crystalline Li<sub>4</sub>Ti<sub>5</sub>O<sub>12</sub> attached on carbon nano-fibers for hybrid supercapacitors, *J. Power Sources* 195 (2010) 6250–6254.
- [25] K. Naoi, S. Ishimoto, J.-i Miyamoto, W. Naoi, Second generation 'nanohybrid supercapacitor': evolution of capacitive energy storage devices, *Energy Environ. Sci.* 5 (2012) 9363–9373.
- [26] M. Salanne, B. Rotenberg, K. Naoi, K. Kaneko, P.-L. Taberna, C. Grey, B. Dunn, P. Simon, Efficient storage mechanisms for building better supercapacitors, *Nat. Energy* 1 (2016) 16070.
- [27] V. Khomenko, E. Raymundo-Piñero, F. Béguin, High-energy density graphite/AC capacitor in organic electrolyte, *J. Power Sources* 177 (2008) 643–651.
- [28] M. Armand, F. Endres, D.R. MacFarlane, H. Ohno, B. Scrosati, Ionic-liquid materials for the electrochemical challenges of the future, *Nat. Mater.* 8 (2009) 621–629.
- [29] D.R. MacFarlane, N. Tachikawa, M. Forsyth, J.M. Pringle, P.C. Howlett, G.D. Elliott, J.H. Davis, M. Watanabe, P. Simon, C.A. Angell, Energy applications of ionic liquids, *Energy Environ. Sci.* 7 (2014) 232–250.
- [30] C. Largeot, P. Taberna, Y. Gogotsi, P. Simon, Microporous carbon-based electrical double layer capacitor operating at high temperature in ionic liquid electrolyte, *Electrochem. Solid-State Lett.* 14 (2011) A174–A176.
- [31] T. Mendes, F. Zhou, A.J. Barlow, M. Forsyth, P.C. Howlett, D. MacFarlane, An ionic liquid based sodium metal-hybrid supercapacitor-battery, *Sustain. Energy Fuels* 2 (2018) 763–771.
- [32] S. Rothermel, P. Meister, G. Schmuelling, O. Fromm, H.-W. Meyer, S. Nowak, M. Winter, T. Placke, Dual-graphite cells based on the reversible intercalation of bis (trifluoromethanesulfonyl) imide anions from an ionic liquid electrolyte, *Energy Environ. Sci.* 7 (2014) 3412–3423.
- [33] T. Yamamoto, T. Nohira, R. Hagiwara, A. Fukunaga, S. Sakai, K. Nitta, S. Inazawa, Charge–discharge behavior of tin negative electrode for a sodium secondary battery using intermediate temperature ionic liquid sodium bis (fluorosulfonyl) amide–potassium bis (fluorosulfonyl) amide, *J. Power Sources* 217 (2012) 479–484.
- [34] K. Beltrop, S. Beuker, A. Heckmann, M. Winter, T. Placke, Alternative electrochemical energy storage: potassium-based dual-graphite batteries, *Energy Environ. Sci.* 10 (2017) 2090–2094.
- [35] D. Weingarth, M. Zeiger, N. Jäckel, M. Aslan, G. Feng, V. Presser, Graphitization as a universal tool to tailor the potential-dependent capacitance of carbon supercapacitors, *Adv. Energy Mater.* 4 (2014) 1400316.
- [36] D. Weingarth, A. Foelske-Schmitz, A. Wokaun, R. Kötz, PTFE bound activated carbon—A quasi-reference electrode for ionic liquids, *Electrochem. Commun.* 18 (2012) 116–118.
- [37] K. Xu, S.P. Ding, T.R. Jow, Toward reliable values of electrochemical stability limits for electrolytes, *J. Electrochem. Soc.* 146 (1999) 4172–4178.
- [38] D. Weingarth, H. Noh, A. Foelske-Schmitz, A. Wokaun, R. Kötz, A reliable determination method of stability limits for electrochemical double layer capacitors, *Electrochim. Acta* 103 (2013) 119–124.
- [39] A. Eftekhari, Energy efficiency: a critically important but neglected factor in battery research, *Sustain. Energy Fuels* 1 (2017) 2053–2060.
- [40] S. Fleischmann, M. Zeiger, A. Quade, A. Kruth, V. Presser, Atomic layer deposited molybdenum oxide/carbon nanotube hybrid electrodes: influence of crystal structure on lithium-ion capacitor performance, *ACS Appl. Mater. Interfaces* 10 (2018) 18675–18684.
- [41] P. Reale, A. Ferriccola, B. Scrosati, Compatibility of the Py<sub>24</sub>TFSI–LiTFSI ionic liquid solution with Li<sub>4</sub>Ti<sub>5</sub>O<sub>12</sub> and LiFePO<sub>4</sub> lithium ion battery electrodes, *J. Power Sources* 194 (2009) 182–189.
- [42] T. Ohzuku, A. Ueda, N. Yamamoto, Zero-strain insertion material of Li[Li<sub>1/3</sub>Ti<sub>5/3</sub>]O<sub>4</sub> for rechargeable lithium cells, *J. Electrochem. Soc.* 142 (1995) 1431–1435.
- [43] N. Yabuuchi, K. Kubota, M. Dahbi, S. Komaba, Research development on sodium-ion batteries, *Chem. Rev.* 114 (2014) 11636–11682.
- [44] Y. Sun, L. Zhao, H. Pan, X. Lu, L. Gu, Y.-S. Hu, H. Li, M. Armand, Y. Ikuhara, L. Chen, Direct atomic-scale confirmation of three-phase storage mechanism in Li<sub>4</sub>Ti<sub>5</sub>O<sub>12</sub> anodes for room-temperature sodium-ion batteries, *Nat. Commun.* 4 (2013) 1870.
- [45] M. Kitta, K. Kuratani, M. Tabuchi, N. Takeichi, T. Akita, T. Kiyobayashi, M. Kohyama, Irreversible structural change of a spinel Li<sub>4</sub>Ti<sub>5</sub>O<sub>12</sub> particle via Na insertion-extraction cycles of a sodium-ion battery, *Electrochim. Acta* 148 (2014) 175–179.
- [46] G. Hasegawa, K. Kanamori, T. Kiyomura, H. Kurata, K. Nakanishi, T. Abe, Hierarchically porous Li<sub>4</sub>Ti<sub>5</sub>O<sub>12</sub> anode materials for Li- and Na-ion batteries: effects of nanoarchitectural design and temperature dependence of the rate capability, *Adv. Energy Mater.* 5 (2015).
- [47] S. Komaba, W. Murata, T. Ishikawa, N. Yabuuchi, T. Ozeki, T. Nakayama, A. Ogata, K. Gotoh, K. Fujiwara, Electrochemical Na insertion and solid electrolyte interphase for hard-carbon electrodes and application to Na-ion batteries, *Adv. Funct. Mater.* 21 (2011) 3859–3867.
- [48] L.Y. Yang, H.Z. Li, J. Liu, S.S. Tang, Y.K. Lu, S. Te Li, J. Min, N. Yan, M. Lei, Li<sub>4</sub>Ti<sub>5</sub>O<sub>12</sub> nanosheets as high-rate and long-life anode materials for sodium-ion batteries, *J. Mater. Chem. A* 3 (2015) 24446–24452.
- [49] M.D. Slater, D. Kim, E. Lee, C.S. Johnson, Sodium-ion batteries, *Adv. Funct. Mater.* 23 (2013) 947–958.
- [50] C. Chen, Y. Wen, X. Hu, X. Ji, M. Yan, L. Mai, P. Hu, B. Shan, Y. Huang, Na<sup>+</sup> intercalation pseudocapacitance in graphene-coupled titanium oxide enabling ultra-fast sodium storage and long-term cycling, *Nat. Commun.* 6 (2015).
- [51] Z. Le, F. Liu, P. Nie, X. Li, X. Liu, Z. Bian, G. Chen, H.B. Wu, Y. Lu, Pseudocapacitive sodium storage in mesoporous single-crystal-like TiO<sub>2</sub>-graphene nanocomposite enables high-performance sodium-ion capacitors, *ACS Nano* 11 (2017) 2952–2960.

- [52] S. Dong, L. Shen, H. Li, P. Nie, Y. Zhu, Q. Sheng, X. Zhang, Pseudocapacitive behaviours of  $\text{Na}_2\text{Ti}_3\text{O}_7$ @CNT coaxial nanocables for high-performance sodium-ion capacitors, *J. Mater. Chem. A* 3 (2015) 21277–21283.
- [53] A. Balducci, R. Dugas, P.-L. Taberna, P. Simon, D. Plee, M. Mastragostino, S. Passerini, High temperature carbon–carbon supercapacitor using ionic liquid as electrolyte, *J. Power Sources* 165 (2007) 922–927.
- [54] R. Lin, P.-L. Taberna, S. Fantini, V. Presser, C.R. Pérez, F. Malbosc, N.L. Rupasinghe, K.B. Teo, Y. Gogotsi, P. Simon, Capacitive energy storage from–50 to 100 C using an ionic liquid electrolyte, *J. Phys. Chem. Lett.* 2 (2011) 2396–2401.
- [55] W.-Y. Tsai, R. Lin, S. Murali, L.L. Zhang, J.K. McDonough, R.S. Ruoff, P.-L. Taberna, Y. Gogotsi, P. Simon, Outstanding performance of activated graphene based supercapacitors in ionic liquid electrolyte from–50 to 80 C, *Nano Energy* 2 (2013) 403–411.
- [56] V. Ruiz, T. Huynh, S. Sivakkumar, A. Pandolfo, Ionic liquid–solvent mixtures as supercapacitor electrolytes for extreme temperature operation, *RSC Adv.* 2 (2012) 5591–5598.

## 1. Supplemental material characterization

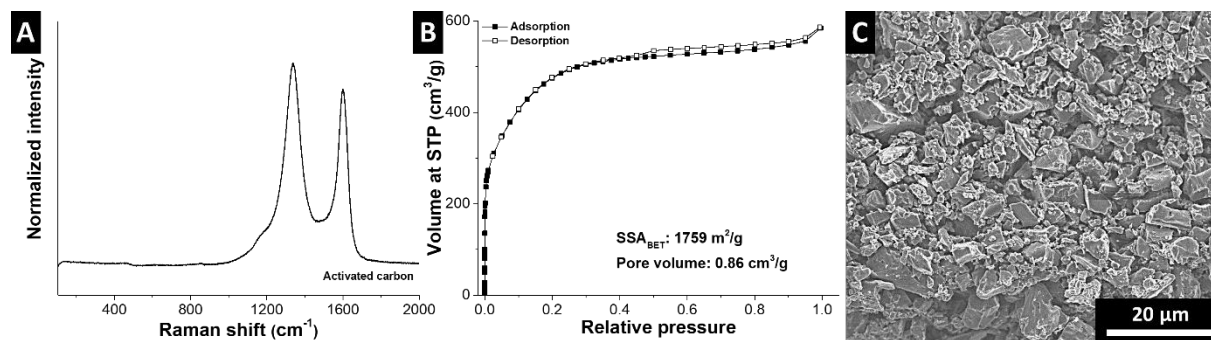


**Fig. S1:** (A) Raman spectrum and (B) nitrogen sorption isotherm and (C) scanning electron micrograph of AC electrodes. Replotted from Ref. [1].

**Table S1:** Properties of PMPyrr-TFSI as given by the supplier.

<b>Ionic liquid</b>	<b>Viscosity</b>	<b>Conductivity</b>
PMPyrr-TFSI	58.7 cP at 25 °C	4.924 mS/cm at 30 °C

## 2. Supplemental electrochemical data

### 2.1 Half-cell data: Activated carbon

To choose a suitable ionic liquid for our study, we evaluated the stability limits of various ionic liquids by so-called R-value testing,[2] [3] which calculates the number of parasitic reactions; an R-value above 0.1 is defined as a non-stable behavior. The results for PMPyrr-TFSI are depicted in **Fig. S2**, where an anodic stability limit of about +2 V vs. carbon is determined.

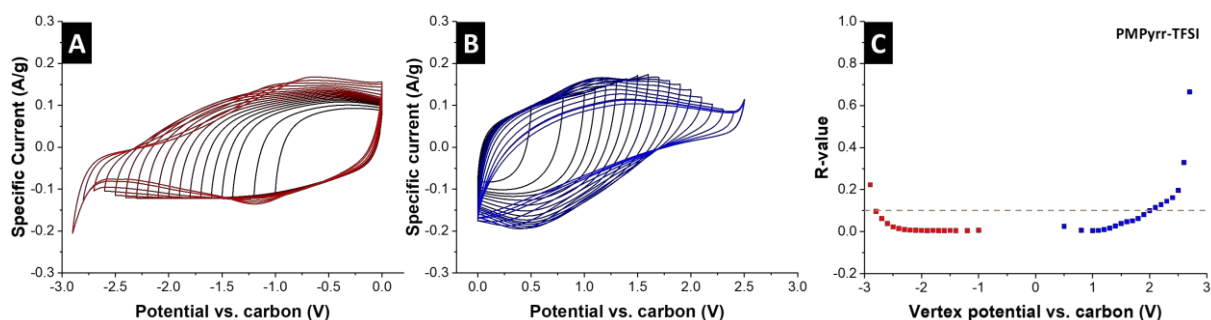


**Fig. S2:** (A) Cathodic stability test at 1 mV/s, (B) anodic stability test at 1 mV/s, and (C) calculated R-values for PMPyrr-TFSI electrolyte.

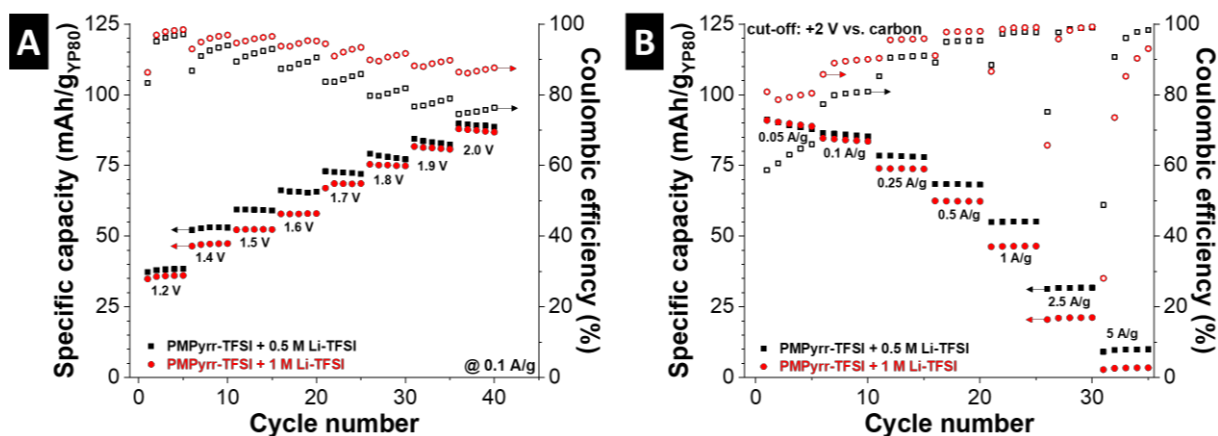


**Fig. S3:** (A) Testing anodic stability between +1.2 V and +2.0 V vs. carbon and (B) rate handling at rates from 50 mA/g to 5 A/g in 0.5 M and 1.0 M Li-TFSI in PMPyrr-TFSI electrolytes.

## 2.2 Half-cell data: Lithium titanate electrodes

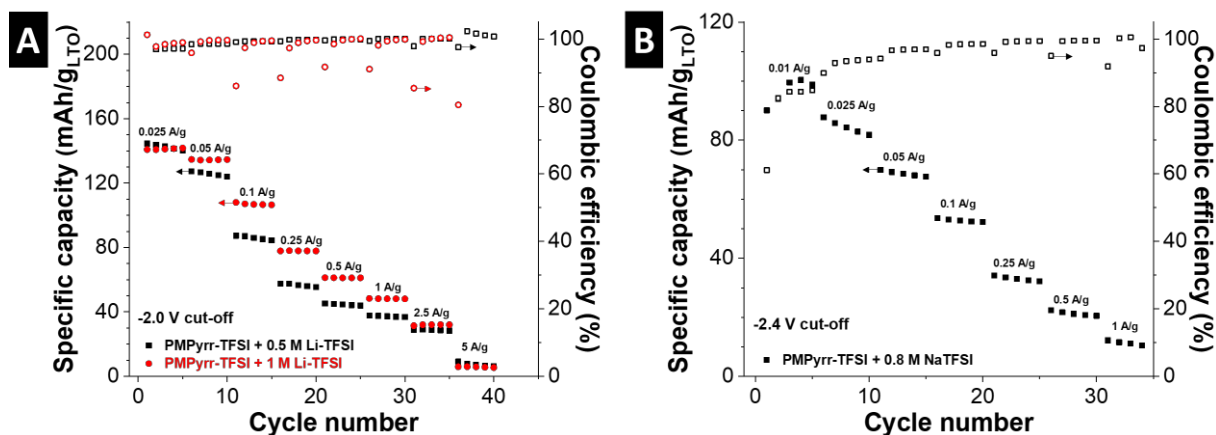


**Fig. S4:** (A) Rate handling from galvanostatic cycling between 0 V and -2.0 V vs. carbon from 25 mA/g to 5 A/g for Li-TFSI electrolytes and (B) rate handling from galvanostatic cycling between 0 V and -2.4 V vs. carbon from 10 mA/g to 1 A/g for Na-TFSI electrolytes, including corresponding Coulombic efficiency.

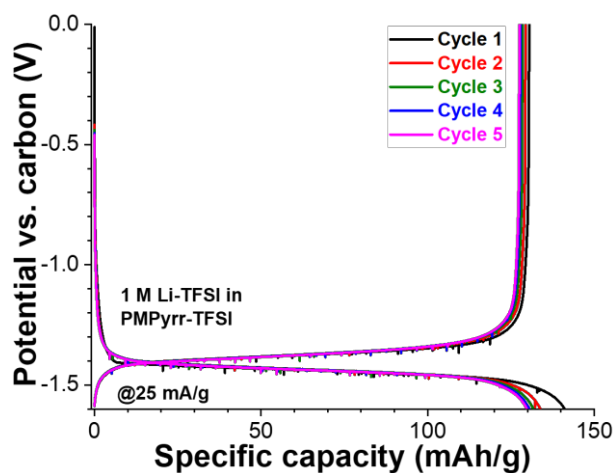


**Fig. S5:** Comparison of first 5 galvanostatic cycles in 1 M Li-TFSI in PMPyrr-TFSI electrolyte at a specific current of 25 mA/g.

### 2.3 AHSC full-cells

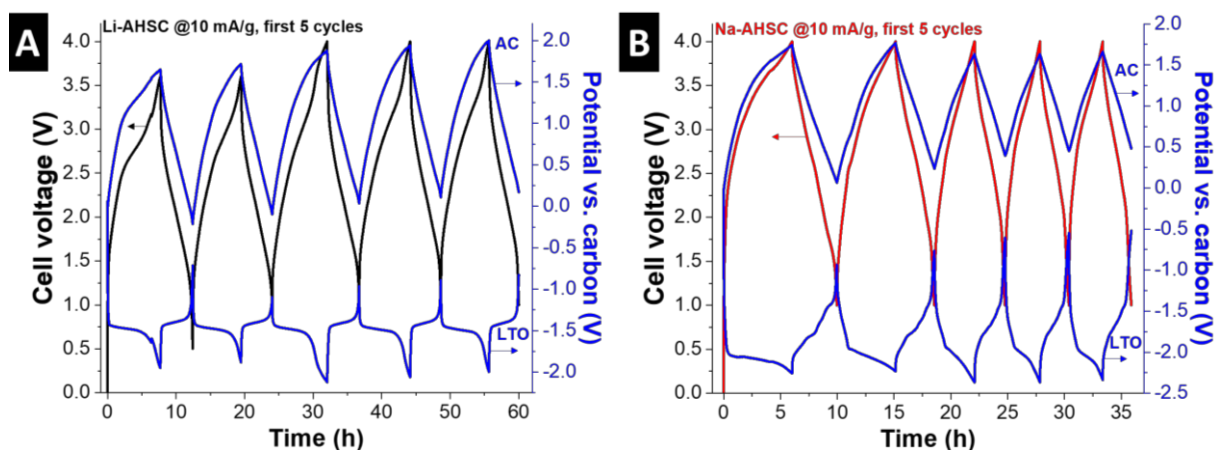


**Fig. S6:** Voltage profiles of first 5 galvanostatic cycles at 10 mA/g for (A) Li-AHSC cell and (B) Na-AHSC cell including potential development at negative and positive electrodes monitored via activated carbon quasi-reference electrode.

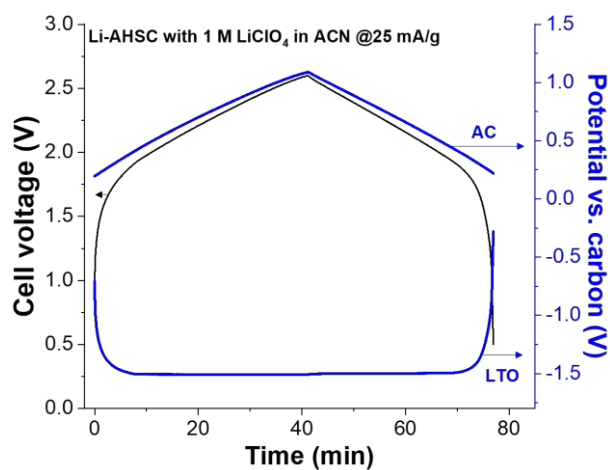


**Fig. S7:** Voltage profile of AHSC cell assembled the same way as described Li-AHSC cells, using 1 M  $\text{LiClO}_4$  in acetonitrile electrolyte and not an IL-based electrolyte. Potential development is monitored by activated carbon spectator quasi-reference electrode.

## 2.4 High temperature operation

For measurements of Li-AHSC cells at 80 °C, we limited the maximum cell voltage to 3.2 V for stable cycling over 3,000 cycles at 2.5 A/g. The first three cycles are shown in **Fig. S8A**. The AC electrode mass of this cell was increased by a factor of 1.76 compared to LTO. When cycling at 80 °C with lower rates between 0.05 A/g and 0.5 A/g (**Fig. S8B-C**), the AC mass was increased by a factor of 2.3 compared to LTO to balance the higher capacity of LTO at lower rates. Also, the maximum cell voltage was decreased to 2.8 V (for 0.05 A/g and 0.1 A/g) or to 3.0 V (for 0.25 A/g and 0.5 A/g) to stay within the stable potential range of +1.2 V vs. carbon for the AC electrode at this temperature.

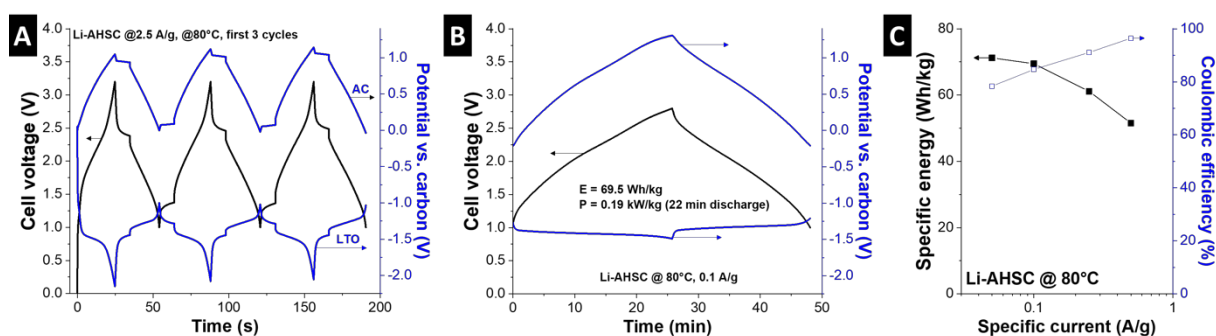


**Fig. S8:** Voltage profiles of (A) first 3 galvanostatic cycles at 2.5 A/g for the stability test and (B) a profile at 0.1 A/g for Li-AHSC cell at 80 °C including potential development at negative and positive electrodes monitored via activated carbon quasi-reference electrode. (C) Rate-handling plot of Li-AHSC cell at 80 °C at rates between 0.05 A/g and 0.5 A/g, including values of the Coulombic efficiency.

## Supplemental References

- [1] S. Fleischmann, N. Jäckel, M. Zeiger, B. Krüner, I. Grobelsek, P. Formanek, S. Choudhury, D. Weingarh, V. Presser, Enhanced electrochemical energy storage by nanoscopic decoration of endohedral and exohedral carbon with vanadium oxide via atomic layer deposition, *Chem. Mater.* 28 (2016) 2802-2813.
- [2] D. Weingarh, H. Noh, A. Foelske-Schmitz, A. Wokaun, R. Kötz, A reliable determination method of stability limits for electrochemical double layer capacitors, *Electrochim. Acta* 103 (2013) 119-124.
- [3] K. Xu, S. P. Ding, T. R. Jow, Toward reliable values of electrochemical stability limits for electrolytes, *J. Electrochem. Soc.* 146 (1999) 4172-4178.

# Understanding interlayer deprotonation of hydrogen titanium oxide for high-power electrochemical energy storage

Simon Fleischmann,<sup>1,2</sup> Kristina Pfeifer,<sup>3</sup> Mathias Widmaier,<sup>2,3</sup>  
Hwirim Shim,<sup>1,2</sup> Öznil Budak,<sup>1,2</sup> Volker Presser<sup>1,2</sup>

<sup>1</sup> INM - Leibniz Institute for New Materials, 66123 Saarbrücken, Germany

<sup>2</sup> Department of Materials Science and Engineering, Saarland University, 66123 Saarbrücken, Germany

<sup>3</sup> Robert Bosch GmbH, Robert-Bosch-Campus 1, 71272 Renningen, Germany

## Citation:

S. Fleischmann, K. Pfeifer, M. Widmaier, H. Shim, Ö. Budak, & V. Presser (2019). Understanding Interlayer Deprotonation of Hydrogen Titanium Oxide for High-Power Electrochemical Energy Storage. ACS Applied Energy Materials, 2(5), 3633-3641.

## Own contributions:

X-ray diffraction measurements, transmission electron microscopy, critical discussion.

# Understanding Interlayer Deprotonation of Hydrogen Titanium Oxide for High-Power Electrochemical Energy Storage

Simon Fleischmann,<sup>†,‡,⊥</sup> Kristina Pfeifer,<sup>§,⊥</sup> Mathias Widmaier,<sup>‡,§</sup> Hwirim Shim,<sup>†,‡</sup> Öznil Budak,<sup>†,‡</sup> and Volker Presser<sup>\*,†,‡,⊥</sup>

<sup>†</sup>INM - Leibniz Institute for New Materials, 66123 Saarbrücken, Germany

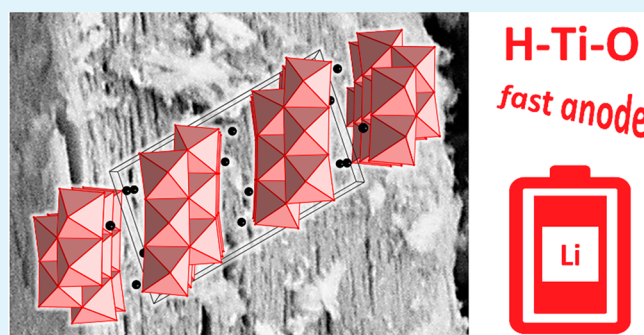
<sup>‡</sup>Department of Materials Science and Engineering, Saarland University, 66123 Saarbrücken, Germany

<sup>§</sup>Robert Bosch GmbH, Robert-Bosch-Campus 1, 71272 Renningen, Germany

## Supporting Information

**ABSTRACT:** Negative electrode materials that possess fast lithium insertion kinetics are in high demand for high power lithium-ion batteries and hybrid supercapacitor applications. In this work, hydrogen titanium oxides are synthesized by a proton exchange reaction with sodium titanium oxide, resulting in the  $\text{H}_2\text{Ti}_3\text{O}_7$  phase. We show that a gradual water release in four steps yields intermediate phases of hydrogen titanate with different degrees of interlayer protonation. In addition, a synthesis route using zinc nitrate is explored yielding  $\text{H}_2\text{Ti}_3\text{O}_7$  with a high rutile content. This material dehydrates already at a lower temperature, resulting in a lamellar rutile titania phase. The hydrogen titanate materials with partially protonated interlayers are tested as negative electrodes in a lithium-ion battery and hybrid supercapacitor setup, showing an improved performance compared to the fully protonated phases. The performance in half-cells reaches around 168 mAh/g, with high retention of 42 mAh/g at 10 A/g. This translates to an energy of 88 Wh/kg for a full-cell with a maximum power of 9.2 kW/kg and high cycling stability over 1000 cycles.

**KEYWORDS:** lithium-ion battery, hybrid capacitor, anode, hydrogen titanate, interlayer protons



## 1. INTRODUCTION

Electrochemical energy storage devices are required to facilitate the transition from fossil to renewable energy sources.<sup>1</sup> Careful cell design and the adaptation of nanostructured materials are promising pathways toward next-generation devices.<sup>2–5</sup> Lithium-ion batteries (LIBs) are currently applied in numerous commercial products like portable electronics or electric vehicles.<sup>6</sup> Most LIBs rely on graphite anodes that present an insertion potential below ca. 0.2 V vs Li/Li<sup>+</sup>,<sup>6</sup> which is favorable to achieve high cell voltages and, in turn, high specific energy. The low anode potential, however, is outside the electrochemical stability window of carbonate-based electrolytes. Consequently, electrolyte reduction takes place during the first charging cycle, and the solid electrolyte interphase (SEI) is formed.<sup>7</sup> This process has several negative consequences, such as the irreversible consumption of lithium ions, resulting in a loss of active material,<sup>8</sup> reduced lithium ion transfer kinetics,<sup>7</sup> and an increased risk of dendrite formation during fast charging.<sup>9</sup>

Alternative anode materials operating at a higher insertion potential (>1 V vs Li/Li<sup>+</sup>) to circumvent SEI formation are in high demand as they offer higher power, better stability, and increased safety.<sup>10</sup> Particularly promising candidates are

polymorphs of titania or titania/carbon hybrids,<sup>11,12</sup> such as anatase  $\text{TiO}_2$ ,<sup>13,14</sup> bronze  $\text{TiO}_2$ ,<sup>15</sup> or rutile  $\text{TiO}_2$ .<sup>16,17</sup> The lithiation reaction occurs according to eq 1:



with a theoretical specific capacity of 335 mAh/g for full lithiation with  $x = 1$ .<sup>16</sup> Compared to spinel lithium titanate ( $\text{Li}_4\text{Ti}_5\text{O}_{12}$ , LTO, theoretical capacity of 175 mAh/g for fully lithiated  $\text{Li}_7\text{Ti}_5\text{O}_{12}$ ),<sup>18</sup> these titanates offer a higher theoretical capacity and require no inactively bonded lithium in their crystal structure. The maximum capacity of titanate materials is dependent on the crystal structure, size, and shape of the polymorph.<sup>19</sup> Bulk rutile exhibits a limited lithium storage capacity of <0.1 Li per  $\text{TiO}_2$ , while nanostructuring can improve the capacity, as demonstrated by Wang et al. for mesoporous rutile with lithium storage of up to 0.55 Li, corresponding to 185 mAh/g.<sup>20</sup> Similarly, anatase shows increased capacities in nanostructured, mesoporous morphology of up to 200 mAh/g.<sup>21</sup> The bronze polymorph of titania,

**Received:** February 21, 2019

**Accepted:** April 18, 2019

**Published:** April 18, 2019

TiO<sub>2</sub>(B), has attracted significant attention for its high maximum specific capacity of over 300 mAh/g<sup>22,23</sup> and favorable Li<sup>+</sup> diffusion properties.<sup>24</sup> The monoclinic structure of bronze titania is composed of corner-sharing TiO<sub>6</sub> octahedra that exhibit channels along the [010] direction with increased lithium mobility.<sup>25</sup>

Hydrogen titanium oxides are being explored as alternatives to anode materials consisting of titania.<sup>24,26</sup> The monoclinic layered hydrogen trititanate (H<sub>2</sub>Ti<sub>3</sub>O<sub>7</sub>) consists of corner- and edge-sharing TiO<sub>6</sub> octahedra with protons positioned in the interlayer and can be obtained by proton exchange reactions with alkali titanates like Na<sub>2</sub>Ti<sub>3</sub>O<sub>7</sub>.<sup>27,28</sup> It is reported that upon heating of H<sub>2</sub>Ti<sub>3</sub>O<sub>7</sub> it gradually deprotonates its interlayer by release of water, forming the intermediates H<sub>2</sub>Ti<sub>6</sub>O<sub>13</sub> and H<sub>2</sub>Ti<sub>12</sub>O<sub>25</sub> before forming TiO<sub>2</sub>(B) above about 450 °C.<sup>27,29</sup> Zhu et al. analyzed the electrochemical lithium-ion storage properties of hydrogen titanium oxides with differently protonated interlayer states.<sup>27</sup> They report that H<sub>2</sub>Ti<sub>3</sub>O<sub>7</sub> exhibits an inferior maximum capacity of 193 mAh/g compared to completely dehydrated TiO<sub>2</sub>(B) with 291 mAh/g, but the cycling stability of H<sub>2</sub>Ti<sub>3</sub>O<sub>7</sub> over 50 cycles was found to be superior.<sup>27</sup> Akimoto et al. have reported that H<sub>2</sub>Ti<sub>12</sub>O<sub>25</sub> exhibits a favorable lithium insertion capacity of ~200 mAh/g over 50 cycles with a constant insertion potential at 1.5–1.6 V vs Li/Li<sup>+</sup>.<sup>30,31</sup> In another work, Lee et al. used H<sub>2</sub>Ti<sub>12</sub>O<sub>25</sub> as negative electrodes in a hybrid supercapacitor setup with activated carbon as the positively polarized electrode, exhibiting up about 40 Wh/kg.<sup>32,33</sup> In a study by Choi et al., the performance of H<sub>2</sub>Ti<sub>12</sub>O<sub>25</sub> was improved by zinc doping, which was assumed to increase the charge storage capacity and lower the polarization of the material.<sup>34</sup> In addition, Guo et al. investigated the impact of the morphology of H<sub>2</sub>Ti<sub>12</sub>O<sub>25</sub> on the electrochemical performance and found that nanorods synthesized in molten NaCl offer attractive rate handling and stability.<sup>35</sup>

Various synthesis routes and testing conditions are reported in the current literature on hydrogen titanates. Our study compares hydrogen titanates synthesized using different routes under the same testing conditions for anodes in lithium-ion batteries and as negative electrodes in hybrid supercapacitors. We synthesized H<sub>2</sub>Ti<sub>3</sub>O<sub>7</sub> by using a proton-exchange reaction of Na<sub>2</sub>Ti<sub>3</sub>O<sub>7</sub> and obtained an intermediate hydrogen titanium oxide phase by annealing at 280 °C, which we label HTO. Our results suggest that hydrogen titanium oxide is present as a protonated titania that crystallographically resembles the bronze phase rather than exhibiting a distinct H<sub>2</sub>Ti<sub>12</sub>O<sub>25</sub> phase. In addition, we have explored for the first time a synthesis route using Zn(NO<sub>3</sub>)<sub>2</sub> yielding protonated rutile. The materials are tested in a carbonate-based electrolyte for lithium-ion batteries, and we used an acetonitrile-based electrolyte for assessing the hybrid supercapacitor performance. The hybrid supercapacitor performance of our materials surpasses past reports of hydrogen titanates in the literature; specifically, we reached up to 90 Wh/kg and 8 kW/kg at 20 Wh/kg with stability over 1000 cycles. The material class represents a promising alternative to lithium titanates for high power negative electrode materials in various electrochemical energy storage applications.

## 2. EXPERIMENTAL SECTION

**2.1. Materials Synthesis.** In the first step, sodium titanate was synthesized as a precursor for the hydrogen titanate materials. Therefore, sodium carbonate (Na<sub>2</sub>CO<sub>3</sub>, Sigma-Aldrich) was dissolved

in water, and anatase titanium oxide nanopowder (TiO<sub>2</sub>, Sigma-Aldrich) was added to the solution with the mass ratio between Na<sub>2</sub>CO<sub>3</sub> and TiO<sub>2</sub> of 1.5 to 3. The mixture was stirred at 70 °C until all water evaporated, before being ground in a mortar. Then, the powder was heat-treated at 800 °C for 20 h in an air atmosphere to obtain the sample Na<sub>2</sub>Ti<sub>3</sub>O<sub>7</sub>. For the zinc nitrate route, the wet mixture contained additionally a small amount of zinc nitrate (Zn(NO<sub>3</sub>)<sub>2</sub>, Sigma-Aldrich) with a mass ratio between Na<sub>2</sub>CO<sub>3</sub>:TiO<sub>2</sub>:Zn(NO<sub>3</sub>)<sub>2</sub> of 1.5:2.9:0.1. All samples yielded from the zinc nitrate route are labeled with “d-”.

The proton exchange was performed in 2 M hydrochloric acid (HCl, Sigma-Aldrich) for 5 days at 60 °C, and the samples were subsequently washed with deionized water until we had reached a pH value of 7. In our work, we have labeled the resulting samples “H<sub>2</sub>Ti<sub>3</sub>O<sub>7</sub>” and “d-H<sub>2</sub>Ti<sub>3</sub>O<sub>7</sub>”, respectively. To obtain the intermediate phase, thermal annealing was performed in air at 280 °C for 7 h. For complete dehydration, the samples were instead annealed in air at 380 °C for 4 h, yielding samples “TiO<sub>2</sub>” and “d-TiO<sub>2</sub>”, respectively.

**2.2. Structural Characterization.** Scanning electron microscopy was performed using a JEOL JSM-7500F system with an acceleration voltage of 3 kV. The samples were mounted on sticky tape and analyzed without the aid of an additional, conductive sputter coating.

X-ray diffraction was conducted with D8 Discover diffractometer from Bruker AXS calibrated to a corundum standard. It employed a copper source (Cu K $\alpha$ , 40 kV, 40 mA) with a Göbel mirror and a 0.5 mm point focus as optics on the source side. Our two-dimensional VANTEC-500 detector covered an angular range of 20° 2 $\theta$ . We recorded three frames using a measurement time of 1000 s with the detector positioned at 20°, 40°, and 60° 2 $\theta$ .

Raman spectroscopy was performed with a Renishaw inVia system equipped with an Nd:YAG laser (532 nm wavelength), a 2400 mm<sup>-1</sup> grating, and a 50 $\times$  objective with a numeric aperture of 0.75. The laser power was ~0.05 mW, the measurement time was 50 s, and five accumulations were obtained.

Thermogravimetric analysis with mass spectroscopy was performed using an STA 409CD-QMS422 (Netzsch) with synthetic air at a flow rate of 75 mL/min and a heating rate of 5 °C/min.

<sup>1</sup>H magic-angle-spinning nuclear magnetic resonance (<sup>1</sup>H MAS NMR) was performed with a Bruker AVANCE III 300 spectrometer at a spinning frequency of 10 kHz, and the chemical shifts were referenced to CDCl<sub>3</sub> in acetone.

Nitrogen sorption experiments were performed with an Autosorb iQ system (Quantachrome) at a temperature of -196 °C. The samples were degassed at 10<sup>2</sup> Pa and 150 °C for 10 h. The relative pressure was increased from 5.7  $\times$  10<sup>-7</sup> to 1.0 in 58 steps, and the specific surface area (SSA) was calculated according to the Brunauer–Emmett–Teller equation (BET; ref 36) in the linear pressure range per recommendation of the International Union of Pure and Applied Chemistry.<sup>37</sup>

**2.3. Electrochemical Characterization.** The electrodes were prepared by mixing the active materials with 10 mass % of conductive additive (C-ENERGY C65, Imerys Graphite & Carbon) and 10 mass % poly(vinylidene fluoride) (PVdF, Solvay) and dispersed in dimethyl sulfoxide ((CH<sub>3</sub>)<sub>2</sub>SO, Sigma-Aldrich) using a DAC400 FVZ speed mixer. The obtained slurry was doctor-bladed on carbon-coated aluminum foils used as current collectors (Ranafoil, Toyo Aluminium) and dried in a fume hood under ambient conditions. Then, the electrodes were dried further in a vacuum oven at 120 °C for 12 h. The dry electrode thickness is about 30  $\pm$  5  $\mu$ m, resulting in a material loading of 4  $\pm$  1 mg/cm<sup>2</sup>.

Activated carbon counter and quasi-reference electrodes for half-cell tests in acetonitrile containing electrolyte were produced by dispersing activated carbon powder (type YP-80F, Kuraray) in ethanol in a mortar and adding 5 mass % polytetrafluoroethylene (PTFE, 60 mass % aqueous solution, Sigma-Aldrich). The mixture was ground until a dough-like slurry was obtained, and then rolled to a thickness of about 500  $\mu$ m. Positive electrodes for hybrid supercapacitor tests were manufactured as described above using 4.4 g of activated carbon (YP-80F, Kuraray), 2.4 g of lithium manganese oxide (LMO, Sigma-Aldrich), 0.4 g of carbon black and

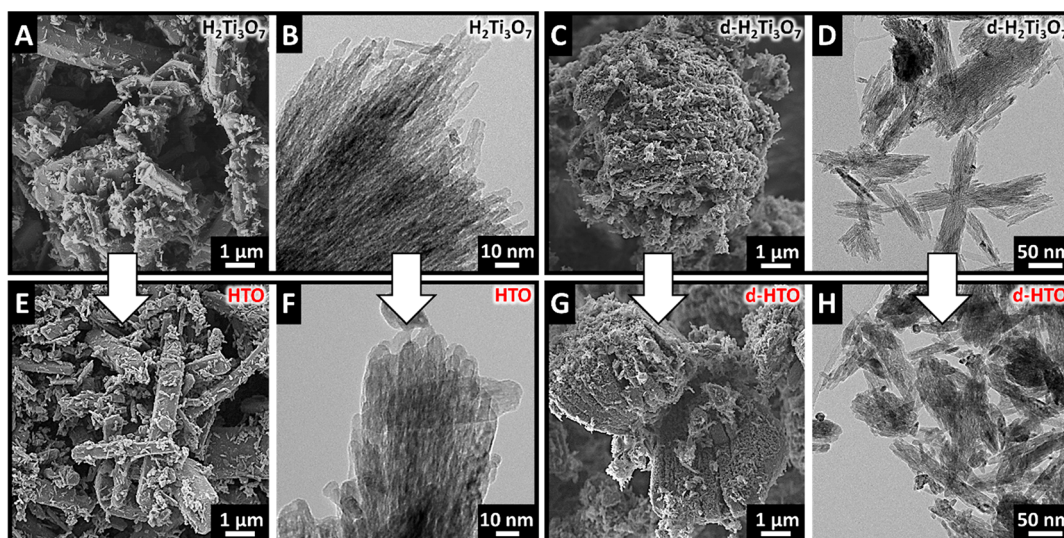


**Figure 1.** Electron micrographs of  $\text{H}_2\text{Ti}_3\text{O}_7$  (A, B) and  $\text{d-H}_2\text{Ti}_3\text{O}_7$  obtained by use of zinc nitrate (C, D). The resulting HTO (E, F) and d-HTO (G, H) materials after annealing at 280 °C. Scanning electron micrographs: A, C, E, G; transmission electron micrographs: B, D, F, H.

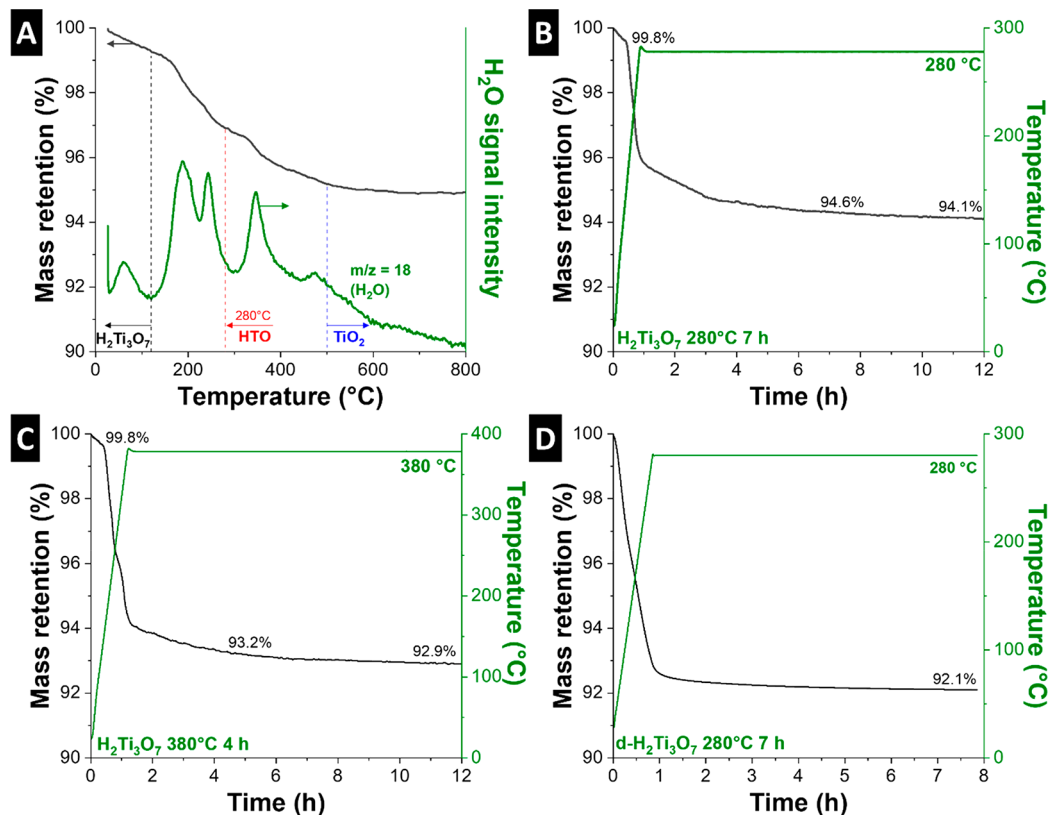


**Figure 2.** Thermogravimetric analysis (TGA) with mass spectroscopy of  $\text{H}_2\text{Ti}_3\text{O}_7$  to 800 °C including  $\text{H}_2\text{O}$  signal (A). TGA of  $\text{H}_2\text{Ti}_3\text{O}_7$  to 280 °C and holding for 7 h (B) and to 380 °C and holding for 4 h (C). TGA of  $\text{d-H}_2\text{Ti}_3\text{O}_7$  to 280 °C and holding for 7 h (D).

0.8 g of PVdF in dimethyl sulfoxide. The dry electrode thickness was  $12 \pm 10 \mu\text{m}$ , and the material loading was  $7 \pm 1 \text{ mg/cm}^2$ .

Electrochemical measurements were performed with a VMP300 system from Bio-Logic Science Instruments by using custom-build poly(ether ether ketone) (PEEK) cells with spring-loaded titanium pistons, as further described elsewhere.<sup>39</sup> All cells were assembled in an argon-filled glovebox (MBraun Labmaster 130,  $\text{O}_2$  and  $\text{H}_2\text{O} < 1 \text{ ppm}$ ). For electrochemical evaluation as lithium-ion battery material, each sample was used as a 12 mm disc electrode and placed against a 10 mm metallic lithium disc electrode, using a 13 mm glass fiber separator (GF/D, Whatman) and 1 M  $\text{LiPF}_6$  in ethylene carbonate/

dimethyl carbonate electrolyte (1:1 by volume; LP30, BASF, battery grade). For half-cell tests aiming toward the hybrid supercapacitor application, we used 1 M  $\text{LiClO}_4$  in acetonitrile (BASF, battery grade) instead due to its superior lithium ion conductivity,<sup>40</sup> low charge transfer resistance, and high electrochemical stability window for high voltage negative electrodes.<sup>41,42</sup> Because of the electrolyte's instability toward lithium, we used 12 mm activated carbon counter electrodes ( $2 \times 500 \mu\text{m}$ , ca. 20 times oversized) and an activated carbon quasi-reference electrode, as established in our previous work.<sup>38</sup> The potential of the carbon quasi-reference was determined to be 3.09 V vs  $\text{Li/Li}^+$ . The specific capacity  $C_{\text{sp}}$  is calculated by integration of the

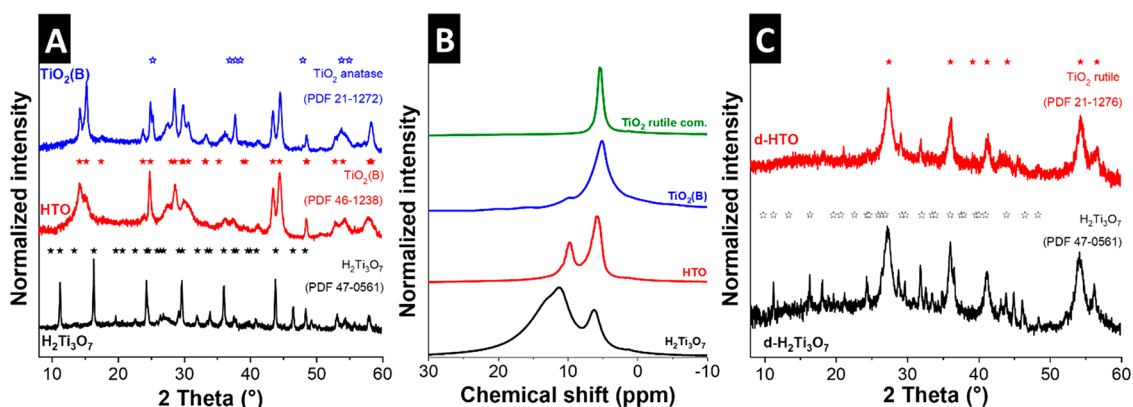


**Figure 3.** X-ray diffractograms of H<sub>2</sub>Ti<sub>3</sub>O<sub>7</sub>, HTO, and TiO<sub>2</sub>(B) (A). <sup>1</sup>H MAS NMR of H<sub>2</sub>Ti<sub>3</sub>O<sub>7</sub> at different states of interlayer deprotonation (B) and XRD of d-H<sub>2</sub>Ti<sub>3</sub>O<sub>7</sub> and d-HTO (C).

specific current  $I/m$ , normalized to the active mass excluding binder and conductive additive, over time  $t - t_0$  during the delithiation step according to eq 2:

$$C_{\text{sp}} = \frac{\int_{t_0}^t I \, dt}{m} \quad (2)$$

Hybrid supercapacitor full-cells were assembled using LMO/AC composite electrodes as the positive electrode (65 mass % AC, 35 mass % commercial LMO, Sigma-Aldrich, described further in ref 43) and HTO (or d-HTO) as the negative electrode. GF/D glass fiber was used as a separator and 1 M LiClO<sub>4</sub> in ACN as an electrolyte. The mass ratio of LMO/AC:HTO was chosen as 3:1. The specific discharge energy  $E_{\text{sp}}$  is obtained by numeric integration of the voltage  $U(t)$  over discharge time  $t - t_0$  with eq 3:

$$E_{\text{sp}} = \frac{I \int_{t_0}^t U(t) \, dt}{M} \quad (3)$$

The specific discharge power was derived by dividing  $E_{\text{sp}}$  by the discharge time. The energy efficiency was derived by dividing by the specific charge energy. The electrochemical performance is reported with respect to the combined mass  $M$  of the active material from HTO or d-HTO, AC, and LMO, excluding the masses of the binder and the conductive additive.

### 3. RESULTS AND DISCUSSION

**3.1. Structural Characterization.** The synthesis of the hydrogen titanium oxides was performed via a solid-state reaction of Na<sub>2</sub>CO<sub>3</sub> with anatase TiO<sub>2</sub> forming Na<sub>2</sub>Ti<sub>3</sub>O<sub>7</sub> and subsequent proton exchange (details in the Supporting Information, Figure S1). Na<sub>2</sub>CO<sub>3</sub> and anatase TiO<sub>2</sub> nanopowders were heated to 800 °C for 20 h. The formed Na<sub>2</sub>Ti<sub>3</sub>O<sub>7</sub> shows a rod-shaped morphology with diameters below 1 μm and a smooth surface. The material was then treated in 2 M HCl at 60 °C for 5 days to exchange sodium with protons in the interlayer of the crystal structure. As seen from scanning and transmission electron micrographs, the obtained H<sub>2</sub>Ti<sub>3</sub>O<sub>7</sub> shows a rodlike morphology with pronounced edges, and additionally smaller needles were formed at the rod surfaces (Figure 1A,B). Furthermore, an alternative synthesis route was explored by adding a small amount of Zn(NO<sub>3</sub>)<sub>2</sub> with a Ti-to-Zn molar ratio of 68:1 to the aqueous solution prior to the solid-state reaction. The resulting d-Na<sub>2</sub>Ti<sub>3</sub>O<sub>7</sub> materials showed significantly larger rodlike features of over 20 μm diameter (Figure S1B). After proton exchange, d-H<sub>2</sub>Ti<sub>3</sub>O<sub>7</sub> shows a flakelike structure of few micrometers size, with smaller needles formed at the surfaces

(Figure 1C,D). In the next step, samples H<sub>2</sub>Ti<sub>3</sub>O<sub>7</sub> and d-H<sub>2</sub>Ti<sub>3</sub>O<sub>7</sub> are partially deprotonated by annealing in an air atmosphere at 280 °C for 7 h to obtain samples HTO and d-HTO, respectively (further described in thermogravimetric analysis part). The morphology of the sample HTO remains rather unchanged (Figure 1E,F), while the lamellar feature became slightly more pronounced for d-HTO after the heat treatment (Figure 1G,H).

Thermogravimetric analysis with mass spectroscopy (TG-MS) was performed to determine the mass and temperature range of H<sub>2</sub>O release during annealing of the H<sub>2</sub>Ti<sub>3</sub>O<sub>7</sub> phase (Figure 2A). During the heating process, the H<sub>2</sub>O signal recorded by mass spectroscopy exhibits four distinct regions of water loss. The first peak ranging from around 40 to 100 °C can be ascribed to the evaporation of water adsorbed at the surface.<sup>44</sup> A further peak is observed at 188 °C. According to the literature, this is related to the transformation of H<sub>2</sub>Ti<sub>3</sub>O<sub>7</sub> to H<sub>2</sub>Ti<sub>6</sub>O<sub>13</sub>, which is associated with the release of 1/6 H<sub>2</sub>O per Ti.<sup>29</sup> The third signal at 243 °C indicates the release of 1/12 further H<sub>2</sub>O per Ti, resulting in the formation of H<sub>2</sub>Ti<sub>12</sub>O<sub>25</sub>.<sup>29</sup> The fourth signal at 346 °C indicates the formation of fully dehydrated TiO<sub>2</sub>(B). Finally, the small signal at around 475 °C may be linked to the release of remaining hydroxyl groups from the lattice. During the entire process, protons are progressively removed from the interlayer of the monoclinic hydrogen titanate material, leading to a densification of the structure and the formation of tunnels that facilitate lithium diffusion.<sup>27</sup>

Based on the determined temperatures of water release, thermogravimetric measurements were performed with heating to and holding at 280 °C (Figure 2B) and 380 °C (Figure 2C), respectively. The ideal mass loss for the release of 1/4 H<sub>2</sub>O or 1/3 H<sub>2</sub>O per Ti to form H<sub>2</sub>Ti<sub>12</sub>O<sub>25</sub> or TiO<sub>2</sub> would be 5.2 or 7.0 mass %, respectively. The required holding time to reach this mass loss was measured to be 7 h at 280 °C and 4 h at 380 °C, respectively. These results confirm that holding at 280 °C for 7 h is a suitable route to synthesize the H<sub>2</sub>Ti<sub>12</sub>O<sub>25</sub> phase (HTO) while holding at 380 °C for 4 h results in complete dehydration. TG measurements of the d-H<sub>2</sub>Ti<sub>3</sub>O<sub>7</sub> material show a high mass loss at relatively low temperatures below 280 °C, suggesting full dehydration at 280 °C (Figure 2D). Consequently, the phase synthesized by the zinc nitrate route contains much weaker bonded interlayer protons than the standard-route H<sub>2</sub>Ti<sub>3</sub>O<sub>7</sub>.

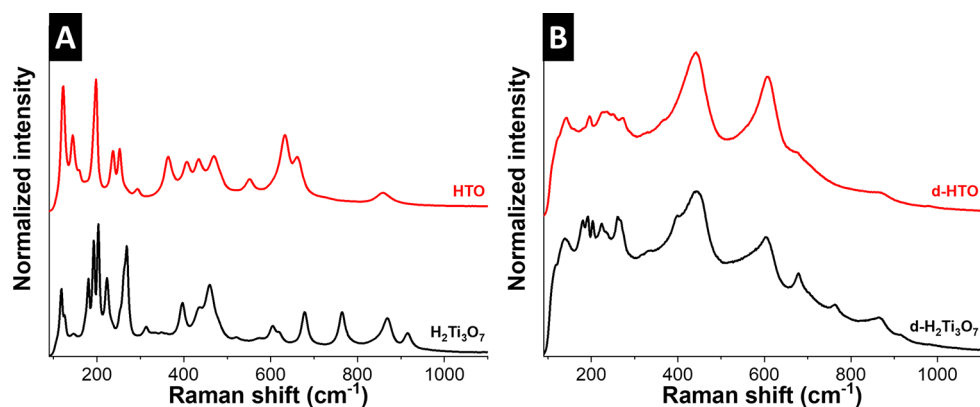


**Figure 4.** Raman spectra of  $\text{H}_2\text{Ti}_3\text{O}_7$  and HTO (A) and  $\text{d-H}_2\text{Ti}_3\text{O}_7$  and  $\text{d-HTO}$  (B) using a laser wavelength of 532 nm.

The crystal structure of the samples was analyzed by X-ray diffraction (XRD), and ideal crystal structures of the associated phases are plotted in Figure S2. For the standard route, hydrogen titanate exhibits the signals of monoclinic  $\text{H}_2\text{Ti}_3\text{O}_7$  with space group  $C2/m$  according to powder diffraction file (PDF) 47-0561 (Figure 3A). After annealing at 280 °C for 7 h, a new monoclinic phase resembling bronze titania (PDF 46-1238,  $\text{TiO}_2(\text{B})$ ) emerges that we label “HTO”. Past studies have analyzed the dehydration behavior of  $\text{H}_2\text{Ti}_3\text{O}_7$  and proposed three-step dehydration, resulting in the intermediate phases  $\text{H}_2\text{Ti}_6\text{O}_{13}$ ,  $\text{H}_2\text{Ti}_{12}\text{O}_{25}$ , and  $\text{TiO}_2(\text{B})$ .<sup>27,29</sup> Accordingly, the obtained HTO phase aligns with monoclinic  $\text{H}_2\text{Ti}_{12}\text{O}_{25}$ . The content of hydrogen containing groups can be traced by the shift toward higher diffraction angles of the monoclinic (110) reflection.<sup>27</sup> The angular position of the latter reflection is at 24.4°  $2\theta$  for  $\text{H}_2\text{Ti}_3\text{O}_7$  and shifted to 24.8°  $2\theta$  for HTO. The similarities of the crystal structure of  $\text{H}_2\text{Ti}_{12}\text{O}_{25}$  and  $\text{TiO}_2(\text{B})$  phases with minor shifts of diffraction angles suggest that a gradual water release occurs during annealing instead of a phase transformation process. Further annealing of  $\text{H}_2\text{Ti}_3\text{O}_7$  at 380 °C for 4 h yields a diffractogram matching with  $\text{TiO}_2(\text{B})$ . Full dehydration is indicated by a further shift of the (110) reflection to 24.93°  $2\theta$  being exactly in line with the ideal signal position of bronze titania according to PDF 46-1238. In addition to this signal, a weak diffraction pattern emerges at this annealing temperature matching anatase titania according to PDF 21-1272. The characteristic diffraction peaks are located at 25.8° and 37.8°  $2\theta$ .

As a further tool to analyze the content of hydrogen containing groups, we performed magic angle spinning nuclear magnetic resonance (NMR) spectroscopy of  $^1\text{H}$  (Figure 3B). We included commercially available rutile  $\text{TiO}_2$  as a reference, showing a single peak at 5.7 ppm in the spectrum. In the absence of hydroxyl groups in bulk rutile, we link the signal to adsorbed surface groups containing hydrogen atoms. Besides these groups, hydrogen titanate samples in different hydrogen containing states exhibit a further NMR signal between 9.5 and 11.5 ppm, which we link to hydrogen species in the bulk of the materials, such as interlayer protons.  $\text{H}_2\text{Ti}_3\text{O}_7$  shows the largest of these signals, confirming the highest hydrogen-containing group content of this sample. A gradual reduction of the peak intensity coincides with progressing interlayer deprotonation at higher annealing temperatures. For the sample annealed at 380 °C for 4 h, no hydrogen was expected to be found in the lattice according to TG and XRD results, but a small NMR signal at around 10 ppm remains. This may

suggest that bronze titania can incorporate small amounts of hydrogen-containing groups.

Samples synthesized by using  $\text{Zn}(\text{NO}_3)_2$  show a distinctly different diffractogram (Figure 3C). While the monoclinic  $\text{H}_2\text{Ti}_3\text{O}_7$  phase is also formed in sample  $\text{d-H}_2\text{Ti}_3\text{O}_7$ , it also features a significant diffraction signal of rutile  $\text{TiO}_2$ , according to PDF 21-1276. The  $2\theta$  positions of the rutile related reflections for  $\text{d-H}_2\text{Ti}_3\text{O}_7$  are slightly lower, with main reflections at 27.2°, 36.0°, and 54.2°  $2\theta$ , compared to the ideal rutile positions at 27.45°, 36.09°, and 54.32°  $2\theta$ , which are likely related to hydrogen-containing groups inside the rutile phase. Interestingly, the addition of a small amount of  $\text{Zn}(\text{NO}_3)_2$  led to the preferred crystallization of the rutile phase. Thermal treatment at 280 °C for 7 h leads to the formation of  $\text{d-HTO}$ . This phase exhibits rutile reflections at slightly higher angular positions as  $\text{d-H}_2\text{Ti}_3\text{O}_7$ , with the main peaks at 27.4°, 36.1°, and 54.2°  $2\theta$ , matching the ideal rutile positions according to PDF 21-1276.

We also recorded Raman spectra of the samples (Figure 4). The Raman spectrum of  $\text{H}_2\text{Ti}_3\text{O}_7$  exhibits several bands at around 200  $\text{cm}^{-1}$  with peak maxima at 180, 193, 203, 223, 263, and 268  $\text{cm}^{-1}$  (Figure 4A). The spectrum resembles previously reported spectra of this phase.<sup>45–48</sup> In particular, we note the Ti–O related band at around 270  $\text{cm}^{-1}$  and a possible Ti–O–H bond related signal at 857  $\text{cm}^{-1}$ .<sup>48</sup> The Raman signal of HTO matches with data from previous reports of  $\text{TiO}_2(\text{B})$ ;<sup>49</sup> in particular, we note the strong  $B_g$ -symmetry Raman bands at 122, 198, 237, and 252  $\text{cm}^{-1}$  along with  $A_g$ -symmetry modes at 144 and 159  $\text{cm}^{-1}$ . The presence of  $\text{TiO}_2(\text{B})$  indicated by Raman aligns with our XRD findings.<sup>50</sup> Both samples synthesized by use of zinc nitrate show the main vibration modes  $E_g$  and  $A_{1g}$  of rutile at around 442 and 604  $\text{cm}^{-1}$ , whereas the rutile signal at 140  $\text{cm}^{-1}$  only shows very weak intensity (Figure 4B).<sup>51</sup> Additionally, several bands around 200  $\text{cm}^{-1}$  indicate the presence of the  $\text{H}_2\text{Ti}_3\text{O}_7$  phase, matching the XRD results. These signals are also found in the  $\text{d-HTO}$  sample.

In addition, we quantified the porosity of the samples by the use of nitrogen gas sorption (Figure S3). The BET surface area of the  $\text{H}_2\text{Ti}_3\text{O}_7$  and HTO samples is around 30  $\text{m}^2/\text{g}$ , whereas the samples synthesized by use of zinc nitrate show a BET surface area between 55 and 75  $\text{m}^2/\text{g}$ . This is in alignment with SEM observations, suggesting a lamellar structure with increased surface area resulting from the zinc nitrate route. The underpinning mechanism for this unique behavior is unclear at this point and was not described in the literature before. It is conceivable that the zinc nitrate synthesis route

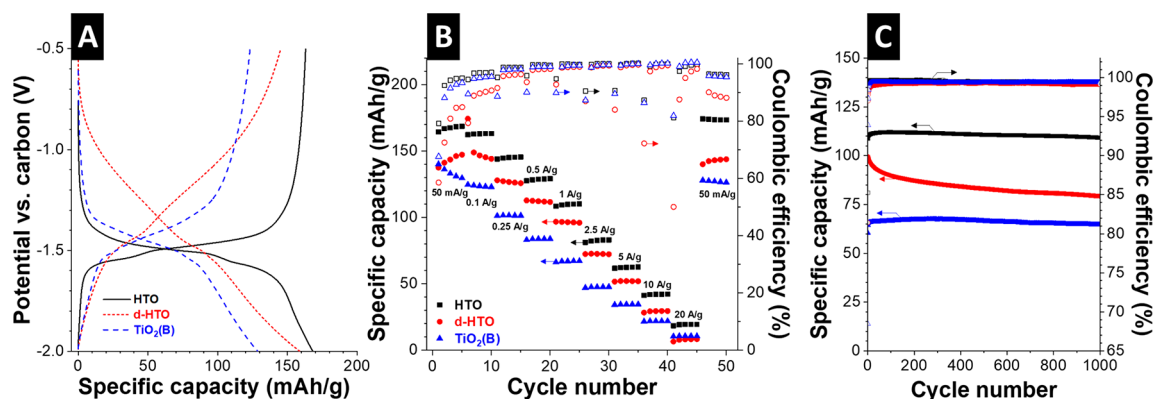


**Figure 5.** Galvanostatic charge/discharge profiles of  $\text{H}_2\text{Ti}_3\text{O}_7$ , HTO, and  $\text{TiO}_2(\text{B})$  at 0.1 A/g in 1 M  $\text{LiClO}_4$  in acetonitrile electrolyte (A). Corresponding rate handling behavior of the materials at cycling rates between 50 mA/g and 20 A/g (B) and cycling stability of the materials at a rate of 1 A/g over 1000 cycles (C).

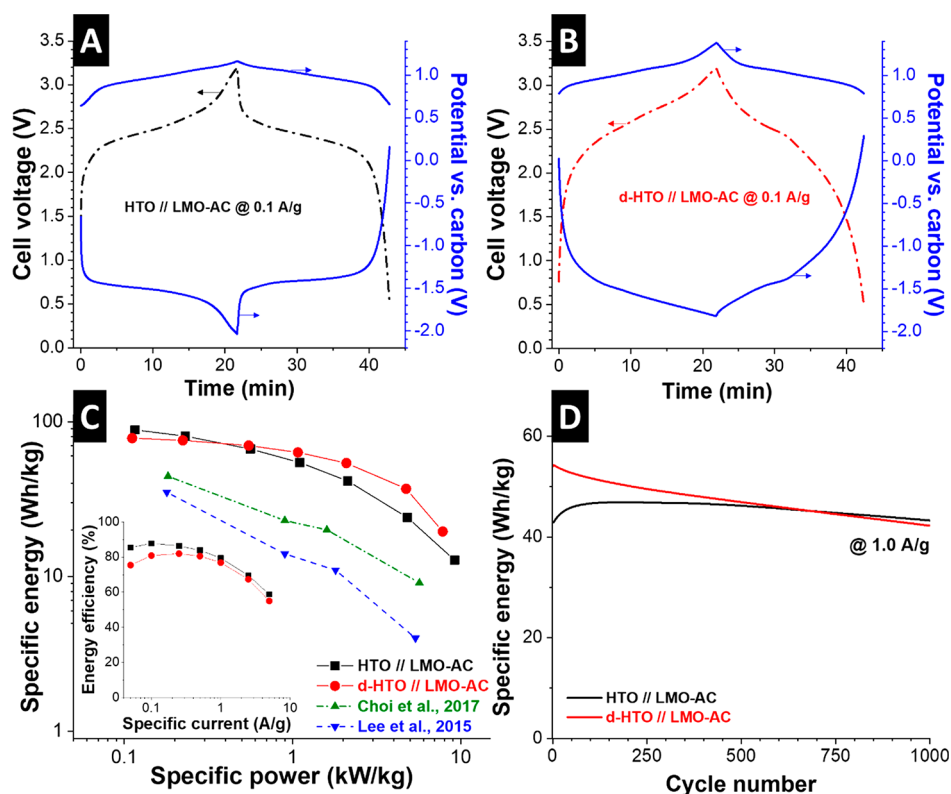


**Figure 6.** Galvanostatic charge/discharge profile including potential evolution at negative and positive electrodes observed by a carbon quasi-reference of a full-cell with HTO (A) or d-HTO (B) as a negative electrode and LMO-AC as a positive electrode. Ragone chart of corresponding cells with energy efficiency values in the inset (C). Cycling stability between 0.5 and 3.2 V cell voltage over 1000 cycles at 1 A/g (D). Data were adapted from Lee et al.<sup>33</sup> and Choi et al.<sup>34</sup>

and the subsequent hydrochloric acid treatment did lead to the delamination of the Ti–O-layers of the  $\text{H}_2\text{Ti}_3\text{O}_7$  phase. This phase consists out Ti–O-sheets which are solely connected to each other by the ionic attraction of interlayer protons (Figure S2D).<sup>52</sup> Such a delamination phenomenon is reminiscent of the synthesis of 2D materials like MXenes.<sup>53</sup>

**3.2. Electrochemical Characterization.** As a first baseline,  $\text{H}_2\text{Ti}_3\text{O}_7$  and the partially dehydrated HTO samples were tested as lithium-ion battery anode using 1 M  $\text{LiPF}_6$  in ethylene carbonate/dimethyl carbonate in a voltage window of 1–3 V vs  $\text{Li}/\text{Li}^+$ . The sample d- $\text{H}_2\text{Ti}_3\text{O}_7$  possesses a better high-rate performance than  $\text{H}_2\text{Ti}_3\text{O}_7$  (Figure S4B). Such a behavior can be explained by the lamellar microstructure and

the associated increased surface area which is formed when  $\text{Zn}(\text{NO}_3)_2$  is added during the synthesis (Figure S1). In this case, the  $\text{Li}^+$  diffusion pathways in the solid are beneficially decreased, and thus an enhanced rate capability is observed. After heat treatment a different trend can be observed, caused by the different phases formed: Sample HTO consists primarily of a high rate capable  $\text{TiO}_2(\text{B})$  phase with small amounts of hydrogen-containing groups, whereas the sample d-HTO is composed out of rutile  $\text{TiO}_2$  (Figure 4). According to the literature, the rutile polymorph shows poor electrochemical performance.<sup>24,54</sup> Follow-up work should thus focus on synthesis optimization to avoid a phase transition into rutile  $\text{TiO}_2$  and further increase the electrochemical performance of

this promising lamellar material. The HTO phase possesses a higher capacity of 185 mAh/g compared to 140 mAh/g of  $\text{H}_2\text{Ti}_3\text{O}_7$  and a superior rate handling with a retention of 80 mAh/g at 1.75 A/g compared to 19 mAh/g (Figure S4). Based on this promising high rate capability, further electrochemical characterization for application in a hybrid supercapacitor was performed only with the HTO and d-HTO samples.

Electrochemical measurements of HTO and d-HTO samples were performed in 1 M  $\text{LiClO}_4$  in acetonitrile as the electrolyte. Additionally, electrodes of the sample  $\text{TiO}_2(\text{B})$  with a fully deprotonated interlayer were tested as a reference. Galvanostatic charge/discharge measurements of the electrodes were conducted in a half-cell setup against an oversized AC counter electrode, and the voltage profile at a current of 0.1 A/g is shown in Figure 5A. HTO shows a relatively constant insertion and deinsertion plateau potential between around  $-1.45$  and  $-1.55$  V vs a carbon quasi-reference electrode. This behavior is consistent with prior reports on  $\text{H}_2\text{Ti}_{12}\text{O}_{25}$  in the literature.<sup>34,35</sup> The d-HTO material, however, shows a sloping charge/discharge profile which resembles previous reports of rutile titania insertion behavior.<sup>16,17</sup> The  $\text{TiO}_2(\text{B})$  electrode show insertion plateaus between  $-1.35$  and  $-1.5$  V vs carbon, exhibiting the highest insertion potential of the tested materials.

We tested the rate handling of all materials at various specific currents, ranging from 50 mA/g to 20 A/g (Figure 5B). The Coulombic efficiency of the first charge/discharge cycle is 80% for HTO and at 59% for d-HTO. It was previously reported that rutile titania exhibits a high irreversible capacity in the first cycle,<sup>16</sup> which is confirmed for the d-HTO material. The maximum capacity of HTO is 169 mAh/g, whereas d-HTO exhibits a maximum of 147 mAh/g. Both materials show superior capacity compared to the reference  $\text{TiO}_2(\text{B})$  material with a reversible capacity of about 130 mAh/g. HTO and d-HTO materials show excellent rate handling behavior, with a retention of 65% of the maximum capacity at a galvanostatic charge/discharge rate of 1 A/g. At very high rates of 10–20 A/g, HTO retains a higher capacity compared to d-HTO, that is, 25–11% compared to 16–8%. Moreover, all materials restored their capacity after returning to a low rate of 50 mA/g after 45 cycles.

The cycling stability was tested over 1000 charge/discharge cycles at a rate of 1 A/g (Figure 5C). The elevated rate was chosen to match the targeted operation conditions in the LIC full-cell application. All materials showed good stability, with HTO retaining 98.4% and d-HTO about 80% after 1000 cycles. The tests indicate that the HTO material synthesized without the addition of  $\text{Zn}(\text{NO}_3)_2$  shows the most favorable half-cell performance.

Hybrid supercapacitor full-cells were then assembled with HTO or d-HTO as the negative electrode and a composite containing 65 mass % of activated carbon (AC) and 35 mass % of lithium manganese oxide (LMO) as the positive electrode (LMO-AC).<sup>18,43</sup> The mass of the positively polarized LMO-AC electrode was chosen 3 times higher as the negative electrode to account for its lower specific capacity. This composition of the positive electrode was demonstrated to provide good performance in a hybrid supercapacitor setup.<sup>43</sup>

The galvanostatic charge/discharge cycle of the HTO/LMO-AC cell at 0.1 A/g is depicted in Figure 6A. The cells were cycled between a cell voltage of 0.5 and 3.2 V. We avoided a deep discharge of the cell to 0 V to prevent a shifting of the potential of individual electrodes outside their stability

windows to improve the cycling stability.<sup>55</sup> During charging, a quick rise in cell voltage to  $\sim 2.0$  V results from the negative HTO electrode reaching its insertion plateau potential at around  $-1.45$  V vs carbon. Simultaneously, the potential profile of the LMO-AC electrode shows two different slopes: The steeper slope up to  $+0.85$  V vs carbon is associated with ion electrosorption at the AC surface, while the following potential regime to  $+1.16$  V vs carbon is dominated by lithium deinsertion from the LMO particles. The discharging step shows a very symmetric behavior of the voltage profile compared to the charging step, resulting in the excellent energy efficiency of the LIC device of 87.7% at 0.1 A/g.

The galvanostatic charge/discharge of the d-HTO/LMO-AC cell at 0.1 A/g cycled between 0.5 and 3.2 V cell voltage is shown in Figure 6B. The voltage increase when charging is less steep than for the HTO cell. This is caused by the behavior of the negative d-HTO electrode, showing a sloping insertion potential between ca.  $-1.2$  and  $-1.8$  V vs carbon. The positive LMO-AC electrode shows the same behavior as described above. The voltage profile during discharge also shows high symmetry, however, but a slight overpotential of the insertion reaction of the negative d-HTO electrode during discharging causes a lower energy efficiency of 80.8%.

The specific energy and power of the cells over a wide range of specific currents between 50 mA/g and 5 A/g is shown in a Ragone plot in Figure 6C. The HTO/LMO-AC cell exhibits maximum energy of 88.5 Wh/kg at 116 W/kg and an energy of 12.76 Wh/kg at 9.2 kW/kg. The d-HTO/LMO-AC cell shows a maximum energy of 78.3 Wh/kg at 111 W/kg and 19.5 Wh/kg at 7.8 kW/kg. The higher performance of the HTO cell is a consequence of the improved capacity and rate handling, which was already observed during half-cell tests. The cells show similar energy efficiency at all cycling currents, as shown in the inset of Figure 6C. Even at the highest current of 5 A/g, the energy efficiency is over 55% for both cells. The comparative Ragone plot in Figure 6C of our data in comparison with values of other asymmetric cells using protonated titanates from the literature underlines the attractive performance of the HTO and d-HTO cells in both power and energy. For example, Choi et al. used Zn-doped  $\text{H}_2\text{Ti}_{11.7}\text{Zn}_{0.3}\text{O}_{24.7}$  as the negative electrode and AC as the positive electrode and obtained a maximum energy of 44.4 Wh/kg,<sup>34</sup> whereas Lee et al. reported on undoped  $\text{H}_2\text{Ti}_{12}\text{O}_{25}$  paired with AC exhibiting a maximum of 35 Wh/kg.<sup>32</sup> The cycling stability of the presented LIC cells is shown in Figure 6D. Over 1000 charge/discharge cycles at 1 A/g, the HTO/LMO-AC cell retains 100% of its initial capacity, whereas the d-HTO/LMO-AC cell shows retention of 81%.

#### 4. CONCLUSIONS

Hydrogen titanate materials were synthesized by a proton exchange reaction with sodium titanate. Annealing of the  $\text{H}_2\text{Ti}_3\text{O}_7$  phase at 280 °C yielded HTO, which we found to have an almost identical crystal structure as bronze titania. Deprotonation of the interlayer of the monoclinic hydrogen titanate material over several steps densifies the structure and leads to tunnel-formation that facilitates lithium diffusion. By use of zinc nitrate as a chemical agent, we obtained hydrogen titanate with a high rutile content. Water extraction of the latter at 280 °C resulted in a lamellar rutile phase. The materials were tested in a lithium-ion battery and in a hybrid supercapacitor setup. It was shown that both HTO and d-HTO showed superior performance compared to the initial

hydrogen titanate phases. Hybrid supercapacitor cells were constructed showing high energy of up to 88 Wh/kg and high power of up to 9.2 kW/kg in an organic electrolyte. The attractive performance metrics underline the potential of the hydrogenated titanate materials in high-power applications.

## ■ ASSOCIATED CONTENT

### ● Supporting Information

The Supporting Information is available free of charge on the ACS Publications website at DOI: 10.1021/acsam.9b00363.

Supporting electron micrographs, ideal crystal structures, supporting Raman spectra, supporting nitrogen gas sorption isotherms, supporting electrochemical data, and supporting calculated resistance values (PDF)

## ■ AUTHOR INFORMATION

### Corresponding Author

\*E-mail: volker.presser@leibniz-inm.de.

### ORCID

Volker Presser: 0000-0003-2181-0590

### Author Contributions

<sup>†</sup>S.F. and K.P. made equal contributions.

### Notes

The authors declare no competing financial interest.

## ■ ACKNOWLEDGMENTS

We acknowledge funding from the German Federal Ministry for Economic Affairs and Energy (BMWi) in support of the HyBaCap project (award number 03ET6113C). The authors thank L. Bommer (Bosch), H.-J. Meyer (Eberhard Karls Universität Tübingen), K. Strohmaier (Eberhard Karls Universität Tübingen), and M. Tuchen (Bosch) for support and helpful discussions. The INM authors thank Eduard Arzt (INM) for his continuing support.

## ■ REFERENCES

- (1) Yang, Z.; Zhang, J.; Kintner-Meyer, M. C.; Lu, X.; Choi, D.; Lemmon, J. P.; Liu, J. Electrochemical energy storage for green grid. *Chem. Rev.* **2011**, *111* (5), 3577–3613.
- (2) Fan, L.; Chen, S.; Ma, R.; Wang, J.; Wang, L.; Zhang, Q.; Zhang, E.; Liu, Z.; Lu, B. Ultrastable Potassium Storage Performance Realized by Highly Effective Solid Electrolyte Interphase Layer. *Small* **2018**, *14* (30), 1801806.
- (3) Wang, L.; Zhang, Q.; Zhu, J.; Duan, X.; Xu, Z.; Liu, Y.; Yang, H.; Lu, B. Nature of extra capacity in MoS<sub>2</sub> electrodes: Molybdenum atoms accommodate with lithium. *Energy Storage Materials*. **2019**, *16*, 37–45.
- (4) Whittingham, M. S. Ultimate Limits to Intercalation Reactions for Lithium Batteries. *Chem. Rev.* **2014**, *114* (23), 11414–11443.
- (5) Salanne, M.; Rotenberg, B.; Naoi, K.; Kaneko, K.; Taberna, P. L.; Grey, C. P.; Dunn, B.; Simon, P. Efficient storage mechanisms for building better supercapacitors. *Nat. Energy*. **2016**, *1*, 16070.
- (6) Tarascon, J.-M.; Armand, M. Issues and challenges facing rechargeable lithium batteries. *Nature* **2001**, *414* (6861), 359–367.
- (7) Goodenough, J. B.; Park, K. S. The Li-ion rechargeable battery: a perspective. *J. Am. Chem. Soc.* **2013**, *135* (4), 1167–1176.
- (8) Verma, P.; Maire, P.; Novak, P. A review of the features and analyses of the solid electrolyte interphase in Li-ion batteries. *Electrochim. Acta* **2010**, *55* (22), 6332–6341.
- (9) Xu, K. Nonaqueous liquid electrolytes for lithium-based rechargeable batteries. *Chem. Rev.* **2004**, *104* (10), 4303–4418.
- (10) Wu, H. B.; Chen, J. S.; Hng, H. H.; Lou, X. W. D. Nanostructured metal oxide-based materials as advanced anodes for lithium-ion batteries. *Nanoscale* **2012**, *4* (8), 2526–2542.

(11) Dörr, T. S.; Fleischmann, S.; Zeiger, M.; Grobelsek, I.; de Oliveira, P. W.; Presser, V. Ordered mesoporous titania/carbon hybrid monoliths for lithium-ion battery anodes with high areal and volumetric capacity. *Chem. - Eur. J.* **2018**, *24* (24), 6358–6363.

(12) Lim, E.; Shim, H.; Fleischmann, S.; Presser, V. Fast and stable lithium-ion storage kinetics of anatase titanium dioxide/carbon onion hybrid electrodes. *J. Mater. Chem. A* **2018**, *6*, 9480–9488.

(13) Wang, J.; Polleux, J.; Lim, J.; Dunn, B. Pseudocapacitive contributions to electrochemical energy storage in TiO<sub>2</sub> (anatase) nanoparticles. *J. Phys. Chem. C* **2007**, *111* (40), 14925–14931.

(14) Xu, J.; Jia, C.; Cao, B.; Zhang, W. Electrochemical properties of anatase TiO<sub>2</sub> nanotubes as an anode material for lithium-ion batteries. *Electrochim. Acta* **2007**, *52* (28), 8044–8047.

(15) Hua, X.; Liu, Z.; Fischer, M. G.; Borkiewicz, O.; Chupas, P. J.; Chapman, K. W.; Steiner, U.; Bruce, P. G.; Grey, C. P. Lithiation thermodynamics and kinetics of the TiO<sub>2</sub> (B) nanoparticles. *J. Am. Chem. Soc.* **2017**, *139* (38), 13330–13341.

(16) Pfanzelt, M.; Kubiak, P.; Fleischhammer, M.; Wohlfahrt-Mehrens, M. TiO<sub>2</sub> rutile - an alternative anode material for safe lithium-ion batteries. *J. Power Sources* **2011**, *196* (16), 6815–6821.

(17) Hu, Y. S.; Kienle, L.; Guo, Y. G.; Maier, J. High lithium electroactivity of nanometer-sized rutile TiO<sub>2</sub>. *Adv. Mater.* **2006**, *18* (11), 1421–1426.

(18) Fleischmann, S.; Widmaier, M.; Schreiber, A.; Shim, H.; Stiemke, F. M.; Schubert, T. J. S.; Presser, V. High voltage asymmetric hybrid supercapacitors using lithium-and sodium-containing ionic liquids. *Energy Storage Materials*. **2019**, *16*, 391–399.

(19) Liu, Z.; Andreev, Y. G.; Armstrong, A. R.; Brutti, S.; Ren, Y.; Bruce, P. G. Nanostructured TiO<sub>2</sub> (B): the effect of size and shape on anode properties for Li-ion batteries. *Prog. Nat. Sci.* **2013**, *23* (3), 235–244.

(20) Wang, D.; Choi, D.; Yang, Z.; Viswanathan, V. V.; Nie, Z.; Wang, C.; Song, Y.; Zhang, J.-G.; Liu, J. Synthesis and Li-ion insertion properties of highly crystalline mesoporous rutile TiO<sub>2</sub>. *Chem. Mater.* **2008**, *20* (10), 3435–3442.

(21) Ren, Y.; Hardwick, L. J.; Bruce, P. G. Lithium intercalation into mesoporous anatase with an ordered 3D pore structure. *Angew. Chem.* **2010**, *122* (14), 2624–2628.

(22) Armstrong, A. R.; Armstrong, G.; Canales, J.; Bruce, P. G. TiO<sub>2</sub>-B nanowires as negative electrodes for rechargeable lithium batteries. *J. Power Sources* **2005**, *146* (1–2), 501–506.

(23) Tsai, M.-C.; Chang, J.-C.; Sheu, H.-S.; Chiu, H.-T.; Lee, C.-Y. Lithium ion intercalation performance of porous laminal titanium dioxides synthesized by sol-gel process. *Chem. Mater.* **2009**, *21* (3), 499–505.

(24) Zhu, G.-N.; Wang, Y.-G.; Xia, Y.-Y. Ti-based compounds as anode materials for Li-ion batteries. *Energy Environ. Sci.* **2012**, *5* (5), 6652–6667.

(25) Arrouel, C.; Parker, S. C.; Islam, M. S. Lithium insertion and transport in the TiO<sub>2</sub>-B anode material: a computational study. *Chem. Mater.* **2009**, *21* (20), 4778–4783.

(26) Wang, C.-M.; Chen, L.; Su, Y.-L.; Yang, G.-L.; Zhang, W.-L. The preparation of H<sub>2</sub>Ti<sub>12</sub>O<sub>25</sub> via multi-method and their rate performance in Lithium ions battery. *Electrochim. Acta* **2016**, *213*, 375–381.

(27) Zhu, G.-N.; Wang, C.-X.; Xia, Y.-Y. Structural transformation of layered hydrogen trititanate (H<sub>2</sub>Ti<sub>3</sub>O<sub>7</sub>) to TiO<sub>2</sub> (B) and its electrochemical profile for lithium-ion intercalation. *J. Power Sources* **2011**, *196* (5), 2848–2853.

(28) Papp, S.; Korosi, L.; Meynen, V.; Cool, P.; Vansant, E. F.; Dekany, I. The influence of temperature on the structural behaviour of sodium tri- and hexa-titanates and their protonated forms. *J. Solid State Chem.* **2005**, *178* (5), 1614–1619.

(29) Morgado Jr, E.; Jardim, P. M.; Marinkovic, B. A.; Rizzo, F. C.; de Abreu, M. A. S.; Zotin, J. L.; Araújo, A. S. Multistep structural transition of hydrogen trititanate nanotubes into TiO<sub>2</sub>-B nanotubes: a comparison study between nanostructured and bulk materials. *Nanotechnology* **2007**, *18* (49), 495710.

- (30) Akimoto, J.; Chiba, K.; Kijima, N.; Hayakawa, H.; Hayashi, S.; Gotoh, Y.; Idemoto, Y. Soft-chemical synthesis and electrochemical property of  $\text{H}_2\text{Ti}_{12}\text{O}_{25}$  as a negative electrode material for rechargeable lithium-ion batteries. *J. Electrochem. Soc.* **2011**, *158* (5), A546–A549.
- (31) Akimoto, J.; Kataoka, K.; Kojima, N.; Hayashi, S.; Gotoh, Y.; Sotokawa, T.; Kumashiro, Y. A novel soft-chemical synthetic route using  $\text{Na}_2\text{Ti}_6\text{O}_{13}$  as a starting compound and electrochemical properties of  $\text{H}_2\text{Ti}_{12}\text{O}_{25}$ . *J. Power Sources* **2013**, *244*, 679–683.
- (32) Lee, S.-H.; Kim, H.-K.; Lee, J. H.; Lee, S.-G.; Lee, Y.-H. Fabrication and electrochemical properties of cylindrical hybrid supercapacitor using  $\text{H}_2\text{Ti}_{12}\text{O}_{25}$  as anode material. *Mater. Lett.* **2015**, *143*, 101–104.
- (33) Lee, S.-H.; Lee, S.-G.; Yoon, J.-R.; Kim, H.-K. Novel performance of ultrathin  $\text{AlPO}_4$  coated  $\text{H}_2\text{Ti}_{12}\text{O}_{25}$  Exceeding  $\text{Li}_4\text{Ti}_5\text{O}_{12}$  in cylindrical hybrid supercapacitor. *J. Power Sources* **2015**, *273*, 839–843.
- (34) Choi, H.-J.; Lee, S.-H.; Kim, J. H.; Kim, H.-K.; Kim, J.-M. Zinc doped  $\text{H}_2\text{Ti}_{12}\text{O}_{25}$  anode and activated carbon cathode for hybrid supercapacitor with superior performance. *Electrochim. Acta* **2017**, *251*, 613–620.
- (35) Guo, Q.; Chen, L.; Shan, Z.; Lee, W. S. V.; Xiao, W.; Liu, Z.; Liang, J.; Yang, G.; Xue, J. High lithium insertion voltage single-crystal  $\text{H}_2\text{Ti}_{12}\text{O}_{25}$  nanorods as a high-capacity and high-rate lithium-ion battery anode material. *ChemSusChem* **2018**, *11* (1), 299–310.
- (36) Brunauer, S.; Emmett, P. H.; Teller, E. Adsorption of gases in multimolecular layers. *J. Am. Chem. Soc.* **1938**, *60* (2), 309–319.
- (37) Thommes, M.; Kaneko, K.; Neimark, A. V.; Olivier, J. P.; Rodriguez-Reinoso, F.; Rouquerol, J.; Sing, K. S. W. Physisorption of gases, with special reference to the evaluation of surface area and pore size distribution (IUPAC Technical Report). *Pure Appl. Chem.* **2015**, *87* (9–10), 1051.
- (38) Widmaier, M.; Krüner, B.; Jäckel, N.; Aslan, M.; Fleischmann, S.; Engel, C.; Presser, V. Carbon as quasi-reference electrode in unconventional lithium-salt containing electrolytes for hybrid battery/supercapacitor devices. *J. Electrochem. Soc.* **2016**, *163* (14), A2956–A2964.
- (39) Weingarh, D.; Zeiger, M.; Jäckel, N.; Aslan, M.; Feng, G.; Presser, V. Graphitization as a universal tool to tailor the potential-dependent capacitance of carbon supercapacitors. *Adv. Energy Mater.* **2014**, *4*, 1400316.
- (40) Beguin, F.; Presser, V.; Balducci, A.; Frackowiak, E. Carbons and electrolytes for advanced supercapacitors. *Adv. Mater.* **2014**, *26* (14), 2219–2251.
- (41) Widmaier, M.; Jäckel, N.; Zeiger, M.; Abuzarli, M.; Engel, C.; Bommer, L.; Presser, V. Influence of carbon distribution on the electrochemical performance and stability of lithium titanate based energy storage devices. *Electrochim. Acta* **2017**, *247* (1), 1006–1018.
- (42) Wang, Q.; Zakeeruddin, S. M.; Exnar, I.; Grätzel, M. 3-Methoxypropionitrile-Based Novel Electrolytes for High-Power Li-Ion Batteries with Nanocrystalline  $\text{Li}_4\text{Ti}_5\text{O}_{12}$  Anode. *J. Electrochem. Soc.* **2004**, *151* (10), A1598–A1603.
- (43) Widmaier, M.; Pfeifer, K.; Bommer, L.; Presser, V. Valence-tuned lithium titanate nanopowder for high-rate electrochemical energy storage. *Batteries & Supercaps.* **2018**, *1* (1), 11–26.
- (44) Henderson, M. A. Evidence for bicarbonate formation on vacuum annealed  $\text{TiO}_2$  (110) resulting from a precursor-mediated interaction between  $\text{CO}_2$  and  $\text{H}_2\text{O}$ . *Surf. Sci.* **1998**, *400* (1–3), 203–219.
- (45) Liu, H.; Zheng, Z.; Yang, D.; Waclawik, E.; Ke, X.; Zhu, H.; Palmer, S.; Frost, R. L. A Raman spectroscopic study on the allocation of ammonium adsorbing sites on  $\text{H}_2\text{Ti}_3\text{O}_7$  nanofibre and its structural derivation during calcination. *J. Raman Spectrosc.* **2010**, *41* (12), 1601–1605.
- (46) Gajovic, A.; Friščić, I.; Plodinec, M.; Iveković, D. High temperature Raman spectroscopy of titanate nanotubes. *J. Mol. Struct.* **2009**, *924–926*, 183–191.
- (47) Qian, L.; Du, Z.-L.; Yang, S.-Y.; Jin, Z.-S. Raman study of titania nanotube by soft chemical process. *J. Mol. Struct.* **2005**, *749* (1–3), 103–107.
- (48) Byeon, S.-H.; Lee, S.-O.; Kim, H. Structure and Raman Spectra of Layered Titanium Oxides. *J. Solid State Chem.* **1997**, *130* (1), 110–116.
- (49) Zukalova, M.; Kalbac, M.; Kavan, L.; Exnar, I.; Graetzel, M. Pseudocapacitive lithium storage in  $\text{TiO}_2$  (B). *Chem. Mater.* **2005**, *17* (5), 1248–1255.
- (50) Jokisaari, J. R.; Bayerl, D.; Zhang, K.; Xie, L.; Nie, Y.; Schlom, D. G.; Kioupakis, E.; Graham, G. W.; Pan, X. Polarization-Dependent Raman Spectroscopy of Epitaxial  $\text{TiO}_2$ (B) Thin Films. *Chem. Mater.* **2015**, *27* (23), 7896–7902.
- (51) Ma, H. L.; Yang, J. Y.; Dai, Y.; Zhang, Y. B.; Lu, B.; Ma, G. H. Raman study of phase transformation of  $\text{TiO}_2$  rutile single crystal irradiated by infrared femtosecond laser. *Appl. Surf. Sci.* **2007**, *253* (18), 7497–7500.
- (52) Kataoka, K.; Kijima, N.; Akimoto, J. Ion-Exchange Synthesis, Crystal Structure, and Physical Properties of Hydrogen Titanium Oxide  $\text{H}_2\text{Ti}_3\text{O}_7$ . *Inorg. Chem.* **2013**, *52* (24), 13861–13864.
- (53) Naguib, M.; Kurtoglu, M.; Presser, V.; Lu, J.; Niu, J.; Heon, M.; Hultman, L.; Gogotsi, Y.; Barsoum, M. W. Two-Dimensional Nanocrystals Produced by Exfoliation of  $\text{Ti}_3\text{AlC}_2$ . *Adv. Mater.* **2011**, *23* (37), 4248–4253.
- (54) Kang, J. W.; Kim, D. H.; Mathew, V.; Lim, J. S.; Gim, J. H.; Kim, J. Particle Size Effect of Anatase  $\text{TiO}_2$  Nanocrystals for Lithium-Ion Batteries. *J. Electrochem. Soc.* **2011**, *158* (2), A59–A62.
- (55) Fleischmann, S.; Zeiger, M.; Quade, A.; Kruth, A.; Presser, V. Atomic layer-deposited molybdenum oxide/carbon nanotube hybrid electrodes: the influence of crystal structure on lithium-ion capacitor performance. *ACS Appl. Mater. Interfaces* **2018**, *10* (22), 18675–18684.

## **Supporting Information**

# **Understanding Interlayer Deprotonation of Hydrogen Titanium Oxide for High-Power Electrochemical Energy Storage**

**Simon Fleischmann,<sup>1,2,‡</sup> Kristina Pfeifer,<sup>3,‡</sup> Mathias Widmaier,<sup>2,3</sup>**

**Hwirim Shim,<sup>1,2</sup> Öznil Budak,<sup>1,2</sup> Volker Presser<sup>1,2,\*</sup>**

<sup>1</sup> INM - Leibniz Institute for New Materials, 66123 Saarbrücken, Germany

<sup>2</sup> Department of Materials Science and Engineering, Saarland University, 66123 Saarbrücken, Germany

<sup>3</sup> Robert Bosch GmbH, Robert-Bosch-Campus 1, 71272 Renningen, Germany

‡ equal contributions

\* Corresponding author's eMail: [volker.presser@leibniz-inm.de](mailto:volker.presser@leibniz-inm.de)

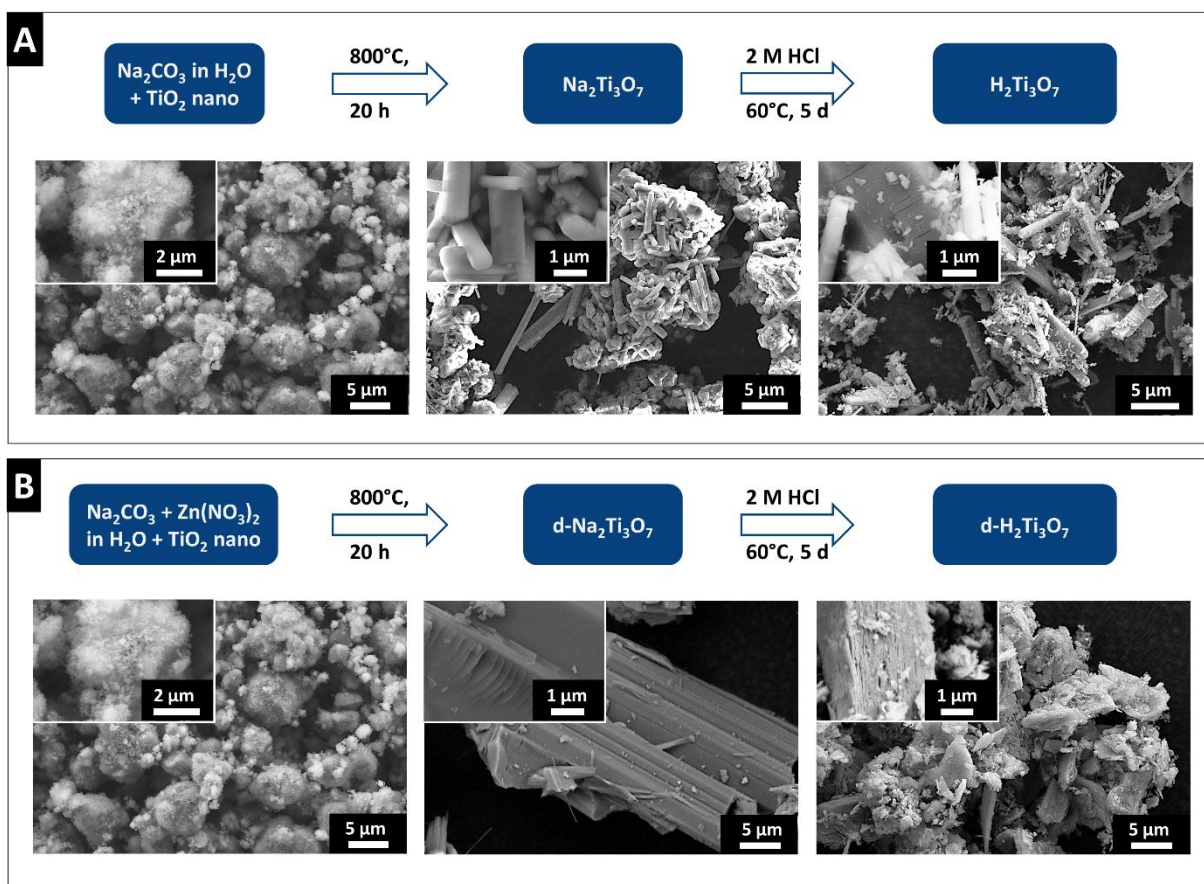


**Fig. S1:** Schematic synthesis procedure of  $\text{H}_2\text{Ti}_3\text{O}_7$  (A) and d- $\text{H}_2\text{Ti}_3\text{O}_7$  (B) including scanning electron micrographs of the precursor, intermediate, and final products.

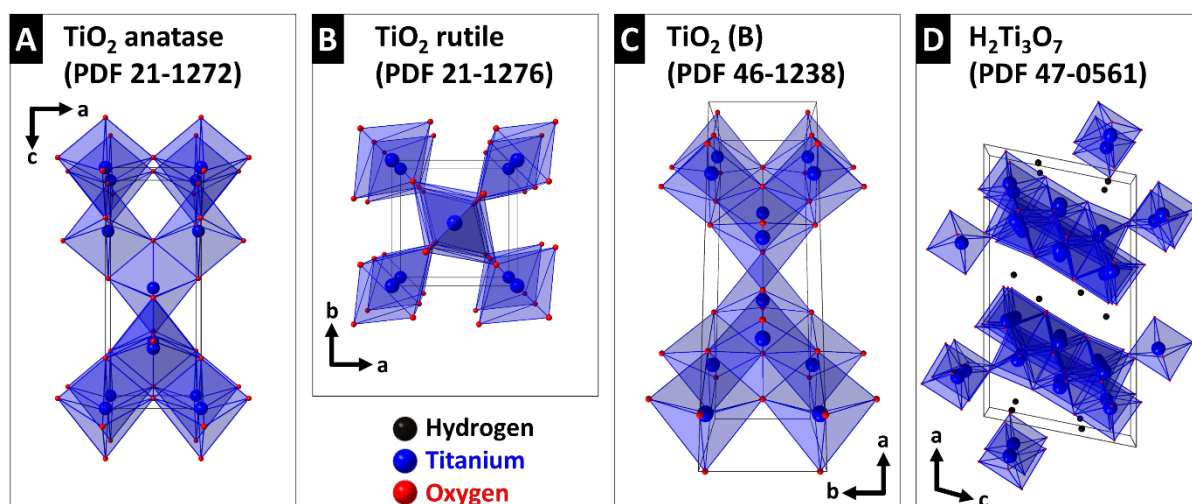


**Fig. S2:** Crystal structures of  $\text{TiO}_2$  anatase (A),  $\text{TiO}_2$  rutile (B), bronze  $\text{TiO}_2$  (C), and fully protonated hydrogen titanium oxide  $\text{H}_2\text{Ti}_3\text{O}_7$  (D).

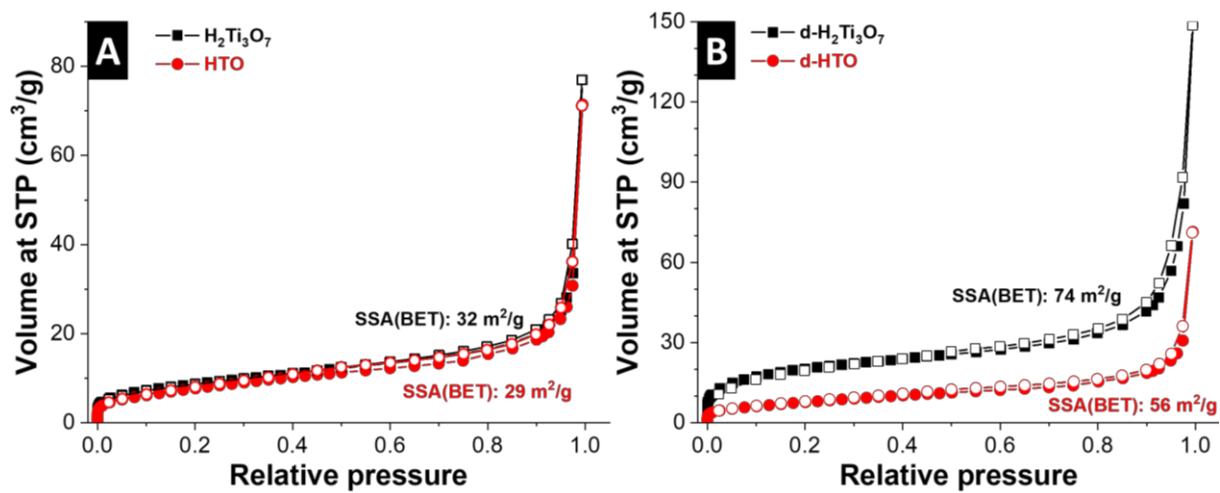


**Fig. S3:** Nitrogen sorption isotherms of H<sub>2</sub>Ti<sub>3</sub>O<sub>7</sub> and HTO (A) and d-H<sub>2</sub>Ti<sub>3</sub>O<sub>7</sub> and d-HTO (B) at -196 °C including calculated BET specific surface area.

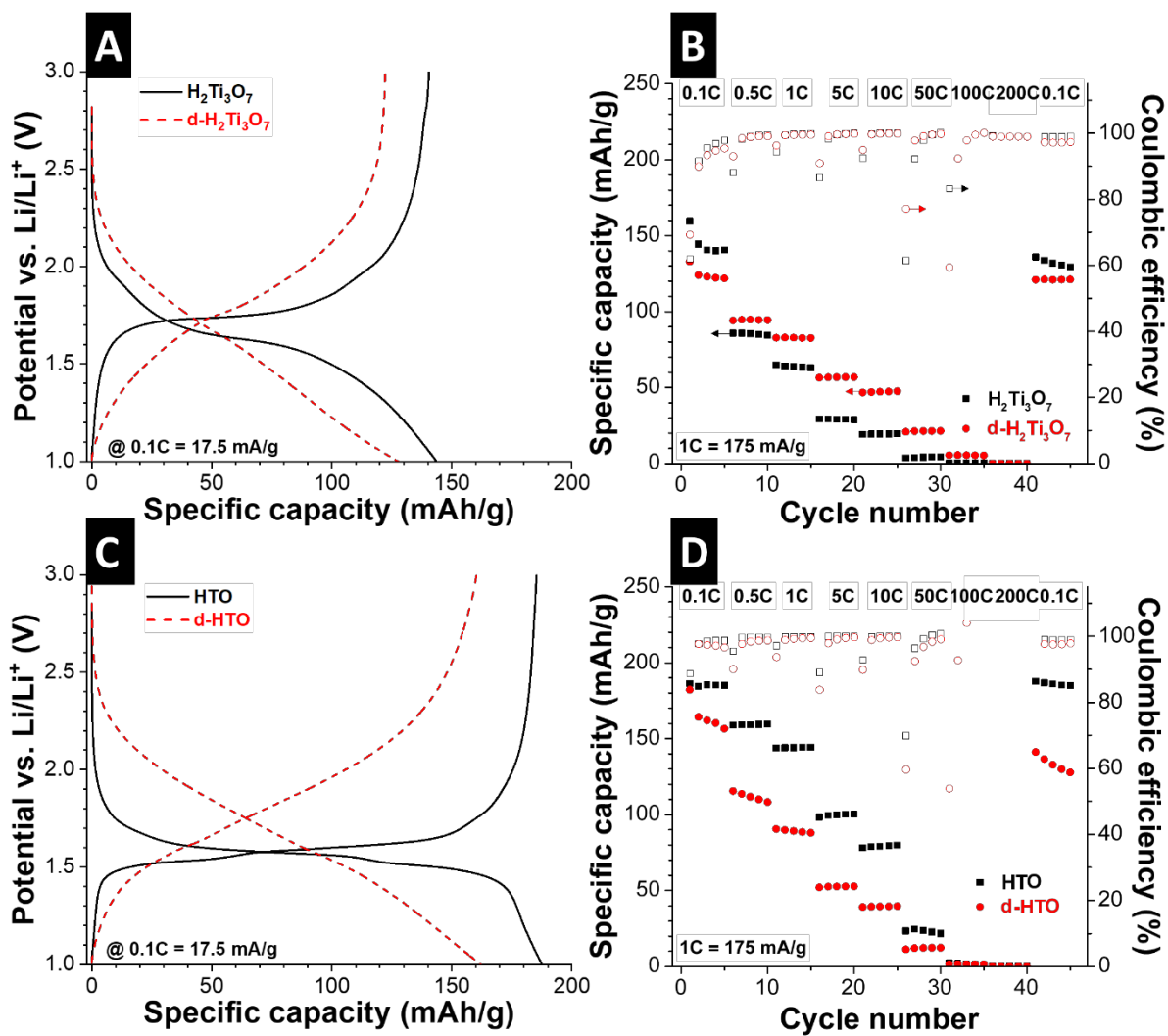


**Fig. S4:** Galvanostatic charge/discharge profiles of  $\text{H}_2\text{Ti}_3\text{O}_7$  and  $\text{d-H}_2\text{Ti}_3\text{O}_7$  at a rate of 17.5 mA/g (A) and corresponding rate handling behavior at rates between 17.5 mA/g and 35 A/g (B). Galvanostatic charge/discharge profiles of HTO and d-HTO at a rate of 17.5 mA/g (C) and corresponding rate handling behavior at rates between 17.5 mA/g and 35 A/g (D). The counter electrode is metallic lithium, 1 M  $\text{LiPF}_6$  in EC/DMC is used as electrolyte.

**Table S1:** Areal resistance of electrodes calculated from potential drop electrochemical rate tests in half-cells. The resistance values were calculated by use of the  $iR$  drop from galvanostatic charge/discharge cycling.

HTO	d-HTO	TiO <sub>2</sub> (B)
2.86 $\Omega\cdot\text{cm}^2$	4.67 $\Omega\cdot\text{cm}^2$	3.88 $\Omega\cdot\text{cm}^2$

## 5. Conclusions and Outlook

My Ph.D. work explored the nanoscale hybridization design of electrode materials and energy storage devices, including the importance of the choice of the electrolyte, to obtain improved lithium- and sodium-ion hybrid batteries. Through the synthesis of nano-scale hybrid material and the subsequent electrochemical benchmarking, my work showed that the carbon substrate has a very important impact on the distribution homogeneity and the physical parameters of the synthesized metal oxide. Thereby, there is a strong influence on the resulting energy storage performance. From investigating different hybrid energy storage device concepts, this work has shown the potential of ionic liquids and the mixed solvent system as a proper electrolyte that enhances safety and performance.

Motivated by the small size and graphitic ordering, this work explores specifically carbon onions as a highly promising carbon material for electrode hybridization with different metal oxides. For comparison, another graphitic carbon nanostructure was also explored for some metal oxide materials, namely, carbon nanohorns. In my work, I used a tailored sol-gel reaction to control the size of the sols via an appropriate selection of chemicals; different metal alkoxides were used for the synthesis of titanium oxide hybrids, titanium niobium oxide hybrids, and lithium titanium oxide hybrids. After the nanosized sol was prepared, the impregnation of carbon onions or carbon nanohorns was conducted, incorporating the sub-micrometer (nano-size) carbon with nanosized metal oxide sols. Subsequent thermal treatment under Argon at high temperatures resulted in nanosized hybrids.

The nanosized anatase  $\text{TiO}_2$ -hybrid material was synthesized after thermal treatment at  $400\text{ }^\circ\text{C}$  with a domain size of below 10 nm. From the electrochemical quantification of the lithium storage kinetics, the rate and cycling performances of the hybrid are superior in comparison to nano- $\text{TiO}_2$ , commercial  $\text{TiO}_2$ , and graphite. The lithium diffusivity was quantified, and in parallel, the evolution of internal resistance for hybrid and non-hybrid  $\text{TiO}_2$  was monitored. As a result, a lower internal resistance of the hybrid  $\text{TiO}_2$  also aligned with a better lithium transport compared to non-hybrid  $\text{TiO}_2$ . This finding confirms that the homogeneous distribution of the conductive carbon is crucial for providing a better charge transport network, enhanced by nanosizing of the electrochemically active metal oxide.

The metal oxide domain size within the TNO-hybrid was 20-30 nm when using carbon onions, yielding  $\text{Ti}_2\text{Nb}_{10}\text{O}_{29}$ . For TNO-hybrids with carbon nanohorns, the metal oxide domains had a size of about 100 nm, and we noted the presence of the electrochemically non-favored niobian rutile phase. The comparison of electrodes based on either hybrid material or the physical mixing or separately prepared carbon and metal oxides served as a baseline to see which of the two design approaches is more promising. The carbon onion-based hybrid materials showed a higher rate performance compared to carbon nanohorn-based hybrids; in contrast, composites of TNO and carbon nanohorns were superior to composites based on TNO and carbon onions. Thereby, hybridization is not always automatically

better than composite strategies: it strongly depends, among others, on the resulting phase distribution homogeneity, phase distribution length scale, and crystal structures.

In addition to TNO and TiO<sub>2</sub>, my work also investigated hybrid materials based on LTO and carbon onions. Two different types of carbon onions were used: one obtained at 1700 °C from vacuum annealing (with a higher degree of graphitic ordering) and one from annealing in Argon at 1300 °C (with a lower degree of graphitic ordering and which had both carbon onions and graphene nanoribbons present). The average metal oxide domain size was about 30 nm, and the hybrid electrodes were investigated as an anode for lithium-ion and sodium-ion batteries. The LTO hybridized with carbon onions treated under Argon yielded the best performance of 188 mAh/g and longevity of 96% initial capacity after 400 cycles. This work further emphasized, as the other two previous works in this thesis, the influence of adequate selection of carbon substrates; the difference in surface area, degree of carbon order, and structure of carbon onions prepared under different conditions were compared, but no direct conclusions could be drawn. The key defining property is less the structure of the carbon itself but its nanoscale distribution and homogeneity within the hybrid, as it appears. The hybrid was also tested for the sodium-ion energy storage, witnessing an excellent longevity performance of maintaining 96% of initial capacity after 500 cycles.

Expanding the hybrid concept to the device level, LTO was used as an anode paired with a composite of LMO and activated carbon as a cathode. Among the variety of electrolyte combination of salt and solvent, ionic liquids, and nitrile- or carbonate-based solvents were selected based on their promising compatibility with the electrode materials. For a comparison of the electrolyte performance, the cell voltage of 2.8 V was selected and electrochemically explored via voltage floating, known to demonstrate a better understanding of performance stability. Considering the real application condition at different weather and temperatures, four different temperature ranges were selected: -10 °C, +25 °C, +60 °C, and +75 °C. Based on this dataset, we see the need for an appropriate combination of lithium-containing salt and solvent to strengthen the stability performance of the hybrid supercapacitors. Also, the widening of the operating temperature must be done carefully due to the possible degradation of the electrode material and electrolyte. The LMO degradation was observed as the voltage floating continued. Specifically, the degradation of the LMO was the weak link of the cell, which led to the overall degradation of the energy storage system because the activated carbon counter-electrode could not compensate for the charge loss. The thermal stability of the ionic liquid was not able to establish anticipated performance stability. Further, the benefit of a mixed solvent system is observed from LiClO<sub>4</sub> in ACN:EC electrolyte, that the narrow temperature range of ACN was remedied by admixing of EC, achieving the best performance at the elevated temperature of +75 °C. The findings from this work show potential of enhanced longevity or performance at various

temperatures by the different proportion of mixture or even employing a different combination of cyclic and non-cyclic solvents.

Ionic liquids with added lithium or sodium salts were investigated as electrolytes for hybrid supercapacitor has LTO and activated carbon for anode and cathode, respectively. This approach allowed a cell voltage of 4 V for LTO based hybrid supercapacitors, which was enabled by the enlarged stability window of activated carbon cathode by using ionic liquid. The high thermal stability of ionic liquids resulted in a stable electrochemical performance at an elevated temperature of +80 °C, which enhanced the safety of the hybrid supercapacitor by reducing the flammability risk. This concept is attractive for applications in the field of an electric vehicle or other fields of application with enhanced safety requirements (e.g., aviation, medical devices). The data confirmed the high potential for a mixed solvent system for the liquid electrolytes, which comprises the findings of the previously mentioned work in this thesis. Employing materials such as hybrid materials has the potential for higher power or energy performance of the hybrid supercapacitors.

Finally, this work also explored hydrogen titanium oxide (HTO) as a novel electrode material for hybrid systems. HTO was synthesized by exposure to hydrochloric acid for proton exchange reaction, followed by thermal treatment at +280 °C. The introduction of zinc nitrate during the synthesis approach yielded d-HTO with a high content of the rutile phase. After the synthesis steps, the different degree of interlayer protonation is observed for HTO and d-HTO. The electrochemical benchmarking of HTO and d-HTO for LIB anodes and demonstrated that the protonated HTO and d-HTO achieve enhanced performance compared to deprotonated samples. The hybrid supercapacitor cells using HTO anode and LMO-activated carbon cathode yielded a promising power (13 kW/kg) and energy performance (88 Wh/kg).

The straightforward synthesis method used in this work and the findings presented in this thesis could provide a guideline for designing the hybrid materials for lithium or sodium ion intercalation. Regarding the suitable selection of carbon substrates, our finding suggests that the size and the degree of order of carbon are crucial. Furthermore, the device level hybridization carries the potential for the further investigation on applications for higher temperature operations, since the work in this thesis only investigated a few systems employing ionic liquid and mixed solvents as electrolytes. As a final recommendation to the development of enhanced electrochemical energy storage cells, one should consider not leaving any stone unturned: improvements in all aspects of electrode material design, electrode type architecture, choice and matching of the electrolyte, and doing so all by considering the power, energy, and sustainability metrics are required for successful development of next-generation energy storage technology.

## 6. References

- [1] IEA, Global Energy Review 2019, Paris, 2019.
- [2] B.d.E.-u.W.e.V. (BDEW), Z.f.S.-u.W.-F.B.-W. (ZSW), Erneuerbaren-Anteil wegen großer Sondereffekte erstmals bei 52 Prozent [www.bdew.de](http://www.bdew.de), 2020.
- [3] IEA, Germany 2020 Energy Policy Review, Paris, 2020, pp. 84-113.
- [4] Z. Yang, J. Zhang, M.C.W. Kintner-Meyer, X. Lu, D. Choi, J.P. Lemmon, J. Liu, Electrochemical Energy Storage for Green Grid, *Chemical Reviews*, 111 (2011) 3577-3613.
- [5] B. Dunn, H. Kamath, J.-M. Tarascon, Electrical Energy Storage for the Grid: A Battery of Choices, *Science*, 334 (2011) 928-935.
- [6] A. Berrada, K. Loudiyi, Chapter 1 - Energy Storage, in: A. Berrada, K. Loudiyi (Eds.) *Gravity Energy Storage*, Elsevier, 2019, pp. 1-23.
- [7] G.G. Amatucci, F. Badway, A. Du Pasquier, T. Zheng, An Asymmetric Hybrid Nonaqueous Energy Storage Cell, *Journal of The Electrochemical Society*, 148 (2001) A930-A939.
- [8] F. Béguin, V. Presser, A. Balducci, E. Frackowiak, Carbons and Electrolytes for Advanced Supercapacitors, *Advanced Materials*, 26 (2014) 2219-2251.
- [9] I. Stadler, Electrical Energy Storage, in: M. Sterner, I. Stadler (Eds.) *Handbook of Energy Storage: Demand, Technologies, Integration*, Springer Berlin Heidelberg, Berlin, Heidelberg, 2019, pp. 191-225.
- [10] H.A. Andreas, Self-Discharge in Electrochemical Capacitors: A Perspective Article, *Journal of The Electrochemical Society*, 162 (2015) A5047-A5053.
- [11] I.S. Ike, I. Sigalas, S. Iyuke, Understanding Performance Limitation and Suppression of Leakage Current or Self-Discharge in Electrochemical Capacitors: A Review, *Physical Chemistry Chemical Physics*, 18 (2016) 661-680.
- [12] J. Lee, P. Srimuk, S. Fleischmann, X. Su, T.A. Hatton, V. Presser, Redox-Electrolytes for Non-Flow Electrochemical Energy Storage: A Critical Review and Best Practice, *Progress in Materials Science*, 101 (2019) 46-89.
- [13] A. González, E. Goikolea, J.A. Barrena, R. Mysyk, Review on Supercapacitors: Technologies and Materials, *Renewable and Sustainable Energy Reviews*, 58 (2016) 1189-1206.
- [14] B. Krüner, J. Lee, N. Jäckel, A. Tolosa, V. Presser, Sub-micrometer Novolac-Derived Carbon Beads for High Performance Supercapacitors and Redox Electrolyte Energy Storage, *ACS Applied Materials & Interfaces*, 8 (2016) 9104-9115.
- [15] J. Gamby, P.L. Taberna, P. Simon, J.F. Fauvarque, M. Chesneau, Studies and Characterisations of Various Activated Carbons used for Carbon/Carbon Supercapacitors, *Journal of Power Sources*, 101 (2001) 109-116.
- [16] K.S.W. Sing, Reporting Physisorption Data for Gas/Solid Systems with Special Reference to the Determination of Surface Area and Porosity (Recommendations 1984), *Pure and Applied Chemistry*, 57 (1985) 603-619.
- [17] K. Fic, G. Lota, M. Meller, E. Frackowiak, Novel Insight into Neutral Medium as Electrolyte for High-voltage Supercapacitors, *Energy & Environmental Science*, 5 (2012) 5842-5850.
- [18] J. Segalini, E. Iwama, P.-L. Taberna, Y. Gogotsi, P. Simon, Steric Effects in Adsorption of Ions from Mixed Electrolytes into Microporous Carbon, *Electrochemistry Communications*, 15 (2012) 63-65.
- [19] N. Jäckel, P. Simon, Y. Gogotsi, V. Presser, Increase in Capacitance by Subnanometer Pores in Carbon, *ACS Energy Letters*, 1 (2016) 1262-1265.
- [20] J. Chmiola, G. Yushin, Y. Gogotsi, C. Portet, P. Simon, P.L. Taberna, Anomalous Increase in Carbon Capacitance at Pore Sizes Less Than 1 Nanometer, *Science*, 313 (2006) 1760.
- [21] N. Jäckel, M. Rodner, A. Schreiber, J. Jeongwook, M. Zeiger, M. Aslan, D. Weingarth, V. Presser, Anomalous or Regular Capacitance? The Influence of Pore Size Dispersity on Double-Layer Formation, *Journal of Power Sources*, 326 (2016) 660-671.
- [22] C. Prehal, C. Koczwarra, N. Jäckel, A. Schreiber, M. Burian, H. Amenitsch, M.A. Hartmann, V. Presser, O. Paris, Quantification of Ion Confinement And Desolvation In Nanoporous Carbon Supercapacitors with Modelling and In Situ X-Ray Scattering, *Nature Energy*, 2 (2017) 16215.
- [23] X. Zang, C. Shen, M. Sanghadasa, L. Lin, High-Voltage Supercapacitors Based on Aqueous Electrolytes, *ChemElectroChem*, 6 (2019) 976-988.

- [24] V. Ruiz, C. Blanco, E. Raymundo-Piñero, V. Khomenko, F. Béguin, R. Santamaría, Effects of Thermal Treatment of Activated Carbon on the Electrochemical Behaviour in Supercapacitors, *Electrochimica Acta*, 52 (2007) 4969-4973.
- [25] V. Khomenko, E. Raymundo-Piñero, E. Frackowiak, F. Béguin, High-Voltage Asymmetric Supercapacitors Operating in Aqueous Electrolyte, *Applied Physics A*, 82 (2006) 567-573.
- [26] X. Bu, L. Su, Q. Dou, S. Lei, X. Yan, A Low-Cost "Water-in-Salt" Electrolyte for a 2.3 V High-rate Carbon-Based Supercapacitor, *Journal of Materials Chemistry A*, 7 (2019) 7541-7547.
- [27] L. Demarconnay, E. Raymundo-Piñero, F. Béguin, A Symmetric Carbon/Carbon Supercapacitor Operating at 1.6V by Using a Neutral Aqueous Solution, *Electrochemistry Communications*, 12 (2010) 1275-1278.
- [28] Q. Gao, L. Demarconnay, E. Raymundo-Piñero, F. Béguin, Exploring the Large Voltage Range of Carbon/Carbon Supercapacitors in Aqueous Lithium Sulfate Electrolyte, *Energy & Environmental Science*, 5 (2012) 9611-9617.
- [29] M. Ue, Mobility and Ionic Association of Lithium and Quaternary Ammonium Salts in Propylene Carbonate and  $\gamma$ -Butyrolactone, *Journal of The Electrochemical Society*, 141 (1994) 3336.
- [30] H. Shim, Ö. Budak, V. Haug, M. Widmaier, V. Presser, Comparison of Organic Electrolytes at Various Temperatures for 2.8 V-Li-Ion Hybrid Supercapacitors, *Electrochimica Acta*, 337 (2020) 135760.
- [31] K. Xu, M.S. Ding, T.R. Jow, Quaternary Onium Salts as Nonaqueous Electrolytes for Electrochemical Capacitors, *Journal of The Electrochemical Society*, 148 (2001) A267.
- [32] M. Ue, Electrochemical Properties of Quaternary Ammonium Salts for Electrochemical Capacitors, *Journal of The Electrochemical Society*, 144 (1997) 2684.
- [33] M. Ue, Chemical Capacitors and Quaternary Ammonium Salts, *Electrochemistry*, 75 (2007) 565-572.
- [34] A.B. McEwen, H.L. Ngo, K. LeCompte, J.L. Goldman, Electrochemical Properties of Imidazolium Salt Electrolytes for Electrochemical Capacitor Applications, *Journal of The Electrochemical Society*, 146 (2019) 1687-1695.
- [35] M. Galiński, A. Lewandowski, I. Stępnik, Ionic Liquids as Electrolytes, *Electrochimica Acta*, 51 (2006) 5567-5580.
- [36] A. Balducci, W.A. Henderson, M. Mastragostino, S. Passerini, P. Simon, F. Soavi, Cycling Stability of a Hybrid Activated Carbon//poly(3-methylthiophene) Supercapacitor with N-butyl-N-methylpyrrolidinium bis(trifluoromethanesulfonyl)imide Ionic Liquid as Electrolyte, *Electrochimica Acta*, 50 (2005) 2233-2237.
- [37] M. Armand, F. Endres, D.R. MacFarlane, H. Ohno, B. Scrosati, Ionic-Liquid Materials for the Electrochemical Challenges of the Future, *Nature Materials*, 8 (2009) 621-629.
- [38] N. Jäckel, S. Patrick Emge, B. Krüner, B. Roling, V. Presser, Quantitative Information about Electrosorption of Ionic Liquids in Carbon Nanopores from Electrochemical Dilatometry and Quartz Crystal Microbalance Measurements, *The Journal of Physical Chemistry C*, 121 (2017) 19120-19128.
- [39] J. Torop, M. Arulepp, J. Leis, A. Punning, U. Johanson, V. Palmre, A. Aabloo, Nanoporous Carbide-Derived Carbon Material-Based Linear Actuators Materials, 3 (2010) 9-25.
- [40] S. Fleischmann, J.B. Mitchell, R. Wang, C. Zhan, D.-e. Jiang, V. Presser, V. Augustyn, Pseudocapacitance: From Fundamental Understanding to High Power Energy Storage Materials, *Chemical Reviews*, 120 (2020) 6738-6782.
- [41] V. Augustyn, P. Simon, B. Dunn, Pseudocapacitive Oxide Materials for High-Rate Electrochemical Energy Storage, *Energy & Environmental Science*, 7 (2014) 1597-1614.
- [42] J.P. Zheng, Hydrous Ruthenium Oxide as an Electrode Material for Electrochemical Capacitors, *Journal of The Electrochemical Society*, 142 (1995) 2699.
- [43] A. Tolosa, S. Fleischmann, I. Grobelsek, A. Quade, E. Lim, V. Presser, Binder-Free Hybrid Titanium-Niobium Oxide/Carbon Nanofiber Mats for Lithium-Ion Battery Electrodes, *ChemSusChem*, 11 (2018) 159-170.
- [44] E. Lim, H. Kim, C. Jo, J. Chun, K. Ku, S. Kim, H. Lee, I.-s. Nam, S. Yoon, K. Kang, J. Lee, Advanced Hybrid Supercapacitor Based on a Mesoporous Niobium Pentoxide/Carbon as HighPerformance Anode, *ACS Nano*, 8 (2014) 8968-8978.
- [45] T.B. Reddy, D. Linden, *Linden's Handbook of Batteries*, McGraw-Hill, New York, 2011.

- [46] M. Broussely, P. Biensan, B. Simon, Lithium Insertion into Host Materials: the Key to Success for Li Ion Batteries, *Electrochimica Acta*, 45 (1999) 3-22.
- [47] M. Yoshio, A. Kozawa, R.J. Brodd, Introduction: Development of Lithium-Ion Batteries, in: M. Yoshio, R.J. Brodd, A. Kozawa (Eds.) *Lithium-Ion Batteries: Science and Technologies*, Springer New York, New York, NY, 2009, pp. xviii-xxvi.
- [48] M.S. Whittingham, F.R. Gamble, The Lithium Intercalates of the Transition metal Dichalcogenides, *Materials Research Bulletin*, 10 (1975) 363-371.
- [49] M.S. Whittingham, Electrointercalation in Transition-Metal Disulphides, *Journal of the Chemical Society, Chemical Communications*, (1974) 328-329.
- [50] J.B. Goodenough, K. Mizushima, *Electrochemical Cell with New Fast Ion Conductors U.S.*, 1981, pp. 1-6.
- [51] M.B. Armand, Intercalation Electrodes, in: D.W. Murphy, J. Broadhead, B.C.H. Steele (Eds.) *Materials for Advanced Batteries*, Springer US, Boston, MA, 1980, pp. 145-161.
- [52] A. Yoshino, K. Sanechika, T. Nakajima, *Secondary Battery U.S.*, 1987, pp. 1-25.
- [53] K. Xu, Nonaqueous Liquid Electrolytes for Lithium-Based Rechargeable Batteries, *Chemical Reviews*, 104 (2004) 4303-4418.
- [54] S.-T. Myung, Y. Hitoshi, Y.-K. Sun, Electrochemical Behavior and Passivation of Current Collectors in Lithium-Ion Batteries, *Journal of Materials Chemistry*, 21 (2011) 9891-9911.
- [55] Y. Ding, Z.P. Cano, A. Yu, J. Lu, Z. Chen, Automotive Li-Ion Batteries: Current Status and Future Perspectives, *Electrochemical Energy Reviews*, 2 (2019) 1-28.
- [56] B. Scrosati, J. Garche, Lithium Batteries: Status, Prospects and Future, *Journal of Power Sources*, 195 (2010) 2419-2430.
- [57] J.M. Tarascon, M. Armand, Issues and Challenges Facing Rechargeable Lithium Batteries, *Nature*, 414 (2001) 359.
- [58] Y. Nishi, Lithium Ion Secondary Batteries; Past 10 Years and the Future, *Journal of Power Sources*, 100 (2001) 101-106.
- [59] T. Ohzuku, Y. Iwakoshi, K. Sawai, Formation of Lithium-Graphite Intercalation Compounds in Nonaqueous Electrolytes and Their Application as a Negative Electrode for a Lithium Ion (Shuttlecock) Cell, *Journal of The Electrochemical Society*, 140 (1993) 2490-2498.
- [60] J.B. Goodenough, K.-S. Park, The Li-Ion Rechargeable Battery: A Perspective, *Journal of the American Chemical Society*, 135 (2013) 1167-1176.
- [61] A.N. Dey, B.P. Sullivan, The Electrochemical Decomposition of Propylene Carbonate on Graphite, *Journal of The Electrochemical Society*, 117 (1970) 222.
- [62] S.S. Zhang, A Review on Electrolyte Additives for Lithium-Ion Batteries, *Journal of Power Sources*, 162 (2006) 1379-1394.
- [63] J. Vetter, P. Novák, M.R. Wagner, C. Veit, K.C. Möller, J.O. Besenhard, M. Winter, M. Wohlfahrt-Mehrens, C. Vogler, A. Hammouche, Ageing Mechanisms in Lithium-Ion Batteries, *Journal of Power Sources*, 147 (2005) 269-281.
- [64] K. Zaghbi, M. Simoneau, M. Armand, M. Gauthier, Electrochemical Study of  $\text{Li}_4\text{Ti}_5\text{O}_{12}$  as Negative Electrode for Li-ion Polymer Rechargeable Batteries, *Journal of Power Sources*, 81-82 (1999) 300-305.
- [65] K. Xu, Electrolytes and Interphases in Li-Ion Batteries and Beyond, *Chemical Reviews*, 114 (2014) 11503-11618.
- [66] T. Ohzuku, A. Ueda, N. Yamamoto, Zero-Strain Insertion Material of  $\text{Li}[\text{Li}_{1/3}\text{Ti}_{5/3}]\text{O}_4$  for Rechargeable Lithium Cells, *Journal of The Electrochemical Society*, 142 (1995) 1431-1435.
- [67] S. Bach, J.P. Pereira-Ramos, N. Baffier, Electrochemical Properties of sol-gel  $\text{Li}_{4/3}\text{Ti}_{5/3}\text{O}_4$ , *Journal of Power Sources*, 81-82 (1999) 273-276.
- [68] Y.H. Rho, K. Kanamura,  $\text{Li}^+$  ion Diffusion in  $\text{Li}_4\text{Ti}_5\text{O}_{12}$  Thin Film Electrode Prepared by PVP Sol-Gel Method, *Journal of Solid State Chemistry*, 177 (2004) 2094-2100.
- [69] B. Yan, M. Li, X. Li, Z. Bai, J. Yang, D. Xiong, D. Li, Novel Understanding of Carbothermal Reduction Enhancing Electronic and Ionic Conductivity of  $\text{Li}_4\text{Ti}_5\text{O}_{12}$  Anode, *Journal of Materials Chemistry A*, 3 (2015) 11773-11781.
- [70] M. Widmaier, K. Pfeifer, L. Bommer, V. Presser, Valence-Tuned Lithium Titanate Nanopowder for High-Rate Electrochemical Energy Storage, *Batteries & Supercaps*, 1 (2018) 11-26.

- [71] K. Liang, H. He, Y. Ren, J. Luan, H. Wang, Y. Ren, X. Huang,  $Ti^{3+}$  Self-Doped  $Li_4Ti_5O_{12}$  with Rich Oxygen Vacancies for Advanced Lithium-Ion Batteries, *Ionics*, 26 (2020) 1739-1747.
- [72] S. Fleischmann, A. Tolosa, V. Presser, Design of Carbon/Metal Oxide Hybrids for Electrochemical Energy Storage, *Chemistry - A European Journal*, 24 (2018) 12143-12153.
- [73] D. Peramunage, K.M. Abraham, Preparation and Battery Applications of Micron Sized  $Li_4Ti_5O_{12}$ , *MRS Proceedings*, 496 (1997) 359.
- [74] S. Sarciaux, A.L.G.L. Salle, D. Guyomard, Y. Piffard, Electrochemical Study of the Lithium Insertion Mechanism into  $Li_4Ti_5O_{12}$ , *Molecular Crystals and Liquid Crystals*, 311 (1998) 63-68.
- [75] H.S. Choi, J.H. Im, T. Kim, J.H. Park, C.R. Park, Advanced Energy Storage Device: A Hybrid BatCap System Consisting of Battery–Supercapacitor Hybrid Electrodes Based on  $Li_4Ti_5O_{12}$ –Activated-Carbon Hybrid Nanotubes, *Journal of Materials Chemistry*, 22 (2012) 16986-16993.
- [76] H. Kim, K.-Y. Park, M.-Y. Cho, M.-H. Kim, J. Hong, S.-K. Jung, K.C. Roh, K. Kang, High-Performance Hybrid Supercapacitor Based on Graphene-Wrapped  $Li_4Ti_5O_{12}$  and Activated Carbon, *ChemElectroChem*, 1 (2014) 125-130.
- [77] C. Chen, H. Xu, T. Zhou, Z. Guo, L. Chen, M. Yan, L. Mai, P. Hu, S. Cheng, Y. Huang, J. Xie, Integrated Intercalation-Based and Interfacial Sodium Storage in Graphene-Wrapped Porous  $Li_4Ti_5O_{12}$  Nanofibers Composite Aerogel, *Advanced Energy Materials*, 6 (2016) 1600322.
- [78] F. Gu, G. Chen, Synthesis and Electrochemical Performances of  $Li_4Ti_5O_{12}/C$  as Anode Material for Lithium-Ion Batteries, *Advanced Materials Research*, 366 (2011) 24-27.
- [79] H.-G. Jung, S.-T. Myung, C.S. Yoon, S.-B. Son, K.H. Oh, K. Amine, B. Scrosati, Y.-K. Sun, Microscale Spherical Carbon-Coated  $Li_4Ti_5O_{12}$  as Ultra High Power Anode Material for Lithium Batteries, *Energy & Environmental Science*, 4 (2011) 1345.
- [80] Q. Cheng, S. Tang, J. Liang, J. Zhao, Q. Lan, C. Liu, Y.-C. Cao, High Rate Performance of the Carbon Encapsulated  $Li_4Ti_5O_{12}$  for Lithium Ion Battery, *Results in Physics*, 7 (2017) 810-812.
- [81] Y.-B. He, F. Ning, B. Li, Q.-S. Song, W. Lv, H. Du, D. Zhai, F. Su, Q.-H. Yang, F. Kang, Carbon Coating to Suppress the Reduction Decomposition of Electrolyte on the  $Li_4Ti_5O_{12}$  Electrode, *Journal of Power Sources*, 202 (2012) 253-261.
- [82] J. Tang, L. Gao, Electrochemical Performance of  $Li_4Ti_5O_{12}/C$  Anode Material Prepared with a Stearic Acid Carbon Source, *Physica Scripta*, 85 (2012) 045802.
- [83] L. Cheng, X.-L. Li, H.-J. Liu, H.-M. Xiong, P.-W. Zhang, Y.-Y. Xia, Carbon-Coated  $Li_4Ti_5O_{12}$  as a High Rate Electrode Material for Li-Ion Intercalation, *Journal of The Electrochemical Society*, 154 (2007) A692-A697.
- [84] M. Widmaier, N. Jäckel, M. Zeiger, M. Abuzarli, C. Engel, L. Bommer, V. Presser, Influence of Carbon Distribution on the Electrochemical Performance and Stability of Lithium Titanate Based Energy Storage Devices, *Electrochimica Acta*, 247 (2017) 1006-1018.
- [85] J. Lee, Y.S. Jung, S.C. Warren, M. Kamperman, S.M. Oh, F.J. DiSalvo, U. Wiesner, Direct Access to Mesoporous Crystalline  $TiO_2$ /Carbon Composites with Large and Uniform Pores for Use as Anode Materials in Lithium Ion Batteries, *Macromolecular Chemistry and Physics*, 212 (2011) 383-390.
- [86] E. Lim, C. Jo, H. Kim, M.-H. Kim, Y. Mun, J. Chun, Y. Ye, J. Hwang, K.-S. Ha, K.C. Roh, K. Kang, S. Yoon, J. Lee, Facile Synthesis of  $Nb_2O_5$ @Carbon Core Shell Nanocrystals with Controlled Crystalline Structure for High-Power Anodes in Hybrid Supercapacitors, *ACS Nano*, 9 (2015) 7497-7505.
- [87] E. Lim, H. Shim, S. Fleischmann, V. Presser, Fast and Stable Lithium-Ion Storage Kinetics of Anatase Titanium Dioxide/Carbon Onion Hybrid Electrodes, *Journal of Materials Chemistry A*, 6 (2018) 9480-9488.
- [88] J.-T. Han, Y.-H. Huang, J.B. Goodenough, New Anode Framework for Rechargeable Lithium Batteries, *Chemistry of Materials*, 23 (2011) 2027-2029.
- [89] J.F. Colin, V. Pralong, M. Hervieu, V. Caignaert, B. Raveau, Lithium Insertion in an Oriented Nanoporous Oxide with a Tunnel Structure:  $Ti_2Nb_2O_9$ , *Chemistry of Materials*, 20 (2008) 1534-1540.
- [90] H. Shim, E. Lim, S. Fleischmann, A. Quade, A. Tolosa, V. Presser, Nanosized Titanium Niobium Oxide/Carbon electrodes for Lithium-Ion Energy Storage Applications, *Sustainable Energy & Fuels*, 3 (2019) 1776-1789.
- [91] X. Wu, J. Miao, W. Han, Y.-S. Hu, D. Chen, J.-S. Lee, J. Kim, L. Chen, Investigation on  $Ti_2Nb_{10}O_{29}$  Anode Material for Lithium-Ion Batteries, *Electrochemistry Communications*, 25 (2012) 39-42.

- [92] J.-T. Han, J.B. Goodenough, 3-V Full Cell Performance of Anode Framework  $\text{TiNb}_2\text{O}_7$ /Spinel  $\text{LiNi}_{0.5}\text{Mn}_{1.5}\text{O}_4$ , *Chemistry of Materials*, 23 (2011) 3404-3407.
- [93] Q. Cheng, J. Liang, Y. Zhu, L. Si, C. Guo, Y. Qian, Bulk  $\text{Ti}_2\text{Nb}_{10}\text{O}_{29}$  as Long-Life and High-Power Li-ion Battery Anodes, *Journal of Materials Chemistry A*, 2 (2014) 17258-17262.
- [94] T. Takashima, T. Tojo, R. Inada, Y. Sakurai, Characterization of Mixed Titanium-Niobium Oxide  $\text{Ti}_2\text{Nb}_{10}\text{O}_{29}$  Annealed in Vacuum as Anode Material for Lithium-Ion Battery, *Journal of Power Sources*, 276 (2015) 113-119.
- [95] L. Hu, L. Luo, L. Tang, C. Lin, R. Li, Y. Chen,  $\text{Ti}_2\text{Nb}_{2x}\text{O}_{4+5x}$  Anode Materials for Lithium-ion Batteries: A Comprehensive Review, *Journal of Materials Chemistry A*, 6 (2018) 9799-9815.
- [96] N. Takami, K. Ise, Y. Harada, T. Iwasaki, T. Kishi, K. Hoshina, High-Energy, Fast-Charging, Long-Life Lithium-Ion Batteries Using  $\text{TiNb}_2\text{O}_7$  Anodes for Automotive Applications, *Journal of Power Sources*, 396 (2018) 429-436.
- [97] A. Casimir, H. Zhang, O. Ogoke, J.C. Amine, J. Lu, G. Wu, Silicon-Based Anodes for Lithium-Ion Batteries: Effectiveness of Materials Synthesis and Electrode Preparation, *Nano Energy*, 27 (2016) 359-376.
- [98] P. Albertus, S. Babinec, S. Litzelman, A. Newman, Status and Challenges in Enabling the Lithium Metal Electrode for High-Energy and Low-Cost Rechargeable Batteries, *Nature Energy*, 3 (2017) 16-21.
- [99] W.-J. Zhang, A Review of the Electrochemical Performance of Alloy Anodes for Lithium-Ion Batteries, *Journal of Power Sources*, 196 (2011) 13-24.
- [100] S.-H. Yu, X. Feng, N. Zhang, J. Seok, H.D. Abruña, Understanding Conversion-Type Electrodes for Lithium Rechargeable Batteries, *Accounts of Chemical Research*, 51 (2018) 273-281.
- [101] D. Choi, W. Wang, Z. Yang, Lithium-Ion Batteries: Material Challenges and Perspectives, in: X. Yuan, H. Liu, J. Zhang (Eds.) *Lithium-Ion Batteries: Advanced Materials and Technologies*, CRC Press, 2011, pp. 1-50.
- [102] M.S. Whittingham, Lithium Batteries and Cathode Materials, *Chemical Reviews*, 104 (2004) 4271-4302.
- [103] J.W. Fergus, Recent Developments in Cathode Materials for Lithium Ion Batteries, *Journal of Power Sources*, 195 (2010) 939-954.
- [104] I. Stadler, B. Riegel, D. Ohms, E. Cattaneo, G. Langer, M. Herrmann, Electrochemical Energy Storage Systems, in: M. Sterner, I. Stadler (Eds.) *Handbook of Energy Storage: Demand, Technologies, Integration*, Springer Berlin Heidelberg, Berlin, Heidelberg, 2019, pp. 227-324.
- [105] P. Knauth, Inorganic Solid Li Ion Conductors: An Overview, *Solid State Ionics*, 180 (2009) 911-916.
- [106] F. Zheng, M. Kotobuki, S. Song, M.O. Lai, L. Lu, Review on Solid Electrolytes for All-Solid-State Lithium-Ion Batteries, *Journal of Power Sources*, 389 (2018) 198-213.
- [107] J.-M. Tarascon, Is Lithium the New Gold?, *Nature Chemistry*, 2 (2010) 510-510.
- [108] G. Patry, A. Romagny, S. Martinet, D. Froelich, Cost Modeling of Lithium-Ion Battery Cells for Automotive Applications, *Energy Science & Engineering*, 3 (2015) 71-82.
- [109] S.-W. Kim, D.-H. Seo, X. Ma, G. Ceder, K. Kang, Electrode Materials for Rechargeable Sodium-Ion Batteries: Potential Alternatives to Current Lithium-Ion Batteries, *Advanced Energy Materials*, 2 (2012) 710-721.
- [110] S. Komaba, W. Murata, T. Ishikawa, N. Yabuuchi, T. Ozeki, T. Nakayama, A. Ogata, K. Gotoh, K. Fujiwara, Electrochemical Na Insertion and Solid Electrolyte Interphase for Hard-Carbon Electrodes and Application to Na-Ion Batteries, *Advanced Functional Materials*, 21 (2011) 3859-3867.
- [111] M.D. Slater, D. Kim, E. Lee, C.S. Johnson, Sodium-Ion Batteries, *Advanced Functional Materials*, 23 (2013) 947-958.
- [112] M.S. Whittingham, Chemistry of Intercalation Compounds: Metal Guests in Chalcogenide Hosts, *Progress in Solid State Chemistry*, 12 (1978) 41-99.
- [113] T. Oshima, M. Kajita, A. Okuno, Development of Sodium-Sulfur Batteries, *International Journal of Applied Ceramic Technology*, 1 (2004) 269-276.
- [114] N. Yabuuchi, K. Kubota, M. Dahbi, S. Komaba, Research Development on Sodium-Ion Batteries, *Chemical Reviews*, 114 (2014) 11636-11682.

- [115] S. Fleischmann, M. Widmaier, A. Schreiber, H. Shim, F.M. Stiemke, T.J.S. Schubert, V. Presser, High Voltage Asymmetric Hybrid Supercapacitors Using Lithium- and Sodium-Containing Ionic Liquids, *Energy Storage Materials*, 16 (2019) 391-399.
- [116] G. Hasegawa, K. Kanamori, T. Kiyomura, H. Kurata, K. Nakanishi, T. Abe, Hierarchically Porous  $\text{Li}_4\text{Ti}_5\text{O}_{12}$  Anode Materials for Li- and Na-Ion Batteries: Effects of Nanoarchitectural Design and Temperature Dependence of the Rate Capability, *Advanced Energy Materials*, 5 (2015) 1400730.
- [117] Y. Sun, L. Zhao, H. Pan, X. Lu, L. Gu, Y.-S. Hu, H. Li, M. Armand, Y. Ikuhara, L. Chen, X. Huang, Direct Atomic-Scale Confirmation of Three-Phase Storage Mechanism in  $\text{Li}_4\text{Ti}_5\text{O}_{12}$  Anodes for Room-Temperature Sodium-Ion Batteries, *Nature Communications*, 4 (2013) 1870.
- [118] M. Dahbi, N. Yabuuchi, K. Kubota, K. Tokiwa, S. Komaba, Negative Electrodes for Na-Ion Batteries, *Physical Chemistry Chemical Physics*, 16 (2014) 15007-15028.
- [119] A. Ponrouch, E. Marchante, M. Courty, J.-M. Tarascon, M.R. Palacín, In Search of an Optimized Electrolyte for Na-ion batteries, *Energy & Environmental Science*, 5 (2012) 8572-8583.
- [120] V. Etacheri, O. Haik, Y. Goffer, G.A. Roberts, I.C. Stefan, R. Fasching, D. Aurbach, Effect of Fluoroethylene Carbonate (FEC) on the Performance and Surface Chemistry of Si-Nanowire Li-Ion Battery Anodes, *Langmuir*, 28 (2012) 965-976.
- [121] R. Jung, M. Metzger, D. Haering, S. Solchenbach, C. Marino, N. Tsiouvaras, C. Stinner, H.A. Gasteiger, Consumption of Fluoroethylene Carbonate (FEC) on Si-C Composite Electrodes for Li-Ion Batteries, *Journal of The Electrochemical Society*, 163 (2016) A1705-A1716.
- [122] M. Dahbi, T. Nakano, N. Yabuuchi, T. Ishikawa, K. Kubota, M. Fukunishi, S. Shibahara, J.-Y. Son, Y.-T. Cui, H. Oji, S. Komaba, Sodium Carboxymethyl Cellulose as a Potential Binder for Hard-carbon Negative Electrodes in Sodium-Ion Batteries, *Electrochemistry Communications*, 44 (2014) 66-69.
- [123] V. Simone, L. Lecarme, L. Simonin, S. Martinet, Identification and Quantification of the Main Electrolyte Decomposition By-product in Na-Ion Batteries through FEC: Towards an Improvement of Safety and Lifetime, *Journal of The Electrochemical Society*, 164 (2016) A145-A150.
- [124] M.M. Doeff, Electrochemical Insertion of Sodium into Carbon, *Journal of The Electrochemical Society*, 140 (1993) L169.
- [125] D.A. Stevens, J.R. Dahn, High Capacity Anode Materials for Rechargeable Sodium-Ion Batteries, *Journal of The Electrochemical Society*, 147 (2000) 1271.
- [126] L. Wu, D. Buchholz, D. Bresser, L. Gomes Chagas, S. Passerini, Anatase  $\text{TiO}_2$  Nanoparticles for High Power Sodium-Ion Anodes, *Journal of Power Sources*, 251 (2014) 379-385.
- [127] L. Zhao, H.-L. Pan, Y.-S. Hu, H. Li, L.-Q. Chen, Spinel Lithium Titanate ( $\text{Li}_4\text{Ti}_5\text{O}_{12}$ ) as Novel Anode Material for Room-Temperature Sodium-Ion Battery, *Chinese Physics B*, 21 (2012) 028201.
- [128] A. Darwiche, M.T. Sougrati, B. Fraise, L. Stievano, L. Monconduit, Facile Synthesis and Long Cycle Life of SnSb as Negative Electrode Material for Na-Ion Batteries, *Electrochemistry Communications*, 32 (2013) 18-21.
- [129] Y. Kim, Y. Park, A. Choi, N.-S. Choi, J. Kim, J. Lee, J.H. Ryu, S.M. Oh, K.T. Lee, An Amorphous Red Phosphorus/Carbon Composite as a Promising Anode Material for Sodium Ion Batteries, *Advanced Materials*, 25 (2013) 3045-3049.
- [130] L. Wu, X. Hu, J. Qian, F. Pei, F. Wu, R. Mao, X. Ai, H. Yang, Y. Cao, Sb-C Nanofibers with Long Cycle Life as an Anode Material for High-Performance Sodium-Ion Batteries, *Energy & Environmental Science*, 7 (2014) 323-328.
- [131] B. Qu, C. Ma, G. Ji, C. Xu, J. Xu, Y.S. Meng, T. Wang, J.Y. Lee, Layered  $\text{SnS}_2$ -Reduced Graphene Oxide Composite - A High-Capacity, High-Rate, and Long-Cycle Life Sodium-Ion Battery Anode Material, *Advanced Materials*, 26 (2014) 3854-3859.
- [132] Z. Huang, H. Hou, C. Wang, S. Li, Y. Zhang, X. Ji, Molybdenum Phosphide: A Conversion-type Anode for Ultralong-Life Sodium-Ion Batteries, *Chemistry of Materials*, 29 (2017) 7313-7322.
- [133] C. Delmas, J.-J. Braconnier, C. Fouassier, P. Hagenmuller, Electrochemical Intercalation of Sodium in  $\text{Na}_x\text{CoO}_2$  Bronzes, *Solid State Ionics*, 3-4 (1981) 165-169.
- [134] J.-Y. Hwang, S.-T. Myung, Y.-K. Sun, Sodium-Ion Batteries: Present and Future, *Chemical Society Reviews*, 46 (2017) 3529-3614.

- [135] D. Cericola, P. Novák, A. Wokaun, R. Kötz, Hybridization of Electrochemical Capacitors and Rechargeable Batteries: An Experimental Analysis of the Different Possible Approaches Utilizing Activated Carbon,  $\text{Li}_4\text{Ti}_5\text{O}_{12}$  and  $\text{LiMn}_2\text{O}_4$ , *Journal of Power Sources*, 196 (2011) 10305-10313.
- [136] D. Cericola, R. Kötz, Hybridization of Rechargeable Batteries and Electrochemical Capacitors: Principles and Limits, *Electrochimica Acta*, 72 (2012) 1-17.
- [137] K. Naoi, S. Ishimoto, J.-i. Miyamoto, W. Naoi, Second Generation 'Nanohybrid Supercapacitor': Evolution of Capacitive Energy Storage devices, *Energy & Environmental Science*, 5 (2012) 9363-9373.
- [138] S.R. Sivakkumar, A.G. Pandolfo, Evaluation of Lithium-Ion Capacitors Assembled with Pre-Lithiated Graphite Anode and Activated Carbon Cathode, *Electrochimica Acta*, 65 (2012) 280-287.
- [139] R. Holze, F. Béguin, E. Frąckowiak, Supercapacitors - Materials, Systems, and Applications, *Journal of Solid State Electrochemistry*, 19 (2015) 1253-1253.
- [140] S. Dsoke, B. Fuchs, E. Gucciardi, M. Wohlfahrt-Mehrens, The Importance of the Electrode Mass Ratio in a Li-ion Capacitor Based on Activated Carbon and  $\text{Li}_4\text{Ti}_5\text{O}_{12}$ , *Journal of Power Sources*, 282 (2015) 385-393.
- [141] K. Naoi, W. Naoi, S. Aoyagi, J.-i. Miyamoto, T. Kamino, New Generation "Nanohybrid Supercapacitor", *Accounts of Chemical Research*, 46 (2013) 1075-1083.
- [142] X. Jia, Y. Kan, X. Zhu, G. Ning, Y. Lu, F. Wei, Building Flexible  $\text{Li}_4\text{Ti}_5\text{O}_{12}$ /CNT Lithium-ion Battery Anodes with Superior Rate Performance and Ultralong Cycling Stability, *Nano Energy*, 10 (2014) 344-352.
- [143] K. Naoi, S. Ishimoto, Y. Isobe, S. Aoyagi, High-Rate Nano-Crystalline  $\text{Li}_4\text{Ti}_5\text{O}_{12}$  Attached on Carbon Nano-Fibers for Hybrid Supercapacitors, *Journal of Power Sources*, 195 (2010) 6250-6254.
- [144] S. Fleischmann, M. Zeiger, N. Jäckel, B. Krüner, V. Lemkova, M. Widmaier, V. Presser, Tuning Pseudocapacitive and Battery-like Lithium Intercalation in Vanadium Dioxide/Carbon Onion Hybrids for Asymmetric Supercapacitor Anodes, *Journal of Materials Chemistry A*, 5 (2017) 13039-13051.
- [145] Y. Tang, F. Huang, W. Zhao, Z. Liu, D. Wan, Synthesis of Graphene-supported  $\text{Li}_4\text{Ti}_5\text{O}_{12}$  Nanosheets for High Rate Battery Application, *Journal of Materials Chemistry*, 22 (2012) 11257-11260.
- [146] Q. Li, Q. Wei, J. Sheng, M. Yan, L. Zhou, W. Luo, R. Sun, L. Mai, Mesoporous  $\text{Li}_3\text{VO}_4$ /C Submicron-Ellipsoids Supported on Reduced Graphene Oxide as Practical Anode for High-Power Lithium-Ion Batteries, *Advanced Science*, 2 (2015) 1500284.
- [147] M.S. Kim, E. Lim, S. Kim, C. Jo, J. Chun, J. Lee, General Synthesis of N-Doped Macroporous Graphene-Encapsulated Mesoporous Metal Oxides and Their Application as New Anode Materials for Sodium-Ion Hybrid Supercapacitors, *Advanced Functional Materials*, 27 (2017) 1603921.
- [148] E. Zhao, C. Qin, H.R. Jung, G. Berdichevsky, A. Nese, S. Marder, G. Yushin, Lithium Titanate Confined in Carbon Nanopores for Asymmetric Supercapacitors, *ACS Nano*, 10 (2016) 3977-3984.
- [149] J. Huang, B.G. Sumpter, V. Meunier, G. Yushin, C. Portet, Y. Gogotsi, Curvature Effects in Carbon Nanomaterials: Exohedral versus Endohedral Supercapacitors, *Journal of Materials Research*, 25 (2010) 1525-1531.
- [150] J.S. Daubert, N.P. Lewis, H.N. Gotsch, J.Z. Mundy, D.N. Monroe, E.C. Dickey, M.D. Losego, G.N. Parsons, Effect of Meso- and Micro-Porosity in Carbon Electrodes on Atomic Layer Deposition of Pseudocapacitive  $\text{V}_2\text{O}_5$  for High Performance Supercapacitors, *Chemistry of Materials*, 27 (2015) 6524-6534.
- [151] S. Fleischmann, A. Tolosa, M. Zeiger, B. Krüner, N.J. Peter, I. Grobelsek, A. Quade, A. Kruth, V. Presser, Vanadia-Titania Multilayer Nanodecoration of Carbon Onions via Atomic Layer Deposition for High Performance Electrochemical Energy Storage, *Journal of Materials Chemistry A*, 5 (2017) 2792-2801.
- [152] J. Hwang, C. Jo, K. Hur, J. Lim, S. Kim, J. Lee, Direct Access to Hierarchically Porous Inorganic Oxide Materials with Three-Dimensionally Interconnected Networks, *Journal of the American Chemical Society*, 136 (2014) 16066-16072.
- [153] C. Jo, Y. Kim, J. Hwang, J. Shim, J. Chun, J. Lee, Block Copolymer Directed Ordered Mesostructured  $\text{TiNb}_2\text{O}_7$  Multimetallic Oxide Constructed of Nanocrystals as High Power Li-Ion Battery Anodes, *Chemistry of Materials*, 26 (2014) 3508-3514.

- [154] T. Yuan, X. Yu, R. Cai, Y. Zhou, Z. Shao, Synthesis of Pristine and Carbon-coated  $\text{Li}_4\text{Ti}_5\text{O}_{12}$  and Their Low-Temperature Electrochemical Performance, *Journal of Power Sources*, 195 (2010) 4997-5004.
- [155] G. Li, X. Wang, X. Ma,  $\text{Nb}_2\text{O}_5$ -Carbon Core-Shell Nanocomposite as Anode Material for Lithium Ion Battery, *Journal of Energy Chemistry*, 22 (2013) 357-362.
- [156] A. Nugroho, W. Chang, S. Jin Kim, K. Yoon Chung, J. Kim, Superior High Rate Performance of Core-Shell  $\text{Li}_4\text{Ti}_5\text{O}_{12}$ /carbon Nanocomposite Synthesized by a Supercritical Alcohol Approach, *RSC Advances*, 2 (2012) 10805-10808.
- [157] E. Lim, W.-G. Lim, C. Jo, J. Chun, M.-H. Kim, K.C. Roh, J. Lee, Rational Design of  $\text{Li}_3\text{VO}_4$ @ Carbon Core-Shell Nanoparticles as Li-ion Hybrid Supercapacitor Anode Materials, *Journal of Materials Chemistry A*, 5 (2017) 20969-20977.
- [158] M. Zeiger, S. Fleischmann, B. Krüner, A. Tolosa, S. Bechtel, M. Baltes, A. Schreiber, R. Moroni, S. Vierrath, S. Thiele, V. Presser, Influence of Carbon Substrate on the Electrochemical Performance of Carbon/Manganese Oxide Hybrids in Aqueous and Organic Electrolytes, *RSC Advances*, 6 (2016) 107163-107179.
- [159] G. Kickelbick, Introduction to Hybrid Materials, *Hybrid Materials*, (2006) 1-48.
- [160] S. Fleischmann, D. Leistenschneider, V. Lemkova, B. Krüner, M. Zeiger, L. Borchardt, V. Presser, Tailored Mesoporous Carbon/Vanadium Pentoxide Hybrid Electrodes for High Power Pseudocapacitive Lithium and Sodium Intercalation, *Chemistry of Materials*, 29 (2017) 8653-8662.
- [161] D.A. Loy, Sol-Gel Processing of Hybrid Organic-Inorganic Materials Based on Polysilsesquioxanes, *Hybrid Materials*, (2006) 225-254.
- [162] E. Talaie, P. Bonnicks, X. Sun, Q. Pang, X. Liang, L.F. Nazar, Methods and Protocols for Electrochemical Energy Storage Materials Research, *Chemistry of Materials*, 29 (2017) 90-105.
- [163] D. Weingarh, M. Zeiger, N. Jäckel, M. Aslan, G. Feng, V. Presser, Graphitization as a Universal Tool to Tailor the Potential-Dependent Capacitance of Carbon Supercapacitors, *Advanced Energy Materials*, 4 (2014) 1400316.
- [164] K. Izutsu, Overview of Electrochemical Techniques, in: K. Izutsu (Ed.) *Electrochemistry in Nonaqueous Solutions*, Wiley-VCH Verlag, 2003, pp. 107-165.
- [165] S. Ardizzone, G. Fregonara, S. Trasatti, "Inner" and "Outer" Active Surface of  $\text{RuO}_2$  Electrodes, *Electrochimica Acta*, 35 (1990) 263-267.
- [166] M. Opitz, J. Yue, J. Wallauer, B. Smarsly, B. Roling, Mechanisms of Charge Storage in Nanoparticulate  $\text{TiO}_2$  and  $\text{Li}_4\text{Ti}_5\text{O}_{12}$  Anodes: New Insights from Scan rate-dependent Cyclic Voltammetry, *Electrochimica Acta*, 168 (2015) 125-132.
- [167] J.W. Dibden, N. Meddings, J.R. Owen, N. Garcia-Araez, Quantitative Galvanostatic Intermittent Titration Technique for the Analysis of a Model System with Applications in Lithium-Sulfur Batteries, *ChemElectroChem*, 5 (2018) 445-454.
- [168] W. Weppner, Determination of the Kinetic Parameters of Mixed-Conducting Electrodes and Application to the System  $\text{Li}_3\text{Sb}$ , *Journal of The Electrochemical Society*, 124 (1977) 1569.
- [169] W. Weppner, R.A. Huggins, Electrochemical Methods for Determining Kinetic Properties of Solids, *Annual Review of Materials Science*, 8 (1978) 269-311.
- [170] C.J. Wen, Thermodynamic and Mass Transport Properties of "LiAl", *Journal of The Electrochemical Society*, 126 (1979) 2258.
- [171] A. Krause, A. Balducci, High Voltage Electrochemical DoubleLayer Capacitor containing Mixtures of Ionic Liquids and Organic Carbonate as Electrolytes, *Electrochemistry Communications*, 13 (2011) 814-817.
- [172] D. Weingarh, A. Foelske-Schmitz, R. Kötz, Cycle versus Voltage Hold - Which is the Better Stability Test for Electrochemical DoubleLayer Capacitors?, *Journal of Power Sources*, 225 (2013) 84-88.
- [173] D. Cericola, P.W. Ruch, A. Foelske-Schmitz, D. Weingarh, R. Kötz, Effect of Water on the Aging of Activated Carbon Based Electrochemical Double Layer Capacitors During Constant Voltage Load Tests, *International Journal of Electrochemical Science*, 6 (2011) 988-996.
- [174] P.W. Ruch, D. Cericola, A. Foelske-Schmitz, R. Kötz, A. Wokaun, Aging of Electrochemical DoubleLayer Capacitors with Acetonitrile-based Electrolyte at Elevated Voltages, *Electrochimica Acta*, 55 (2010) 4412-4420.

- [175] K. Fic, A. Płatek, J. Piwek, J. Menzel, A. Ślesiński, P. Bujewska, P. Galek, E. Frąckowiak, Revisited Insights Into Charge Storage Mechanisms in Electrochemical Capacitors with Li<sub>2</sub>SO<sub>4</sub>-based Electrolyte, *Energy Storage Materials*, 22 (2019) 1-14.
- [176] K. Xu, M.S. Ding, T. Richard Jow, A Better Quantification of Electrochemical Stability Limits for Electrolytes in Double Layer Capacitors, *Electrochimica Acta*, 46 (2001) 1823-1827.
- [177] K. Xu, Toward Reliable Values of Electrochemical Stability Limits for Electrolytes, *Journal of The Electrochemical Society*, 146 (1999) 4172.
- [178] D. Weingarh, H. Noh, A. Foelske-Schmitz, A. Wokaun, R. Kötz, A Reliable Determination Method of Stability Limits for Electrochemical Double Layer Capacitors, *Electrochimica Acta*, 103 (2013) 119-124.
- [179] D. Moosbauer, S. Jordan, F. Wudy, S.S. Zhang, M. Schmidt, H.J. Gores, Determination of Electrochemical Windows of Novel Electrolytes for Double Layer Capacitors by Stepwise Cyclic Voltammetry Experiments, *Acta Chimica Slovenica*, 56 (2009) 218-224.